UNIVERSITY OF ALBERTA

THE RESPONSE OF COUPLED PROTON SPIN SYSTEMS TO IN VIVO NUCLEAR MAGNETIC RESONANCE SPECTROSCOPY EXPERIMENTS

BY

RICHARD BRYAN THOMPSON ©

A thesis submitted to the Faculty of Graduate Studies and Research in partial fulfillment of the requirements for the degree of DOCTOR OF PHILOSOPHY

In

MEDICAL SCIENCES – BIOMEDICAL ENGINEERING

Edmonton, Alberta

Fall 1999

National Library of Canada
Acquisitions and Bibliographic Services
395 Wellington Street
Ottawa ON K1A 0N4
Canada

Bibliothèque nationale du Canada
Acquisitions et services bibliographiques
395, rue Wellington
Ottawa ON K1A 0N4
Canada

Your file Votre référence

Our file Notre référence

The author has granted a non-exclusive licence allowing the National Library of Canada to reproduce, loan, distribute or sell copies of this thesis in microform, paper or electronic formats.

L'auteur a accordé une licence non exclusive permettant à la Bibliothèque nationale du Canada de reproduire, prêter, distribuer ou vendre des copies de cette thèse sous la forme de microfiche/film, de reproduction sur papier ou sur format électronique.

The author retains ownership of the copyright in this thesis. Neither the thesis nor substantial extracts from it may be printed or otherwise reproduced without the author's permission.

L'auteur conserve la propriété du droit d'auteur qui protège cette thèse. Ni la thèse ni des extraits substantiels de celle-ci ne doivent être imprimés ou autrement reproduits sans son autorisation.

0-612-46933-6

Canada

University of Alberta

Library Release Form

Name of Author: Richard Bryan Thompson

Title of Thesis: The Response of Coupled Proton Spin Systems to In Vivo Nuclear Magnetic Resonance Spectroscopy Experiments

Degree: Ph.D.

Year this Degree Granted: 1999

Permission is hereby granted to the University of Alberta Library to reproduce single copies of this thesis and to lend or sell such copies for private, scholarly, or scientific research purposes only.

The author reserves all other publication and other rights in association with the copyright in the thesis, and except as hereinbefore provided, neither the thesis nor any substantial portion thereof may be printed or otherwise reproduced in any material form whatever without the author's prior written permission.

Richard Thompson

Richard Bryan Thompson
10145-84th Avenue, # 6
Edmonton, AB
T6E 2G3

DATE: Oct. 4, 1999

University of Alberta

Faculty of Graduate Studies and Research

The undersigned certify that they have read, and recommend to the Faculty of Graduate Studies and Research for acceptance, a thesis entitled **The Response of Coupled Proton Spin Systems to In Vivo Nuclear Magnetic Resonance Spectroscopy Experiments** submitted by **Richard Bryan Thompson** in partial fulfillment of the requirements for the degree of **Doctor of Philosophy** in **Medical Sciences – Biomedical Engineering**.

Dr. P.S. Allen (Supervisor)

Dr. B.D. Sykes

Dr. R.E.D. McClung

Dr. A.H. Willman

Dr. W.R.W. Martin

Dr. P.C. Van Zijl

DATE: Oct. 4, 1999

For my Mom and Dad who have made everything possible

For Gillian who has made it all worth while

ABSTRACT

In-vivo proton magnetic resonance spectroscopy (MRS) boasts the capability to provide quantifiable metabolite information (spectra) acquired from living tissue, an established procedure for the target metabolites containing uncoupled spin groups. Unfortunately, the majority of the metabolite spin systems found in-vivo comprise systems of scalar-coupled spins that, unlike the uncoupled groups, contribute complex multiplets of peaks with elaborate responses to the pulse sequences used to observe them. In addition to these complex signal modulations, the similarity of several of the proton spin systems found in-vivo results in significant spectral overlap, making unique identification problematic. Furthermore, metabolite quantification is hampered by a limited signal to noise ratio, inherent to NMR techniques, necessitating an optimization of the metabolite signal yield. The objective of this thesis was to evaluate and optimize the response of several of the metabolite spin systems found in-vivo to the realistic NMR pulse sequences used to observe them.

To provide a framework in which the most demanding strongly-coupled spin systems could be treated, including the influence of time-dependent radio frequency pulses, a numerical method of evaluation that incorporated the density matrix representation of the spin systems was developed. The Hamiltonian used included, in addition to the Zeeman interaction, the rf pulses, the gradient pulses, the chemical shielding interaction, as well as the scalar and dipolar coupling interactions.

The response of several scalar-coupled spin systems found in-vivo, including lactate, glutamate and glutamine, as well the aspartyl group of N-acetylaspartate, to a variety of in-vivo pulse sequences was calculated. A complete single voxel multiple quantum filter sequence was developed for the observation of glutamate, providing discrimination from the nearly identical glutamine resonances. The response of the coupled-spin systems to the single voxel PRESS and STEAM sequences were also calculated, with a focus on the characterization and optimization of those responses for the purposes of quantification. Finally, the influence of the direct dipole-dipole interaction, on the responses of both the Cr / PCr spins found in muscle and a concentrated pool of water spins, to in-vivo pulse sequences, were calculated. The calculated metabolite responses were in excellent agreement to both phantom and in-vivo results at 3 T.

ACKNOWLEDGEMENTS

First and foremost I would like to acknowledge the efforts of my supervisor, Dr. Peter Allen, whose scientific lucidity and guidance has made my years in Biomedical Engineering worthwhile. Additionally, his ceaseless fundraising and administrative efforts has made the In-Vivo NMR unit a first class research facility and an excellent learning center. I would like to thank Dr. Zoltan Koles and Dr. Rick Snyder for serving as chairmen at my candidacy and final exams, respectively, but more importantly, for their approachability and willingness to help with any problems I had over the years. I greatly appreciate the investment of time by my supervisory committee members, Dr. Ted McClung, Dr. Brian Sykes and Dr. Gwyn Hughes. Additionally, I was honored to have Dr. Peter Van Zijl as the external examiner at my defense, who managed to come up with dozens of probing questions with an advance reading of my thesis limited to his flight into Edmonton.

The staff at the NMR facility is deserving of great praise. On a daily basis Dr. Chris Hanstock was a wellspring of practical NMR knowledge and provided an ever friendly ear for discussions of any nature. Dr. Alan Wilman's graduate work in NMR spectroscopy provided the starting point for my own research, and his enthusiasm for NMR was always inspiring. Karim Damji taught me the fine art of r.f. coil design and to appreciate the patient and thorough demeanor. Nothing technical could have been accomplished without the efforts of Dan Gheorghiu, who makes everything that has a power cord work. I must thank Carol Tymchuck for taking the headache out of scholarships, publishing and the countless daily tasks that would have otherwise driven me insane years ago. I also appreciate the ever present Maisie 'panic button' Goh for not letting me get too relaxed.

Fellow graduate students (Dr.) Christian Beaulieu and (Dr.) Mark Does must be acknowledged for countless rounds of golf, pints of beer, hours of poker, and for being excellent ISMRM traveling companions and true friends. To maintain perspective, my long time friends Jamie Brown, Stephen Toal and Derek Hermanutz always provided the balance I needed, be it through sport, drink, music or humor. I would also like to thank Nick, Jim, Osama, Kim, Steven, Keith and Atiyah for companionship and soccer, which should be an integral part of any workplace.

I appreciate funding received from the Alberta Heritage Foundation for Medical Research (AHFMR), the Natural Sciences and Engineering Research Council of Canada (NSERC), and the University of Alberta, allowing me to live above the poverty line.

Most importantly, I must thank my parents, Murray and Cecile, who have supported me in every aspect during my over two decades of schooling. Nothing would be possible without them. I also appreciate the support of my brother, Grant, and sisters, Susan and Danielle, and their families. Finally, I have to praise the patience and support of Gillian Mah. Her undying faith in me, tolerance of the strange hours I keep, and her insistence that some day I will 'discover something' kept me going over the years, that and the sustenance provided by Mr. and Mrs. Mah's home cooking.

Table of Contents

	Page
Chapter 1 Introduction and Background	1
1.1 Introduction	1
1.2 Spin ½ States	5
1.2.1 Spin Vector Space	6
1.2.2 Spin Operators	7
1.2.3 The Operator Matrix Representation	7
1.2.4 Expectation Values of Operators	9
1.3 The Density Matrix	12
1.3.1 Statistical Interpretation of the Density Matrix – Populations and Coherence	13
1.3.2 Density Matrix at Thermal Equilibrium – Spins in a Static Magnetic Field	16
1.3.3 Time Evolution of the Density Matrix – Time Independent Hamiltonians	21
1.3.4 Radio-Frequency Pulses and the Density Matrix – Generation of Coherence	23
1.3.5 Chemical Shift – Off Resonance Excitation	29
1.3.6 Scalar Coupling	34
1.3.6.1 The Two Pulse Experiment	42
1.3.6.1a Weak Coupling and the Product Operator Formalism	42
1.3.6.1b The Full Coupling Model and Numerical Solutions of the Density Matrix	45
1.3.7 Magnetic Field Gradients	48
1.3.7.1 Gradients and R.F. Pulses – Spectrally to Spatially Selective Excitation	51
1.3.7.2 Gradients and Coupled Spin Systems – Coherence Selection	54
1.3.8 Direct Spin-Spin Coupling - Dipolar Coupling	55
1.4 The Metabolite Spin Systems	58
1.5 References	66
Chapter 2 Numerical Methods	78
2.1 Introduction	78
2.2 Simulation Structure	81
2.3 Transverse Magnetization – FID (Spectrum) Calculation	85
2.4 Time-Dependent Hamiltonians – An Approximate Method of Evaluation	90
2.4.1 Shaped Radio-Frequency Pulses	90
2.4.1.1 Shaped R.F. Pulses – Spatial Distribution of Coherences	94
2.4.1.2 Shaped R.F. Pulses – The Integrated Effect - The Transformation Matrix	97
2.5 Pulse Sequence Optimization	109
2.6 References	112
Chapter 3 A New Multiple Quantum Filter Design Procedure for Use on Strongly Coupled Spin Systems Found In Vivo: Its Application to Glutamate	114
3.1 Introduction	114
3.2 Composite Double Quantum Filter Design	115
3.2.1 The Pulses	116
3.2.2 The Timings	118
3.2.3 The Procedure	118
3.3 Testing of the Composite DQF Design	124
3.4 Summary and Conclusions	128
3.5 References	131

Chapter 4 The Role of the N-actylaspartate Multiplet in the Quantification of Brain Metabolites 134

4.1 Introduction 134
4.2 Response of PRESS (TE_1 and TE_2 Dependence) 136
4.2.1 Hard Pulse Limit 137
4.2.2 Selective Pulses Induced Slice Effects 139
4.3 Discussion 142
4.4 References 143

Chapter 5 A Demonstration of the Sources of Variability in the Response of Coupled Spins to the PRESS Sequence and their Potential Impact on Metabolite Quantification 146

5.1 Introduction 146
5.2 Intra-180°-Pulse Effects in the PRESS Sequence (Weak Coupling Illustration 148
5.3 Strong Coupling Effects in the PRESS Sequence (Glu Illustartion) 153
5.4 Experimental Results 157
5.5 Summary and Discussion 159
5.6 References 162

Chapter 6 The Response of Metabolites with Coupled Spins to the STEAM Sequence 165

6.1 Introduction 165
6.2 Numerical Methods 167
6.3 The STEAM Sequence 167
6.3.1 R.F. Pulse Design Effects 179
6.3.2 ZQC Effects -in TM 172
6.3.3 The Acquisition Period 174
6.4 In-Vivo Validation 182
6.5 Discussion 183
6.6 References 186

Chapter 7 The Residual Intra-molecular Dipolar Coupling of the Cr / PCr Methyl Resonance in Resting Human Medial Gastrocnemius Muscle and the Influence of Inter-molecular Dipolar Coupling of Water in In Vivo Multiple Quantum Filters 188

7.1 Intra-Molecular Dipolar Coupling (Cr / PCr) 188
7.1.1 Introduction 188
7.1.2 Methods 190
7.1.3 Results and Discussion 192
7.2 Inter-Molecular Dipolar Coupling (Water) 197
7.2.1 Introduction 197
7.2.2 The Multiple Quantum Filter 198
7.2.3 Theory 200
7.2.4 Results 202
7.2.5 Discussion 207
7.3 References 209

Chapter 8 Concluding Remarks 212

8.1 The Utility of a Numerical Approach in NMR Problem Solving 213
8.1.1 Time-Dependent Hamiltonians 214
8.1.2 Pulse Sequence Optimization 214
8.2 Future Applications 215

Appendix I The Weak Coupling Product Operator Transformation Rules for a Two Spin System 216

Appendix II Matrix Representation of the Two-Spin Cartesian Basis Operators (Spin-½ System) 219

Appendix III Evaluation of the chemical shifts and scalar couplings for select Metabolite Spin systems 220

Appendix IV The CRAZED Pulse Sequence – Product Operator Evaluation of the Tip Angle Signal Dependence 228

Appendix V MATLAB™ PROGRAMS 231

LIST OF TABLES

		Page
1.1	Aspartate (Asp) Scalar-Couplings and Chemical Shifts	60
1.2	Creatine (Cr) and Choline (Cho) Scalar-Couplings and Chemical Shifts	60
1.3	γ-Amino Butyric Acid (GABA) Scalar-Couplings and Chemical Shifts	61
1.4	Glutamate (Glu) Scalar-Couplings and Chemical Shifts	61
1.5	Glutamine (Gln) Scalar-Couplings and Chemical Shifts	62
1.6	Glutathione (GSH) Scalar-Couplings and Chemical Shifts	62
1.7	Glycine (Gly) Scalar-Couplings and Chemical Shifts	63
1.8	Lactate (Lac) Scalar-Couplings and Chemical Shifts	63
1.9	Myo-Inositol (Ino) Scalar-Couplings and Chemical Shifts	64
1.10	N-Acetylaspartate (NAA) Scalar-Couplings and Chemical Shifts	64
1.11	N-Acetylaspartateglutamate (NAAG) Scalar-Couplings and Chemical Shifts	65
1.12	Taurine (Tau) Scalar-Couplings and Chemical Shifts	65
2.1	Transformation Matrix Efficiency – The ABX Spin-System	105
3.1	Chemical Shifts, δ ppm, and Scalar Coupling J Hz, For the AMNPQ Systems of Glu and Gln	119

LIST OF FIGURES

		Page
1-1	Energy level diagram of a 1-member spin ½ system in a static magnetic field	17
1-2	A vector model representation of spin ½ thermal equilibrium in a static magnetic field B_o	20
1-3	A simple pulse acquire NMR experiment	26
1-4	The Fourier transformation of the NMR transverse magnetization	28
1-5	The Evolution of the Cartesian Magnetization Components of an Uncoupled Spin System Throughout a Excitatory Rectangular r.f. Pulse	33
1-6	Proton Spectrum of an AX spin system – Example	34
1-7	Energy level diagram of a 2-member spin ½ system in a static magnetic field	38
1-8	The Density Matrix Representations of In-Phase and Anti-phase Coherences	40
1-9	Free Evolution of the In-Phase and Anti-phase Coherences of an AX Spin System Excited From Thermal Equilibrium	46
1-10	Generation of ZQC and DQC For an AX Spin System Excited With a Two-Pulse Experiment as a Function of the Inter-Pulse Delay	47
1-11	An Illustration of the Dephasing Effects of Magnetic Field Gradients	50
1-12	The Rectangular Excitation Pulse – Fourier Transformation Predictions of Frequency Selective Excitation	51
1-13	Spectral Excitation Profile of the Cartesian Magnetization Components of an Uncoupled Spin System – Excitation by a 1 ms Rectangular Pulse	52
1-14	A Comparison of the Calculated NMR Excitation Profile and Fourier Predictions for a Rectangular Excitation Pulse	53
1-15	The Molecular Structures and NMR Visible Protons of the Abundant Brain Metabolites	58
1-16	A Calculated (1 Hz) Pulse Acquire Spectrum for a Unit Contribution of Aspartate (Asp)	60
1-17	A Calculated (1 Hz) Pulse Acquire Spectrum for a Unit Contribution of Creatine (Cr) and Choline (Cho)	60
1-18	A Calculated (1 Hz) Pulse Acquire Spectrum for a Unit Contribution of γ-Amino Butyric Acid (GABA)	61
1-19	A Calculated (1 Hz) Pulse Acquire Spectrum for a Unit Contribution of Glutamate (Glu)	61

1-20 A Calculated (1 Hz) Pulse Acquire Spectrum for a Unit Contribution of Glutamine (Gln) 62
1-21 A Calculated (1 Hz) Pulse Acquire Spectrum for a Unit Contribution of Glutathione (GSH) 62
1-22 A Calculated (1 Hz) Pulse Acquire Spectrum for a Unit Contribution of Glycine (Gly) 63
1-23 A Calculated (1 Hz) Pulse Acquire Spectrum for a Unit Contribution of Lactate (Lac) 63
1-24 A Calculated (1 Hz) Pulse Acquire Spectrum for a Unit Contribution of Myo-Inositol (Ino) 64
1-25 A Calculated (1 Hz) Pulse Acquire Spectrum for a Unit Contribution of N-Acetylaspartate (NAA) 64
1-26 A Calculated (1 Hz) Pulse Acquire Spectrum for a Unit Contribution of N-Acetylaspartateglutamate (NAAG) 65
1-27 A Calculated (1 Hz) Pulse Acquire Spectrum for a Unit Contribution of Taurine (Tau) 65

2-1 The Two Pulse COSY Experment 80
2-2 A Pulse Sequence Comprising Two Rectangular Pulses and Two Delays is sectioned into Four Segments, Corresponding to Four Time-Independent Hamiltonians 81
2-3 A Storage Matrix Containing Evolution Operators Used in the Simulation of NMR Pulse Sequences 83
2-4 The Raising Operator for a Two-Spin System is Transformed to a Frame of Reference in which the System Hamiltonian is Diagonal 87
2-5 Spectra Excited from an AB Spin System by a Two-pulse Experiment are Calculated Using Two Different Approaches 89
2-6 A Time-Dependent R.F. Pulse Envelope is Segmented into Consecutive Time-Independent Rectangular Components 91
2-7 The Excitation Profile of a $\pi/2$ Sinc-Pulse is Calculated and the Error in the Profile is Displayed as a Function of the Number of Segments used to Model the Time-Dependent R.F. Envelope 92
2-8 The Single-Voxel STEAM, PRESS and DQF Sequences 93

2-9 The Excitation Profile of a $\pi/2$ Sinc-Pulse is Calculated for Two Spin Species with Different Chemical Shifts 95
2-10 The Spatial Distribution of Several Transverse Coherences Excited by a Spectrally Selective π pulse are Illustrated 96
2-11 The Mathematical Implementation of the Transformation Matrix is Illustrated 99
2-12 The Influence of a Simple Two-Step Phase-Cycling Routine used for Spatially-Selective Excitation is Illustrated for a Refocusing Pulse 101
2-13 A Cartesian Product Operator Transformation Matrix for a Two-Spin System and a 3 ms Optimized Sinc-Like Refocusing Pulse 102
2-14 A Cartesian Product Operator Transformation Matrix for a Two-Spin System and a 2 ms Gaussian Refocusing Pulse 103
2-15 A Single Element Transformation Matrix for a Two-Spin System and a 3 ms Optimized Sinc-Like Refocusing Pulse 104
2-16 A Single Element Transformation Matrix for a Two-Spin System and a 2 ms Gaussian Refocusing Pulse 104
2-17 Calculated PRESS (112 ms, 24 ms) NAA ABX spectra, With Two Dimensions of Spatial Localization Provided by Optimized Sinc-Like Refocusing Pulses 106
2-18 Calculated PRESS (112 ms, 24 ms) NAA ABX Spectra, With No Spatial Localization (Hard Pulse Model) 107
2-19 Calculated PRESS (112 ms, 24 ms) NAA ABX Spectra, With Two Dimensions of Spatial Localization Provided by GausSian Refocusing Pulses 107
2-20 A Pulse Acquire Spectrum from an ABC Spin System 109
2-21 A Filled Contour Plot Displays the Peak Value of on ABC Spin System as a Function of the PRESS Timings 110
2-22 Calculated ABC PRESS Spectra for Timings A) (16 ms, 16 ms) and B) (110 ms, 20 ms). 111

3-1 A Schematic Diagram of a Single Voxel Double Quantum Filter 116
3-2 Calculated Multiplet Spectra for the MNPQ Spins of Both Glu and Gln at a Field Strength of 3 T 120
3-3 A Contour Plot Displays the Efficiency of a DQF Designed to Excite a Target Glu Resonance Line as a function of the DQF Echo times 122

3-4 A Contour Plot Displays the Efficiency of a DQF Designed to Excite a Target Glu Resonance Line as a function of Read Pulse Properties 123
3-5 A Plot Displays the Efficiency of a DQF Designed to Excite a Target Glu Resonance Line as a function of the DQF Mixing Time 123
3-6 A Comparison of Calculated and Experimental Glu Spectra Excited with an Optimized Glu DQF Sequence 124
3-7 A Comparison of Calculated, Experimental Phantom and In-Vivo Spectra Excited with an Optimized Glu DQF Sequence 125
3-8 A Comparison of Calculated Glu and Gln Spectra Excited with an Optimized Glu DQF Sequence 126
3-9 A Demonstration of the Spatial Integrity of the Single Voxel DQF Sequence Optimized to Observe Glu 127

4-1 Calculated Pulse Acquire Spectra for the Significantly Contribution Brain Metabolites in the 2.0 to 2.8 ppm Range 135
4-2 A Filled Contour Plot Displays the Peak Value of the NAA AB Multiplet as a Function of the PRESS Echo Times (Hard Pulse Model 137
4-3 A Comparison of Calculated and Experimental NAA AB Spectra for Several PRESS Echo-Time Combinations (Hard Pulse Model 138
4-4 A Filled Contour Plot Displays the Peak Value of the NAA AB Multiplet as a Function of the PRESS Echo Times (Soft Pulse Model 139
4-5 The Spatial Distribution of Two NAA ABX Transverse Coherences Excited by the PRESS Refocusing Pulses over Two Dimensions are Illustrated 140
4-6 A Comparison of Calculated and Experimental NAA AB Spectra for Several PRESS Echo-Time Combinations (Soft Pulse Model 141

5-1 Transformation Matrices of a Representative Set of Lactate Coherences for Five Variants of a π Refocusing Pulse 149
5-2 An Illustration of the Slice Distribution of Several Transverse Coherences Excited by Several Variants of a π Refocusing Pulse 151
5-3 A Contour Plot Displays the Integrated Lactate Doublet Intensity as a Function of the PRESS Echo Times 153

5-4 Contour Plots Display the Peak Value of the Glu PQ Multiplet as a Function of the PRESS Echo Times for Both Hard Pulse and Soft Pulse Models 155
5-5 The Evolution of the Glu Transverse Coherences During the First PRESS Echo time are Displayed 156
5-6 A Comparison of Calculated and Experimental Glu PRESS Spectra for Two Echo-Time Combinations 158

6-1 A Schematic Diagram Illustrates the Evolution of the Key Coupled-Spin Coherences Throughout the STEAM Sequence 168
6-2 Transformation Matrices of a Representative Set of Lactate Coherences for Two Variants of a $\pi/2$ Pulse Used in the STEAM Sequence 170
6-3 The Spatial Distribution of Two NAA ABX Transverse Coherences Excited by the Two STEAM $\pi/2$ Pulses over Two Dimensions are Illustrated 171
6-4 The Evolution of Lactate and NAA (ABX) ZQC Terms, from a Single Initial ZQC Term, Throughout the STEAM Mixing Period is Illustrated 173
6-5 A Filled Contour Plot Displays the Integrated Lactate Doublet Intensity as a Function of the STEAM Timings TE and TM 175
6-6 Filled Contour Plots Display the Contributions of Two NAA ABX Transverse Coherences as a Function of the STEAM Timings TE and TM 177
6-7 A Filled Contour Plot Displays Peak Value of the NAA AB Multiplet as a Function of the STEAM Timings TE and TM 178
6-8 Numerically Calculated and Measured STEAM NAA Spectra 179-180
6-9 A Filled Contour Plot Displays the Intensity of the Upfield Glu PQ resoncance as a Function of the STEAM Timings TE and TM 181
6-10 Numerically Calculated and Measured STEAM Glu Spectra 182
6-11 Numerically Calculated and Measured In-Vivo STEAM Brain Spectra are Compared 183

7-1 A Typical PRESS-Localised Proton Cr / PCr Spectrum Obtained From 2x2x3 cm^3 of Resting Medial Gastrocnemius Muscle at 3T 192
7-2 A Series of Numerically Calculated Spectra Illustrating the Predicted Dipolar Evolution of the Cr/PCr Triplet as a Function of TE for a Symmetric PRESS Sequence 194

7-3 Calculated and Measured Values of the TE Evolution of the Central Peak of the Cr / PCr Methyl Triplet 196
7-4 The CRAZED Pulse Sequence 199
7-5 The Single Voxel Double Quantum Filter Pulse Sequence and the Pseudo-CRAZED Pulse Sequence Contained Within It 200
7-6 The Measured CRAZED Signal Dependence on the Ratio of the Second to the First Filter Gradient Areas 202
7-7 The Measured Free Induction Decay Excited by the CRAZED Pulse Sequence for the Double Quantum Filter Gradient Ratio, 1:2 203
7-8 The Measured Double Quantum CRAZED Signal is Plotted as a Function of the Gradient Angle to the Main Field, Along with Theoretical Dependence 203
7-9 The Measured Double Quantum CRAZED Signal is Plotted as a Function of the Tip Angle, $\alpha°$, of the Second Pulse, Along with Theoretical Dependence 204
7-10 The Spectral Selectivity of the CRAZED Pulse Sequence Incorporating a Spectrally Selective Pulse 205
7-11 An Imaging Evaluation of the Single Voxel Double Quantum Filter Sequence 206
7-12 Single voxel DQ Filtered Glu Phantom Spectra 208

AIII-1 A 500 MHz NAAG Pulse Acquire Spectrum 220
AIII-2 A 500 MHz NAAG Spectrum – ABX Group Characterization 221
AIII-3 A 500 MHz NAAG Pulse Acquire Spectrum 221
AIII-4 A 500 MHz NAAG Pulse Acquire Spectrum – $AMNP_2$ group characterization 222
AIII-5 A 500 MHz Glu Pulse Acquire Spectrum 223
AIII-6 A 500 MHz Glu spectrum – A Group Characterization 223
AIII-7 A 500 MHz Glu spectrum – MNPQ Group Characterization 224
AIII-8 A 500 MHz Gln Pulse Acquire Spectrum 225
AIII-9 A 500 MHz Gln spectrum – A Group Characterization 225
AIII-10 A 500 MHz Gln spectrum – MNPQ Group Characterization 226
AIII-11 A 500 MHz Ino spectrum – AM_2N_2P Group Characterization 227

AV-1 The Main NMR Simulation Window 231
AV-2 Specifying a Metabolite Spin System on the Main Simulation Window 232
AV-3 The Pulse Sequence Editor Window 233

AV-4 Specification of a DQF Sequence Along with the Corresponding Sequence of R.F. Pulses and Gradients 234
AV-5 Specification of a coupled Two Spin System in an Field Strength of 3 T 236
AV-6 Specification of a Spin-Echo Pulse Sequence in the Sequence Editor Window 226
AV-7 A Spin-Echo Pulse Sequence with a Spatially Selective Optimized Sinc Refocusing Pulse and a Hard Excitation Pulse 238
AV-8 The Simulation Results Window 241
AV-9 The Results Window Displays an Aspartate Pulse Acquire Spectrum 242
AV-10 The Results Window Displays a Contour Plot of the Peak Value of the Aspartate AB Multiplet as a Function of PRESS Echo Times 243
AV-11 The Results Window Displays a Contour Plot of Expectation Values of the ABX Spin Operator $2I_{1_z}I_{2_x}$ as a Function of Press Echo Times 244

LIST OF SYMBOLS AND ABBREVIATIONS

$A_{x,y,z}$	Cartesian spin angular momentum operators
Acq	Signal acquisition time
Asp	Aspartic acid
B_o	Static magnetic field
B_1	Radio-frequency magnetic field
Cho	Choline
COSY	Correlation Spectroscopy
Cr	Creatine
CRAZED	COSY revamped with asymmetric z-gradient echo detection
DQC	Double quantum cohernce
DQF	Double quantum filter
$\delta\omega$	Chemical shift difference
E	Energy
FWHM	Full width half maximum
G	Static magnetic field gradient
GABA	γ-Aminobutyric Acid
γ	Gyromagnetic or magnetogyric ratio
Glc	Glucose
Gln	Glutamine
Glu	Glutamate
Gly	Glycine
$\hbar$	Plank's constant divided by 2π
$\mathcal{H}$	Hamiltonian
I	Spin angular momentum operator
I_X, I_Y, I_Z	Cartesian spin operators
Id	The identity matrix
Ins	Myo-inositol
J	scalar coupling constant

k	Boltzmann's constant
Lac	Lactic acid
m	Magnetic quantum number
MR	Magnetic resonance
MRI	Magnetic resonance imaging
MRS	Magnetic resonance spectroscopy
MQC	Multiple quantum coherence
MQF	Multiple quantum filter
NAA	N-acetylaspartate
NAAG	N-acetylaspartatylglutamate
NMR	Nuclear magnetic resonance
PCr	Phosphocreatine
PRESS	Point resolved spectroscopy
r	Radial distance
r.f.	Radio frequency
ρ	Spin density operator (matrix)
SG	Stern-Gerlach
S/N	Signal-to-noise ratio
SQC	Single quantum coherence
STEAM	Stimulated echo acquisition mode
T	Absolute temperature
T_1	Longitudinal relaxation time constant
T_2	Transverse relaxation time constant
Tau	Taurine
TQC	Triple quantum coherence
TQF	Triple quantum filter
TE	Echo time
TM	Mixing time
τ	Evolution time
μ	Nuclear magnetic moment
ω	Angular frequency

ω_o	Larmor frequency
$\omega_{r.f.}$	r.f. frequency
ω_{rot}	Rotating frame frequency
Ψ	Spin wave function
ZQC	Zero quantum coherence

CHAPTER 1

Introduction

1.1 Introduction

Proton (^{1}H) nuclear magnetic resonance (NMR) techniques when applied in-vivo are used to observe the signals from water and high concentration metabolites, and to a lesser degree, lipid signals. The spatial distribution of the water and lipid signals are commonly observed with the clinical application called magnetic resonance imaging (MRI). MRI uses the water signals to elicit structural and functional information from tissue in the CNS, PNS and vascular systems, as well as from muscle and it's connective tissues. The information acquired from water using magnetic resonance imaging is environmental in nature, and reflects local water properties such as concentration, flow, diffusion, relaxation, magnetic coupling or preferred molecular orientation. On the other hand, to obtain insight into the underlying biochemical mechanisms of tissue pathology and metabolism, the metabolite NMR signal can provide information not available from the water protons. For example, lactate is a chemical index of glycolytic metabolism and hence of ischemia in tissues that normally depend on oxidative metabolism. Lactate can thus be used as an indicator of ischemic trauma around a stroke center in the brain (1-8), providing information not attainable with magnetic resonance imaging, or other non-invasive examinations. Among the wealth of other current magnetic resonance spectroscopy (MRS) applications that focus on the brain are the study of aging (9-12), neurodegenerative diseases such as Parkinsons disease (PD) (13-19), amyotrophic lateral sclerosis (ALS) (20-28), multiple sclerosis (MS) (29-38) and Alzheimers disease (39-45), Huntingtons corea (46-48), as well as bipolar disorder (49-58), epilepsy (59-65), cancer (66-72) and HIV/AIDS (73-82).

Despite it's potential to elicit biochemical information non-invasively, proton MRS has not achieved the clinical standing of it's sister technique, MRI, for two primary reasons. Firstly, the metabolites typically comprise coupled spin systems that contribute complex multiplets of peaks with elaborate responses to the sequences used to observe them. Such behavior can be described only with use of quantum mechanical techniques. The water proton response, on the other hand, tends to be simple and can be described with vector models. This first issue is the focus of the thesis, wherein an analysis of the

most demanding coupled proton spins systems is included. The analysis encompasses all aspects of the realistic in-vivo MRS pulse sequences, including spatial localization, and allows for the quantitative calculation (and measurement) of spectra as well as the optimization of the coupled spin response to the those sequences.

The second confounding factor is the relatively low concentration of brain metabolites. Even the most concentrated metabolites are only 0.025% as abundant as brain water, or in absolute concentrations, 10 mM versus ~20 to 55 M (83), respectively. The low metabolite abundance in conjunction with the noise inherent in both the tissue sample, and the electronics used to receive and amplify the NMR signal, represent the primary limitation of in-vivo NMR spectroscopy, namely, the low signal to noise ratio. This restriction dictates the array of metabolites that are potential candidates for in-vivo MRS detection. For example, assuming a spatial resolution of 2 cm in each dimension, the minimum observable metabolite concentration is presently of the order of 0.5 mM to 1 mM (pure H_20 is 55 M) assuming an examination length tolerable by human subjects, ranging from 15 to 60 minutes (84-86). The experiment length is determined by the number of averages, N_{ave}, needed to increase the metabolite signal above the noise signal, where the signal to noise ratio increases as $\sqrt{N_{ave}}$. The brain metabolites with concentrations that surpass the 1 mM minimum include N-acetlyaspartate (NAA), N-acetlyaspartylglutamate (NAAG), creatine (Cr), choline (Cho), glutamate (Glu), glutamine (Gln), lactate (Lac), γ-aminobutyric acid (GABA), aspartate (Asp), taurine (Tau), myo-inositol (Ins), and perhaps glycine (Gly) and glutathione (GSH). Unfortunately, several other interesting chemical species found in brain are of only μM (acetylcholine, dopamine, noradrenaline, serotonin and Histamine) or even nM (substance P, somatostatin, and luteinizing-hormone-releasing hormone) concentration (87), placing them well below the present in-vivo NMR signal to noise threshold outlined above.

Unlike the simple water spectrum, which comprises a single unobscured resonance peak, the majority of the metabolites listed above contribute multiple resonance peaks, which are further split by scalar coupling into complex multiplets. What is more, the similarity of the chemical structures of several of the metabolites results in similar spectra that can be overlapping, making unique identification

problematic. Additionally, the scalar coupling gives rise to modulations in the yield and line shape of the metabolite spectra that are functions of the parameters of the pulse sequence used to observe the spins. Identification and quantification of each individual metabolite spectrum therefore requires knowledge of the responses, of all metabolites whose spectra are overlapping, to the sequences used to observe them. The response of some of the simpler metabolite spin systems to some of the standard observing sequences, including STEAM (88-93), PRESS (94-109) and MQFs (110-119), have previously been characterized, allowing the resulting metabolite yield and line shapes to be predicted, if not optimized. Most of these analyses have included sequence parameters such as inter-pulse timings and hard pulse tip angles (90-93, 98, 101-106, 108, 112-117, 119), although few (120,121) have incorporated the *complete* set of influences that can result in signal modulation (including spatial localization), and in those cases, only for the weakly coupled spin system lactate, the simplest of the weakly-coupled spin groups found in-vivo. Of the thirteen brain metabolites previously listed, ten of them contain spins which are scalar coupled, and of these, eight are strongly coupled at in-vivo field strengths, 1.5 T to 4.0 T, placing them outside of the scope of these previous studies.

The analyses in this thesis pertain to all of the previously identified in-vivo spin systems (metabolites), and include several sources of signal variability, particularly the realistic slice-selective r.f. pulses. Several specific examples of pulse sequences are considered, including a multiple quantum filter in chapter 3, the PRESS sequence in chapters 4, 5, and 7 and the STEAM sequence in chapter 6. The responses of several coupled spin metabolites to these pulses sequences are calculated, including those of Lac, Glu, Gln, the aspartyl group of NAA and a dipolar coupled variation of the Cr / PCr methyl group. While this collection of metabolites and in-vivo pulses sequences is not exhaustive, the techniques developed in this thesis are robust and can be applied to virtually any ^{1}H spin system and in-vivo NMR experiment.

In the following sections of the introduction, the mathematical tools used to represent the state of the spin system as well as those used to evolve that system through an NMR pulse sequence are derived. To describe the interaction of the proton spins with the magnetic fields of their native molecular environment as well as with the external

fields applied as the NMR experiment, the tools of quantum mechanics provide an elegant framework. In section 1.2 the vector representation of the spin-1/2 system is introduced, leading to the matrix representation of the spin operators. A brief description of spin wavefunctions and the expectation values of operators leads to a discussion of the mixed state description of spin systems and finally then to the density matrix representation in section 1.3. Throughout section 1.3 the density matrix representation is developed as a tool to depict the properties of realistic spin systems, stressing the basic concepts of energy level population and coherence. To describe the generation of spin coherence, the dynamic equations of the density matrix are developed from the time-dependent Schrödinger wave equation, the result being the Liouville-von Neumann equation. Solutions to this powerful equation are derived in the remainder of section 1.3 in the context of both the fundamental spin properties including chemical shift, scalar-coupling and dipolar-coupling, as well as the applied fields including the static, radio-frequency and gradient magnetic fields. Finally, in section 1.4, the metabolite spin systems found in-vivo, particularly in brain, are described (chemical shifts, scalar-couplings and structures).

Chapter 2 outlines the numerical implementation of the density matrix evolution equations developed in Chapter 1. Throughout this second chapter the generality of the simulation approach and the efficiency of the numerical calculations are outlined. In each of the subsequent chapters, 3 to 7, the numerical approach is used to characterize and optimize the coupled-spin metabolite response to the aforementioned sequences (STEAM, PRESS and an in-vivo double quantum filter).

1.2 . Spin ½ States

It was determined as early as the 1920's that the electron possesses a quantized magnetic moment (122,123), even if prepared to a state of zero orbital angular momentum, based on experiments by German physicists Stern and Gerlach. This led to the postulate that these particles have an intrinsic spin angular momentum, with quantization rules analogous to the orbital case. Incorporating the orbital angular momentum conventions one can define the spin angular momentum operator, **I**, such that $\mathbf{I}^2$ has eigenvalues I(I+1), where I is half integer or integer. One can also simultaneously define eigenvalues, m, for one component of **I**, say I_Z, such that m is one of -I, -I+1, ..., I. For spin ½ systems, such as the electron and the proton, m can then take on discrete values of -½ and ½. The spin angular momentum is defined as $\mathbf{J} = \hbar\mathbf{I}$, where Plank's constant, $\hbar$, represents the fundamental quantum of action, where action is a physical quantity of dimension [energy] x [time] = [length] x [momentum]. The magnetic moment is parallel to the spin angular momentum, so that one can write $\mu = \gamma\mathbf{J}$, where γ is a constant called the gyromagnetic (or magnetogyric) ratio, which is governed by the nuclear structure. A decade after Stern and Gerlach's original experiments, it was determined that the proton, like the electron, also possesses a quantized magnetic moment (124). Isotopes that possess a non-vanishing magnetic moment include ^{1}H, ^{2}H, ^{3}H, ^{13}C, ^{19}F and ^{31}P to name a few, each of which have a unique gyromagnetic ratio. The ^{1}H nucleus consists of a single proton, so will from this point on be referred to as such.

The NMR experiment, which uses the nuclei as a probe, consists of various externally applied magnetic fields, including static, spatially varying and temporally varying components. Additionally, the nuclei are influenced by the magnetic fields produced by neighboring nuclei and electrons, both from within the host molecule as well as from neighboring molecules. It is convenient to describe the interactions of the proton spin with these magnetic fields via non-relativistic quantum mechanics. The fundamental postulates and mathematical development of non-relativistic quantum mechanics are provided in several introductory texts, that referred to most in the writing of this thesis being "Modern Quantum Mechanics" by J. J. Sakurai (125).

1.2.1 Spin Vector Space

To describe the properties of the proton spin as well as its interaction with external magnetic fields, the elementary mathematical vector space methods of quantum mechanics will be introduced. In the language of quantum mechanics the properties of the proton spin, or it's physical state, is represented by a state vector. For example, in the Strern-Gerlach (SG) experiment that led to the postulate of the existence of the spin angular momentum, the free electron in a silver atom was found to posses two distinct spin orientations or spin states, called spin up and spin down. Incorporating Dirac's **bra** and **ket** notation for basis state representation (125), the spin ket can be represented by a two element column vector, with two orthogonal components, corresponding to spin up and spin down states, with row vectors for the associated bra vectors.

$$|\uparrow\rangle = \begin{vmatrix} 1 \\ 0 \end{vmatrix} \quad |\downarrow\rangle = \begin{vmatrix} 0 \\ 1 \end{vmatrix} \quad \langle\uparrow| = \langle 1\ 0| \quad \langle\downarrow| = \langle 0\ 1|. \tag{1-1}$$

These vectors satisfy orthonormality criteria

$$\langle a|a'\rangle = \delta_{aa'}, \text{ where } a = \uparrow \text{ or } \downarrow, \tag{1-2}$$

as well, they form a complete basis set, represented mathematically as

$$\sum_a |a\rangle\langle a| = \text{Id, where Id is the identity matrix.} \tag{1-3}$$

An arbitrary ket can be expanded in terms of a complete set of orthonormal kets, such as those introduced in Eq. (1-1), if all the kets share the same vector space. The dimensionality of this vector space is determined by the number of alternative states the system can exist in, two in the case of a single proton or electron, both of which are spin ½ systems.

1.2.2 Spin Operators

Each of the observable (and several non-observable) quantities associated with the spin has a corresponding operator, a mathematical abstraction that allows the properties of the observable to be represented in vector space. For example, the SG apparatus *measured* the $\hat{z}$-component of the magnetic moment of the beam of silver atoms, which is parallel and proportional to the spin angular momentum, by moving the atoms through a magnetic field. The operator corresponding to this measured spin angular momentum is the spin operator I_Z. The two possible values of the electron spin angular momentum were found by Stern and Gerlach to be $\pm\hbar/2$, corresponding to the eigenvalues of I_Z, $\pm$½. When one is in the eigenbasis of the operator I_Z, the spin up and spin down kets are eigenkets of I_Z, allowing one to write the eigenvalue equations

$$I_Z|\uparrow\rangle_Z = +1/2|\uparrow\rangle_Z \quad \text{and} \quad I_Z|\downarrow\rangle_Z = -1/2|\downarrow\rangle_Z \,, \tag{1-4}$$

where the 'Z' subscripts indicates that the basis vectors are eigenkets of the operator I_Z. The SG apparatus contained a $\hat{z}$-directed magnetic field, defining the direction of quantization arbitrarily as the $\hat{z}$-direction. Rotating this field to the $\hat{x}$ or $\hat{y}$ direction will result in identical eigenvalue equations (1-4) for operators I_X or I_Y, respectively. However, the properties of the I_X and I_Y operators in the I_Z eigenbasis are not represented by eigenvalue equations. The transverse operator equations will be defined in terms of the eigenvalue equations above following an introduction of the matrix representation of operators.

1.2.3 The Operator Matrix Representation

Every spin operator can be expressed as a matrix, which will prove to be the most pragmatic form when a numerical quantum mechanical approach is used to describe the spin dynamics of the large and strongly coupled spin systems found in-vivo. The matrix form of an operator, A, can be derived by employing the completeness relation of Eq. (1-3). Because the identity matrix can be multiplied by any other matrix of the same dimension without altering it, one can express any operator, A, as

$$A = \sum_{a''} \sum_{a'} |a''\rangle\langle a''| A |a'\rangle\langle a'|. \tag{1-5}$$

Expanding the sums, this operator can be expressed explicitly in matrix form as

$$A = \begin{pmatrix} \langle a_1|A|a_1\rangle & \langle a_1|A|a_2\rangle & \cdots \\ \langle a_2|A|a_1\rangle & \langle a_2|A|a_2\rangle & \cdots \\ \vdots & \vdots & \ddots \end{pmatrix}, \tag{1-6}$$

where for the case of the single proton $a_1 = \uparrow$ and $a_2 = \downarrow$. For this simplest of cases, one can then express the I_Z operator as

$$I_Z = \begin{pmatrix} \langle\uparrow|I_Z|\uparrow\rangle & \langle\uparrow|I_Z|\downarrow\rangle \\ \langle\downarrow|I_Z|\uparrow\rangle & \langle\downarrow|I_Z|\downarrow\rangle \end{pmatrix} = \begin{pmatrix} 1/2\langle\uparrow|\uparrow\rangle & -1/2\langle\uparrow|\downarrow\rangle \\ 1/2\langle\downarrow|\uparrow\rangle & -1/2\langle\downarrow|\downarrow\rangle \end{pmatrix} = 1/2 \begin{pmatrix} 1 & 0 \\ 0 & -1 \end{pmatrix}, \tag{1-7}$$

utilizing Eqs. (1-1) and (1-2) to simplify the matrix elements.

The operators I_X and I_Y can be expressed in matrix form, in the I_Z eigenbasis, by incorporating the matrix form of I_Z shown in Eq. (1-7) into the commutation relations for the I_X, I_Y and I_Z operators, as shown below.

$$[I_X, I_Y] = I_X I_Y - I_Y I_X = iI_Z \quad [I_Y, I_Z] = iI_X \quad [I_Z, I_X] = iI_Y \tag{1-8}$$

These relations are equivalent to the commutation relations derived originally for the orbital angular momentum operators (125). The resulting I_X and I_Y matrix representations are shown in Eq. (1-9).

$$I_X = 1/2 \begin{pmatrix} 0 & 1 \\ 1 & 0 \end{pmatrix} \text{ and } I_Y = i/2 \begin{pmatrix} 0 & -1 \\ 1 & 0 \end{pmatrix} \tag{1-9}$$

Utilizing the I_X and I_Y matrix forms from Eq. (1-9), as well as Eq. (1-6), the general operator matrix form, the following relations for I_X and I_Y, in the I_Z eigenbasis, can be determined.

$$I_x\left|\uparrow\right\rangle_z = +1/2\left|\downarrow\right\rangle_z, \quad I_x\left|\downarrow\right\rangle_z = -1/2\left|\uparrow\right\rangle_z \tag{1-10}$$

$$I_y\left|\uparrow\right\rangle_z = +i/2\left|\downarrow\right\rangle_z, \quad I_y\left|\downarrow\right\rangle_z = -i/2\left|\uparrow\right\rangle_z \tag{1-11}$$

From this point on, the eigenbasis is assumed to be that of the operator I_Z, reflecting the convention of a $\hat{z}$-directed main magnetic field in NMR physics, allowing the 'Z' subscript to dropped from the vector kets.

1.2.4 Expectation Values of Operators

The state function of a quantum system is represented by a linear combination of basis functions that form a complete set of states, such as the those defined in Eq. (1-1). The state function, usually called the wavefunction, contains all of the information pertaining to the system, and is represented mathematically as

$$\Psi = \sum_a c_a\left|a\right\rangle = c_\uparrow\left|\uparrow\right\rangle + c_\downarrow\left|\downarrow\right\rangle, \text{ for a single proton.} \tag{1-12}$$

The probability that a single spin, represented by a wavefunction $\Psi = \sum_a c_a\left|a\right\rangle$, exists in the eigenstate, $\left|a'\right\rangle$, is given by

$$\text{probability} = \left|\left\langle a'\middle|\Psi\right\rangle\right|^2 = \left|c_a\right|^2. \tag{1-13}$$

Conservation of this probability means that the sum of the individual probabilities must equal unity, or in the case of the single proton,

$$\left|c_\uparrow\right|^2 + \left|c_\downarrow\right|^2 = 1, \tag{1-14}$$

where $c_\uparrow$ and $c_\downarrow$ are complex numbers, and must have magnitudes ≤ 1.

Like so many of the fundamental postulates in physics, Eq. (1-13) cannot be proved, rather it was proposed out of intuition and verified by extensive experimentation.

In NMR, the most useful form of information regarding the spin system is the average measured value of an observable, or equivalently, *expectation value* of an operator. The expectation value of an operator A with respect to the wavefunction, Ψ, is expressed as

$$\langle A \rangle \equiv \langle \Psi | A | \Psi \rangle . \tag{1-15}$$

Physical significance can be attached to this equation by applying the completeness relation (1-3) to Eq. (1-15) as follows

$$\langle A \rangle = \sum_{a''} \sum_{a'} \langle \Psi | a'' \rangle \langle a'' | A | a' \rangle \langle a' | \Psi \rangle , \tag{1-16}$$

allowing one to separate the expectation equation into meaningful components by evaluating one of the sums (a''), resulting in

$$\langle A \rangle = \sum_{a'} x_{a'} \, |\langle a' | \Psi \rangle|^2 = \sum_{a'} x_{a'} \, |c_{a'}|^2 , \tag{1-17}$$

where $x_{a'}$ is the eigenvalue from $A|a'\rangle = x_{a'}|a'\rangle$. The conjugate relationship $\langle \Psi | a' \rangle = \langle a' | \Psi \rangle^*$ was used to simplify this expression. Equation (1-17) is then readily interpretable as a measured value (an eigenvalue), $x_{a'}$, weighted by the probability of the system existing in that state, $|a'\rangle$, given by $|c_{a'}|^2$, from Eq. (1-13).

While the measurement of individual events yields the discrete eigenvalues, $x_{a'}$, realistic macroscopic samples are represented by mixtures of wavefunctions,

corresponding to a collection of spins which are not identically prepared. For example, at one extreme is a sample containing a completely random mixture of dipoles, yielding no net magnetization (dipole moment per unit volume), which corresponds to a random collection of complex coefficients, $c\uparrow_N$ and $c\downarrow_N$, for N wavefunctions. At the far extreme from the completely random mixture of states is the ideal case of a system described by a single wavefunction, Ψ, representing a system in a *pure* state. That is to say that every spin in our system is represented by the same state, for example $c\uparrow = 1$ and $c\downarrow = 0$. The most general treatment of a system of spins requires that the system is in a state that is not completely known, somewhere between the completely random mixture of states and the pure state, commonly termed a *mixed* state. Section 1.3 describes the tools necessary to treat the dynamics of mixed states, the most important tool of which is the density operator, or equivalently, density matrix.

1.3 The Density Matrix

The average measured value of an observable for the case of a pure system, an ensemble of identically prepared members, is the expectation value of that operator, as shown in Eq. (1-15). If the system is not prepared such that all members are identical, then the system is mixed, and Eq. (1-15) cannot be directly applied. A mixed system is a statistical mixture of N pure states, each of which has a relative weighting, W_α, representing the probability of finding the system in that pure state. Conservation of this probability allows one to write

$$0 \le W_\alpha \le 1 \qquad \text{and} \qquad \sum_{\alpha=1}^{N} W_\alpha = 1. \tag{1-18}$$

The expectation value, as expressed in Eq. (1-16), can then be rewritten to include the mixture of states

$$\langle A \rangle = \sum_{\alpha=1}^{N} \sum_{a''} \sum_{a'} W_\alpha \langle \Psi_\alpha | a'' \rangle \langle a'' | A | a' \rangle \langle a' | \Psi_\alpha \rangle, \tag{1-19}$$

where the expressions $\langle a' | \Psi_\alpha \rangle$ and $\langle \Psi_\alpha | a'' \rangle$ are simply numbers and as such can be reordered in the sum to give

$$\langle A \rangle = \sum_{\alpha=1}^{N} \sum_{a''} \sum_{a'} \langle a' | \Psi_\alpha \rangle W_\alpha \langle \Psi_\alpha | a'' \rangle \langle a'' | A | a' \rangle. \tag{1-20}$$

We can now define the density operator from this rearranged expectation value equation as

$$\rho = \sum_{\alpha=1}^{N} |\Psi_\alpha\rangle W_\alpha \langle \Psi_\alpha|, \tag{1-21}$$

and substitute this new operator back into Eq. (1-20) to obtain

$$\langle A \rangle = \sum_{a''} \sum_{a'} \underbrace{\langle a'' | \rho | a' \rangle}_{\text{system statistical information}} \overbrace{\langle a' | A | a'' \rangle}^{\text{operator information}} = \sum_{a''} \langle a'' | \rho A | a'' \rangle = \mathrm{Tr}\,(\rho A). \qquad (1\text{-}22)$$

Although the manipulations of Eq. (1-19) to define the density operator may appear arbitrary, the objective was to separate the observable of interest, A, an operator, from the ensemble statistical information contained in the wavefunctions and their weightings. The incredibly simple equation that results tells us that if we know the density operator (matrix) we can calculate the expectation value of any operator, A, with a single matrix multiplication and subsequent summing of the resulting diagonal elements. *It is important to note that elements in the density matrix are a function of the eigenbasis,* $|a'\rangle$*, but the resulting expectation value given by the trace is independent of this basis.*

The density matrix can be expanded in the basis of Cartesian operators, I_X, I_Y and I_Z, along with the identity matrix, Id as

$$\rho = m_1 Id + m_2 I_Z + m_3 I_X + m_4 I_Y, \qquad (1\text{-}23)$$

where the m's are real numbers. Each number, m_1, m_2, ... etc., is the expectation value of the corresponding operator, for example, $m_3 = \langle I_X \rangle$. The usefulness of this expansion lies in the correspondence of the coefficients (m_1 to m_4) to meaningful physical phenomena, particularly longitudinal and transverse magnetization. These important concepts will be developed in the following sections.

1.3.1 Statistical Interpretation of the Density Matrix – Populations and Coherence

Equations (1-18) to (1-22), while valuable mathematical derivations, are without a clear physical significance. Considering an individual element in the density matrix can provide insight into the physical correspondences of these mathematical expressions. Each element in the density matrix can be expressed explicitly as

$$\rho_{n,n'} = \langle n|\rho|n'\rangle = \sum_{\alpha=1}^{N}\langle n|\Psi_\alpha\rangle W_\alpha \langle \Psi_\alpha|n'\rangle = \sum_{\alpha=1}^{N} W_\alpha c_n^{\alpha} c_{n'}^{\alpha *} . \qquad (1\text{-}24)$$

From this expression, we can see directly that any matrix element is the weighted average of the coefficient product, $c_n c_{n'}^*$, over the entire system, often expressed as $\overline{c_n c_{n'}^*}$. One can immediately identify the conjugate symmetry across the density matrix diagonal, by writing $\rho_{n',n} = \overline{c_{n'} c_n^*} = \overline{(c_n c_{n'}^*)^*} = \rho_{n,n'}^*$, for $n \neq n'$, meaning the density matrix satisfies Hermitian requirements. A Hermitian operator satisfies the expression $\langle \alpha|A|\beta\rangle = \langle \beta|A|\alpha\rangle^*$. The complete set of information contained in the density matrix can then be said to lie in the upper triangular region including the diagonal.

Each coefficient, c_n, is a complex number, so can be expressed as a vector with a magnitude and a phase, allowing the coefficient product to be expressed as

$$c_n c_{n'}^* = |c_n||c_{n'}|\exp(i(\varphi_n - \varphi_{n'})) . \qquad (1\text{-}25)$$

For the off-diagonal elements, $n \neq n'$, a random distribution of phases, φ_n, will result in the sum in Eq. (1-24) averaging to zero for a large sample of spins. The requirement for non-vanishing off-diagonal elements is then clearly a statistical correlation or *coherence* between states $|n\rangle$ and $|n'\rangle$, resulting in $\overline{\exp(i(\varphi_n - \varphi_{n'}))} > 0$.

The $n = n'$ elements have a constant zero phase because $c_n c_n^* = |c_n|^2$ is always real, meaning coherence is not necessary for finite diagonal elements. Rather, these diagonal elements represent the probability of finding the spin in the state represented by the ket $|n\rangle$, or in other words, the relative population of the state. Recall, from Eq. (1-13), that $|c_n|^2$ is the probability that a spin system exists in the state $|n\rangle$ upon measurement of the system. Comparing two extremes, a pure state and a completely random mixed state is illustrative in this case. A pure state is represented by identically

prepared spins, for example, all in the spin-up state $|\uparrow\rangle$, or $c_\uparrow = 1$ and $c_\downarrow = 0$, resulting in a density matrix

$$\rho_{pure} = \begin{pmatrix} c_\uparrow^{\,2} & c_\downarrow c_\uparrow \\ c_\uparrow c_\downarrow & c_\downarrow^{\,2} \end{pmatrix} = \begin{pmatrix} 1 & 0 \\ 0 & 0 \end{pmatrix}. \tag{1-26}$$

A completely random mixture will have an equal probability of being in either of the states $|\uparrow\rangle$ or $|\downarrow\rangle$, therefore $|c_\uparrow| = |c_\downarrow|$, as well as having a random distribution of phases, eliminating the off-diagonal elements, resulting in

$$\rho_{random} = \begin{pmatrix} 0.5 & 0 \\ 0 & 0.5 \end{pmatrix}. \tag{1-27}$$

Expressing these extreme density matrices in terms of the Cartesian operators, from Eq. (1-23), we find that $\rho_{pure} = I_Z + Id/2$, or $m_1 = \frac{1}{2}$, $m_2 = 1$ and $\rho_{random} = Id/2$, or $m_1 = \frac{1}{2}$, $m_2 = 0$. The Cartesian component weightings m_1 and m_2 can be expressed in terms of the generalized density matrix elements as

$$m_1 = \langle Id \rangle = \overline{c_\uparrow^* c_\uparrow} + \overline{c_\downarrow^* c_\downarrow}, \; m_2 = \langle I_Z \rangle = \overline{c_\uparrow^* c_\uparrow} - \overline{c_\downarrow^* c_\downarrow}. \tag{1-28}$$

The identity matrix contribution, m_1, is recognizable as Eq. (1-14), the conservation of probability or normalization equation. Both the pure and random mixture density matrices satisfy the normalization condition, which is to say $Tr(\rho_{pure} Id) = 1$ and $Tr(\rho_{random} Id) = 1$, as will be the case for every density matrix which falls between these two extremes. The contribution from the Id matrix will thus be dropped for all subsequent density matrix calculations because it is a static term and is not representative of magnetization in a physical sense.

From Eq. (1-28), the expectation value of the I_Z operator, m_2, corresponds to the probability difference of each of the two states being occupied, or equivalently the population difference between the two states. The pure state represents the largest population polarization possible, $Tr(\rho_{pure} I_Z) = 1$, while the random mixture represents the

minimum, $Tr(\rho_{random} I_Z) = 0$. It is the population difference that makes NMR an exploitable phenomenon, creating the net magnetization that interacts with the applied fields in an NMR experiment, leading to the radiation of energy containing the sought after information.

Both scenarios considered so far, the pure and random mixture of states, have no off-diagonal contributions, or no coherence between the spin up and spin down states, meaning m_3 and $m_4 = 0$. The expectation values of the transverse operators I_X and I_Y, are shown in Eq. (1-29) in terms of the general form of the density matrix elements.

$$m_3 = \langle I_X \rangle = \overline{c_\uparrow^* c_\downarrow} + \overline{c_\uparrow^* c_\downarrow} \quad m_4 = \langle I_Y \rangle = i(\overline{c_\uparrow^* c_\downarrow} - \overline{c_\uparrow^* c_\downarrow})) \tag{1-29}$$

To derive the relative populations of the quantum states, m_2, for a realistic NMR experiment, and display how coherence between those states, m_3 and m_4, is generated, the mathematical description of quantum mechanical systems developed so far will be focused to include a fundamental component of the NMR experiment, the main static magnetic field, most commonly termed $\mathbf{B_o}$. This main field strength determines the population difference between the states, defining the thermal equilibrium density matrix as somewhere between the two extremes displayed in (1-26) and (1-27), somewhere between a pure state and a random mixture. Additionally, the main field creates the conditions necessary to generate coherence between the states.

1.3.2 Density Matrix at Thermal Equilibrium – Spins in a Static Magnetic Field

The $\mathbf{B_o}$ field interacts with the magnetic moments of the nuclei, μ, with an energy that is given by

$$\xi = -\mu \cdot \mathbf{B_o} = -\gamma \hbar \mathbf{I} \cdot \mathbf{B_o} \tag{1-30}$$

where $\mathbf{I}$ is the spin angular momentum operator. Assuming $\mathbf{B_o}$ is oriented in the $\hat{z}$-direction, we can write the operator form the interaction energy, the Hamiltonian, as

$$\mathcal{H}_{B_o} \equiv \xi = -\gamma\hbar I_Z B_o. \tag{1-31}$$

From the time-independent Schrödinger wave equation, the energy eigenstates are solutions of

$$\mathcal{H}\Psi = E\Psi, \tag{1-32}$$

where, specifically, the wavefunction states are eigenstates of the operator I_Z, the sole operator is the Hamiltonian ($\mathcal{H} = -\gamma\hbar B_o I_Z$), and the energy eigenvalue is given by E. For a spin ½ system, such as the proton, the eigenvalues of I_Z are $\pm$½, as shown in Eq. (1-4), resulting in two energy eigenvalues,

$$E = \pm\tfrac{1}{2}\gamma\hbar B_o, \tag{1-33}$$

as shown in Figure 1-1.

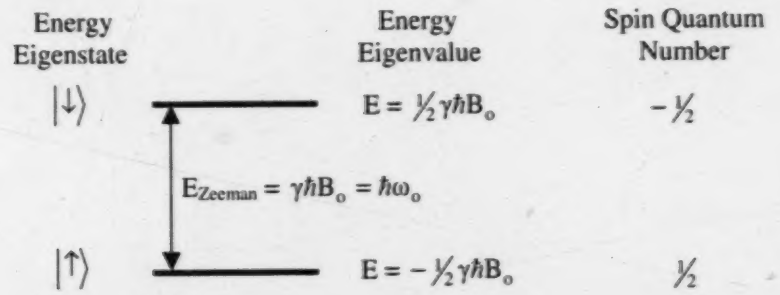

Figure 1-1 Energy level diagram of a spin ½ system in a static magnetic field, B_o. If a spin changes states in this field, the corresponding change in energy is either released or absorbed as electromagnetic radiation at a frequency $\omega_o = \gamma B_o$.

Figure 1-1 illustrates the two stationary eigenstate solutions of the time-independent Schrödinger wave equation for a single spin ½ system, the transition between which results in the characteristic spectral line at a frequency

$$\omega_o = \gamma B_o, \tag{1-34}$$

known as the Larmor frequency.

The thermal equilibrium distribution of eigenstate populations in a given external static field is dictated by the Boltzmann distribution (126)

$$\rho_{nn} = \frac{\exp(-\beta E_n)}{\sum_{1}^{N} \exp(-\beta E_1)}, \tag{1-35}$$

which gives the probability of finding a spin in one of its eigenstates, $|n\rangle$, where $\beta = 1/kT$, k = Boltzmann's constant, T the temperature in Kelvin, and N is number of energy levels. E_n takes on values of $\pm\frac{1}{2}\gamma\hbar B_o$ for a spin ½ system, as shown in (1-33). The Boltzmann distribution of populations is applicable to canonical ensembles, systems with a fixed number of members (spins), in weak thermal contact with a much larger heat reservoir (126). The sum in the denominator is a normalization factor, allowing each element to be expressed as a fractional population.

Prior to being exposed to a static magnetic field there is no energy difference between states, meaning a sample of spin ½ nuclei has an equal probability of being in either the spin up or spin down states. This sample is unmagnetized as a result of the random distribution of magnetic dipole moments. The presence of a B_o field defines a new thermal equilibrium condition in which the spin up state becomes the preferred state. The result is a magnetization of the sample, an alignment of the dipole moments, defined as the magnetic dipole moment per unit volume, **M**. The achievement of this equilibrium must be accompanied by a net number of transitions from the spin down to the spin up state, the preferred state in the static field. The willingness of the system as a whole to support this energy difference, or population difference between states, is determined by the system temperature and main field strength. The spin system and thermal pool equalize their temperatures via a transfer of energy from the spin system to the lattice though the process of *spin-lattice* relaxation (127). In liquid samples, thermal motion acts as the primary mechanism for this spin-lattice or T_1 relaxation.

From equation (1-35), for $\beta E_n << 1$, we can approximate the exponential terms with a first order expansion

$$\exp(-\beta E_n) = 1 - \beta E_n + \text{higher order terms,} \qquad (1\text{-}36)$$

which, for a spin ½ system, with only two energy levels and two corresponding diagonal elements, we get

$$\rho_{11} \approx \tfrac{1}{2}(1 + \gamma\hbar\beta B_o) \text{ and } \rho_{22} \approx \tfrac{1}{2}(1 - \gamma\hbar\beta B_o). \qquad (1\text{-}37)$$

In matrix form, this thermal equilibrium density matrix is

$$\rho_{Eq} = \begin{pmatrix} \tfrac{1}{2}(1+\gamma\hbar\beta B_o) & 0 \\ 0 & \tfrac{1}{2}(1-\gamma\hbar\beta B_o) \end{pmatrix} = \tfrac{1}{2}\,\mathrm{Id} + (\gamma\hbar\beta B_o)\, I_Z, \qquad (1\text{-}38)$$

where we have used the matrix form of the operator I_Z from Eq. (1-7), and Id is the identity matrix. As described in section 1.3.1, the identity matrix is a static term that can be discarded, leaving us with

$$\rho_{Eq} = (\gamma\hbar\beta B_o)\, I_Z. \qquad (1\text{-}39).$$

The thermal equilibrium magnetization of such an ensemble can be calculated by incorporating the dipole moment per spin, given by $\mu = \gamma\mathbf{J} = \gamma\hbar\,\mathbf{I}$, and the spin density, η, resulting in

$$M_Z = \eta\gamma\hbar\,(\gamma\hbar\beta B_o) = \eta\gamma^2\hbar^2\beta B_o \qquad (1\text{-}40)$$

The first order approximation used to derive this result appears to be justifiable for even the largest field strengths used in high field spectrometers, for example 800 MHz (18.75 T), for which $\gamma\hbar\beta B_o \sim 10^{-4} << 1$ at room temperature. Although, it has been suggested by Warren (128) and others (129,130) that the truncation of higher order terms, as in Eq. 1-36, is not trivial to justify. Nevertheless, the higher order terms, even if

significant in magnitude, will not contribute to the observable NMR signal following excitation by typical pulse sequences. Although, as shown in Chapter 7, the multiple quantum filter sequence is capable of transforming the higher order terms to transverse magnetization in the form of a unexpected contamination water signal.

The operator components of Eq. (1-38), I_Z and Id, are strikingly similar to the two extreme density matrices displayed in Eqs. (1-26) and (1-27), which correspond to, respectively, a pure state and a completely random mixture of states. In fact, we can rewrite Eq. (1-38) as

$$\rho_{Eq} = (1 - \gamma\hbar\beta B_o)\begin{pmatrix} \frac{1}{2} & 0 \\ 0 & \frac{1}{2} \end{pmatrix} + \gamma\hbar\beta B_o \begin{pmatrix} 1 & 0 \\ 0 & 0 \end{pmatrix}, \qquad (1\text{-}41)$$

which is clearly a linear combination of a completely random mixture of states and a pure state. An energy level model of the thermal equilibrium distribution of states is shown in Fig. 1-2.

Figure 1-2 An energy level representation of spin ½ thermal equilibrium in a static magnetic field B_o. The relative contributions from the random mixture and pure states are a function of B_o, the system temperature, T, and the spin gyromagnetic ratio, γ.

Equation (1-41) displays how the experimentalist can control the NMR usable spin population by varying B_o and T, as well as exposing the bane of NMR spectroscopy, the fact that the density matrix is almost completely a random mixture of states at room temperature. At in-vivo field strengths, 1.5 T to 4.0 T, and body temperature T = 310° K, $\gamma\hbar\beta B_o \sim 10^{-5}$, meaning ~99.99% of the total spin population will exist as an essentially random mixture, from which no measurable information can be ascertained. Nevertheless, the attainable population differences are still sufficient to give rise to a usable amount observable magnetization. The generation of this observable

magnetization, which corresponds to the generation of coherence between states, is best described with the tools of density matrix dynamics, or how the matrix evolves under the influence of a Hamiltonian, $\mathcal{H}$. To describe how the density matrix evolves over time, a differential equation that ρ satisfies is derived in section 1.3.3.

1.3.3 Time Evolution of the Density Matrix – Time Independent Hamiltonians

To find a differential equation that describes the evolution of the density matrix under the influence of a Hamiltonian, $\mathcal{H}$, the influence of this Hamiltonian on the elements of the density matrix must be established. Fortunately, the influence of a Hamiltonian on a system wavefunction is described by the famous time-dependent Schrödinger wave equation (125), shown in Eq. (1-42).

$$i\hbar\frac{\partial}{\partial t}\Psi(t)=\mathcal{H}\Psi(t) \tag{1-42}$$

To provide the transition from the Schrödinger wave equation to a differential equation describing the evolution of the density operator, consider again the spin ½ system, for which $\Psi = c_\uparrow|\uparrow\rangle + c_\downarrow|\downarrow\rangle$. The time dependence of the wavefunction is contained in the coefficients, $c_\uparrow$ and $c_\downarrow$, the very same coefficients that make up the density matrix. To extract individual spin-state expressions, we can rewrite the time-dependent Schrödinger wave equation using the expansion in spin up and spin down states, giving

$$i\hbar\left(\frac{\partial c_\uparrow}{\partial t}|\uparrow\rangle+\frac{\partial c_\downarrow}{\partial t}|\downarrow\rangle\right)=\mathcal{H}\left(c_\uparrow|\uparrow\rangle+c_\downarrow|\downarrow\rangle\right). \tag{1-43}$$

Multiplying Eq. (1-43) on the left by $\langle\uparrow|$ or $\langle\downarrow|$, and utilizing the eigenket orthonormality, as shown in Eq. (1-2), allows each coefficient differential to be expressed independently as

$$\frac{\partial c_\uparrow}{\partial t} = -i/\hbar\,(c_\uparrow\langle\uparrow|\mathcal{H}|\uparrow\rangle + c_\downarrow\langle\uparrow|\mathcal{H}|\downarrow\rangle), \text{ and} \tag{1-44a}$$

$$\frac{\partial c_\downarrow}{\partial t} = -i/\hbar\,(c_\uparrow\langle\downarrow|\mathcal{H}|\uparrow\rangle + c_\downarrow\langle\downarrow|\mathcal{H}|\downarrow\rangle). \tag{1-44b}$$

Consider next, the time differential for a single density matrix element, recalling that a single element is simply a product of wavefunction coefficients, as shown in Eq. (1-24), for example, $\langle\uparrow|\rho|\downarrow\rangle = \overline{c_\uparrow c_\downarrow^*}$. Differentiating both sides with respect to time yields,

$$\frac{\partial}{\partial t}\langle\uparrow|\rho|\downarrow\rangle = \frac{\partial}{\partial t}(\overline{c_\uparrow c_\downarrow^*}) = \overline{c_\uparrow \frac{\partial}{\partial t}(c_\downarrow^*)} + \overline{c_\downarrow^* \frac{\partial}{\partial t}(c_\uparrow)}. \tag{1-45}$$

Substituting the time derivatives from Eq. (1-44a) and (1-44b) into Eq. (1-45) allows it to be rewritten, after some rearranging, as

$$\frac{\partial}{\partial t}\langle\uparrow|\rho|\downarrow\rangle = -i/\hbar\,\{\langle\uparrow|\rho\mathcal{H}|\downarrow\rangle - \langle\uparrow|\mathcal{H}\rho|\downarrow\rangle\} = \langle\uparrow|-i[\rho,\mathcal{H}]|\downarrow\rangle, \tag{1-46}$$

or equivalently,

$$\frac{\partial}{\partial t}\rho = -i[\rho,\mathcal{H}/\hbar]. \tag{1-47}$$

This differential equation, called the Liouville-von Neumann equation, is the governing relation for all density matrix dynamics considered in this thesis. For the cases in which $\mathcal{H}$ is time-independent, Eq. (1-47) has the simple solution

$$\rho(t) = \exp(-i\mathcal{H}t/\hbar)\,\rho(0)\exp(i\mathcal{H}t/\hbar). \tag{1-48}$$

The utility of Eq. (1-48), which will be termed the density operator evolution equation, will be demonstrated throughout the remainder of the thesis, where it will be developed into a general tool used to evaluate the evolution of the density matrix for a

wide range of spin systems and NMR experiments. There exists no general solution to the Liouville-von Neumann equation for arbitrary time-dependent Hamiltonians, although exceptions have been reported (131). Section 1.3.4 outlines a simple example incorporating this powerful equation, specifically, the transformation of the density matrix by a radio frequency pulse, displaying how coherence is generated in nuclear magnetic resonance.

1.3.4 Radio-Frequency Pulses and the Density Matrix – Generation of Coherence

The evaluation of Eq. (1-48) to calculate the evolution of the density matrix requires that both the density matrix at t = 0, $\rho(0)$, and the system Hamiltonian be known. We will assume the system is in a state of thermal equilibrium so $\rho(0) = (\gamma\hbar\beta B_o)I_Z$, from Eq. (1-39). The thermal equilibrium density matrix coefficient, $\gamma\hbar\beta B_o$, is a constant over time, so will be replaced by unity to simplify the density matrix presentation. To model excitation of the spins with an r.f. field, the Hamiltonian must include the main static magnetic field, previously defined as $\mathcal{H}_{B_o} = -\gamma\hbar B_o I_Z$, and the r.f. pulse, assumed to have an oscillatory time dependence (a linearly polarized field)

$$\mathcal{H}_{rf} = -\gamma\hbar B_1 \cos(\omega t) I_X, \tag{1-49}$$

giving rise to a total Hamiltonian

$$\mathcal{H} = \mathcal{H}_{B_o} + \mathcal{H}_{rf} = -\gamma\hbar B_o I_Z - \gamma\hbar B_1 \cos(\omega t) I_X. \tag{1-50}$$

If $|B_1| << |B_o|$ (a criterion met for all in-vivo experiments) only the field component that rotates in the same sense (and frequency) as the nuclear spins will act on the spins (132). This component is described by a circularly polarized field applied in the plane transverse to the main field, namely, the x-y plane, with a constant amplitude, $B_{1_{Amp}}$. A circularly polarized field can be expressed

$$B_1(t) = B_{1_{Amp}}(\cos(\omega t+\varphi)\, I_X + \sin(\omega t+\varphi)\, I_Y), \tag{1-51}$$

where ω is the frequency of oscillation, and φ is a constant phase term.

To incorporate the Hamiltonian of Eq. (1-50) into Eq. (1-48) it must first be rendered time-independent, an operation carried out by a transformation into a frame of reference rotating at the radio-frequency, $\omega_{rot} = \omega_{r.f.}$, around the z-axis. Working in the rotating frame of reference is a method of great utility in simplifying NMR calculations, and once established will be the assumed frame of reference for the remainder of the thesis. The transformation can be made by defining a new wavefunction,

$$\Psi(t)^{rot} = \exp(i\omega_{rot}tI_Z)\Psi(t), \tag{1-52a}$$

$$\text{or equivalently } \Psi(t) = \exp(-i\omega_{rot}tI_Z)\Psi(t)^{rot}, \tag{1-52b}$$

where $\Psi(t)^{rot}$ differs from $\Psi(t)$ by a rotation through an angle of ωt, and the operator I_Z specifies the axis of rotation as the $\hat{z}$-axis. We can substitute this new wavefunction and its derivative, shown in Eq. (1-53), into the time-dependent Schrödinger wave equation, from Eq. (1-42).

$$\frac{\partial\Psi(t)}{\partial t} = -i\omega_{rot}I_Z\exp(-i\omega_{rot}tI_Z)\Psi(t)^{rot} + \exp(-i\omega_{rot}tI_Z)\frac{\partial\Psi(t)^{rot}}{\partial t} \tag{1-53}$$

The time-dependent Schrödinger wave equation can now be expressed in terms of the transformed wavefunction,

$$i\hbar(-i\omega_{rot}I_Z\exp(-i\omega_{rot}tI_Z)\Psi(t)^{rot} + \exp(-i\omega_{rot}tI_Z)\frac{\partial\Psi(t)^{rot}}{\partial t}) = \mathcal{H}\exp(-i\omega_{rot}tI_Z)\Psi(t)^{rot}, \tag{1-54}$$

where $\mathcal{H}$ is defined in Eq. (1-50).

Equation (1-54) can be simplified by rearranging terms and multiplying on the left by $\exp(i\omega_{rot}tI_Z)$, resulting in

$$i\hbar\frac{\partial\Psi(t)^{rot}}{\partial t} = \{\hbar(\omega_{rot} + \gamma B_o)I_Z + \gamma\hbar B_{1Amp}(\cos(\varphi)I_X + \sin(\varphi)I_Y)\}\,\Psi(t)^{rot}, \qquad (1\text{-}55)$$

where the time-independent rotating frame Hamiltonian is

$$\mathcal{H}^{rot} = \{\hbar(\omega_{rot} + \gamma B_o)I_Z + \gamma\hbar B_{1Amp}(\cos(\varphi)I_X + \sin(\varphi)I_Y)\}\,. \qquad (1\text{-}56)$$

If the r.f. pulse is applied at resonance, $\omega_{rot} = \omega_{r.f.} = -\gamma B_o$, and along the x-axis ($\varphi = 0$), the rotating frame Hamiltonian will be reduced to $\mathcal{H}^{rot} = \gamma\hbar B_{1Amp} I_X$. This result *can* be inserted in our density matrix evolution Eq. (1-48), resulting in

$$\rho(t) = \exp(-i\,\gamma B_{1Amp} I_X\, t)\; I_Z \exp(i\,\gamma B_{1Amp} I_X\, t), \qquad (1\text{-}57)$$

which can be evaluated by expanding the exponential operator terms as power series, removing the operator I_X from the exponent. This series expansion can be re-grouped into related trigonometric series, resulting in Eq. (1-58). Appendix I contains the derivation of this and several other related expansions, as well as general rules for the application of the resulting trigonometric equations.

$$\exp(-i\,\gamma B_{1Amp} I_X\, t) = \cos(\gamma B_{1Amp} t/2)\; Id - i\,\sin(\gamma B_{1Amp} t/2)\; 2I_X \qquad (1\text{-}58)$$

Equation (1-58) can be substituted into Eq. (1-57) and simplified to

$$\rho(t) = I_Z \cos(\gamma B_{1Amp} t) + I_Y \sin(\gamma B_{1Amp} t). \qquad (1\text{-}59)$$

Expressing Eq. (1-59) in matrix form, in the I_Z eigenbasis, depicts the generation of coherence between the spin up and spin down states, $\overline{c_1 c_2^*}$, as a function of the r.f. pulse tip angle

$$\rho(t) = \begin{pmatrix} \cos(\gamma B_{1Amp} t) & -i \sin(\gamma B_{1Amp} t) \\ i \sin(\gamma B_{1Amp} t) & -\cos(\gamma B_{1Amp} t) \end{pmatrix}, \tag{1-60}$$

where $\overline{c_1 c_2^*} = -i \sin(\gamma B_{1Amp} t)$. When $\gamma B_{1Amp} t = \pi/2$, the population difference between the states goes to zero and the coherence between the states is maximized. The $\pi/2$ or 90° pulse is commonly used to maximally excite spin systems from thermal equilibrium, to maximize the signal to noise ratio of the resulting signal.

We now have the tools necessary to describe the simplest NMR pulse sequence, the pulse-acquire experiment, which consists of exposing a spin population in thermal equilibrium to a pulse of polarized r.f. energy. The detectable NMR signal generated by the r.f. pulse can be calculated by evaluating the expectation value of the magnetic moment in the transverse plane for times t = 0 to t = t_{acq}, the acquisition time, as shown in Fig. 1-3.

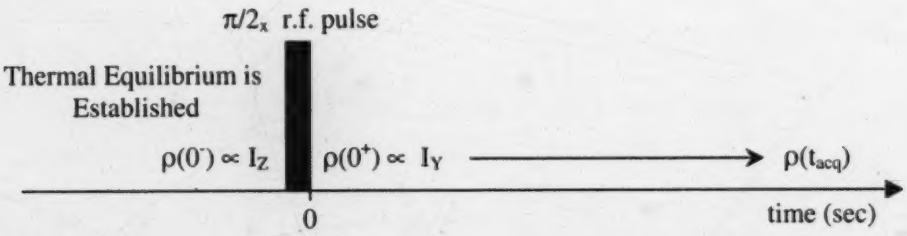

Figure 1-3 A simple pulse acquire NMR experiment. The on resonance r.f. pulse excites the thermal equilibrium density operator to the transverse plane.

The magnetization that evolves in the acquisition period is described by a complex signal, having both $\hat{x}$ and $\hat{y}$ Cartesian components, both of which can be collected with quadrature detection (detection of a circularly polarized field). This complex signal has corresponding transverse operators, known as the raising (1-61a) and lowering (1-61b) operators.

$$I_+ = I_X + iI_Y = \begin{pmatrix} 0 & 1 \\ 0 & 0 \end{pmatrix} \tag{1-61a}$$

$$I_- = I_X - iI_Y = \begin{pmatrix} 0 & 0 \\ 1 & 0 \end{pmatrix} \tag{1-61b}$$

I_+ is called the raising operator because it acts on $|\downarrow\rangle$ to produce $|\uparrow\rangle$, and the complementary lowering operator, I_-, acts on $|\uparrow\rangle$ to produce $|\downarrow\rangle$.

The complex transverse magnetization can be calculated from the expectation value of the raising operator

$$M_+(t) = \eta\gamma\hbar\langle I_+\rangle = \eta\gamma\hbar \mathrm{Tr}(\rho(t)I_+), \tag{1-62}$$

where η is the spin density and $\rho(t)$ is the density operator at a time t after the r.f. pulse is applied, as shown in Fig. 1-3.

If we assume excitation by a $\pi/2_X$ pulse, meaning $\rho(0) = I_Y$ in the detection period, and detection in the laboratory frame, we can apply Eq. (1-48) directly, resulting in

$$\rho(t) = \exp(-iI_Z\gamma B_o t)\, I_Y \exp(iI_Z\gamma B_o t). \tag{1-63}$$

Incorporating the trigonometric transformations, derived in Appendix I, to Eq. (1-63), the density matrix during acquisition can be expressed

$$\rho(t) = I_Y\cos(\omega_o t) + I_X\sin(\omega_o t) = 1/2\begin{pmatrix} 0 & \sin(\omega_o t) - i\cos(\omega_o t) \\ \sin(\omega_o t) + i\cos(\omega_o t) & 0 \end{pmatrix}. \tag{1-64}$$

Substituting this result into Eq. (1-22) allows the expectation value of the transverse magnetization to be calculated, shown in Eq. (1-65).

$$\langle I_+\rangle = \mathrm{Tr}(\rho(t)I_+) = 1/2(\sin(\omega_o t) - i\cos(\omega_o t)) = i/2\exp(\omega_o t) \tag{1-65}$$

Fourier transformation of this signal results in a single complex peak at a frequency ω_o, which is typically displayed as a real signal, zero order phase corrected to a purely absorptive phase, as shown in Fig. 1-4. This NMR signal detected in the laboratory frame is in the form of an e.m.f. induced in a receiver coil, generated by a time-varying flux that is produced by the precessing magnetic moments. The transmitter frequency is subtracted from the detected radio-frequency signal to allow the resulting spectrum of frequencies to be displayed in the rotating frame of reference.

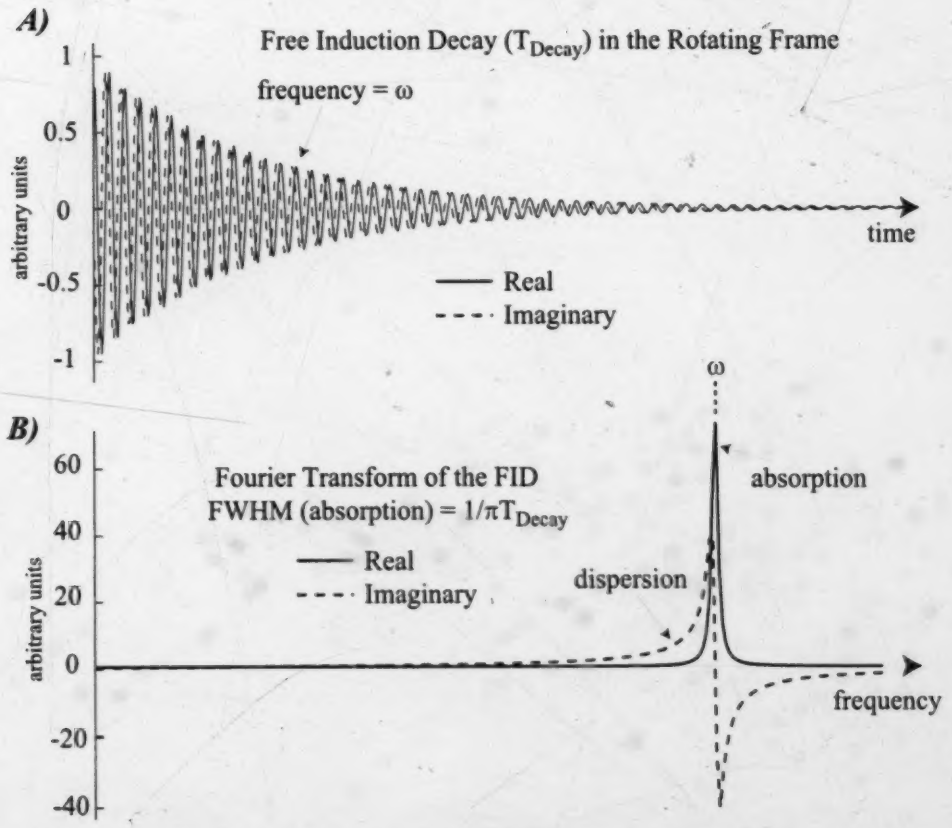

Figure 1-4 A) A rotating frame free induction decay (FID) from a single uncoupled spin system following excitation by a $\pi/2$ pulse, acquired at a frequency offset, $\omega = \omega_o - \omega_{rot}$. The signal is composed of a real and imaginary component, as shown in Eq. (1-65). A single mono-exponential decay, T_{Decay}, of the time-domain signal is assumed. B) The Fourier transformation of the FID is also composed of a real (absorptive) and imaginary (dispersive) component.

The $\pi/2$ excitation pulse considered above comprised the most elementary NMR experiment, namely, the on-resonance excitation of an uncoupled spin ½ system. A more general treatment of the same excitation requires a revisiting of the rotating frame Hamiltonian from Eq. (1-56), $\mathcal{H}^{rot} = \{\hbar(\omega_{rot} + \gamma B_o)I_Z + \gamma\hbar B_{1Amp}(\cos(\varphi)I_X + \sin(\varphi)I_Y)\}$. In general, on-resonance excitation, $\omega_{rot} = -\gamma B_o$, is possible only if there is a single resonance frequency representing the entire sample of spins being excited, an uninteresting problem that has utility primarily in determining magnetic moments of nuclei. An immediate consequence of off-resonance excitation is a rotating frame Hamiltonian that will have contributions from non-commuting operators, for example, I_Z and I_X. Evaluation of exponential operators containing non-commuting terms is not possible with the simple series expansion method shown in Eq. (1-58). In practice, the occurrence of such Hamiltonians, with non-commuting elements, tends to be the rule rather than the exception. For that reason a general evaluation method for such cases is provided below with an introduction to chemical shielding in section 1.3.5.

1.3.5 Chemical Shift – Off Resonance Excitation

If NMR spectroscopy was used only to observe non-interacting proton ensembles, a Hamiltonian including only static field and r.f. components would be sufficient, but then an NMR spectrometer would have limited practical application. It is when we examine the magnetic properties of chemical bonds in organic molecules that the power of NMR spectroscopy becomes clear. A hydrogen nucleus within a molecule is surrounded by an electron cloud, with the potential of producing a magnetic field at the nucleus. When placed in a magnetic field, B_o, the charged electron cloud will undergo a Larmor precession about the main field direction, producing a field that is diamagnetic in nature. The electron current is such that the resulting field opposes the field that produced the current (i.e. Lenz's Law). The reduction in the main field at the location of the nucleus is directly proportional to the magnitude of the applied field, B_o (134). One can express the altered field as a function of the applied field and a shielding constant, σ, as

$$B_o^{shifted} = B_o(1-\sigma), \qquad (1\text{-}66)$$

or in terms of resonant frequency

$$\omega_o^{shifted} = \omega_o (1-\sigma). \qquad (1\text{-}67)$$

For the protons in organic molecules, the ^1H chemical shifts are of the order of 1 to 10 parts per million (ppm) of the main field.

The reference by which the proton chemical shifts are measured is not the unshielded free proton, due to the unavailability of such a solution, rather the proton resonance from the unreactive molecule tetramethylsilane (TMS), $(CH_3)_4Si$, is the commonly defined as the $\sigma = 0$ ppm reference. The chemical shift of a given resonance at ω_a can thus be defined as

$$\sigma_a = \frac{\omega_a - \omega_{TMS}}{\omega_o} x10^6 \text{ ppm}, \qquad (1\text{-}68)$$

where ω_o is the Larmor Frequency. In liquid samples, the chemical shift we measure is isotropic, meaning it is independent of the sample orientation relative to the main field.

The majority of proton resonances from the metabolites found in-vivo have chemical shifts in the range of 1 ppm to 5 ppm, a span of about only 500 Hz at a field strength of 3 T, whereas the main field is approximately 128 MHz at this field strength. This distribution of resonant frequencies, albeit small compared to the main field, necessarily precludes on-resonance excitation for all species considered, prompting a consideration of the influence of off-resonance excitation. For all future references, the rotating frame will be assumed to be precessing at the TMS resonance, allowing the rotating frame Hamiltonian to expressed in terms of the TMS-referenced chemical shift values.

Returning now to the rotating frame Hamiltonian, $\mathcal{H}^{rot}$, the general case of an r.f. pulse applied off-resonance can be expressed

$$\mathcal{H}^{rot} = \{\hbar\omega_a I_Z + \gamma\hbar B_{1Amp}(\cos(\varphi)I_X + \sin(\varphi)I_Y)\}, \qquad (1\text{-}69)$$

where $\omega_a = (\sigma_a\omega_o)x10^{-6}$ in the rotating frame.

To calculate the density operator throughout or following the application of such a pulse, exponential operator expressions of the form $\exp(i\mathcal{H}^{rot}t/\hbar)$, in $\rho(t) = \exp(-i\mathcal{H}^{rot}t/\hbar)\rho(0)\exp(i\mathcal{H}^{rot}t/\hbar)$, must be evaluated. As shown in Eq. (1-69), $\mathcal{H}^{rot}$ contains non-commuting terms, thereby excluding the method of series expansions, derived in Appendix I (130). *From this point onwards, the Hamiltonian is assumed to be represented in the rotating frame of reference, allowing us to drop the $\mathcal{H}^{rot}$ notation.*

A powerful and general method of evaluating the exponential of an arbitrary Hamiltonian involves diagonalizing the Hamiltonian matrix by a transformation to an alternate frame of reference. While a wavefunction (vector) transformation is carried out with a single operation, $\Psi_{transformed} = U\Psi$, as in Eq. (1-52), operator (matrix) transformations require the conjugate pair operation, $A_{transformed} = UAU^{-1}$.

$$\mathcal{H}_{diag} = U\,\mathcal{H}U^{-1} \qquad (1\text{-}70)$$

The calculation of the diagonal Hamiltonian and the unitary operator, U, is a matter of determining the eigenvalues and corresponding eigenvectors of the rotating frame Hamiltonian, $\mathcal{H}$. Each diagonal element of $\mathcal{H}_{diag}$ is an eigenvalue of $\mathcal{H}$, and columns of U are formed from the corresponding eigenvectors. If the n^{th} eigenvalue is D_n, and the n^{th} eigenvector, V_n, we can write

$$\mathcal{H}_{diag} = \begin{pmatrix} D_1 & & & \\ & D_2 & & 0 \\ & & D_3 & \\ & 0 & & \ddots \\ & & & & D_n \end{pmatrix}, \qquad (1\text{-}71)$$

$$\text{and } U = \begin{pmatrix} V_1 & V_2 & V_3 & \cdots & V_n \end{pmatrix}. \qquad (1\text{-}72)$$

The proton system we have considered up to this point has just two eigenvalues and two eigenvectors, but as we shall see in the following section, the coupled proton spin systems (spin ½ systems), in general, have 2^N such values, for N-spin systems.

We can express the density matrix at time = 0, $\rho(0)$, and at time = t, $\rho(t)$, in this new frame of reference as $\rho(0)_{diag} = U\rho(0)U^{-1}$ and $\rho(t)_{diag} = U\rho(t)U^{-1}$, where the 'diag' subscript refers the frame in which $\mathcal{H}$ is diagonal. Rewriting Eq. (1-48) in this modified frame

$$U\rho(t)U^{-1} = \rho(t)_{diag} = \exp(-i\mathcal{H}_{diag}t/\hbar)\rho(0)_{diag}\exp(i\mathcal{H}_{diag}t/\hbar), \qquad (1\text{-}73)$$

and then acting on left and right sides of (1-73) with U^{-1} and U, respectively, to return to the rotating frame of reference, yields

$$\rho(t) = U^{-1}\exp(-i\mathcal{H}_{diag}t/\hbar)\,U\rho(0)U^{-1}\exp(i\mathcal{H}_{diag}t/\hbar)U, \qquad (1\text{-}74)$$

where the defining expression for $\rho(0)_{diag}$ was substituted back into (1-74). The diagonal form of the Hamiltonian is desirable because of the ease of its evaluation. The exponential of a diagonal matrix is also a diagonal matrix, with each new diagonal element simply the scalar exponential of the argument diagonal element. The exponential operator in Eq. (1-74) can then be expressed as

$$\exp(i\mathcal{H}_{diag}t/\hbar) = \begin{pmatrix} \exp(iD_1t/\hbar) & & & & \\ & \exp(iD_2t/\hbar) & & 0 & \\ & & \exp(iD_3t/\hbar) & & \\ & 0 & & \ddots & \\ & & & & \exp(iD_nt/\hbar) \end{pmatrix}. \qquad (1\text{-}75)$$

The density matrix evolution equation shown in Eq. (1-74) is appropriate for any time-independent Hamiltonian, and will be applied extensively in the remaining chapters of this thesis. The utility of this equation lies in its numerical rather than algebraic application due to the complexity of the algebraic eigenvalue and eigenvector calculations, especially for the more demanding coupled systems of five or six spins.

As a simple illustrative example, consider the application of a 5 ms rectangular r.f. pulse oriented along the x-axis in the rotating frame with a tip angle of $\pi/2$ radians, applied 75 Hz off resonance. From the pulse tip angle $\gamma B_{1_{Amp}} t = \pi/2$ radians, $\gamma B_{1_{Amp}} = 100\pi$ radians/sec for the 5ms pulse, allowing the rotating frame Hamiltonian to be written $\mathcal{H} = 150\pi\hbar I_Z + 100\pi\hbar I_X$, from Eq. (1-69). Equation (1-74) was evaluated numerically at time intervals of 50 μs throughout the 5 ms r.f. pulse, assuming the system originated from thermal equilibrium, $\rho(0) = I_Z$. At the end of each of the 50 μs intervals the expectation values of the I_X, I_Y and I_Z operators were evaluated from the density matrix at that time, using Eq. (1-22). Figure 1-5 displays the evolution of these operators over the course of the 5 ms r.f. pulse.

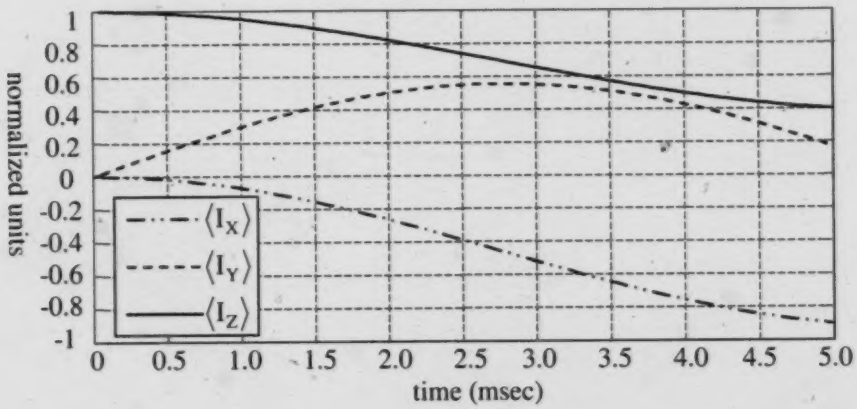

Figure 1-5 The time-evolution of the expectation values of the Cartesian spin components of a singe spin-1/2 system throughout a 5 ms $\pi/2$ rectangular r.f. pulse, applied 75 Hz off resonance.

The chemical shielding effect follows a path of influence from the main field → electrons → nucleus, but there also exists interactions that are independent of the main

field. Nuclei can influence their neighboring nuclei along a path of influence from nucleus[1] → electrons → nucleus[2] through a number of mechanisms, the most common of which is called indirect scalar or J-coupling, as well as along a direct path from nucleus[1] → nucleus[2], which is direct dipolar coupling. Section 1.3.6 outlines the incorporation of the scalar coupling interaction into the density matrix framework already established, while the direct dipole-dipole interaction is presented in section 1.3.8.

1.3.6 Scalar Coupling

As was described in section 1.3.5, the resonant frequency of a proton within a molecule (in a static magnetic field) is influenced by the magnetic properties of the electron distribution around the proton in the molecule. For example, the molecule 1,1-dibromo-2,2-dichloroethane, $CH_{(1)}Br_2CH_{(2)}Cl_2$ has two non-equivalent hydrogen, $H_{(1)}$ and $H_{(2)}$, with different chemical shifts, ω_1 and ω_2. But rather than contributing single peaks at these two frequencies, the NMR spectrum of this molecule contains four peaks, as shown in Fig. 1-6, a consequence of the scalar coupling interaction between the two protons.

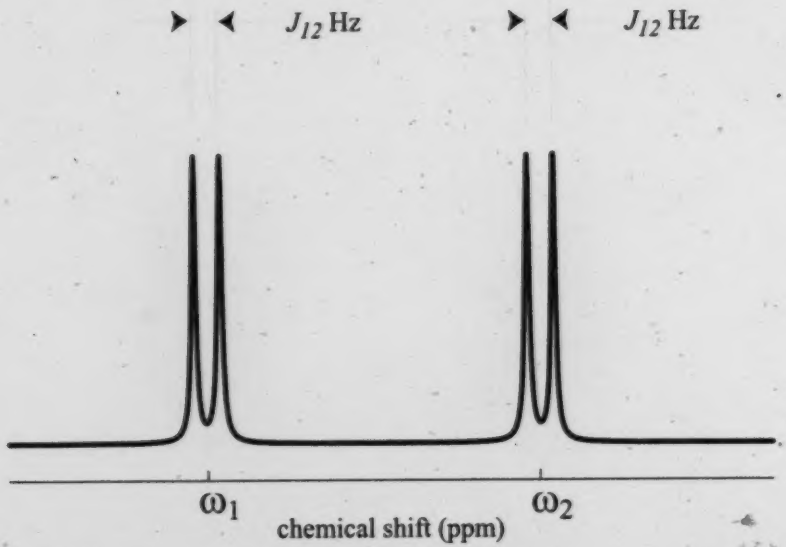

Figure 1-6 A pulse-acquire spectrum of a weakly-coupled two-spin system. The scalar or 'J' coupling between two spins, $spin_1$ and $spin_2$, is characterized by a constant scalar number, J_{12}, in Hz.

The mechanism responsible for this phenomenon is the hyperfine contact interaction, a perturbation of the electron wavefunction at the location of the nucleus, significant only when the wavefunctions have *s*-character, giving them a finite probability of existing at the nucleus (133). The influence of the proton dipolar field on the electron is a polarization of the electron distribution near the nucleus, resulting in the favoring of an electron spin orientation anti-parallel to the proton. The Pauli exclusion principle for electrons in covalent bonds requires that the pair of bonding electrons must have anti-parallel spin orientations, meaning the second electron will favor the spin orientation parallel to the proton. The resulting polarization of the second electron communicates the spin-state of the proton over a distance through the electron cloud. This electron field polarization can extend through several bonds (although with a reduction of influence with an increasing number of bonds) communicating the proton spin states between distant bonded pairs. Of particular interest in proton spectroscopy is the interaction between protons through H_1-C-H_2 and H_1-C-C-H_2 bonds. The interaction Hamiltonian between two such protons, with spin angular moments $\mathbf{I_1}$ and $\mathbf{I_2}$, includes the chemical shift terms as well as the scalar coupling product term, $\mathbf{I_1}\cdot\mathbf{I_2}$,

$$\mathcal{H} = -\hbar(\omega_1 I_{1_z} + \omega_2 I_{2_z} - 2\pi J_{12}\, \mathbf{I_1}\cdot\mathbf{I_2}), \qquad (1\text{-}76)$$

where the proportionality constant, J_{12} (Hz), is the measure of the field perturbation by $spin_1$ at the location of $spin_2$, and vice-versa. The dot-product form of the coupling term reflects the dependence of the interaction on the relative orientation of the coupled proton spins, averaged over all molecular orientations (134). The product term, $\mathbf{I_1}\cdot\mathbf{I_2}$, is invariant under the transformation to the rotating frame from the lab frame, so is equivalent in either frame.

Because the system now contains *two* interacting spins, the wavefunction must be appended to include the additional spin states. The two-spin kets contain information about both spins, with a total of four possible spin states, $|\uparrow\uparrow\rangle$, $|\uparrow\downarrow\rangle$, $|\downarrow\uparrow\rangle$, and $|\downarrow\downarrow\rangle$, giving rise to a two spin wavefunction

$$\Psi = \sum_a c_a|a\rangle = c_{\uparrow\uparrow}|\uparrow\uparrow\rangle + c_{\uparrow\downarrow}|\uparrow\downarrow\rangle + c_{\downarrow\uparrow}|\downarrow\uparrow\rangle + c_{\downarrow\downarrow}|\downarrow\downarrow\rangle. \qquad (1\text{-}77)$$

The previous development of the single spin density matrix and its dynamic equations from sections 1.2 to 1.3.4 are equally applicable to the two spin system, or to any arbitrary coupled N-spin system of protons for that matter. The two-spin energy eigenvalues and thermal equilibrium density matrix will be calculated to illustrate the general properties of multiple spin systems, but first, consider the general form of the density matrix for the two-spin system. Substituting Eq. (1-77) into Eq. (1-21) yields

$$\rho = |\Psi\rangle\langle\Psi| = \begin{array}{c} \\ \langle\uparrow\uparrow| \\ \langle\uparrow\downarrow| \\ \langle\downarrow\uparrow| \\ \langle\downarrow\downarrow| \end{array} \begin{array}{c} \begin{array}{cccc} |\uparrow\uparrow\rangle & |\uparrow\downarrow\rangle & |\downarrow\uparrow\rangle & |\downarrow\downarrow\rangle \end{array} \\ \begin{pmatrix} \overline{c^*_{\uparrow\uparrow}c_{\uparrow\uparrow}} & \overline{c^*_{\uparrow\downarrow}c_{\uparrow\uparrow}} & \overline{c^*_{\downarrow\uparrow}c_{\uparrow\uparrow}} & \overline{c^*_{\downarrow\downarrow}c_{\uparrow\uparrow}} \\ \overline{c^*_{\uparrow\uparrow}c_{\uparrow\downarrow}} & \overline{c^*_{\uparrow\downarrow}c_{\uparrow\downarrow}} & \overline{c^*_{\downarrow\uparrow}c_{\uparrow\downarrow}} & \overline{c^*_{\downarrow\downarrow}c_{\uparrow\downarrow}} \\ \overline{c^*_{\uparrow\uparrow}c_{\downarrow\uparrow}} & \overline{c^*_{\uparrow\downarrow}c_{\downarrow\uparrow}} & \overline{c^*_{\downarrow\uparrow}c_{\downarrow\uparrow}} & \overline{c^*_{\downarrow\downarrow}c_{\downarrow\uparrow}} \\ \overline{c^*_{\uparrow\uparrow}c_{\downarrow\downarrow}} & \overline{c^*_{\uparrow\downarrow}c_{\downarrow\downarrow}} & \overline{c^*_{\downarrow\uparrow}c_{\downarrow\downarrow}} & \overline{c^*_{\downarrow\downarrow}c_{\downarrow\downarrow}} \end{pmatrix} \end{array} . \qquad (1\text{-}78)$$

Like the single spin system, the diagonal elements correspond to the populations of each state, and the off-diagonal elements correspond to coherences between the states. Unlike the single spin system, there are a variety of spin state coherences, that are best categorized using the two-spin density matrix expansion in the basis of the Cartesian operators. While the single-spin system density matrix has a basis of four operators, the two-spin system is described by all possible two-term products of each of the four basis elements for each spin. Specifically, each basis term is a product of the individual spin operators, (I_{1X}, I_{1Y}, I_{1Z}, Id) and (I_{2X}, I_{2Y}, I_{2Z}, Id), giving rise to 16 terms, in a variety of categories. The matrix form of each of these operators is provided in Appendix II.

Longitudinal	I_{1Z}, I_{2Z}, $I_{1Z}I_{2Z}$, Id
Transverse in-phase coherence	I_{1X}, I_{1Y}, I_{2X}, I_{2Y}
Transverse anti-phase coherence	$I_{1X}I_{2Z}$, $I_{1Z}I_{2X}$, $I_{1Y}I_{2Z}$, $I_{1Z}I_{2Y}$
Multiple quantum coherence	$I_{1X}I_{2X}$, $I_{1Y}I_{2Y}$, $I_{1X}I_{2Y}$, $I_{1Y}I_{2X}$

(1-79)

Incorporating the coupled, rotating frame Hamiltonian, $\mathcal{H} = -\hbar(\omega_1 I_{1_z} + \omega_2 I_{2_z} - 2\pi J \mathbf{I_1}\cdot\mathbf{I_2})$, into the time-independent Schrödinger wave equation, the energy eigenstates are solutions of $\mathcal{H}\Psi = E\Psi$, but *only* in the basis in which $\mathcal{H}$ is diagonal. The coupled spin Hamiltonian shown above is not diagonal in the two spin I_Z eigenbasis due to the transverse terms in $\mathbf{I_1}\cdot\mathbf{I_2} = I_{1_X}I_{2_X} + I_{1_Y}I_{2_Y} + I_{1_Z}I_{2_Z}$, as illustrated in the matrix representation of the Hamiltonian

$$\mathcal{H} = \hbar/2 \begin{pmatrix} -\omega_1 - \omega_2 + \pi J & 0 & 0 & 0 \\ 0 & -\omega_1 + \omega_2 - \pi J & 2\pi J & 0 \\ 0 & 2\pi J & \omega_1 - \omega_2 - \pi J & 0 \\ 0 & 0 & 0 & \omega_1 + \omega_2 + \pi J \end{pmatrix}. \quad (1\text{-}80)$$

Fortuitously, we solved this eigenvalue problem in section 1.3.5, where we expressed a transformed Hamiltonian as a diagonal matrix formed from its eigenvalues, using Eq. (1-70). The diagonal form of this Hamiltonian is

$$\mathcal{H}_{diag} = \hbar/2 \begin{pmatrix} -\omega_1 - \omega_2 + \pi J & 0 & 0 & 0 \\ 0 & \{-\chi - \pi J\} & 0 & 0 \\ 0 & 0 & \{\chi - \pi J\} & 0 \\ 0 & 0 & 0 & \omega_1 + \omega_2 + \pi J \end{pmatrix}, \quad (1\text{-}81)$$

where $\chi = [(\omega_1 - \omega_2)^2 + (2\pi J)^2]$, and the eigenvalues, the values along the diagonal, correspond to four energy levels

$$\begin{aligned} E_{\uparrow\uparrow} &= \hbar/2(-\omega_1 - \omega_2 + \pi J), \\ E_{\uparrow\downarrow} &= \hbar/2\{-[(\omega_1 - \omega_2)^2 + (2\pi J)^2]^{1/2} - \pi J\}, \\ E_{\downarrow\uparrow} &= \hbar/2\{[(\omega_1 - \omega_2)^2 + (2\pi J)^2]^{1/2} - \pi J\}, \\ E_{\downarrow\downarrow} &= \hbar/2(+\omega_1 + \omega_2 + \pi J). \end{aligned} \quad (1\text{-}82)$$

The frequencies ω_1 and ω_2 are defined in the rotating frame, so transformation to the laboratory frame energies requires addition of the rotating frame offset, ω_{rot}, resulting in $\omega_1^{lab} = \omega_1 + \omega_{rot}$, and $\omega_2^{lab} = \omega_2 + \omega_{rot}$.

Figure 1-7 contains the two-spin analog to the single spin energy level diagram from Fig, 1-1, along with the corresponding transition energies.

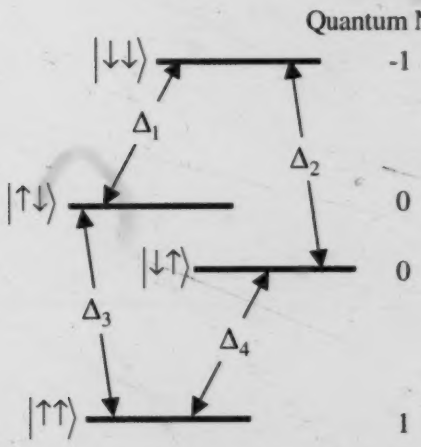

Single Quantum Transitions

$\Delta_1 = E_{\downarrow\downarrow} - E_{\uparrow\downarrow} \rightarrow \hbar(\omega_1 + \pi J)$ for $\delta\omega >> 2\pi J$

$\Delta_2 = E_{\downarrow\downarrow} - E_{\downarrow\uparrow} \rightarrow \hbar(\omega_2 + \pi J)$ for $\delta\omega >> 2\pi J$

$\Delta_3 = E_{\uparrow\downarrow} - E_{\uparrow\uparrow} \rightarrow \hbar(\omega_2 - \pi J)$ for $\delta\omega >> 2\pi J$

$\Delta_4 = E_{\downarrow\uparrow} - E_{\uparrow\uparrow} \rightarrow \hbar(\omega_1 - \pi J)$ for $\delta\omega >> 2\pi J$

Double Quantum Transition

$E_{\downarrow\downarrow} - E_{\uparrow\uparrow} = \hbar(\omega_1 + \omega_2)$

Zero Quantum Transition

$E_{\uparrow\downarrow} - E_{\downarrow\uparrow} = \hbar\,[(\delta\omega)^2 + (2\pi J)^2]^{1/2}$

Figure 1-7 Energy level diagram of a 2-member spin ½ system in a static magnetic field, B_o, and the corresponding energies of the coherent transitions. The *order* of the coherence is defined as the difference of the quantum numbers associated with the energy levels, giving rise the transition labels, zero, single and double quantum coherences. The $\delta\omega$ term in the ZQC transition is equal to the chemical shift difference $\omega_1 - \omega_2$.

The thermal equilibrium density matrix for an N-spin-½ system is the sum the individual equilibrium matrices, the I_{N_Z}, which, for the two spin system, is

$$\rho_{Eq} = \gamma\hbar\beta B_0/2\left\{\begin{pmatrix}1&0&0&0\\0&1&0&0\\0&0&-1&0\\0&0&0&-1\end{pmatrix}+\begin{pmatrix}1&0&0&0\\0&-1&0&0\\0&0&1&0\\0&0&0&-1\end{pmatrix}\right\} = \gamma\hbar\beta B_0\begin{pmatrix}1&0&0&0\\0&0&0&0\\0&0&0&0\\0&0&0&-1\end{pmatrix} \quad (1\text{-}83)$$

The generation of coherence, or non-zero off-diagonal elements, is achieved exactly as outlined for the single spin system in section 1.3.4, utilizing r.f pulses.

Although, unlike the single spin system, which has but one coherence type, corresponding to the transverse magnetization, the coupled spin groups posses categories of coherences, only some of which will contribute to the observable magnetization, while others are invisible to direct detection. The elements in the density matrix can be labeled by category, each according to order of the coherence between states (1-84).

$$\begin{array}{c} \\ \langle\uparrow\uparrow| \\ \langle\uparrow\downarrow| \\ \langle\downarrow\uparrow| \\ \langle\downarrow\downarrow| \end{array} \begin{array}{c} \begin{array}{cccc} |\uparrow\uparrow\rangle & |\uparrow\downarrow\rangle & |\downarrow\uparrow\rangle & |\downarrow\downarrow\rangle \end{array} \\ \begin{pmatrix} \text{Pop} & \text{SQC}_2 & \text{SQC}_1 & \text{DQC} \\ \text{SQC}_2 & \text{Pop} & \text{ZQC} & \text{SQC}_1 \\ \text{SQC}_1 & \text{ZQC} & \text{Pop} & \text{SQC}_2 \\ \text{DQC} & \text{SQC}_1 & \text{SQC}_2 & \text{Pop} \end{pmatrix} \end{array} \qquad (1\text{-}84)$$

Each of the element categories, Pop, SQC, ZQC and DQC, is outlined below and expressed in terms of the two-spin Cartesian basis operators.

Pop (Population Elements) (I_{1z}, I_{2z}, $I_{1z}I_{2z}$, and Id)

Each of these basis terms comprises a different combination of the four populations, $\overline{c^*_{\uparrow\uparrow}c_{\uparrow\uparrow}}$, $\overline{c^*_{\uparrow\downarrow}c_{\uparrow\downarrow}}$, $\overline{c^*_{\downarrow\uparrow}c_{\downarrow\uparrow}}$, and $\overline{c^*_{\downarrow\downarrow}c_{\downarrow\downarrow}}$. I_{1z} and I_{2z} represent the thermal equilibrium magnetizations, as shown in Eq. (1-83), representing the static population differences between the states. The identity matrix (Id) contribution is discarded, as described in section 1.3.1. $I_{1z}I_{2z}$, often termed the longitudinal Z-order term, is a population distribution that is rarely produced over the course of in-vivo NMR experiments, and has no contribution at thermal equilibrium in the high temperature approximation model. Although, as mentioned in section 1.3.2, thermal equilibrium contributions from products of longitudinal terms, such as $I_{1z}I_{2z}$, will become significant if the high temperature truncation of the Boltzmann distribution of populations becomes invalid (128).

SQC$_1$ and SQC$_2$ (Single Quantum Coherences) (I_{1_X}, I_{1_Y}, I_{2_X}, I_{2_Y}, $I_{1_X}I_{2_Z}$, $I_{1_Y}I_{2_X}$, $I_{1_Z}I_{2_X}$, $I_{1_Z}I_{2_Y}$)

These eight basis terms are labeled *single quantum* coherences because the coherence they represent is between states whose quantum numbers differ by 1, as indicated by the Δ_1 to Δ_4 transitions in Fig. 1-7. The single term coherences, I_{1_X}, I_{1_Y} etc., termed the *in-phase* coherences, correspond to the observable transverse magnetization as outlined in section 1.3.4, while the product terms, of the form $I_{N_{Transverse}}I_{N'_{Longitudinal}}$, are termed *anti-phase* coherence, and unlike the in-phase terms, do not directly contribute to the observable magnetization. These two SQC classes are best contrasted by comparing their matrix elements, as shown in Fig. 1-8, where the I_{1_X} and $I_{1_X}I_{2_Z}$ matrices are displayed.

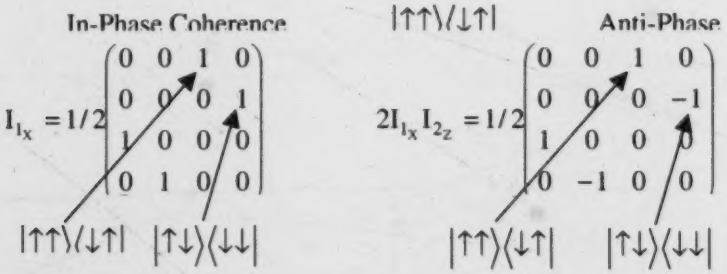
In-Phase Coherence
$I_{1_X} = 1/2$
$\begin{pmatrix} 0 & 0 & 1 & 0 \\ 0 & 0 & 0 & 1 \\ 1 & 0 & 0 & 0 \\ 0 & 1 & 0 & 0 \end{pmatrix}$
$|\uparrow\uparrow\rangle\langle\downarrow\uparrow|$
$|\uparrow\downarrow\rangle\langle\downarrow\downarrow|$
$|\uparrow\uparrow\rangle\langle\downarrow\uparrow|$
Anti-Phase
$2I_{1_X}I_{2_Z} = 1/2$
$\begin{pmatrix} 0 & 0 & 1 & 0 \\ 0 & 0 & 0 & -1 \\ 1 & 0 & 0 & 0 \\ 0 & -1 & 0 & 0 \end{pmatrix}$
$|\uparrow\uparrow\rangle\langle\downarrow\uparrow|$
$|\uparrow\downarrow\rangle\langle\downarrow\downarrow|$

Figure 1-8 Matrix representations of two two-spin single quantum product operator terms, an in-phase and an anti-phase term. The non-zero matrix elements correspond to coherence between the states indicated in the outer products.

Both the in-phase and anti-phase single quantum coherence terms shown in Fig. 1-8 comprise two coherences (along with the conjugate elements in the lower triangular region), both of which correspond to the spin labeled '$spin_1$', as can be verified by inspecting the inner product term associated with each element. These coherences correspond to the energy level transitions Δ_1 and Δ_4 from the energy level diagram in Fig. 1-7. The $I_{1_X}I_{2_Z}$ matrix is distinguished from I_{1_X} by the negative element, which can be interpreted as a 180° phase shift or *anti-phase* relationship between the two transitions. That is to say, when the transitions Δ_1 and Δ_4 have a relative phase difference of 180° between them, the coherence is termed anti-phase, and is termed in-phase when the transitions are in-phase.

The in-phase and anti-phase terms provide a tool, and a useful language, to represent the relative phase of the transitions Δ_1 and Δ_4 for $spin_1$, or equivalently Δ_2 and Δ_3 for $spin_2$, a phase difference that evolves under the influence of the scalar coupling, as shown in section 1.3.6.1a.

ZQC (Zero Quantum Coherence) $(I_{1X}I_{2X} + I_{1Y}I_{2Y}, I_{1X}I_{2Y} - I_{1Y}I_{2X})$

The two spin system has a single ZQC contribution, with a real and an imaginary component, often termed $ZQC_X = I_{1X}I_{2X} + I_{1Y}I_{2Y}$ and $ZQC_Y = I_{1X}I_{2Y} - I_{1Y}I_{2X}$, respectively. From Fig. 1-7, the ZQ coherence is between the $|\uparrow\downarrow\rangle$ and $|\downarrow\uparrow\rangle$ states, both of which have quantum numbers of 0, and an energy difference of $E_{\uparrow\downarrow} - E_{\downarrow\uparrow} = \hbar[(\delta\omega)^2 + (2\pi J)^2]^{1/2}$, a directly undetectable transition.

DQC (Double Quantum Coherence) $(I_{1X}I_{2X} - I_{1Y}I_{2Y}, I_{1X}I_{2Y} + I_{1Y}I_{2X})$

The two spin system has a single DQC contribution, with a real and an imaginary component, like the ZQC, and likewise, are often termed $DQC_X = I_{1X}I_{2X} - I_{1Y}I_{2Y}$ and $DQC_Y = I_{1X}I_{2Y} + I_{1Y}I_{2X}$, respectively. From Fig. 1-7, the DQ coherence is between the states $|\uparrow\uparrow\rangle$ and $|\downarrow\downarrow\rangle$, which have quantum numbers 1 and –1 respectively, a difference of 2, and an energy difference of $E_{\downarrow\downarrow} - E_{\uparrow\uparrow} = \hbar(\omega_1 + \omega_2)$, a directly undetectable transition as was the case with the ZQC.

The ZQC's and DQC's fall into a broader category of coherence called multiple quantum coherence (MQC). Spin-½ systems with N-spins are capable of generating MQC's ranging from zero-order to N-order, for example, a three spin system can generate ZQC, DQC as well as triple quantum coherence (TQC), none of which contribute directly to the observable magnetization. Under normal circumstances, when the thermal equilibrium density matrix is composed of longitudinal terms I_{N_Z}, the application of at least two r.f. pulses is necessary to generate MQC's, with a preparation period between the pulses, τ. The generation of MQC's by the two pule experiment is illustrated with algebriac methods in section 1.3.6.1a, and numerical methods in section 1.3.6.1b.

In the past, the majority of NMR teaching texts have utilized the algebraic product operator formalism of Sorensen (135) to illustrate the evolution of coherences throughout NMR pulse sequences. These techniques have also been the standard for in-vivo pulse sequence design and optimization when the target metabolites contain coupled spin groups (90-93, 98, 101-106, 108, 112-117, 119, 121). While the algebraic representation of the density operator is an excellent illustrative tool, the large and often strongly coupled spin systems and the complex pulse sequences considered in this thesis are prohibitively demanding of this approach. As has been alluded to throughout the introduction, a numerical approach to evaluating the evolution of the density operator is favorable due to the robustness of the general solution methods, particularly Eq. (1-74). Continuing with the development of the numerical approaches to be employed throughout the remainder of the thesis, the generation of anti-phase and the two-spin coherences throughout the simplest pulse sequence of two pulses is illustrated.

1.3.6.1 The Two Pulse Experiment

A series of two r.f. pulses, applied to a system in thermal equilibrium, with a variable inter-pulse evolution period of τ ms is the simplest NMR experiment that can be used to generate each of the basis terms introduced for the scalar-coupled two spin system. In this treatment, the r.f. pulses will be assumed to be sufficiently short so as to qualify as 'hard' pulses, meaning all chemical shift and scalar coupling evolutions occurring during the pulse can be disregarded, or $\mathcal{H} \cong \mathcal{H}_{rf}$ during this interval. During the evolution period, the system energy operator is the rotating frame two-spin scalar-coupled Hamiltonian, $\mathcal{H} = -\hbar(\omega_1 I_{1_z} + \omega_2 I_{2_z} - 2\pi \mathbf{J} \mathbf{I_1} \cdot \mathbf{I_2})$. This two-pulse experiment is evaluated, first, using algebraic product operator techniques utilizing an approximate scalar-coupled Hamiltonian, and secondly, using numerical techniques employing Eq. (1-74).

1.3.6.1a Weak Coupling and the Product Operator Formalism

If the frequency difference between the two resonances, $\delta\omega_{12} = \omega_2 - \omega_1$, is much larger than the scalar coupling, $\delta\omega_{12} >> 2\pi J_{12}$, the system is termed *weakly* coupled. A

factor of 10 is typically regarded as a sufficient ratio to ensure weak coupling, i.e. $\delta\omega_{12}/2\pi J_{12} \geq 10$. The weakly coupled systems can be approximated with a truncated rotating frame Hamiltonian $\mathcal{H} = -\hbar(\omega_1 I_{1_z} + \omega_2 I_{2_z} - 2\pi J I_{1_z} I_{2_z})$, which is desirable because it is diagonal in the I_Z eigenbasis, resulting in a drastic simplification of algebraic calculations incorporating scalar coupling. Unlike the complete or 'strong' coupling Hamiltonian, which contains all of the non-commuting terms, I_X, I_Y and I_Z, the diagonal Hamiltonian contains only commuting elements, allowing the exponential operators in the density matrix evolution equation, $\rho(t) = \exp(-i\mathcal{H}t/\hbar)\rho(0)\exp(i\mathcal{H}t/\hbar)$, to be evaluated directly using operator algebra. Utilizing the commutative properties of exponential operators, shown in Eqs. (1-85a) and (1-85b),

$$\exp(A + B) = \exp(A)\exp(B) \text{ iff } [A,B] = 0, \text{ and} \tag{1-85a}$$

$$\exp(A)\exp(B) = \exp(B)\exp(A) \text{ iff } [A,B] = 0, \tag{1-85b}$$

the density matrix evolution equation can be rewritten, by separating and reordering the elements, as

$$\rho(t) = R_{J_{12}}^{-1} R_{S_2}^{-1} \overbrace{R_{S_1}^{-1} \rho(0) R_{S_1}}^{\text{chemical shielding for spin1 ... etc.}} R_{S_2} R_{J_{12}} \tag{1-86}$$

where $R_{S_1} = \exp(i\omega_1 I_{1_z} t)$, $R_{S_2} = \exp(i\omega_2 I_{1_z} t)$ and $R_{J_{12}} = \exp(-i2\pi J I_{1_z} I_{2_z} t)$. Evaluating Eq. (1-86) from the inside-out, as indicated, the operator pairs can be applied sequentially, first the individual chemical shift terms, and finally the scalar coupling term, although this order is arbitrary. It is important to note that only by truncating the Hamiltonian can the terms be reordered to simplify the calculations to this extent, allowing each exponential term, R, to be expanded as a power series to remove the operator from the argument, as was shown in Eq. (1-58).

We now have the necessary tools to evaluate the two-pulse experiment using the product operator algebra. The first element of the experiment is a hard excitation pulse, described by a Hamiltonian containing only an r.f. component, a scenario evaluated

previously in section 1.3.4, for an x-directed pulse, where equilibrium magnetization was excited according to $\rho(t) = I_Z \cos(\gamma B_{1Amp} t) + I_Y \sin(\gamma B_{1Amp} t)$. A complete set of hard r.f. pulse excitation rules are defined in Appendix I. Setting $(\gamma B_{1Amp} t) = \pi/2$ to maximally excite the spins yields $\rho(0^+) = I_{1Y} + I_{2Y}$. Free evolution of these transverse terms in the rotating frame can then be calculated by applying Eq. (1-86) along with the transformation rules derived in Appendix I, one phenomenon at a time, as shown in Eqs. (1-87a) to (1-87c).

$$\rho(\tau)_{S_1} = R_{S_1}^{-1}\rho(0^+)R_{S_1} = I_{1Y}\cos(\omega_1\tau) - I_{1X}\sin(\omega_1\tau) + I_{2Y} \quad (1\text{-}87a)$$

$$\rho(\tau)_{S_1+S_2} = R_{S_2}^{-1}\rho(\tau)_{S_1}R_{S_2} = I_{1Y}\cos(\omega_1\tau) - I_{1X}\sin(\omega_1\tau) + I_{2Y}\cos(\omega_2\tau) - I_{2X}\sin(\omega_2\tau) \quad (1\text{-}87b)$$

$$\rho(\tau)_{S_1+S_2+J_{12}} = R_{J_{12}}^{-1}\rho(\tau)_{S_1+S_2}R_{J_{12}} = \{I_{1Y}\cos(\pi J\tau) - 2I_{1X}I_{2Z}\sin(\pi J\tau)\}\cos(\omega_1\tau) -$$
$$\{I_{1X}\cos(\pi J\tau) + 2I_{1Y}I_{2Z}\sin(\pi J\tau)\}\sin(\omega_1 t) + \{I_{2Y}\cos(\pi J\tau) - 2I_{2X}I_{1Z}\sin(\pi J\tau)\}\cos(\omega_2\tau) -$$
$$\{I_{2X}\cos(\pi J\tau) + 2I_{2Y}I_{1Z}\sin(\pi J\tau)\}\sin(\omega_2\tau) \quad (1\text{-}87c)$$

Each of the eight SQC terms is found in Eq. (1-87c), but no ZQC, DQC or longitudinal Z-order terms are produced at this stage of the two-pulse experiment.

Application of the second pulse, again a hard $\pi/2_X$ pulse, after the evolution time, τ, transforms each of the operator terms in Eq. (1-87c) according to the r.f. rotation rules derived in Appendix I, for example, $I_Z \xrightarrow{\gamma B_{1Amp} t I_X} I_Z\cos(\gamma B_{1Amp} t) + I_Y\sin(\gamma B_{1Amp} t)$. Defining Eq. (1-87c) as $\rho(\tau^-)$, the density matrix prior to the 2nd r.f. pulse, the density matrix following the second pulse, $\rho(\tau^+)$, is

$$\rho(\tau^+) = \{I_{1Z}\cos(\pi J\tau) + 2I_{1X}I_{2Y}\sin(\pi J\tau)\}\cos(\omega_1\tau) - \{I_{1X}\cos(\pi J\tau) - 2I_{1Z}I_{2Y}\sin(\pi J\tau)\}\sin(\omega_1\tau) +$$
$$\{I_{2Z}\cos(\pi J\tau) + 2I_{2X}I_{1Y}\sin(\pi J\tau)\}\cos(\omega_2\tau) - \{I_{2X}\cos(\pi J\tau) - 2I_{2Z}I_{1Y}\sin(\pi J\tau)\}\sin(\omega_2\tau). \quad (1\text{-}88)$$

The $I_{1X}I_{2Y}$ and $I_{2X}I_{1Y}$ terms can be grouped to represent the ZQC and DQC terms created by the second r.f. pulse

$$ZQC_X = 0, \tag{1-89a}$$

$$ZQC_Y = \sin(\pi J\tau)\{\cos(\omega_1\tau) - \cos(\omega_2\tau)\}, \tag{1-89b}$$

$$DQC_X = 0, \text{ and} \tag{1-89c}$$

$$DQC_Y = \sin(\pi J\tau)\{\cos(\omega_1\tau) + \cos(\omega_2\tau)\}. \tag{1-89d}$$

If the second pulse of this experiment was not an ideal hard pulse, chemcial shift evolutions during the pulse would have resulted in a non-zero contribution from the longitudinal Z-order term. The utility of the weak coupling approximation and the associated simple product operator transformations has perhaps caused this approach to be used in border-line scenarios, to describe the evolution of in-vivo spin systems which do not meet the factor of 10 ratio, with no verification of the errors induced by the approximation. In particular, the metabolite spin systems GABA (112,113,116) and glutamate (136) have been treated with weak-coupling models without meeting the factor of 10 criterion. To avoid such pitfalls, the weak coupling approximation is never invoked in this thesis, save to exemplify the hazards of this approximation.

1.3.6.1b The Full Coupling Model and Numerical Solutions of the Density Matrix

The evaluation of the two-pulse experiment is now repeated using a numerical approach, without the weak coupling approximation used in 1.3.6.1a. Figure 1-9 illustrates the operator evolutions for a two-spin proton system excited from thermal equilibrium magnetization by a hard $\pi/2_X$ pulse. This evaluation is for times $\tau = 0$ to 200 ms following excitation by the first pulse, but prior to the second pulse. Included is a comparison of the numerical results with the weak coupling predictions of Eq. (1-87c), plotted on both Fig. 1-9A and 1-9B. The spin system modeled has chemical shifts $\omega_1 = 0$ ppm and $\omega_2 = 0.78125$ ppm, and a scalar coupling of 10 Hz, which, in an external field of 3 T (128 MHz), gives rise to a shift separation of $\delta\omega = 100$ Hz, falling exactly on the weak-coupling cutoff, $\delta\omega_{12}/2\pi J_{12} \geq 10$. Equation (1-74) is used to evaluate the density matrix at 0.5 ms intervals, from which the expectation values of all of the 8 SQ basis operators are calculated.

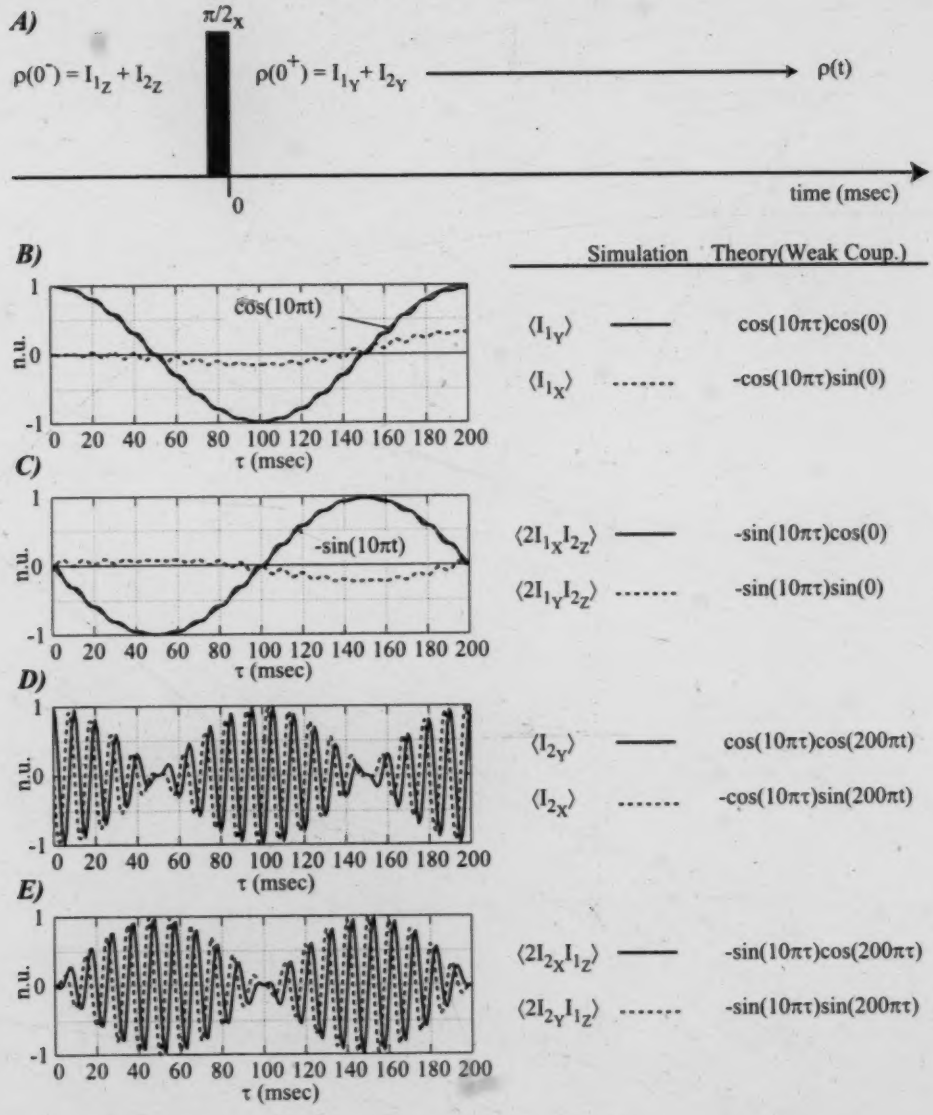

Figure 1-9 The eight SQC or transverse product operator components of the two-spin density matrix are displayed following excitation by an ideal π/2 pulse, shown in A). One chemical shift term was specified at 0 ppm to clearly illustrate the deviation of the weak coupling predictions, from the full coupling response, calculated numerically. The non-zero I_{1_X} and $2I_{1_Y}I_{2_Z}$ contributions in B) and C) result from the influence of the $I_{1_X}I_{2_X}$ and $I_{1_Y}I_{2_Y}$ terms dropped in the weak-coupling approximation, but included in the numerical model. The spin$_2$ SQ terms (ω_2 = 0.78125 ppm) are shown in D) and E).

Figure 1-10 displays the generation of ZQC and DQC components by the second $\pi/2_X$ pulse, along with a direct comparison of the numerical results to the algebraic product operator predictions, from Eq. (1-89), displayed, in this case, as an error resulting from the weak coupling approximation.

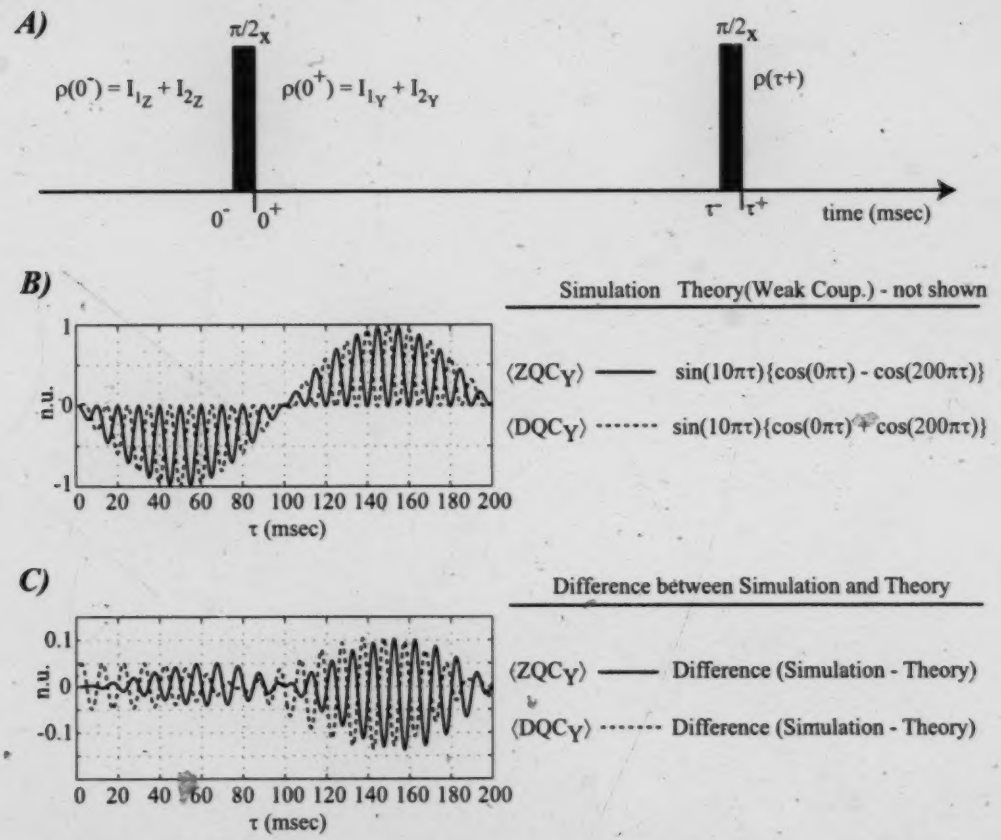

Figure 1-10 The production of ZQC and DQC terms of the two-spin density matrix calculated with the numerical model are displayed in B) following excitation by a sequence of two ideal $\pi/2$ pulses, with an inter-pulse delay of τ ms, shown in A). The difference between the weak-coupling product operator predictions and the complete numerical model are shown in C).

While it is possible to derive algebraic product operator evolution equations of the form of Eq. (1-87c) from the full strongly coupled Hamiltonian (1-76) used in the numerical model (137), the proliferation of the algebraic terms quickly becomes unmanageable as the number of spins increase beyond two. For example, in a recent

publication, Wilman and Allen (91) provided the product operator calculation of the yield of the AB portion of the ABX spin group of NAA following the PRESS sequence. The algebraic result contains an astonishing 131,072 additions and multiplications of sinusoids and exponentials, with quadratic arguments. The algebraic response of the larger strongly coupled spin groups, such as the five spin systems glutamate and glutamine, will require the addition and multiplication of millions of sinusoids, nullifying any advantage of the closed algebraic form. Even if these algebraic expressions were calculated with the aid of computer methods, such as MAPLE or Mathematica (105,119,138-140) the influence of the shaped r.f. pulses, used in every in-vivo sequence, could not be calculated due to the time-dependence of such a Hamiltonian, invalidating Eq. (1-48), the density operator evolution equation. The legitimacy of the algebraic product operator equations, such as those derived in Appendix I, require the validity of Eq. (1-48). Utilizing Eq. (1-74), the numerical calculation of the density matrix or the expectation value of any the component operators is a general problem handled identically for any definable Hamiltonian, or any spin system, with up to six spins in this thesis. What is more, the inclusion of the influence of shaped r.f. pulses is possible using approximate methods, based again on Eq. (1-74), as is outlined in detail in section 1.3.7.1 and chapter 2, *Numerical Methods in In-vivo NMR Spectroscopy*.

1.3.7 Magnetic Field Gradients

All spin system representations in sections 1.3 to 1.3.6 are defined in a spin vector space with a dimensionality that depends only the number of spins, with no dependence on the spatial coordinates of the spin system. For example, the chemical shielding and scalar coupling phenomena, while arising from the spatial distribution of electrons in a molecule, are represented by scalar constants without spatial dependence, particularly for systems of isotropic liquids. Nevertheless, an essential element of the in-vivo NMR experiment is the acquisition of metabolite signal from target tissue regions in the body, corresponding to regions of pathology or unique function. From a practical standpoint, the elimination of unwanted out of volume *contaminating* signal is equally essential. To spatially localize or encode the NMR signal to the target tissue, spatial variations in the main static magnetic field, termed magnetic field gradients, are employed to differentiate regions of space. The vast majority of in-vivo NMR experiments employ gradients for

the purposes of spatial localization, or spatial encoding in imaging applications, while a limited number of applications employ r.f. coil geometry, exclusively, to limit the volume of interest.

The influence of a linear gradient field is represented mathematically much like the chemical shielding interaction, as a deviation of the main magnetic field strength,

$$B = B_o + \mathbf{G}\cdot\mathbf{r}, \tag{1-90}$$

however, the gradient shift is spatially dependent while the chemical shift is species dependent. The gradient magnetic field is always directed along the z-axis, parallel to the main field, although the direction of its variation over space can be along any axis. The corresponding shift in resonance frequency is given by the usual Larmor equation,

$$\omega = -\gamma(B_o + \mathbf{G}\cdot\mathbf{r}). \tag{1-91}$$

The rotating frame gradient Hamiltonian

$$\mathcal{H}_{Grad} = -\gamma\hbar\,\mathbf{G}\cdot\mathbf{r}I_Z, \tag{1-92}$$

has a contribution from the I_Z operator alone, like the chemical shielding Hamiltonian, giving rise to evolutions identical in form to the chemical shielding terms (see Appendix I), for example $I_Y \xrightarrow{-\gamma\hbar\mathbf{G}\cdot\mathbf{r}I_Z} I_Y\cos(\gamma\mathbf{G}\cdot\mathbf{r}t) - I_X\sin(\gamma\mathbf{G}\cdot\mathbf{r}t)$. The influence of the gradient can readily be interpreted as imparting a phase to all transverse terms, for example, the magnetization in the transverse (rotating) plane, according to

$$\theta_{Grad} = -\gamma\mathbf{G}\cdot\mathbf{r}t. \tag{1-93}$$

The application of a gradient of given amplitude and length is said to *de-phase* the magnetization over space, because of the resulting dependence of the magnetization phase on the position in space. The transverse magnetization is completely de-phased when the resulting sum of the magnetization over the entire sample approaches zero.

The large coils that produce the magnetic field gradients for in-vivo experiments have large inductances that force the driving currents to rise slowly on the NMR time-scale, from 100's to 1000's of μsec's, resulting in time-dependent gradient waveforms. The phase induced by the gradients in these cases can be expressed more generally by the integral,

$$\theta_{Grad} = -\gamma \int \mathbf{G} \cdot \mathbf{r} dt \,. \qquad (1\text{-}94)$$

Figure 1-11 illustrates the influence of a gradient pulse on uncoupled transverse magnetization.

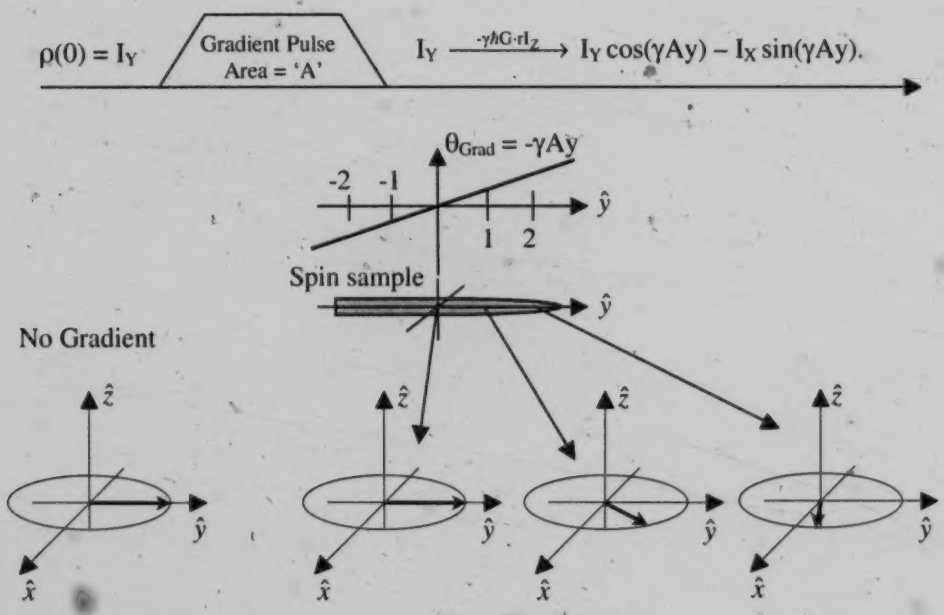

Figure 1-11 Application of a gradient pulse ($\hat{y}$ - varying), G(t), of area 'A'=$\int$G(t)dt encodes a phase to the transverse magnetization that is proportion to the sample location in space, y.

1.3.7.1 Gradients and R.F. Pulses – Spectrally to Spatially Selective Excitation

While ideal hard r.f. pulses of infinitesimal length excite all frequencies equivalently, pulses of finite length will excite a bandwidth of frequencies around the r.f. carrier frequency with a characteristic profile, a function of the pulse envelope. Although closely approximated by the Fourier transform, the resulting frequency excitation profile deviates from the linear Fourier theory due to the non-linearity of the rotations associated with NMR evolutions, increasingly so with an increase in the r.f. pulse tip angle. Figure 1-12 displays a rectangular r.f. envelope and the corresponding Fourier transform distribution of frequencies, the well known sinc(x) = sin(x)/x shape.

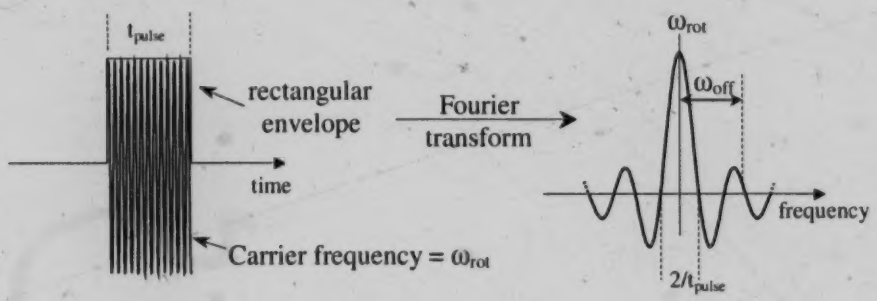

Figure 1-12 An r.f. pulse with a rectangular envelope excites a distribution of frequencies around the carrier frequency that is approximated with the Fourier transform of the envelope, the well known sinc distribution.

To generate the NMR frequency excitation profile of the rectangular r.f pulse shown in Fig. 1-12, several frequencies around the r.f. carrier frequency, assumed to be the rotating frame frequency, must be simulated separately, each one corresponding to a different off-resonance excitation, ω_{off}. If the r.f. pulse is applied concurrently with a magnetic field gradient, the spectral excitation profile of the pulse is transduced to spatial excitation, because each point in space in the gradient field corresponds to a frequency, $\omega(\mathbf{r}) = -\gamma(B_o + \mathbf{G}\cdot\mathbf{r})$. Fortuitously, the off-resonance excitation problem was solved in section 1.3.5 for an uncoupled spin system, where the chemical shielding influence was incorporated into the rotating frame r.f. pulse Hamiltonian, $\mathcal{H}$ =

$\{\hbar\omega_{off}I_Z + \gamma\hbar B_{1Amp}(\cos(\varphi)I_X + \sin(\varphi)I_Y)\}$. Assuming an x-directed pulse, $\varphi = 0°$, with a tip angle of $\pi/2$ radians ($\gamma B_{1Amp} t_{pulse} = \pi/2$), the rotating frame Hamiltonian becomes

$$\mathcal{H} = \hbar(\omega_{off}I_Z + \pi/(2t_{pulse})I_X). \tag{1-95}$$

Figure 1-13 displays the expectation values of the single spin Cartesian operators following excitation from thermal equilibrium as a function of the offset, ω_{off}. Equation (1-74) is evaluated numerically for a pulse length 1 msec, and offsets ranging from -4000 Hz to 4000 Hz at 50 Hz intervals, allowing the density matrix, and thus the operator expectation values to be calculated over the range of offsets.

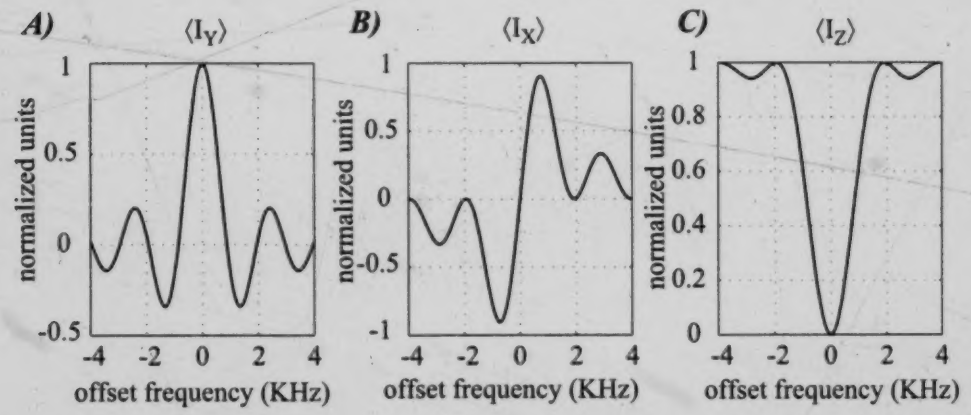

Figure 1-13 The single spin Cartesian operator expectation values are displayed in A), B) and C), following excition with a 1 msec rectangular pulse, from thermal equilibrium, as a function of resonance offset, ω_{off}, from equation(1-94). The $\pi/2_X$ pulse tips the magnetization completely to I_Y only for on-resonance excitation, as expected. The density matrix was evaluated for offsets of -4000 Hz to 4000 Hz at 50 Hz intervals, for a total of 161 seperate simulations.

While the Fourier profile from Fig. 1-12 closely approximates the NMR excitation profile shown from Fig. 1-13 A), there is a still a notable deviation, as is shown in Fig. 1-14A, for the case of the 1 msec $\pi/2$ rectangular pulse. The RMS deviation of the Fourier profile from the NMR excitation profile is exacerbated by an increase in the r.f. pulse tip angle, as shown in Fig. 1-14B, due to the increase in the non-linearity with increasing r.f. amplitude.

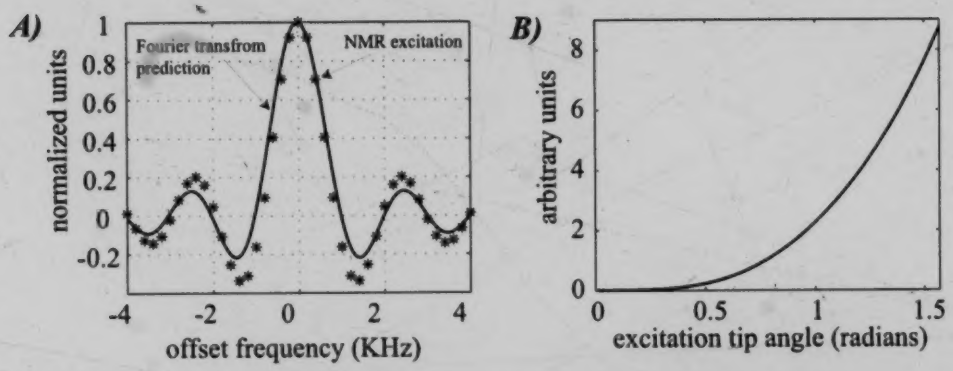

Figure 1-14 A) A direct comparison of the excitation frequency profile of a 1 ms rectangular pulse predicted with Fourier transform and NMR theory. B) The RMS deviation of the Fourier excitation profile from the NMR excitation profile as a function of the hard pulse tip angle (normalized to the tip angle).

The application of a magnetic field gradient, say along the y-axis ($\mathbf{G}\cdot\mathbf{r} = G_y y$), concurrent with the rectangular pulse will yield an identical excitation profile, incorporating the simple transformation $\omega_{off} \rightarrow \gamma G_y y$ from Eq. (1-91). For a given gradient strength, G_y, the frequency axes in Figs. 1-13 and 1-14 can be replaced with position, $y = (\omega_{off})/\gamma G_y$. For example, the application of a gradient, G_y = 0.25 G/cm, concurrent with the 1 ms rectangular pulse will excite a sinc-like profile with a central lobe width $2/t_{pulse}$ = 2000 Hz, or y = (2*pi*2000)/(2.676e4*0.25) = 1.8784 cm, using γ (^{1}H) = 2.676e4 radians s G.

The non-uniform magnitude and phase profile of the transverse magnetization ($M_{trans} \propto \langle I_X \rangle + i\langle I_Y \rangle$) excited by the rectangular r.f. pulse are not appropriate for spatially selective excitation in in-vivo NMR spectroscopy, rather, a constant phase and rectangular 'top-hat' profile are desired. The purpose of such an excitation is to limit the source of the NMR signal to a targeted region of tissue, minimizing the signal arising from outside the target region. For example, if pathological tissue and healthy tissue are simultaneously excited, the metabolite abnormalities of the pathology will be diluted by the healthy tissue metabolite signal. Additionally, the need to optimize the signal yield, to overcome the low signal to noise ratio inherent to in-vivo NMR spectroscopy, requires a uniform excitation with a minimum phase variation over the excitation slice. This ideal profile allows all regions of the excitation space to experience the same optimized tip

angles, providing 100 % excitation and no destructive dephasing of the signal over space, essentially, hard pulse excitation with spatial selectivity. The r.f. pulse shape that will provide the desired excitation is necessarily time-dependent, resulting in a time-dependent Hamiltonian that cannot be incorporated into the solution techniques presented thus far, particularly Eq. (1-74), or its predecessors. An approximate method of solution is presented in chapter 2, *Numerical Methods in In-Vivo NMR Spectroscopy*, where a detailed analysis of the influence of spatially selective pulses in in-vivo NMR is provided.

1.3.7.2 Gradients and Coupled Spin Systems – Coherence Selection

When magnetic field gradients are applied to coupled spin systems, each spin in the system, for example $\mathbf{I_1}$ and $\mathbf{I_2}$ in the two-spin system, will experience the gradient, resulting in evolutions of the form $I_Y \xrightarrow{-\gamma\hbar G\cdot rI_Z} I_Y \cos(\gamma\mathbf{G}\cdot\mathbf{r}t) - I_X \sin(\gamma\mathbf{G}\cdot\mathbf{r}t)$ for each spin. The gradient evolutions can be applied separately to each spin because the $\mathbf{I_1}$ and $\mathbf{I_2}$ operators commute, resulting in products of trigonometric evolutions, giving rise to sums and differences of the trigonometric arguments. For example, under gradient evolution, the product term, $2I_{1Y}I_{2Y} = ZQC_X - DQC_X$, evolves as

$$2I_{1Y}I_{2Y} \xrightarrow{-\gamma\hbar G\cdot rI_{1_Z}} \xrightarrow{-\gamma\hbar G\cdot rI_{2_Z}} 2I_{1Y}I_{2Y}\cos(\gamma\mathbf{G}\cdot\mathbf{r}t)\cos(\gamma\mathbf{G}\cdot\mathbf{r}t) - 2I_{1X}I_{2Y}\sin(\gamma\mathbf{G}\cdot\mathbf{r}t)\cos(\gamma\mathbf{G}\cdot\mathbf{r}t)$$
$$-2I_{1Y}I_{2X}\sin(\gamma\mathbf{G}\cdot\mathbf{r}t)\cos(\gamma\mathbf{G}\cdot\mathbf{r}t) + 2I_{1X}I_{2X}\sin(\gamma\mathbf{G}\cdot\mathbf{r}t)\sin(\gamma\mathbf{G}\cdot\mathbf{r}t)$$

$$= I_{1Y}I_{2Y}(1 + \cos(2\gamma\mathbf{G}\cdot\mathbf{r}t)) - (I_{1X}I_{2Y} + I_{1Y}I_{2X})\sin(2\gamma\mathbf{G}\cdot\mathbf{r}t) + I_{1X}I_{2X}\ (1 - \cos(2\gamma\mathbf{G}\cdot\mathbf{r}t)). \quad (1\text{-}96)$$

Grouping terms from this expression, we can write

$$ZQC_X - DQC_X \rightarrow ZQC_X - (DQC_X\cos(2\gamma\mathbf{G}\cdot\mathbf{r}t)) + DQC_Y\sin(2\gamma\mathbf{G}\cdot\mathbf{r}t))). \quad (1\text{-}97)$$

Generally speaking, the magnetic field gradients encode the various coherences, ZQC, SQC, DQC, … etc., with a phase that is proportional to the order of the coherence, p, allowing the coherences to be discriminated based on that order. The phase induced by

a gradient on the coherences of a coupled spin system can then be expressed as a function of the coherence order as

$$\theta_{Grad} = -p\gamma\int Grdt\,. \qquad (1\text{-}98)$$

Singly acting gradients are typically employed as destroyers of magnetization (save for those concurrent with r.f pulses), while pairs of gradients are used to de-phase and subsequently re-phase the magnetization when the signal is sought after. The selective retention of coherence orders with gradient methods, termed *gradient filtering*, utilizes such a gradient pair to de-phase and subsequently re-phase orders of coherence with specific ratios. For example, magnetization prepared to DQC will be encoded with twice the spatial frequency as SQC, although both orders may be entirely de-phased by a large area gradient. If the de-phased system is excited by an additional r.f. pulse, transferring the DQC to SQC, a gradient of twice the area of the first will be required to re-phase the DQC-encoded signal. In this way, only that magnetization that existed as DQC during the first of the gradient pair will be re-phased as SQC by the second gradient, selectively retaining a coherence order ratio of 2:1. This method of filtering is especially effective for eliminating the signal contribution from the uncoupled spin systems, which cannot be excited to a state of MQC. A detailed treatment of such a MQF, targeted for specific resonances of the Glu spin system, incorporating single-voxel localization, is provided in Chapter 3.

1.3.8 Direct Spin-Spin Coupling - Dipolar Coupling

The scalar-coupling phenomenon described in section 1.3.6 originates from the interaction of *coupled* protons through the electron clouds that bond the nuclei together. Neighboring protons also interact directly though space via their magnetic moments, termed the direct dipolar interaction. The Hamiltonian for this dipolar interaction between two spins with an inter-nuclear vector, $\mathbf{r}_{12}$, is

$$\mathcal{H}_{Dip} = \frac{\gamma^2\hbar^2}{r_{12}^3}(\mathbf{I}_1\cdot\mathbf{I}_2 - 3(\mathbf{I}_1\cdot\mathbf{r}_{12})(\mathbf{I}_2\cdot\mathbf{r}_{12})). \qquad (1\text{-}99)$$

It is common practice in NMR to decompose the dipolar Hamiltonian into components with clearly definable roles, of which there are six, termed the A to F terms.

$$\mathcal{H}_{Dip} = \frac{\gamma^2\hbar^2}{r_{12}^3}(A + B + C + D + E + F) \qquad (1\text{-}100)$$

$A = (1\text{-}3\cos^2\theta_{12})\, I_{1Z}I_{2Z}$

$B = -1/4(1\text{-}3\cos^2\theta_{12})\,(I_{1+}I_{2-} + I_{1-}I_{2+})$

} The A and B operator components are similar to the scalar coupling terms

$C = -3/2(\sin\theta_{12}\cos\theta_{12}\exp(-i\varphi_{12}))\,(I_{1Z}I_{2+} + I_{1+}I_{2Z})$

$D = C^*$

$E = -3/4(\sin^2\theta_{12}\exp(-i2\varphi_{12}))\, I_{1+}I_{2+}$

$F = E^*$

} The C to F components are a source of the longitudinal and transverse dipolar relaxation phenomena, characterized by the rate constants T_1 and T_2, respectively.

The C to F terms can be incorporated into the density matrix formalism to generate the relaxation superoperator (127), the rigorous incorporation of relaxation for coupled spin systems. Nevertheless, treating relaxation with simple rate constants, T_1 and T_2, greatly simplifies the dynamic equations of the density matrix, so the superoperator equations are not included in this thesis. A complete derivation of the superoperator dynamics is provided by Ernst (141).

The dipolar Hamiltonian including only the A and B terms, termed the truncated dipolar Hamiltonian, can be employed within the framework of density matrix dynamics developed thus far. The A and B terms together are also referred to as the *secular* terms, because their effect is to alter the Zeeman eigenstates but do not contribute to the *time-dependent* relaxation as do the C to F terms. The truncated Hamiltonian is often expressed, for a sample of N spins, as

$$\mathcal{H}_{Dip} = \frac{\gamma^2\hbar^2}{4}\sum_{j,k}^{N}\frac{(1-3\cos^2\theta_{jk})}{r_{jk}^3}(3I_{jZ}I_{kZ} - \mathbf{I}_j\cdot\mathbf{I}_k). \qquad (1\text{-}101)$$

Because the magnitude of this interaction depends strongly on the spatial coordinates of the interacting nuclei, particularly the distribution of inter-nuclear angles, the θ_{jk}, samples comprising isotropic liquids where molecular motion is rapid on the NMR time scale experience no net $\mathcal{H}_{Dip}$ due to destructive averaging. Nevertheless, there do exist ordered tissues that exhibit preferred molecular orientations, producing a distribution of θ_{jk}'s that is not random, creating sufficient anisotropy to result in finite dipolar coupling effects (142-146). Chapter 7 details the residual dipolar coupling effects of the Cr / PCr methyl resonance in the medial gastrocnemius muscle. Intra-molecular dipolar coupling within each methyl triplet of spins is believed to be responsible for the observed dipolar coupling effect. Incorporating the truncated dipolar Hamiltonian from Eq. (1-101) into the existing simulation framework, a model is developed that accurately predicts the response of the Cr / PCr methyl resonance to the single voxel PRESS sequence. The model includes the influence of realistic slice-selective pulses, whose distribution of tip angles over space influences the distribution of coherences at detection. Additionally, a distribution of residular dipolar coupling constants was included in the model, representing the distribution of preferred molecular orientations throughout the volume of interest, a 2 x 2 x 3 cm^3 region of interest. It is proposed that the preferred molecular orientations correspond to the distribution of muscle fibers in the VOI.

The requisite anisotropy for finite secular dipolar influence can also be generated by externally applied fields, in particular, by the gradient magnetic fields used for spatial localization and coherence selection. Chapter 7 outlines a scenario in which the dipolar fields from the massive water pool found in-vivo, in concert with the gradients intended for multiple quantum filtering, can generate an unwanted and unexpected contaminant water signal. Chapter 7 provides a detailed analysis of the single voxel multiple quantum filter sequence designed for in-vivo use (see chapter 3), with a focus the influence of the truncated dipolar Hamiltonian, revealing the coherence pathways for the water signal through the MQF sequence.

1.4 The Metabolite Spin Systems

The ^{1}H NMR visible brain metabolites of mM concentration comprise relatively small (2-10 backbone carbons), mobile molecular structures, and as such, contribute narrow spectral lines with widths dominated by the magnetic field inhomogeneities rather than by dipolar broadening. Line widths of 3 to 4 Hz are commonly reported at field strengths of 1.5 T (147,148), and 4 to 5 Hz at 3 T (97,99,118,144,149). For a given field strength and pH (~7.2 in healthy brain), the metabolite line shapes are determined by the chemical shielding and scalar coupling constants unique to each structure. Figure 1-15 displays the molecular structures of several of the abundant brain metabolites, along with their visible proton spin groups.

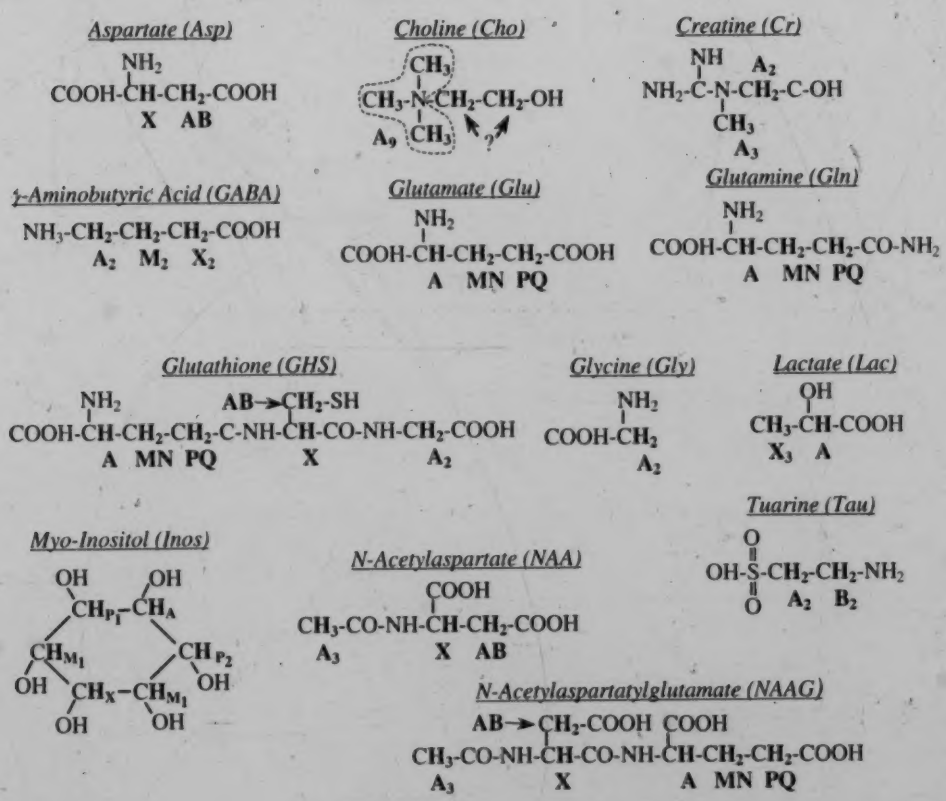

Figure 1-15 The molecular structures and NMR visible protons of the abundant brain metabolites.

The spin system letter classification is the standard Pople notation (150) with identical letters for magnetically equivalent protons (A_3), close letters representing strong coupling (AB) and distant letters, weak coupling (AX). From Fig. 1-15, the **NH** and **OH** protons most commonly exist in a steady state of exchange with their aqueous environment (assuming sufficient acid catalyst) and the host molecule, causing the protons to experience a weighted average of the magnetic fields in these environments. If the time of residence on a given molecule is much less than 1/J, where J is the scalar coupling (Hz) of the **NH** or **OH** proton to the non-exchanging **CH** protons, the protons become decoupled. This averaging tends to collapses multiplets into broad single peaks, often making them NMR invisible, especially under in-vivo conditions where signal to noise is limited.

The series of tables that follow list the metabolite chemical shifts and scalar couplings for the molecules displayed in Fig. 1-15. Several of these values were reported previously in the literature (138-140,151,152) and others were calculated over the course of this thesis, particularly, the glutamate, glutamine, myo-inositol and NAAG shifts and couplings (see appendix III). Along with these constants, a calculated pulse acquire spectrum is plotted for each metabolite, incorporating a line width of 1 Hz and a field strength of 3 T. While a 1 Hz line width cannot be achieved in-vivo, the narrow lines help to illustrate the characteristic multiplet structures for each spin system.

Table 1-1 Aspartate (Asp) Scalar-Couplings and Chemical Shifts

Spin Groups	Chemical Shifts (ppm)	Scalar Couplings (Hz)
ABX	ω_A=2.82, ω_B=2.69, ω_X=3.90	J_{AB}=17.6, J_{AX}=4.0, J_{BX}=8.2

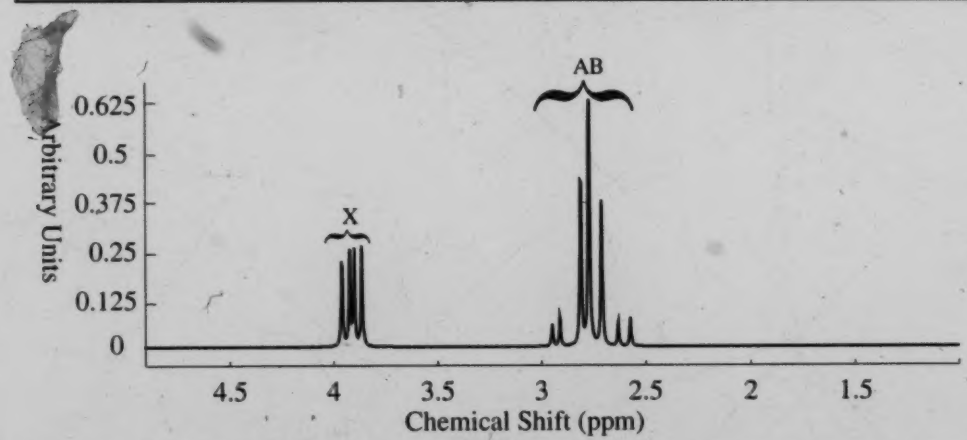

Figure 1-16 A calculated pulse acquire spectrum for a unit contributions of aspartate (3 T), line-broadened to 1 Hz FWHM.

Table 1-2 Creatine (Cr) and Choline (Cho) Scalar-Couplings and Chemical Shifts

Spin Groups	Chemical Shifts (ppm)	Scalar Couplings (Hz)
Cr A_3, A_2	ω_{A_3}=3.02, ω_{A_2}=3.94	NA
Cho A_3	ω_{A_3}=3.22	NA

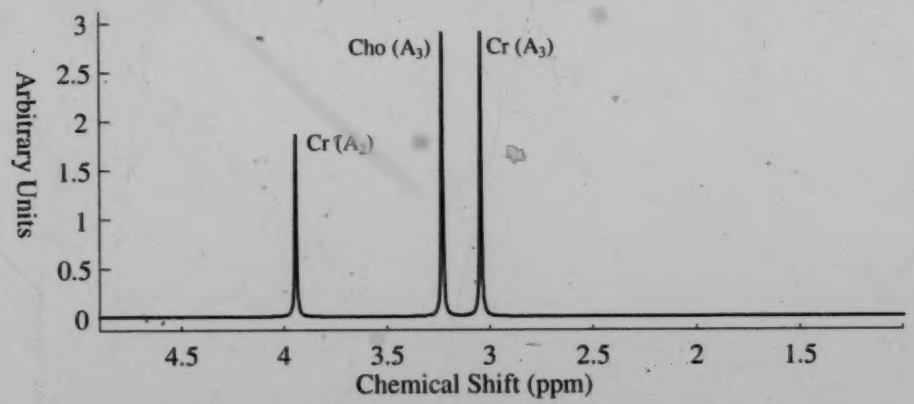

Figure 1-17 Pulse acquire spectrum calculated for a unit contributions of creatine and choline in a static field of 3 T, line-broadened to 1 Hz FWHM.

Table 1-3 γ-Amino Butyric Acid (GABA) Scalar-Couplings and Chemical Shifts

Spin Groups	Chemical Shifts (ppm)	Scalar Couplings (Hz)
$A_2M_2X_2$	ω_A=3.01, ω_M=1.91, ω_X=2.31	J_{AM}=7.3, J_{MX}=7.3

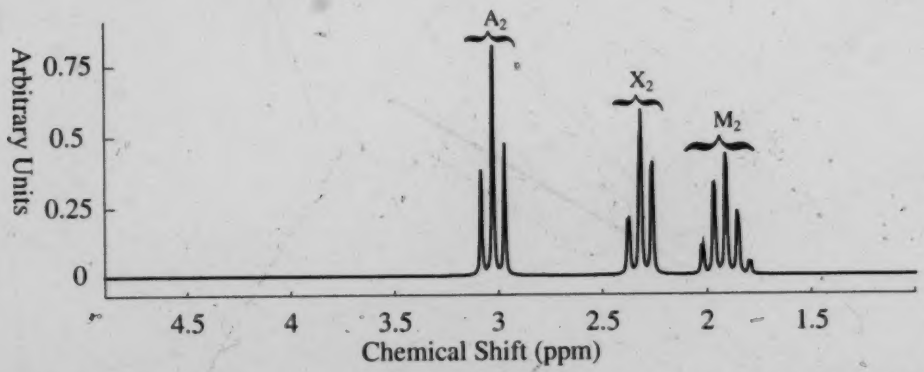

Figure 1-18 Pulse acquire spectrum calculated for a unit contributions of GABA in a static field of 3 T, line-broadened to 1 Hz FWHM.

Table 1-4 Glutamate (Glu) Scalar-Couplings and Chemical Shifts

Spin Groups	Chemical Shifts (ppm)	Scalar Couplings (Hz)
AMNPQ	ω_A=3.75, ω_M=2.06, ω_N=2.14, ω_P=2.35, ω_Q=2.37	J_{AM}=7.33, J_{AN}=4.65, J_{MN}=-14.85, J_{MP}=6.43, J_{NP}=8.47, J_{MQ}=8.39, J_{NQ}=6.89, J_{PQ}=-15.89

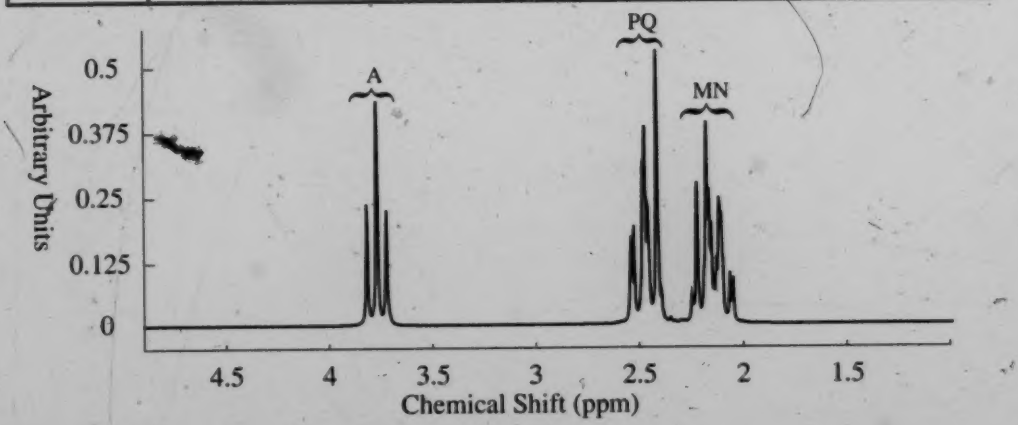

Figure 1-19 Pulse acquire spectrum calculated for a unit contributions of glutamate in a static field of 3 T, line-broadened to 1 Hz FWHM. In-vivo, the PQ multiplet is least obscured by overlapping resonances, making it the target group in most applications.

Table 1-5 Glutamine (Gln) Scalar-Couplings and Chemical Shifts

Spin Groups	Chemical Shifts (ppm)	Scalar Couplings (Hz)
AMNPQ	ω_A=3.76, ω_M=2.13, ω_N=2.15, ω_P=2.45, ω_Q=2.47	J_{AM}=6.53, J_{AN}=5.84, J_{MN}=-14.45, J_{MP}=6.33, J_{NP}=9.16, J_{MQ}=9.25, J_{NQ}=6.35, J_{PQ}=-15.55

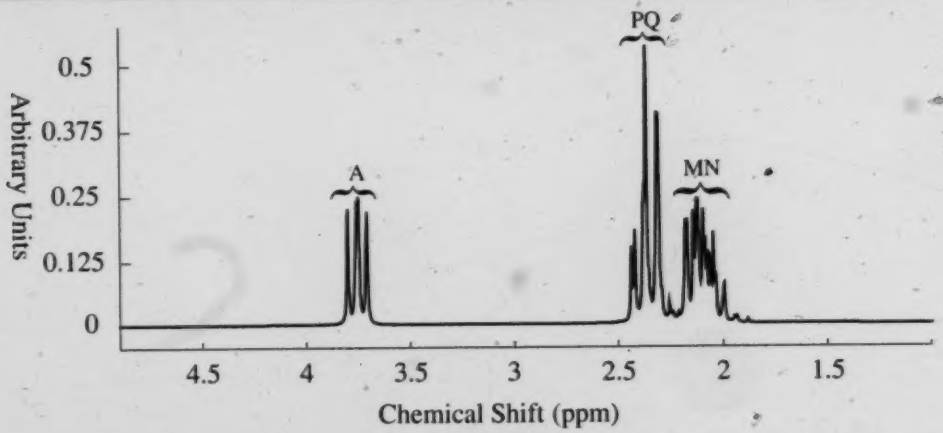

Figure 1-20 Pulse acquire spectrum calculated for a unit contributions of glutamine in a static field of 3 T, line-broadened to 1 Hz FWHM. In-vivo, the PQ multiplet is least obscured by overlapping resonances, making it the target group in most applications.

Table 1-6 :Glutathione (GSH) Scalar-Couplings and Chemical Shifts

Spin Groups	Chemical Shifts (ppm)	Scalar Couplings (Hz)
A_2	ω_{A_2}=3.767	NA
ABX	ω_A=4.56, ω_B=2.922, ω_X=2.959	J_{AB}=-14.2, J_{AX}=4.92, J_{BX}=7.30
AM_2PQ	ω_A=3.772, ω_M=2.155, ω_P=2.532, ω_Q=2.561	J_{AM}=6.25, J_{MP}=7.70, J_{MQ}=7.70, J_{PQ}=-15.40

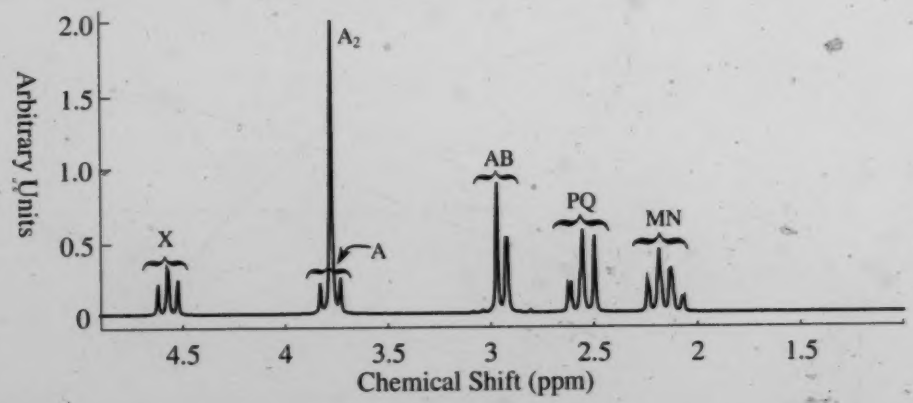

Figure 1-21 Pulse acquire spectrum calculated for a unit contributions of Glutathione in a static field of 3 T, line-broadened to 1 Hz FWHM.

Table 1-7 :Glycine (Gly) Scalar-Couplings and Chemical Shifts

Spin Groups	Chemical Shifts (ppm)	Scalar Couplings (Hz)
A_2	ω_{A_2}=3.56	NA

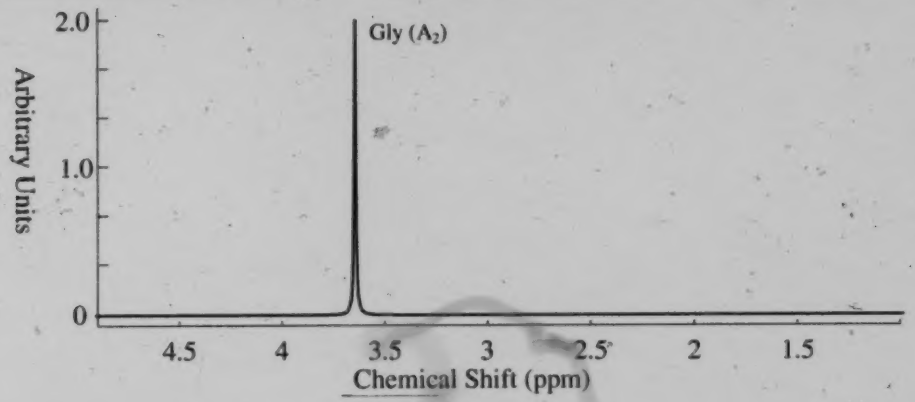

Figure 1-22 Pulse acquire spectrum calculated for a unit contributions of Glycine in a static field of 3 T, line-broadened to 1 Hz FWHM.

Table 1-8 :Lactic Acid (Lac) Scalar-Couplings and Chemical Shifts

Spin Groups	Chemical Shifts (ppm)	Scalar Couplings (Hz)
AX_3	ω_A=4.0908, ω_X=1.3125	J_{AX}=6.933

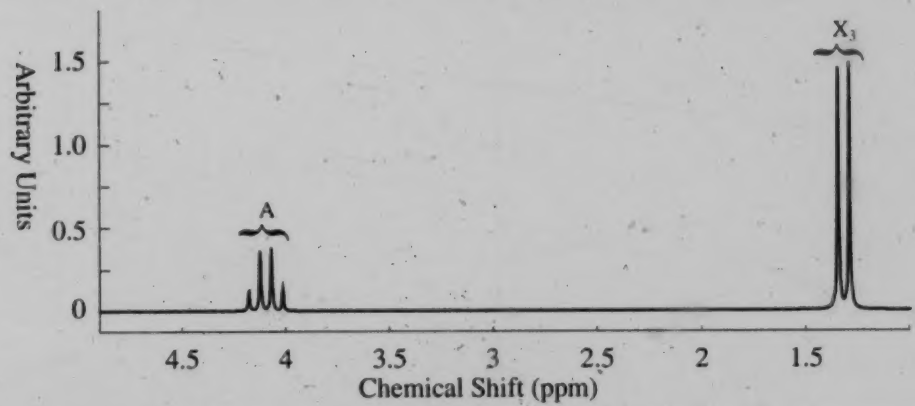

Figure 1-23 Pulse acquire spectrum calculated for a unit contributions of lactate in a static field of 3 T, line-broadened to 1 Hz FWHM.

Table 1-9 Myo-Inositol (m-Inos) Scalar-Couplings and Chemical Shifts

Spin Groups	Chemical Shifts (ppm)	Scalar Couplings (Hz)
AM_2N_2P	ω_A=3.28, ω_M=3.62, ω_N=3.54, ω_P=4.06	J_{AM}=9.2, J_{MN}=9.8, J_{NP}=2.7

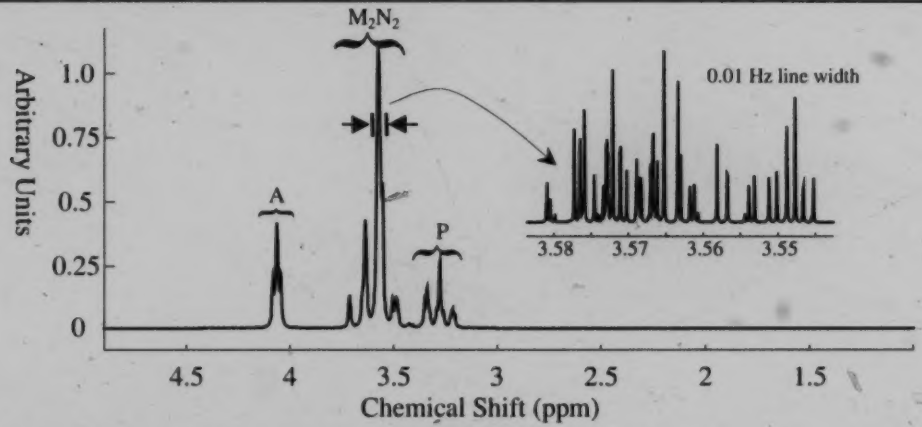

Figure 1-24 Pulse acquire spectrum calculated for a unit contributions of myo-inositol in a static field of 3 T, line-broadened to 1 Hz FWHM.

Table 1-10 N-Acetylaspartate (NAA) Scalar-Couplings and Chemical Shifts

Spin Groups	Chemical Shifts (ppm)	Scalar Couplings (Hz)
A_3	ω_{A_3}=2.023	NA
ABX	ω_A=2.52, ω_B=2.70, ω_X=4.40	J_{AB}=15.5, J_{AX}=10.1, J_{BX}=3.7

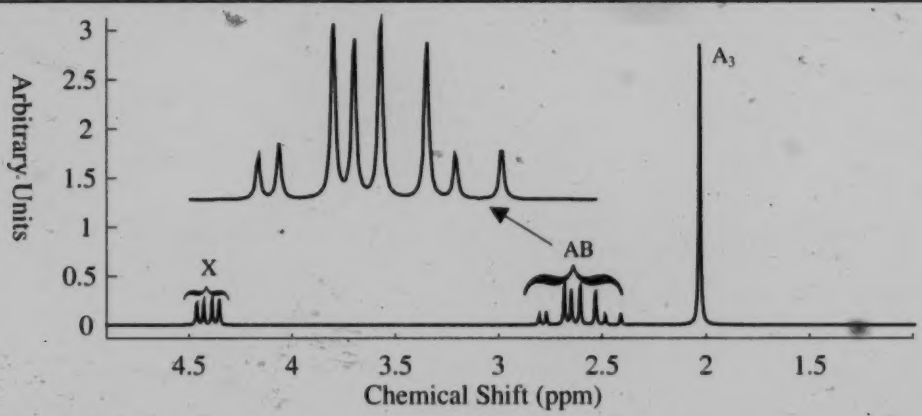

Figure 1-25 Pulse acquire spectrum calculated for a unit contribution of N-acetylaspartate in a static field of 3 T, line-broadened to 1 Hz FWHM. NAA is most commonly quantified by means of it's methyl A_3 singlet, while the strongly coupled AB group is important due to it's overlap with other metabolite spectra.

Table 1-11 N-Acetylaspartylglutamate (NAAG) Scalar-Couplings and Chemical Shifts

Spin Groups	Chemical Shifts (ppm)	Scalar Couplings (Hz)
A_3	ω_{A_3}=2.05	NA
ABX	ω_A=2.75, ω_B=2.55, ω_X=4.62	J_{AB}=-15.9, J_{AX}=4.37, J_{BX}=9.50
AMNPQ	ω_A=4.15, ω_M=1.91, ω_N=2.07, ω_P=2.42,	J_{AM}=8.45, J_{AN}=4.6, J_{MN}=-14.0, J_{MP_1}=8.3, J_{MP_2}=8.5, J_{NP_1}=8.1, J_{NP_2}=7.3

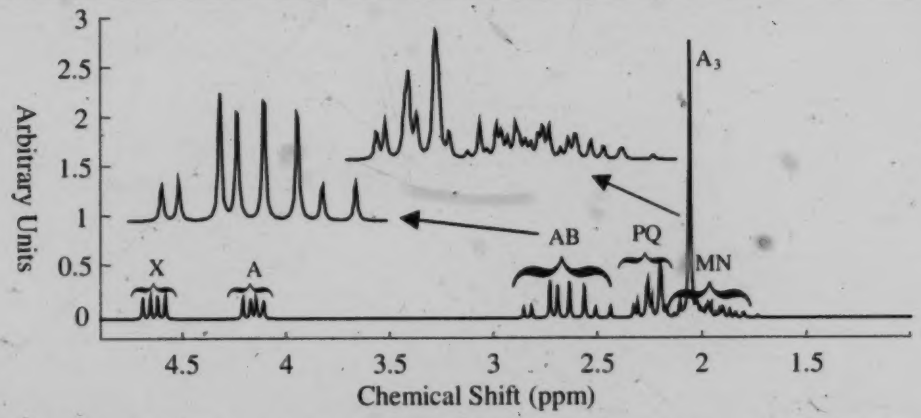

Figure 1-26 Pulse acquire spectrum calculated for a unit contributions of NAAG in a static field of 3 T, line-broadened to 1 Hz FWHM.

Table 1-12 Taurine (Tau) Scalar-Couplings and Chemical Shifts

Spin Groups	Chemical Shifts (ppm)	Scalar Couplings (Hz)
A_2B_2	ω_A=3.44, ω_B=3.27	J_{AB}=6.70

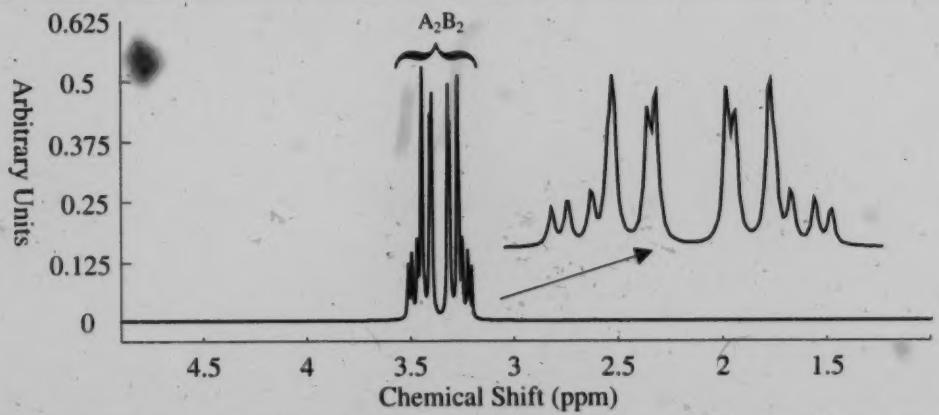

Figure 1-27 Pulse acquire spectrum calculated for a unit contributions of taurine in a static field of 3 T, line-broadened to 1 Hz FWHM.

1.5 References

1. Yl Chan, D. K. Yeung, Sf Leung, and G. Cao. Proton magnetic resonance spectroscopy of late delayed radiation- induced injury of the brain. *J.Magn Reson.Imaging* **10**, 130-137 (1999).

2. H. Mehmet, X. Yue, J. Penrice, E. Cady, J. C. Wyatt, C. Sarraf, M. Squier, and A. D. Edwards. Relation of impaired energy metabolism to apoptosis and necrosis following transient cerebral hypoxia-ischaemia. *Cell Death. Differ.* **5**, 321-329, (1998).

3. R. Corbett, A. Laptook, B. Kim, G. Tollefsbol, S. Silmon, and D. Garcia. Maturational changes in cerebral lactate and acid clearance following ischemia measured in vivo using magnetic resonance spectroscopy and microdialysis. *Brain Res. Dev. Brain Res.* **113**, 37-46 (1999).

4. J. D. Hanrahan, I. J. Cox, A. D. Edwards, F. M. Cowan, J. Sargentoni, J. D. Bell, D. J. Bryant, M. A. Rutherford, and D. Azzopardi. Persistent increases in cerebral lactate concentration after birth asphyxia. *Pediatr. Res.* **44**, 304-311 (1998).

5. J. M. Wardlaw, I. Marshall, J. Wild, M. S. Dennis, J. Cannon, and S. C. Lewis. Studies of acute ischemic stroke with proton magnetic resonance spectroscopy: relation between time from onset, neurological deficit, metabolite abnormalities in the infarct, blood flow, and clinical outcome. *Stroke* **29**, 1618-1624 (1998).

6. L. C. Hsu, J. F. Lirng, J. L. Fuh, S. J. Wang, H. Y. Shyu, and H. C. Liu. Proton magnetic resonance spectroscopy in deep cerebral venous thrombosis. *Clin. Neurol. Neurosurg.* **100**, 27-30 (1998).

7. Federico, I. L. Simone, V. Lucivero, P. Giannini, G. Laddomada, D. M. Mezzapesa, and C. Tortorella. Prognostic value of proton magnetic resonance spectroscopy in ischemic stroke. *Arch. Neurol.* **55**, 489-494, (1998).

8. K. Kamada, M. Saguer, M. Moller, K. Wicklow, M. Katenhauser, H. Kober, and J. Vieth. Functional and metabolic analysis of cerebral ischemia using magnetoencephalography and proton magnetic resonance spectroscopy. *Ann. Neurol.* **42**, 554-563, (1997).

9. N. Lundbom, A. Barnett, S. Bonavita, N. Patronas, J. Rajapakse, Tedeschi, and G. Di Chiro. MR image segmentation and tissue metabolite contrast in 1H spectroscopic imaging of normal and aging brain. *Magn. Reson. Med.* **41**, 841-845 (1999).

10. D. E. Saunders, F. A. Howe, Boogaart A. van den, J. R. Griffiths, and M. M. Brown. Aging of the adult human brain: in vivo quantitation of metabolite content with proton magnetic resonance spectroscopy. *J. Magn. Reson. Imaging* **9**, 711-716 (1999).

11. Pfefferbaum, E. Adalsteinsson, D. Spielman, E. V. Sullivan, and K. O. Lim. In vivo spectroscopic quantification of the N-acetyl moiety, creatine, and choline from

large volumes of brain gray and white matter: effects of normal aging. *Magn. Reson. Med.* **41**, 276-284 (1999).

12. J. Murashita, T. Kato, T. Shioiri, T. Inubushi, and N. Kato. Age-dependent alteration of metabolic response to photic stimulation in the human brain measured by ^{31}P MR-spectroscopy. *Brain Res.* **818**, 72-76 (1999).

13. B. D. Ross, T. Q. Hoang, S. Bluml, D. Dubowitz, O. V. Kopyov, D. B. Jacques, A. Lin, K. Seymour, and J. Tan. In vivo magnetic resonance spectroscopy of human fetal neural transplants. *NMR Biomed.* **12**, 221-236 (1999).

14. S. D. Taylor-Robinson, N. Turjanski, S. Bhattacharya, J. P. Seery, J. Sargentoni, D. J. Brooks, D. J. Bryant, and I. J. Cox. A proton magnetic resonance spectroscopy study of the striatum and cerebral cortex in Parkinson's disease. *Metab. Brain. Dis.* **14**, 45-55 (1999).

15. L. Brownell, B. G. Jenkins, D. R. Elmaleh, T. W. Deacon, R. D. Spealman, and O. Isacson. Combined PET/MRS brain studies show dynamic and long-term physiological changes in a primate model of Parkinson disease. *Nat. Med.* **4**, 1308-1312 (1998).

16. Y. Choe, J. W. Park, K. S. Lee, B. C. Son, M. C. Kim, B. S. Kim, T. S. Suh, H. K. Lee, and K. S. Shinn. Neuronal laterality in Parkinson's disease with unilateral symptom by in vivo 1H magnetic resonance spectroscopy. *Invest. Radiol.* **33**, 450-455 (1998).

17. T. Q. Hoang, S. Bluml, D. J. Dubowitz, R. Moats, O. Kopyov, D. Jacques, and B. D. Ross. Quantitative proton-decoupled 31P MRS and 1H MRS in the evaluation of Huntington's and Parkinson's diseases. *Neurology* **50**, 1033-1040 (1998).

18. F. Federico, I. L. Simone, V. Lucivero, G. Iliceto, M. De Mari, P. Giannini, D. M. Mezzapesa, A. Tarantino, and P. Lamberti. Proton magnetic resonance spectroscopy in Parkinson's disease and atypical parkinsonian disorders. *Mov. Disord.* **12**, 903-909, (1997).

19. G. Tedeschi, I. Litvan, S. Bonavita, A. Bertolino, N. Lundbom, N. J. Patronas, and M. Hallett. Proton magnetic resonance spectroscopic imaging in progressive supranuclear palsy, Parkinson's disease and corticobasal degeneration. *Brain* **120**, 1541-1552 (1997).

20. C. M. Ellis, A. Simmons, C. Andrews, J. M. Dawson, S. C. Williams, and P. N. Leigh. A proton magnetic resonance spectroscopic study in ALS: correlation with clinical findings. *Neurology* **51**, 1104-1109 (1998).

21. W. Block, J. Karitzky, F. Traber, C. Pohl, E. Keller, R. R. Mundegar, R. Lamerichs, H. Rink, F. Ries, H. H. Schild, and F. Jerusalem. Proton magnetic resonance spectroscopy of the primary motor cortex in patients with motor neuron disease: subgroup analysis and follow-up measurements [see comments]. *Arch. Neurol.* **55**, 931-936 (1998).

22. S. Kalra, N. R. Cashman, A. Genge, and D. L. Arnold. Recovery of N-acetylaspartate in corticomotor neurons of patients with ALS after riluzole therapy. *Neuroreport* **9**, 1757-1761 (1998).

23. Cwik, C. C. Hanstock, P. S. Allen, and W. R. Martin. Estimation of brainstem neuronal loss in amyotrophic lateral sclerosis with in vivo proton magnetic resonance spectroscopy. *Neurology* **50**, 72-77 (1998).

24. E. P. Pioro. MR spectroscopy in amyotrophic lateral sclerosis/motor neuron disease. *J. Neurol. Sci.* **152** Suppl., S49-S53 (1997).

25. O. Gredal, S. Rosenbaum, S. Topp, M. Karlsborg, P. Strange, and L. Werdelin. Quantification of brain metabolites in amyotrophic lateral sclerosis by localized proton magnetic resonance spectroscopy. *Neurology* **48**, 878-881 (1997).

26. J. M. Knight, A. P. Jones, J. P. Redmond, and I. C. Shaw. Identification of brain metabolites by magnetic resonance spectroscopy in MND/ALS. *J. Neurol. Sci.* **139** Suppl:104-109 (1996).

27. M. Giroud, P. Walker, D. Bernard, M. Lemesle, D. Martin, N. Baudouin, F. Brunotte, and R. Dumas. Reduced brain N-acetyl-aspartate in frontal lobes suggests neuronal loss in patients with amyotrophic lateral sclerosis [published erratum appears in Neurol Res 1997 Aug;19(4):456]. *Neurol. Res.* **18**, 241-243 (1996).

28. P. Jones, W. J. Gunawardena, C. M. Coutinho, J. A. Gatt, I. C. Shaw, and J. D. Mitchell. Preliminary results of proton magnetic resonance spectroscopy in motor neurone disease (amytrophic lateral sclerosis). *J. Neurol. Sci.* **129** Suppl:85-89 (1995).

29. P. Sarchielli, O. Presciutti, G. P. Pelliccioli, R. Tarducci, G. Gobbi, P. Chiarini, A. Alberti, F. Vicinanza, and V. Gallai. Absolute quantification of brain metabolites by proton magnetic resonance spectroscopy in normal-appearing white matter of multiple sclerosis patients. *Brain* **122** (Pt 3):513-521 (1999).

30. J. Foong, L. Rozewicz, C. A. Davie, A. J. Thompson, D. H. Miller, and M. A. Ron. Correlates of executive function in multiple sclerosis: the use of magnetic resonance spectroscopy as an index of focal pathology. *J. Neuropsychiatry Clin. Neurosci.* **11**, 45-50, (1999).

31. N. de Stefano, P. M. Matthews, L. Fu, S. Narayanan, J. Stanley, G. S. Francis, J. P. Antel, and D. L. Arnold. Axonal damage correlates with disability in patients with relapsing-remitting multiple sclerosis. Results of a longitudinal magnetic resonance spectroscopy study. *Brain* **121** (Pt 8):1469-1477 (1998).

32. N. de Stefano, Z. Caramanos, M. C. Preul, G. Francis, J. P. Antel, and D. L. Arnold. In vivo differentiation of astrocytic brain tumors and isolated demyelinating lesions of the type seen in multiple sclerosis using 1H magnetic resonance spectroscopic imaging. *Ann. Neurol.* **44**, 273-278 (1998).

33. Falini, G. Calabrese, M. Filippi, D. Origgi, S. Lipari, B. Colombo, G. Comi, and G. Scotti. Benign versus secondary-progressive multiple sclerosis: the potential role of proton MR spectroscopy in defining the nature of disability. *AJNR Am. J. Neuroradiol.* **19**, 223-229 (1998).

34. N. de Stefano, A. Federico, and D. L. Arnold. Proton magnetic resonance spectroscopy in brain white matter disorders. *Ital. J. Neurol. Sci.* **18**, 331-339 (1997).

35. P. Sarchielli, O. Presciutti, R. Tarducci, G. Gobbi, A. Alberti, G. P. Pelliccioli, A. Orlacchio, and V. Gallai. 1H-MRS in patients with multiple sclerosis undergoing treatment with interferon beta-1a: results of a preliminary study. *J. Neurol. Neurosurg. Psychiatry* **64**, 204-212 (1998).

36. P. A. Narayana, T. J. Doyle, D. Lai, and J. S. Wolinsky. Serial proton magnetic resonance spectroscopic imaging, contrast- enhanced magnetic resonance imaging, and quantitative lesion volumetry in multiple sclerosis. *Ann. Neurol.* **43**, 56-71 (1998).

37. W. D. Rooney, D. E. Goodkin, N. Schuff, D. J. Meyerhoff, D. Norman, and M. W. Weiner. 1H MRSI of normal appearing white matter in multiple sclerosis. *Mult. Scler.* **3**, 231-237 (1997).

38. S. E. Rose, G. I. de Zubicaray, D. Wang, G. J. Galloway, J. B. Chalk, S. C. Eagle, J. Semple, and D. M. Doddrell. A 1H MRS study of probable Alzheimer's disease and normal aging: implications for longitudinal monitoring of dementia progression. *Magn. Reson. Imaging* **17**, 291-299 (1999).

39. Pfefferbaum, E. Adalsteinsson, D. Spielman, E. V. Sullivan, and K. O. Lim. In vivo brain concentrations of N-acetyl compounds, creatine, and choline in Alzheimer disease. *Arch. Gen. Psychiatry* **56**, 185-192 (1999).

40. D. L. Rhinehart, L. A. Cox, and B. W. Long. MR spectroscopy of Alzheimer disease. *Radiol. Technol.* **70**, 23-28 (1998).

41. D. Ross, S. Bluml, R. Cowan, E. Danielsen, N. Farrow, and J. Tan. In vivo MR spectroscopy of human dementia. *Neuroimaging Clin. N. Am.* **8**, 809-822 (1998).

42. F. Lazeyras, H. C. Charles, L. A. Tupler, R. Erickson, O. B. Boyko, and K. R. Krishnan. Metabolic brain mapping in Alzheimer's disease using proton magnetic resonance spectroscopy. *Psychiatry Res.* **82**, 95-106 (1998).

43. N. Schuff, D. L. Amend, D. J. Meyerhoff, J. L. Tanabe, D. Norman, G. Fein, and M. W. Weiner. Alzheimer disease: quantitative H-1 MR spectroscopic imaging of frontoparietal brain. *Radiology* **207**, 91-102 (1998).

44. N. Schuff, D. Amend, F. Ezekiel, S. K. Steinman, J. Tanabe, D. Norman, W. Jagust, J. H. Kramer, J. A. Mastrianni, G. Fein, and M. W. Weiner. Changes of hippocampal N-acetyl aspartate and volume in Alzheimer's disease. A proton MR spectroscopic imaging and MRI study. *Neurology* **49**, 1513-1521 (1997).

45. J. W. Pettegrew, W. E. Klunk, K. Panchalingam, R. J. McClure, and J. A. Stanley. Magnetic resonance spectroscopic changes in Alzheimer's disease. *Ann. N. Y. Acad. Sci.* **826**, 282-306 (1997).

46. B. G. Jenkins, H. D. Rosas, Y. C. Chen, T. Makabe, R. Myers, M. MacDonald, B. R. Rosen, M. F. Beal, and W. J. Koroshetz. 1H NMR spectroscopy studies of Huntington's disease: correlations with CAG repeat numbers. *Neurology* **50**, 1357-1365 (1998).

47. T. Q. Hoang, S. Bluml, D. J. Dubowitz, R. Moats, O. Kopyov, D. Jacques, and B. D. Ross. Quantitative proton-decoupled 31P MRS and 1H MRS in the evaluation of Huntington's and Parkinson's diseases. *Neurology* **50**, 1033-1040 (1998).

48. L. Harms, H. Meierkord, G. Timm, L. Pfeiffer, and A. C. Ludolph. Decreased N-acetyl-aspartate/choline ratio and increased lactate in the frontal lobe of patients with Huntington's disease: a proton magnetic resonance spectroscopy study. *J. Neurol. Neurosurg. Psychiatry* **62**, 27-30 (1997).

49. H. Hamakawa, T. Kato, T. Shioiri, T. Inubushi, and N. Kato. Quantitative proton magnetic resonance spectroscopy of the bilateral frontal lobes in patients with bipolar disorder. *Psychol. Med.* **29**, 639-644 (1999).

50. P. H. Silverstone, C. C. Hanstock, and S. Rotzinger. Lithium does not alter the choline/creatine ratio in the temporal lobe of human volunteers as measured by proton magnetic resonance spectroscopy. *J. Psychiatry Neurosci.* **24**, 222-226 (1999).

51. M. Castillo, L. Kwock, H. E. Courvoisie, S. R. Hooper, and R. S. Greenwood. Proton MR spectroscopy in psychiatric and neurodevelopmental childhood disorders: early experience. *Neuroimaging Clin. N. Am.* **8**, 901-912 (1998).

52. T. Kato, T. Inubushi, and N. Kato. Magnetic resonance spectroscopy in affective disorders. *J. Neuropsychiatry Clin. Neurosci.* **10**, 133-147 (1998).

53. H. Hamakawa, T. Kato, J. Murashita, and N. Kato. Quantitative proton magnetic resonance spectroscopy of the basal ganglia in patients with affective disorders. *Eur. Arch. Psychiatry Clin. Neurosci.* **248**, 53-58 (1998).

54. T. Kato, H. Hamakawa, T. Shioiri, J. Murashita, Y. Takahashi, S. Takahashi, and T. Inubushi. Choline-containing compounds detected by proton magnetic resonance spectroscopy in the basal ganglia in bipolar disorder. *J. Psychiatry Neurosci.* **21**, 248-254 (1996).

55. T. Kato, K. Fujii, T. Shioiri, T. Inubushi, and S. Takahashi. Lithium side effects in relation to brain lithium concentration measured by lithium-7 magnetic resonance spectroscopy. *Prog.Neuropsychopharmacol.Biol.Psychiatry* **20**, 87-97 (1996).

56. G. S. Sachs, P. F. Renshaw, B. Lafer, A. L. Stoll, A. R. Guimaraes, J. F. Rosenbaum, and R. G. Gonzalez. Variability of brain lithium levels during maintenance treatment: a magnetic resonance spectroscopy study. *Biol. Psychiatry* **38**, 422-428 (1995).

57. R. F. Deicken, G. Fein, and M. W. Weiner. Abnormal frontal lobe phosphorous metabolism in bipolar disorder. *Am.J.Psychiatry* **152**, 915-918 (1995).

58. T. Kato, T. Inubushi, and S. Takahashi. Relationship of lithium concentrations in the brain measured by lithium- 7 magnetic resonance spectroscopy to treatment response in mania. *J. Clin. Psychopharmacol.* **14**, 330-335 (1994).

59. K. J. Seymour, S. Bluml, J. Sutherling, W. Sutherling, and B. D. Ross. Identification of cerebral acetone by 1H-MRS in patients with epilepsy controlled by ketogenic diet. *MAGMA.* **8**, 33-42 (1999).

60. C. O. Duc, A. H. Trabesinger, O. M. Weber, D. Meier, M. Walder, H. G. Wieser, and P. Boesiger. Quantitative 1H MRS in the evaluation of mesial temporal lobe epilepsy in vivo. *Magn. Reson. Imaging* **16**, 969-979 (1998).

61. P. Parker, C. D. Ferrie, S. Keevil, M. Newbold, T. Cox, M. Maisey, and R. O. Robinson. Neuroimaging and spectroscopy in children with epileptic encephalopathies. *Arch. Dis. Child* **79**, 39-43 (1998).

62. E. Holopainen, M. E. Valtonen, M. E. Komu, P. H. Sonninen, T. E. Manner, N. M. Lundbom, and M. L. Sillanpaa. Proton spectroscopy in children with epilepsy and febrile convulsions. *Pediatr. Neurol.* **19**, 93-99 (1998).

63. Connelly, W. Van Paesschen, D. A. Porter, C. L. Johnson, J. S. Duncan, and D. G. Gadian. Proton magnetic resonance spectroscopy in MRI-negative temporal lobe epilepsy. *Neurology* **51**, 61-66 (1998).

64. J. A. Stanley, F. Cendes, F. Dubeau, F. Andermann, and D. L. Arnold. Proton magnetic resonance spectroscopic imaging in patients with extratemporal epilepsy. *Epilepsia* **39**, 267-273 (1998).

65. M. Najm, Y. Wang, D. Shedid, H. O. Luders, T. C. Ng, and Y. G. Comair. MRS metabolic markers of seizures and seizure-induced neuronal damage. *Epilepsia* **39**, 244-250 (1998).

66. M. E. Meyerand, J. M. Pipas, A. Mamourian, T. D. Tosteson, and J. F. Dunn. Classification of biopsy-confirmed brain tumors using single-voxel MR spectroscopy. *AJNR Am. J. Neuroradiol.* **20**, 117-123 (1999).

67. W. Luan and J. Zhang. In vivo hydrogen-1 magnetic resonance spectroscopy study of human intracranial tumors. *Chin Med. J.(Engl.)* **111**, 56-58 (1998).

68. P. J. Foxall, J. M. Singer, J. M. Hartley, G. H. Neild, M. Lapsley, J. K. Nicholson, and R. L. Souhami. Urinary proton magnetic resonance studies of early ifosfamide-induced nephrotoxicity and encephalopathy. *Clin. Cancer Res.* **3**, 1507-1518 (1997).

69. J. S. Taylor, R. J. Ogg, and J. W. Langston. Proton MR spectroscopy of pediatric brain tumors. *Neuroimaging Clin. N. Am.* **8**, 753-779 (1998).

70. M. Castillo and L. Kwock. Proton MR spectroscopy of common brain tumors. *Neuroimaging Clin. N. Am.* **8**, 733-752 (1998).

71. N. De Stefano, Z. Caramanos, M. C. Preul, G. Francis, J. P. Antel, and D. L. Arnold. In vivo differentiation of astrocytic brain tumors and isolated demyelinating lesions of the type seen in multiple sclerosis using 1H magnetic resonance spectroscopic imaging. *Ann. Neurol.* **44**, 273-278 (1998).

72. N. Girard, Z. J. Wang, A. Erbetta, L. N. Sutton, P. C. Phillips, L. B. Rorke, and R. A. Zimmerman. Prognostic value of proton MR spectroscopy of cerebral hemisphere tumors in children. *Neuroradiology* **40**, 121-125 (1998).

73. H. E. Moller, P. Vermathen, M. G. Lentschig, G. Schuierer, S. Schwarz, D. Wiedermann, S. Evers, and I. W. Husstedt. Metabolic characterization of AIDS

dementia complex by spectroscopic imaging. *J. Magn Reson. Imaging* **9**, 10-18 (1999).

74. M. Salvan, S. Lamoureux, G. Michel, S. Confort-Gouny, P. J. Cozzone, and J. Vion-Dury. Localized proton magnetic resonance spectroscopy of the brain in children infected with human immunodeficiency virus with and without encephalopathy. *Pediatr. Res.* **44**, 755-762 (1998).

75. J. Vion-Dury, A. M. Salvan, S. Confort-Gouny, and P. J. Cozzone. [Brain proton magnetic resonance spectroscopy. Indications for diagnosis and follow-up of HIV-related encephalopathy in the adult]. *Presse Med.* **27**, 1398-1405 (1998).

76. M. J. Harrison, S. P. Newman, M. A. Hall-Craggs, C. J. Fowler, R. Miller, B. E. Kendall, M. Paley, I. Wilkinson, B. Sweeney, S. Lunn, S. Carter, and I. Williams. Evidence of CNS impairment in HIV infection: clinical, neuropsychological, EEG, and MRI/MRS study. *J. Neurol. Neurosurg. Psychiatry* **65**, 301-307 (1998).

77. D. Marcus, S. D. Taylor-Robinson, J. Sargentoni, J. G. Ainsworth, G. Frize, P. J. Easterbrook, S. Shaunak, and D. J. Bryant. 1H MR spectroscopy of the brain in HIV-1-seropositive subjects: evidence for diffuse metabolic abnormalities. *Metab Brain Dis.* **13**, 123-136 (1998).

78. L. Simone, F. Federico, C. Tortorella, C. F. Andreula, G. B. Zimatore, P. Giannini, G. Angarano, V. Lucivero, P. Picciola, D. Carrara, A. Bellacosa, and P. Livrea. Localised 1H-MR spectroscopy for metabolic characterisation of diffuse and focal brain lesions in patients infected with HIV. *J. Neurol. Neurosurg. Psychiatry* **64**, 516-523 (1998).

79. N. De Stefano, A. Federico, and D. L. Arnold. Proton magnetic resonance spectroscopy in brain white matter disorders. *Ital. J. Neurol. Sci.* **18**, 331-339 (1997).

80. M. Salvan, J. Vion-Dury, S. Confort-Gouny, F. Nicoli, S. Lamoureux, and P. J. Cozzone. Brain proton magnetic resonance spectroscopy in HIV-related encephalopathy: identification of evolving metabolic patterns in relation to dementia and therapy. *AIDS Res. Hum. Retroviruses* **13**, 1055-1066 (1997).

81. M. Salvan, J. Vion-Dury, S. Confort-Gouny, F. Nicoli, S. Lamoureux, and P. J. Cozzone. Cerebral metabolic alterations in human immunodeficiency virus-related encephalopathy detected by proton magnetic resonance spectroscopy. Comparison between sequences using short and long echo times. *Invest Radiol.* **32**, 485-495, (1997).

82. D. Wilkinson, R. F. Miller, K. A. Miszkiel, M. N. Paley, M. A. Hall-Craggs, T. Baldeweg, I. G. Williams, S. Carter, S. P. Newman, B. E. Kendall, J. Catalan, R. J. Chinn, and M. J. Harrison. Cerebral proton magnetic resonance spectroscopy in asymptomatic HIV infection. *AIDS* **11**, 289-295 (1997).

83. P. T. Beall, S. R. Amtey and S. R. Kasturi, "NMR Data Handbook for Biomedical Applications", Pergamon Press, New York, 1984

84. Y. Wang and S. J. Li. Differentiation of metabolic concentrations between gray matter and white matter of human brain by in vivo 1H magnetic resonance spectroscopy. *Magn Reson. Med.* **39**, 28-33 (1998).

85. F. G. Woermann, M. A. McLean, P. A. Bartlett, G. J. Parker, G. J. Barker, and J. S. Duncan. Short echo time single-voxel 1H magnetic resonance spectroscopy in magnetic resonance imaging-negative temporal lobe epilepsy: different biochemical profile compared with hippocampal sclerosis. *Ann. Neurol.* **45**, 369-376, (1999).

86. S. Bonavita, F. Di Salle, and G. Tedeschi. Proton MRS in neurological disorders. *Eur. J. Radiol.* **30**, 125-131 (1999).

87. P. L. McGeer, Sir J. C. Eccles and E. G. McGeer, "Molecular Neurobiology of the Mammalian Brain", pp. 155, Plenum Press, New York, (1987).

88. J. Frahm, K.D. Merboldt and W. Hanicke, Localized proton spectroscopy using stimulated echoes. *J. Magn. Reson.* **72**, 502 (1987).

89. J. Frahm, H. Bruhn, M. L. Gyngell, K. D. Merboldt, W. Hanicke, and R. Sauter. Localized high-resolution proton NMR spectroscopy using stimulated echoes: initial applications to human brain in vivo. *Magn. Reson. Med.* **9**, 79-93 (1989).

90. K. Straubinger, F. Schick, and O. Lutz. Influence of pulse angle variations on stimulated echo acquisition mode proton nuclear magnetic resonance spectra of AB spin systems: theory and experiments with citrate. *MAGMA.* **7**, 88-94 (1998).

91. H. Wilman and P. S. Allen. Observing N-acetyl aspartate via both its N-acetyl and its strongly coupled aspartate groups in in vivo proton magnetic resonance spectroscopy. *J. Magn Reson. B* **113**, 203-213 (1996).

92. H. Wilman and P. S. Allen. The response of the strongly coupled AB system of citrate to typical 1H MRS localization sequences. *J. Magn Reson. B* **107**, 25-33 (1995).

93. T. Ernst and J. Hennig. Coupling effects in volume selective 1H spectroscopy of major brain metabolites. *Magn. Reson. Med.* **21**, 82-96 (1991).

94. R. E. Gordon and R. J. Ordidge, Volume selection for high resolution NMR studies. Abstracts of the Society of Magnetic Resonance in Medicine, 3rd Annual Meeting, New York, p. 272, (1984).

95. P. A. Bottomly, Selective volume method for performing localized NMR spectroscopy. US Patent 4,480,228 (1984).

96. R. J. Ordidge, M. R. Bendall, R. E. Gordon and A. Connelly, Magnetic Resonance in Biology and Medicine (G. Govil, C. L. Khetraplal and A. Saran, Eds.), pp. 387-397, McGraw-Hill, New Dehli, (1985).

97. R. B. Thompson and P. S. Allen. Sources of variability in the response of coupled spins to the PRESS sequence and their potential impact on metabolite quantification. *Magn. Reson. Med.* **41**, 1162-1169 (1999).

98. K. Straubinger, F. Schick, and O. Lutz. Influence of pulse angle variations on stimulated echo acquisition mode proton nuclear magnetic resonance spectra of AB spin systems: theory and experiments with citrate. *MAGMA.* **7**, 88-94 (1998).

99. R. B. Thompson and P. S. Allen. The role of the N-acetylaspartate multiplet in the quantification of brain metabolites. *Biochem. Cell Biol.* **76**, 497-502 (1998).

100. W. Dreher and D. Leibfritz. Detection of homonuclear decoupled in vivo proton NMR spectra using constant time chemical shift encoding: CT-PRESS. *Magn Reson. Imaging* **17**, 141-150 (1999).

101. Marshall and J. Wild. A systematic study of the lactate lineshape in PRESS-localized proton spectroscopy. *Magn. Reson. Med.* **40**, 72-78 (1998).

102. Marshall and J. M. Wild. Calculations and experimental studies of the lineshape of the lactate doublet in PRESS-localized 1H MRS. *Magn. Reson. Med.* 38, 415-419 (1997).

103. H. Wilman and P. S. Allen. Observing N-acetyl aspartate via both its N-acetyl and its strongly coupled aspartate groups in in vivo proton magnetic resonance spectroscopy. *J. Magn. Reson. B* **113**, 203-213 (1996).

104. R. V. Mulkern, J. L. Bowers, S. Peled, R. A. Kraft, and D. S. Williamson. Citrate signal enhancement with a homonuclear J-refocusing modification to double-echo PRESS sequences [published erratum appears in *Magn. Reson. Med.* 1997 Mar;37(3):477]. *Magn. Reson. Med.* **36**, 775-780 (1996).

105. K. Straubinger, F. Schick, and O. Lutz. Computer-algebra calculations and measurements on AB spin systems for double-spin-echo sequences. *MAGMA.* **3**, 109-118 (1995).

106. H. Wilman and P. S. Allen. The response of the strongly coupled AB system of citrate to typical 1H MRS localization sequences. *J. Magn. Reson.* B **107**, 25-33 (1995).

107. F. Schick, T. Nagele, U. Klose, and O. Lutz. Lactate quantification by means of press spectroscopy--influence of refocusing pulses and timing scheme. *Magn. Reson. Imaging* **13**, 309-319 (1995).

108. T. Ernst and J. Hennig. Coupling effects in volume selective 1H spectroscopy of major brain metabolites. *Magn. Reson. Med.* **21**, 82-96 (1991).

109. C. T. Moonen, M. von Kienlin, P. C. van Zijl, J. Cohen, J. Gillen, P. Daly, and G. Wolf. Comparison of single-shot localization methods (STEAM and PRESS) for in vivo proton NMR spectroscopy. *NMR Biomed.* **2**, 201-208 (1989).

110. C. H. Sotak, D. Freeman and R.E. Hurd, *J. Magn. Reson.*, **78**, 355-362 (1988).

111. R.E. Hurd and D. Freeman, *Proc. Natl. Acad. Sci. USA.*, **86**, 4402-4409 (1989).

112. A.H. Wilman and P.S. Allen, In-vivo NMR Detection Strategies for γ-aminobutyric Acid, Utilizing Proton Spectrosocpy and Coherences Pathway Filtering with Gradients. *J. Magn. Reson.*, **101**, 165-171 (1993).

113. A.H. Wilman and P.S. Allen. Yield enhancement of the double quantum filter sequence designed for the detection of GABA in proton spectroscopy of brain, *J. Magn. Reson.*, **109**, 169-174 (1995).

114. A.H. Wilman and P.S. Allen, The response of the strongly coupled AB system of Citrate to typical ^{1}H MRS Localization Sequences, *J. Magn. Reson.*, B **107**, 25-33 (1995).

115. L. Jouvensal, P.G. Carlier and G. Bloch, Practical Implementation of Single Voxel Double Quantum Editing on a Whole-Body NMR Spectrometer: Localized Monitoring of Lactate in the Human Leg During Exercise, *Magn. Reson. Med.*, **36**, 487-490 (1996).

116. J.R. Keltner, L.L. Wald, B. de B. Frederick, and P.F. Renshaw, In Vivo Detection of GABA in Human Brain Using a Localized Double Quantum Filter Technique, *Magn. Reson. Med.*, **37**, 366-371 (1997).

117. J.R. Keltner, L.L. Wald, P.J. Ledden, Y-C.I. Chen, R.T. Matthews, E.H.G.K. Kusestermann, J.R. Baker B.R. Posen and B.G. Jenkins, A Localized Double-Quantum Filter for the In-Vivo detection of Brain Glucose, *Magn. Reson. Med.*, **39**, 651-656 (1998).

118. R.B. Thompson and P.S. Allen. A New Multiple Quantum Filter Design Procedure for Use on Strongly Coupled Spin Systems Found In Vivo: Its Application to Glutamate, *Magn. Reson. Med.*, **39**, 762-771 (1998).

119. H. Trabesinger, .M. Weber, C.O. Duc and P. Boesiger, Detection of Glutathione in the Human Brain In Vivo by Means of Double Quantum Coherence Filtering, *Magn. Reson. Med.*, **42**, 283-289 (1999).

120. J. Slotboom, A.F. Mehlkopf and W.M.M.J. Bovee. The Effects of Frequency Selective RF Pulses on J-Coupled Spin-1/2 Systems, *J. Magn. Reson.*, A **108**, 38-50 (1994).

121. I. Marshall and J. Wild. A systematic study of the lactate lineshape in PRESS-localized proton spectroscopy. *Magn. Reson. Med.* **40**, 72-78 (1998).

122. O. Stern, Z. *Phys.*, **7**, 249 (1921).

123. W. Gerlach and O. Stern, *Ann. Phys. Leipzig.*, **74**, 673 (1924).

124. I. Estermann and O. Stern, Z. Phys., **85**, 17 (1933).

125. J. J. Sakurai, "Modern Quantum Mechanics", Addison-Wesley Publishing Company, Inc., New York, (1985).

126. F. Reif, "Fundamentals of Statistical and Thermal Physics", McGraw-Hill, New York, (1965).

127. N. Bloembergen, E. M. Purcell and R. V. Pound, Relaxation effects in nuclear magnetic resonance absorption, *Phys. Rev.* **73**, 679 (1948).

128. W.S. Warren, W. Richter, A.H. Andreotti and B.T. Farmer II, Generation of Impossible cross peaks between Bulk Water and Biomolecules in Solution NMR, *Science*, **262**, 2005-2009 (1993).

129. A. Abergam and M. Goldman, "Nuclear Magnetism: Order and Disorder", Clarendon Press, Oxford, (1982).

130. C.P. Slichter, "Principles of Magnetic Resonance", Springer-Verlag, Berlin, (1990).

131. W. S. Warren, *In* "Advances in Magnetic Resonance", Vol. 12, pp 248-384, Academic Press, Inc., San Diego, (1987).

132. F. Bloch and A. Siegert, *Phys. Rev.*, **57**, 522 (1940).

133. N. F. Ramsey, *Phys. Rev.*, **78**, 699 (1950).

134. E. L. Hahn and D. E. Maxwell, *Phys. Rev.*, **84**, 580 (1951).

135. O. W. Sorensen, G. W. Eich, M. H. Levitt, G. Bodenhausen and R. R. Ernst, *Prog. In NMR Spect.*, **16**, 163 (1983).

136. J. W. Pan, G. F. Mason, G. M. Pohost, and H. P. Hetherington. Spectroscopic imaging of human brain glutamate by water-suppressed J- refocused coherence transfer at 4.1 T. *Magn. Reson. Med.* **36**, 7-12 (1996).

137. L. Kay and R.E. McClung, Product Operator Description of AB and ABX Spin Systems, *J. Magn. Reson.*, **77**, 258-273 (1988).

138. B. J. Soher, K. Young, V. Govindaraju, and A. A. Maudsley. Automated spectral analysis III: application to in vivo proton MR spectroscopy and spectroscopic imaging. *Magn. Reson. Med.* **40**, 822-831 (1998).

139. K. Young, B. J. Soher, and A. A. Maudsley. Automated spectral analysis II: application of wavelet shrinkage for characterization of non-parameterized signals. *Magn. Reson. Med.* **40**, 816-821 (1998).

140. K. Young, V. Govindaraju, B. J. Soher, and A. A. Maudsley. Automated spectral analysis I: formation of a priori information by spectral simulation. *Magn. Reson. Med.* **40**, 812-815, (1998).

141. R. R. Ernst, G. Bodenhausen and A. Wokaun, "Principles of Nuclear Magnetic Resonance in One and Two Dimensions", Clarendon Press, Oxford, (1987).

142. R. Kreis and C. J. Boesch, Liquid-crystal-like structures of human muscle demonstrated by in vivo observation of direct dipolar coupling in localized proton magnetic resonance spectroscopy, *J. Magn. Reson.* B **104**, 189-92 (1994).

143. R. Kreis and C. J. Boesch, Spatially localized, one- and two-dimensional NMR spectroscopy and in vivo application to human muscle., *J. Magn. Reson.* B **113** 103-118 (1996).

144. Hanstock, C.C., Thompson, R.B., Trump, M.E., Gheorghiu, D., Hochachka, P.W., and Allen, P.S., The Residual Intra-molecular Dipolar Coupling of the Cr / PCr Methyl Resonance in Resting Human Medial Gastrocnemius Muscle, *In Press, Magn. Reson. Med.*, (1999).

145. U. Eliav and G. Navon, A study of dipolar interactions and dynamic processes of water molecules in tendon by 1H and 2H homonuclear and heteronuclear multiple-quantum-filtered NMR spectroscopy. *J Magn. Reson.*, **137**, 295-310 (1999).

146. I. Asllani, E. Shankland, T. Pratum and M. Kushmerick, Anisotropic Orientation of Lactate in Skeletal Muscle Observed by Dipolar Coupling in (1)H NMR Spectroscopy. *J Magn. Reson.*, **139**, 213-224 (1999).

147. R. Gruetter, S. A. Weisdorf, V. Rajanayagan, M. Terpstra, H. Merkle, C. L. Truwit, M. Garwood, S. L. Nyberg, and K. Ugurbil. Resolution improvements in in vivo 1H NMR spectra with increased magnetic field strength. *J. Magn. Reson.* **135**, 260-264 (1998).

148. M. Terpstra, P. M. Andersen, and R. Gruetter. Localized eddy current compensation using quantitative field mapping. *J. Magn. Reson.* **131**, 139-143 (1998).

149. D. A. Kelley, L. L. Wald and J. M. Star-Lack, Lactate detection at 3T: compensating J coupling effects with BASING, *J. Magn. Reson. Imag.*, **9**, 732-7 (1999).

150. J. A. Pople, W. G. Eich and H. J. Bernstein, "High Resolution Nuclear Magnetic Resonance", McGraw-Hill, New York, (1959).

151. K. L. Behar and T. Ogino, Assignment of resonance in the 1H spectrum of rat brain by two-dimensional shift correlated and J-resolved NMR spectroscopy, *Magn. Reson. Med.* **17**, 285-303 (1991).

152. V. Govindaraju, V. J. Basus, G. B. Matson, and A. A. Maudsley. Measurement of chemical shifts and coupling constants for glutamate and glutamine. *Magn. Reson. Med.* **39**, 1011-1013 (1998).

CHAPTER 2

Numerical Methods in In-Vivo NMR Spectroscopy

2.1 Introduction

Chapter 1 outlined a matrix method designed for the calculation of the evolution of the density matrix in response to the component interactions that make up an NMR pulse sequence. Within the rotating frame of reference, these elemental interactions include i) r.f. pulses, ii) magnetic field gradients, iii) chemical shielding, iv) scalar coupling and iv) dipolar coupling. If each of the these five Hamiltonian components is time-independent, then Eq. (1-74), $\rho(t) = U^{-1} \exp(-i\mathcal{H}_{diag}t/\hbar)\, U\, \rho(0)\, U^{-1} \exp(i\mathcal{H}_{diag}t/\hbar)\, U$, can be used to evaluate the evolution of the density matrix as a function of time, from any initial state, $\rho(0)$. The expectation value of any operator can be calculated from the density matrix, allowing the distribution of coherences to be calculated at any point throughout the NMR pulse sequence, including the transverse magnetization directly following the sequence. This chapter outlines the general framework for the numerical implementation of Eq. (1-74), outlining time saving algorithms, as well as the need for these efficient methods.

In-vivo NMR pulse sequences necessarily comprise several r.f. pulses, gradients, and inter-pulse delays, requiring the definition of several distinct Hamiltonians throughout the sequence. Section 2.2 describes a definition of a pulse sequence as a series of Hamiltonian *segments*, and includes the basic mathematical operations necessary to evolve the density matrix through the sequence. Several simple and robust time-saving approaches are introduced. Section 2.3 describes the efficient generation of the metabolite spectrum (FID) directly from the density matrix following the application of the pulse sequence. Section 2.4 provides an approximate solution method for time-dependent Hamiltonians, with a particular focus on time-dependent r.f. pulses commonly used to provide spatially selective excitation. Section 2.5 outlines methods of sequence characterization, incorporating the methodology of sections 2.2 to 2.4, allowing the coupled spin response to be optimized and the sources of variability to be identified.

In all sections, there is a focus on the efficiency of the tasks to be carried out, due to the large number of numerical operations associated with matrix multiplications. For example, the largest spin group considered in this thesis, a six-spin proton system, is described by a density matrix containing 64 x 64 complex elements, requiring 64^3 = 262144 complex multiplications and $64^3 - 64^2$ = 258048 complex additions for a single matrix multiplication. To implement the matrix multiplications and all other numerical operations, the high level language MATLAB™ is utilized. The MATLAB™ environment is ideal for NMR simulations due to its efficient matrix multiplication algorithm and massive library of built in functions, including the eigenvalue and eigenvector calculations required for the evaluation Eq. (1-74). The computational time required to simulate a given NMR sequence is determined primarily by the time required for a matrix multiplication, an operation that may be carried out from hundred's to million's of times for a single simulation. *On a Pentium II 400 MHz PC running MATLAB 5, the multiplication of two 64 x 64 complex matrices takes ~ 20 msec.* This value, although seemingly instantaneous for a single multiplication, bounds the number of such multiplications to ~ 180,000 per hour, confining the scope of the simulations that are approachable due to time restraints.

Consider a specific application of Eq. (1-74), to generate a two-dimensional COSY (chapter 1, ref 141) data set, with a 2048 point time domain FID, and excitation by a the standard pulse sequence with a variable inter-pulse delay, τ_{delay}, as shown in Fig. 2-1. Each direct application of Eq. (1-74), to calculate $\rho(n)$, and the corresponding transverse magnetization at each point, $M_+(n)$, requires at least 6 matrix multiplications, or 6 x 2048 = 12288 multiplications for a single FID calculation. If N_{delays} separate delays, of length τ_{delay}, are to be simulated, each with a corresponding FID, a minimum of (N_{delays} x 12288) matrix multiplications are necessary, requiring a minimum of ~ (N_{delays}/15) hours[1] for the total simulation. The computational time can be drastically reduced by enhancing this 'brute force approach' with step-saving algorithms and alternate approaches, to be introduced in the following sections. For example, 256 six-spin FIDs (2048 pts) can be calculated in 0.12 hours[1] utilizing an eigenvalue approach, described in section 2-3, versus the 17.1 hours[1] needed for a direct calculation, ~140 times faster. In the remainder of this chapter, numerical methods for the calculation of

[1]Pentium II 400 MHz PC running MATLAB 5

the response of the metabolite spin-systems to in-vivo NMR pulse sequences, particularly for multiple values of any of a cohort of sequence parameters, are developed. Algorithms designed for efficiency and generality allow a variety of pulse sequences and the most demanding (six-spin) systems to be considered, including the influence of the realistic slice-selective r.f. pulses integral to the in vivo experiment.

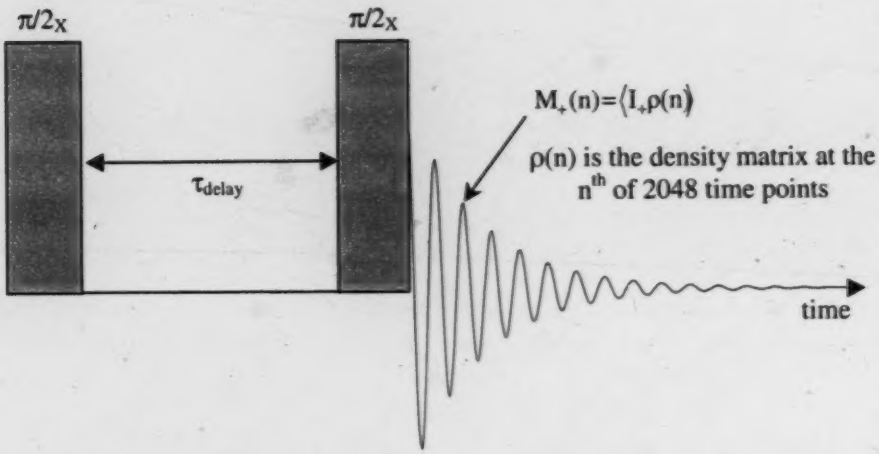

Figure 2-1 The COSY experiment, a standard two-dimensional NMR pulse sequence. The transverse magnetization of a proton spin system excited by the two pulse sequence with a variable inter-pulse delay is calculated at 2048 points in time directly following the 2^{nd} pulse.

Previously, numerical methods that incorporate the density matrix representation of the nuclear spin systems have been reported (1,2), although with a focus on high-field applications.

2.2 Simulation Structure

Every pulse sequence can be treated as a series of S independent *segments*, each of which has a unique Hamiltonian, $\mathcal{H}_n$, for n = 1 to S. If each of the S segments is described by a time-independent Hamiltonian, the general inter-segment relationship is given by the discrete implementation of Eq. (1-74),

$$\rho_n = U_n^{-1} \exp(-i\mathcal{H}_{n_{diag}} t_n / \hbar)\, U_n \rho_{n-1} U_n^{-1} \exp(i\mathcal{H}_{n_{diag}} t_n / \hbar)\, U_n \qquad (2\text{-}1)$$

where ρ_n is the density matrix at the end of the n^{th} segment, $\mathcal{H}_{n_{diag}}$ is the diagonal eigenvalue matrix for the n^{th} segment, and t_n is the segment length. Each of the segments can be characterized by a time-independent rotating frame Hamiltonian,

$$\mathcal{H}_n = \mathcal{H}_{r.f._n} + \mathcal{H}_{shift_n} + \mathcal{H}_{coup_n} + \mathcal{H}_{grad_n} + \mathcal{H}_{dip_n}, \qquad (2\text{-}2)$$

where, for example, four such components exist for the pulse sequence of Fig. 2-2.

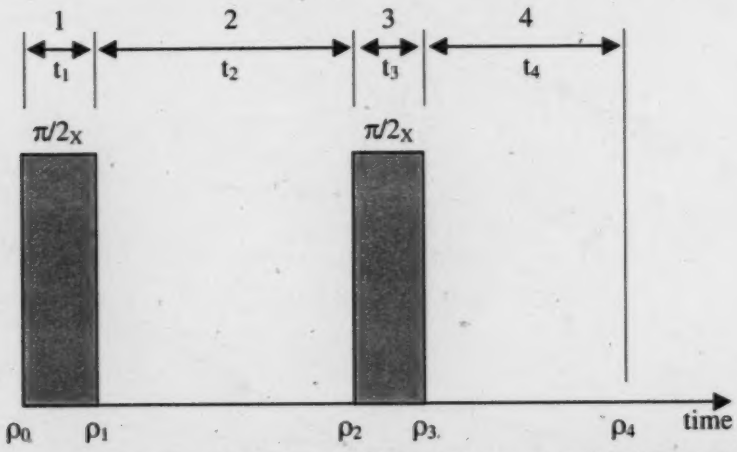

Figure 2-2 A pulse sequence is broken up into components, r.f. pulses and inter-pulse delays, in each of which the segment Hamiltonian is time-independent, allowing Eq. (2-1) to be applied to each segment.

Given the complete segment Hamiltonian, the corresponding eigenvalues, $\mathcal{H}_{n_{diag}}$, and eigenvectors, U_n, can be utilized in Eq. (2-1) to calculate the density matrix at the segment endpoint.

To reduce the number of calculations needed to evolve the density matrix, Eq. (2-1) can be expressed in a condensed form

$$\rho_n = V_n^{-1} \rho_{n-1} V_n \tag{2-3}$$

where the operator V_n is called the evolution operator, defined

$$V_n = U_n^{-1} \exp(i\mathcal{H}_{n_{diag}} t_n / \hbar) U_n. \tag{2-4}$$

If the desired simulation information is the density matrix or the magnetization FID *following* the pulse sequence, the density matrix does not need to be calculated at the intermediate segments, rather, the evolution operator alone can be calculated for each segment. For example, the density matrix following the four segment example in Fig. 2-2 can be represented as

$$\rho_4 = V_4^{-1} V_3^{-1} V_2^{-1} V_1^{-1} \rho_0 V_1 V_2 V_3 V_4. \tag{2-5}$$

Defining $V_{Tot} = V_1 V_2 V_3 V_4$, it is trivial to show that $V_{Tot}^{-1} = V_4^{-1} V_3^{-1} V_2^{-1} V_1^{-1}$, or, generally,

$$\rho_S = V_{Tot}^{-1} \rho_0 V_{Tot}. \tag{2-6}$$

Calculating the density matrix, ρ_S, using Eq. (2-6) requires 3S + 1 matrix multiplications for an S-segment sequence, while calculating the density matrix at the end of each segment, each individual ρ_n, to arrive at ρ_S requires 6S matrix multiplications, approximately twice as many.

It is often desirable to calculate the response of a spin-system to multiple values of sequence parameters, to characterize and optimize that response, or to model multi-dimensional NMR sequences such as the COSY experiment from Fig 2-1. For example, the pulse sequence in Fig. 2-2 contains two evolution periods, both of which will modify the density matrix following the four-segment experiment. A general approach has been developed for the treatment of multi-value simulations, based on the storage of the evolution operators for each segment. Several evolution operators can be generated for each segment, corresponding to variations in a segment property such as length (τ_n) or position in a gradient field (r in $\gamma \mathbf{G} \cdot \mathbf{r} t$), as displayed schematically in Fig. 2-3. The variation of a segment property is equivalent to a variation in the segment Hamiltonian, resulting in multiple evolution operators for a single segment, M_S variations for each of the S segments. The evolution operators can then be combined to most efficiently calculate the desired results, be that the expectation value of an observable throughout or following the sequence, over the range of the variables simulated.

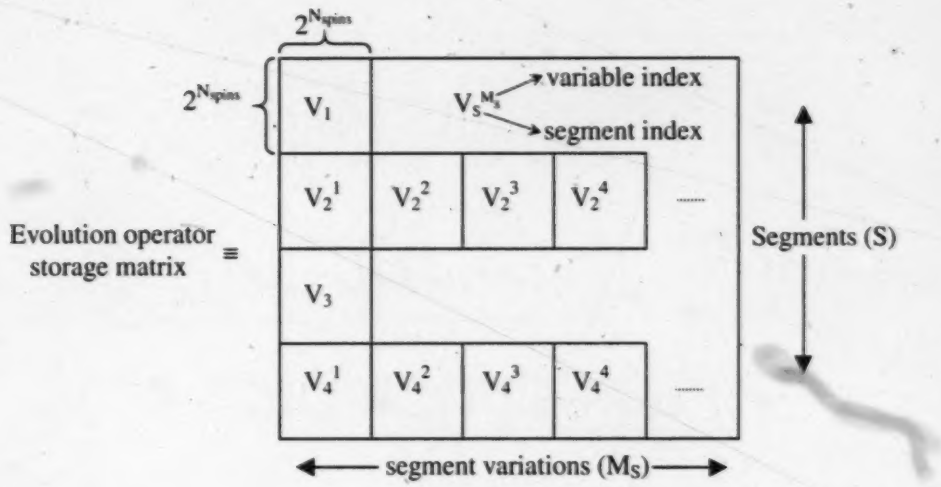

Figure 2-3 A schematic diagram of the matrix utilized to store the evolution operators that are subsequently used to calculate the density matrix throughout or following an NMR pulse sequence.

Generally, for a sequence of S segments with M_S variations per segment, there are a total of $\prod_S M_S$ outcomes. The calculation of each evolution operator matrix, 'V', as shown in Figure 2-3 requires 2 matrix multiplications, for a total of $2\sum_S M_S$ multiplications to generate the storage matrix. The calculation of each of the V_{Tot} matrices from Eq. (2-6) requires S-1 multiplications, for example $V_{Tot} = V_1V_2V_3V_4$ for a 4 segments experiment, requiring 3 multiplications. Including the two additional multiplications required to generate $\rho_n = V_{Tot}^{-1}\rho_0 V_{Tot}$, $\sim 2\sum_S M_S + (S+1)\prod_S M_S$ matrix multiplications are needed to generate $\prod_S M_S$ resulting density matrices. On the other hand, the direct brute force calculation, with two multiplications per 'V' and 2S calculations to generate the density matrix from the evolution operators, as shown in Eq. (2-5), requires $(2 \times 2 \times S)\prod_S M_S$ total matrix multiplications, $\sim 4S/(S+1)$ times as many as the method introduced above.

In addition to reducing the number of requisite matrix multiplications, collecting the evolution operators in a storage matrix results in an overall matrix geometry that allows the component operator elements to be combined with a general algorithm. Using this approach, the calculation of the density matrix becomes independent of the number of spins in the system (N_{spins}), sequence segments (S) or variations in a given segment (M_S). This generality allows a single program to be used to simulate any sequence of Hamiltonian segments, including the variations in any segment parameter.

2.3 Transverse Magnetization – FID (Spectrum) Calculation

The metabolite information acquired with ^{1}H NMR spectroscopy is contained in the free induction decay acquired following the pulse sequence. While the state of the spin system following the excitation is embodied by the density matrix, the assessment of the percentage yield and exact line shape used to quantify the metabolite signals in practice requires the calculation of the transverse magnetization as measured by the experimentalist. The most direct method of FID calculation is to evaluate the expectation value of the raising operator, I_+, at each of the discrete sample points, $n\Delta t$, using the density matrix at each point,

$$M_+(n\Delta t) \propto \langle I_+(n\Delta t) \rangle = Tr(I_+ \rho(n\Delta t)). \tag{2-7}$$

For example, a typical in-vivo ^{1}H NMR spectroscopy experiment might include the acquisition of 2048 data points with a bandwidth in the range of 1000 Hz to 2500 Hz, or Δt = 0.4 msec to 1 msec. Utilizing Eq. (2-3), $\rho_n = V_n^* \rho_{n-1} V_n$, to calculate the density matrix at each of the 2048 FID points for a six-spin system requires at least 4096 matrix multiplications, requiring ~ 1.5 minutes of computation[1], which becomes restrictive if hundreds or thousands of FIDs need to be calculated. Fortunately, there exists a much faster method to produce an identical result, using an eigenvalue approach.

The FID, and its corresponding spectrum are composed of discrete transition frequencies, each with a complex weighting corresponding to an amplitude and phase. Recall from section 1.3.6 that the phase difference between the transitions corresponded to the existence of anti-phase coherence. It is possible to generate the FID by calculating the individual transition frequencies, and weighting each transition by a complex coefficient corresponding to it's relative weighting. This approach, represented mathematically by Eq. (2-8), avoids the time consuming matrix multiplications used in the direct method shown in Eq. (2-7).

$$M_+(n\Delta t) = \sum_q a_q \exp(i2\pi n \Delta t f_q) \tag{2-8}$$

---

[1]Pentium II 400 MHz PC running MATLAB 5

Each spin system has a discrete number of transitions, q, with characteristic transition frequencies, f_q, that are a function of the field strength, the chemical shifts, scalar couplings, and if present, dipolar couplings. The complex coefficient weightings, a_q, reflect the spin-ensemble information following excitation, and are extracted from the density matrix existing at the onset of the signal acquisition period. The method used to determine these values, the f_q and a_q, is best illustrated with a specific example, a two-spin scalar-coupled spin-½ system. The eigenvalue solution methods outlined in chapter 1.3.5 are enlisted to derive this solution method.

First, a change of basis is required to allow the 'q' transitions to be easily identified. Transforming the free evolution rotating frame Hamiltonian to a frame of reference in which it is diagonal, $\mathcal{H}'_{diag} = U\,\mathcal{H}'U^{-1}$, utilizes the rotation matrices, U, formed from the eigenvectors of $\mathcal{H}'$, which themselves, define a new basis in which the Hamiltonian is diagonal. For example, the strongly coupled two-spin system, defined by $\mathcal{H}' = \mathcal{H}'_{shift} + \mathcal{H}'_{coup} = -\hbar(\omega_1 I_{1_z} + \omega_2 I_{2_z} - 2\pi J\, \mathbf{I_1}\cdot\mathbf{I_2})$, has off diagonal elements from the scalar coupling Hamiltonian, as shown in Eq. (1-80). For the specific values ω_1 = 2 ppm, ω_2 = 2.5 ppm and J = 20 Hz, and a main field strength of 3 T, the basis transformation required to diagonalize the Hamiltonian matrix is given by four new basis vectors, the Hamiltonian eigenvectors,

$$|\uparrow\uparrow\rangle = \begin{pmatrix}1\\0\\0\\0\end{pmatrix} \rightarrow \begin{pmatrix}1\\0\\0\\0\end{pmatrix}, |\uparrow\downarrow\rangle = \begin{pmatrix}0\\1\\0\\0\end{pmatrix} \rightarrow \begin{pmatrix}0\\-.989\\.151\\0\end{pmatrix}, |\downarrow\uparrow\rangle = \begin{pmatrix}0\\0\\1\\0\end{pmatrix} \rightarrow \begin{pmatrix}0\\.151\\.989\\0\end{pmatrix}, |\downarrow\downarrow\rangle = \begin{pmatrix}0\\0\\0\\1\end{pmatrix} \rightarrow \begin{pmatrix}0\\0\\0\\1\end{pmatrix} \quad (2\text{-}9)$$

The advantage of this representation is that the single quantum coherences between the newly defined states, now linear combinations of the original bases, each correspond to one of the 'q' system transitions. The corresponding transition energies (f_q) are given by the differences between the energy eigenvalues of the *new* spin states. The relative weighting of each transition, a_q, can be calculated as an expectation value. In the diagonalized frame of reference, each of the non-zero elements in the transverse

magnetization operator (matrix), I_+, corresponds to one of the q discrete transitions, as shown in Fig. 2-4, providing a direct and simple measure of the number of transitions with a non-zero weighting.

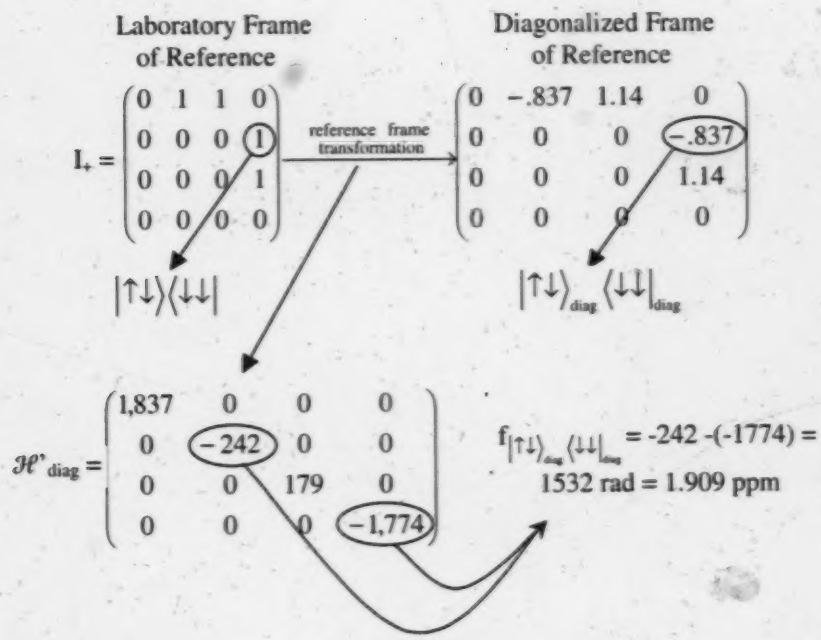
Laboratory Frame
of Reference
Diagonalized Frame
of Reference
reference frame
transformation
$I_+ =$
$\begin{pmatrix} 0 & 1 & 1 & 0 \\ 0 & 0 & 0 & 1 \\ 0 & 0 & 0 & 1 \\ 0 & 0 & 0 & 0 \end{pmatrix}$
$\begin{pmatrix} 0 & -.837 & 1.14 & 0 \\ 0 & 0 & 0 & -.837 \\ 0 & 0 & 0 & 1.14 \\ 0 & 0 & 0 & 0 \end{pmatrix}$
$|\uparrow\downarrow\rangle\langle\downarrow\downarrow|$
$|\uparrow\downarrow\rangle_{diag}\langle\downarrow\downarrow|_{diag}$
$\mathcal{H}'_{diag} =$
$\begin{pmatrix} 1{,}837 & 0 & 0 & 0 \\ 0 & -242 & 0 & 0 \\ 0 & 0 & 179 & 0 \\ 0 & 0 & 0 & -1{,}774 \end{pmatrix}$
$f_{|\uparrow\downarrow\rangle_{diag}\langle\downarrow\downarrow|_{diag}}$ = -242 -(-1774) =
1532 rad = 1.909 ppm

Figure 2-4 The matrix form of the two-spin raising operator, I_+, is transformed to a frame of reference in which the free evolution Hamiltonian (i.e. no r.f. or gradient components are present) is diagonal. In this new frame of reference the single quantum coherence between the basis states have a transition frequency equal to the energy difference between the eigenstates. For example, the circled matrix element above has a characteristic frequency given by $f_{|\uparrow\downarrow\rangle_{diag}\langle\downarrow\downarrow|_{diag}}$.

The relative weighting of the transitions, the a_q, for example, for the circled element in Fig. 2-4, $|\uparrow\downarrow\rangle_{diag}\langle\downarrow\downarrow|_{diag}$, corresponding to the 1.909 ppm line, is given by the expectation value of the corresponding transition operator, I_{Trans_q}, a matrix with a single non-zero element, as shown in Eq. (2-10).

$$\left\langle I_{Trans_q} \right\rangle = Tr(\rho I_{Trans_q}) = Tr\left(\begin{pmatrix} \rho_{11} & \rho_{12} & \cdots & \\ \rho_{21} & \rho_{22} & \cdots & \\ \vdots & \vdots & \ddots & \\ & \rho_{42} & & \end{pmatrix} \begin{pmatrix} 0 & 0 & 0 & 0 \\ 0 & 0 & 0 & -.837 \\ 0 & 0 & 0 & 0 \\ 0 & 0 & 0 & 0 \end{pmatrix} \right) = -.837*\rho_{42}. \quad (2\text{-}10)$$

Utilizing Eq. (2-10) and information from Fig. 2-4, the four transitions of the two-spin system considered thus far have relative weightings given by

$$a_1 = -.837*\rho_{21},\ a_2 = 1.14*\rho_{31},\ a_3 = -.837*\rho_{42},\ a_4 = 1.14*\rho_{43}. \quad (2\text{-}11)$$

with the corresponding transition frequencies

$$f_1 = (1837 + 242)\ \text{rad} = 2.591\ \text{ppm},\ f_2 = (1837 - 179)\ \text{rad} = 2.066\ \text{ppm},$$
$$f_3 = (-242 + 1774)\ \text{rad} = 1.909\ \text{ppm, and}\ f_4 = (179 + 1774)\ \text{rad} = 2.434\ \text{ppm}. \quad (2\text{-}12)$$

The density matrix elements in Eq. (2-11) are assumed to be from the frame of reference in which the Hamiltonian is diagonal.

Consider, as a specific example, the application of the pulse sequence of Fig. 2-1, with τ_{delay} = 5 msec, assuming ideal hard pulses, to this most recently considered two-spin system, ω_1 = 2 ppm, ω_2 = 2.5 ppm and J = 20 Hz, and a main field strength of 3 T. The spectra (Fourier transformation of the transverse magnetization) calculated using the direct method, utilizing Eq. (2-7), and the eigenvalue method, inserting the resulting a's and f's into Eq. (2-8), are shown in Figs. 2-5A) and 2-5B), respectively.

Depending on the number of spins and the number of transitions, q, in the system, the eigenvalue method is from 10's to 100's of times faster than the direct method. This efficiency is crucial for applications involving multiple simulations, with variations of key sequence parameters such as inter-pulse delays or r.f pulse tip angles. Such multi-parameter calculations are necessary to both characterize and optimize the response of the coupled spin systems to the in-vivo pulse sequences used in practice, or to simulate multi-dimensional approaches.

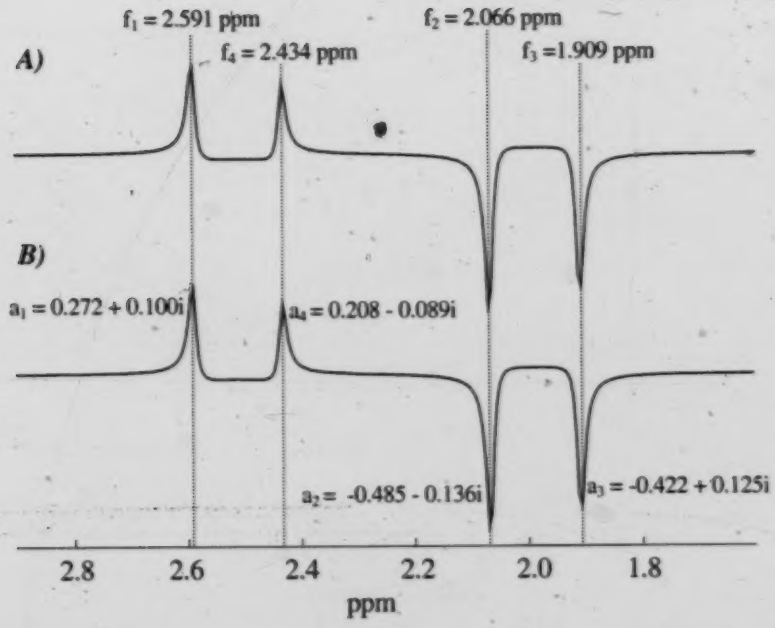

Figure 2-5 Numerically calculated two-spin spectra, for the spin system defined above, following excitation by the two-pulse sequence shown in Fig. 2-1, with τ_{delay} = 5 msec. Spectrum A) is generated from a 2048 point FID calculated using the direct method, using Eq. (2-7), while the spectrum in B) is generated using the eigenvalue method, from an FID calculated with Eq. (2-8). Both FIDs were line-broadened to 2 Hz using an exponential weighting in the time domain. The a_1 to a_4 values used to generate spectrum B) were calculated using Eq. (2-11). The two calculated spectra are identical to 1 part in 10^8, although the eigenvalue approach required ~ 5 % as long to calculate.

2.4 Time-Dependent Hamiltonians – An Approximate Method of Evaluation

The valid application of Eq. (1-74), the evolution motor for the numerical evaluation of the density matrix, requires that the Hamiltonian be time-independent. While several of the Hamiltonian components, including the chemical shift, scalar coupling, and main field components are normally constants in time, the gradients fields, and more often the r.f. field components, can be time-varying. Section 2.4.1 details the incorporation of shaped r.f. pulses, used for spectrally and spatially selective excitation, into the numerical simulation framework developed thus far.

2.4.1 Shaped Radio-Frequency Pulses

To model shaped r.f. pulses, most often designed to excite a rectangular bandwidth of frequencies, or equivalently, a rectangular slice of space in a magnetic gradient field, approximate methods need to be incorporated. It has been previously suggested (chapter 1, ref 141, for example) that dividing the time-dependent Hamiltonian into shorter time-independent segments would allow exact methods to be applied in each segment, with the validity of the approximation improving with the fineness of the divisions asymptotically towards the exact solution. Fortunately, this approach is merely a variation of the simulation framework introduced in section 2.2, where the NMR experiment was evaluated by segmentation of the sequence into time-independent Hamiltonians. Figure 2-6 displays a sample segmentation of a time-dependent sinc-shaped r.f. pulse, a member of the family of shapes most commonly used for spatially (spectrally) selective excitation in in-vivo NMR spectroscopy.

The sinc family of shapes are derived by approximating the NMR frequency excitation profiles with Fourier transform theory, a similarity outlined in section 1.3.7. The inverse Fourier transform of the ideal rectangular frequency profile is the sinc = sin(t)/t shape, similar to the envelope shown in Fig. 2-6. Although, as was illustrated in Fig 1-14, Fourier transform theory only approximates the NMR time/frequency relationship, and as a consequence the true sinc shape is not employed in practice, rather, variations, including the sinc-Gaussian, sinc-Hamming, sinc-Hanning and numerous numerically optimized shapes (3-10) are more commonly employed.

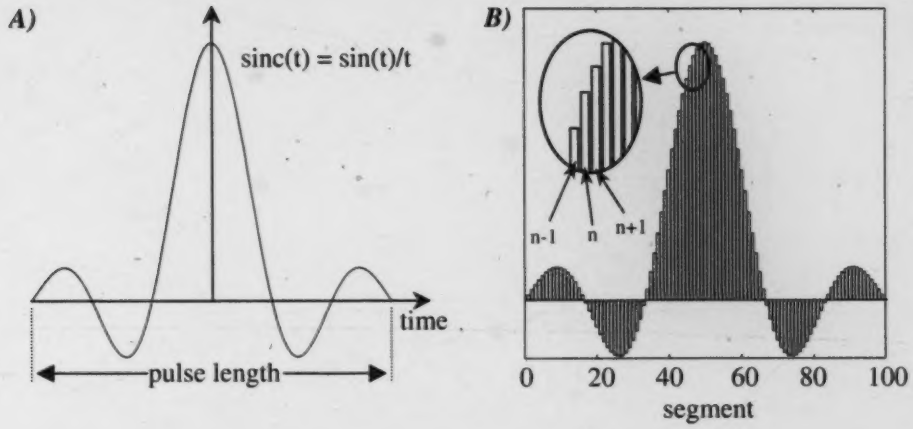

Figure 2-6 The continuous time domain r.f. pulse envelope, a truncated sinc function, shown in A), is segmented into 100 time-independent rectangular pulses in B).

The evaluation of the density matrix throughout or following the application of a segmented time-dependent Hamiltonian incorporates the same protocol used for segmented sequences of pulses and delays, where $\rho_n = U_n^{-1} \exp(-i\mathcal{H}'_{n_{diag}} t_n / \hbar)\, U_n \rho_{n-1} U_n^{-1} \exp(i\mathcal{H}'_{n_{diag}} t_n / \hbar)\, U_n$, from Eq. (2-1). The Hamiltonian in n^{th} segment is defined by the r.f. pulse envelope, given by sinc(nΔt-length/2) in Fig. 2-6, where $\Delta t = \text{length}/N_S$, and N_S is the number of segments.

The value of Δt that is sufficiently small to *effectively* approximate the time-dependent Hamiltonian is a subjective determination, a function of the tolerance for error. For example, the spectral selection profile of the sinc shaped pulse in Fig. 2-6 can be calculated as a function of the number of segments, N_S, as shown in Fig. 2-7. The deviation of the profile as a function of the number of segments, N_S, from the "$N_S \rightarrow \infty$" profile is a good measure of the error induced by the degree of segmentation because the error can be determined as a function of the offset, $\omega_{off} = -\gamma G \cdot r$, as well as N_S. The $N_S \rightarrow \infty$ profile is approximated by N_S = 10,000 segments.

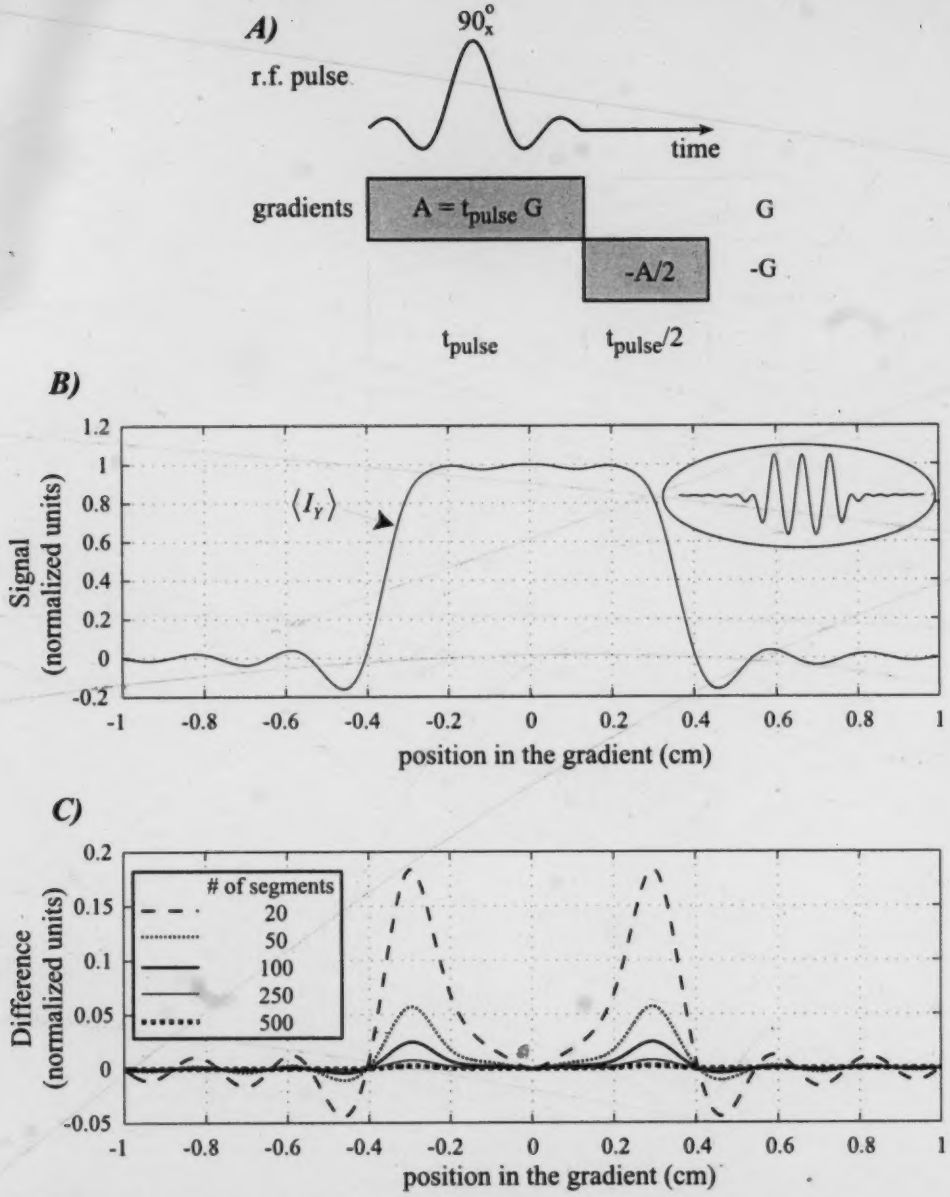

Figure 2-7 A spatially selective sinc-shaped $\pi/2$ excitation pulse is shown in A). The second gradient pulse, termed the refocusing lobe, re-phases gradient evolutions that occur during the excitation r.f. pulse, resulting in the uniform phase slice profile shown in B). In the absence of this refocusing lobe, the phase of the excited transverse magnetization (only one channel of which is shown, I_Y) will vary across the slice, as shown in the inset. The error resulting from the segmentation of the sinc pulse (into rectangular components) as a function of the number of segments is shown in C). All segments are equal in length.

The pulse sequences used for single voxel ^1H spectroscopy typically limit the region of tissue from which signal is received with three spectrally selective r.f pulses applied with mutually orthogonal gradients. Of the tens or hundreds of such single voxel pulse sequences proposed in the past, some consist exclusively of spatially selective pulses, the most popular of which are the PRESS (chapter 1, ref. 94-96) and STEAM (chapter 1, ref. 88,89) sequences. Other, more involved sequences comprise several pulses for the purpose of both spatial localization and the alteration of the coherences throughout and following the pulse sequence, such as the multiple quantum filter (MQF) sequence (chapter 1, ref. 110,111). Each of these three approaches, PRESS, STEAM and MQ filtering, is considered in detail in chapters 3 to 7. In each chapter, the coupled-spin response to the particular pulse sequence is exemplified with metabolite systems found in-vivo, such as lactate (AX_3), glutamate (AMNPQ) and NAA (A_3 and ABX). Figure 2-8 illustrates the general form of each of these pulse sequences used for practical in-vivo single voxel spectroscopy.

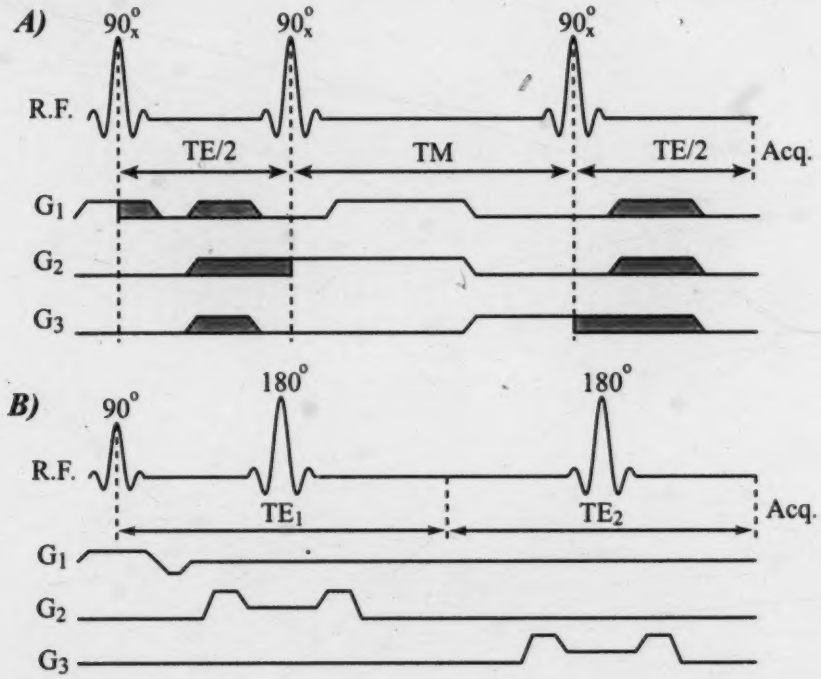

Figure 2-8 (A and B) A) The STEAM and B) the PRESS in vivo pulse sequences.

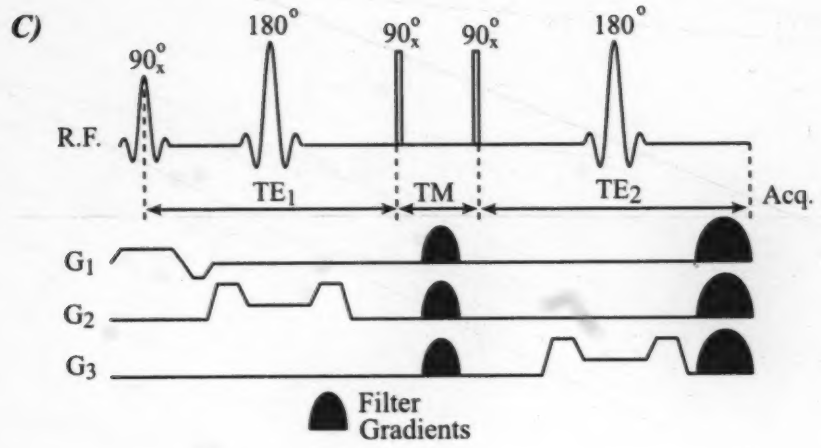

Figure 2-8 (C) C) The DQF in-vivo pulse sequence.

2.4.1.1 Shaped R.F Pulses – Spatial Distribution of Coherences

The localized signal acquired using the single voxel techniques is equivalent to the sum of the signal excited from the sample within the r.f. coil assembly. If the excitation profiles of the three slice selective pulses are perfectly rectangular with a uniform phase, then every point within the volume of interest will experience an identical sequence of pulses, and spins outside the voxel can be disregarded. In this ideal case, only one sequence of pulses need be simulated to calculate the metabolite yield and line shape (sum of signal over space), a scenario that is assumed when approximating single voxel sequences with hard pulse models. On the other hand, if the pulses excite a distribution of tip angles over space due to imperfect excitation profiles and chemical shift induced voxel offsets (see Fig. 2-9), several locations in space must be simulated to model the different *effective* pulse sequences experienced. The non-ideal slice profiles correspond to the practical reality of shaped r.f. pulses, whose finite length and amplitude dictates that there are always profile deviations from the ideal case described above. In Fig. 2-9, the spatial distribution of I_Y magnetization excited in a spin-echo with a slice

selective excitation pulse is illustrated. The hard 180° pulse was included to refocus the chemical shift evolutions.

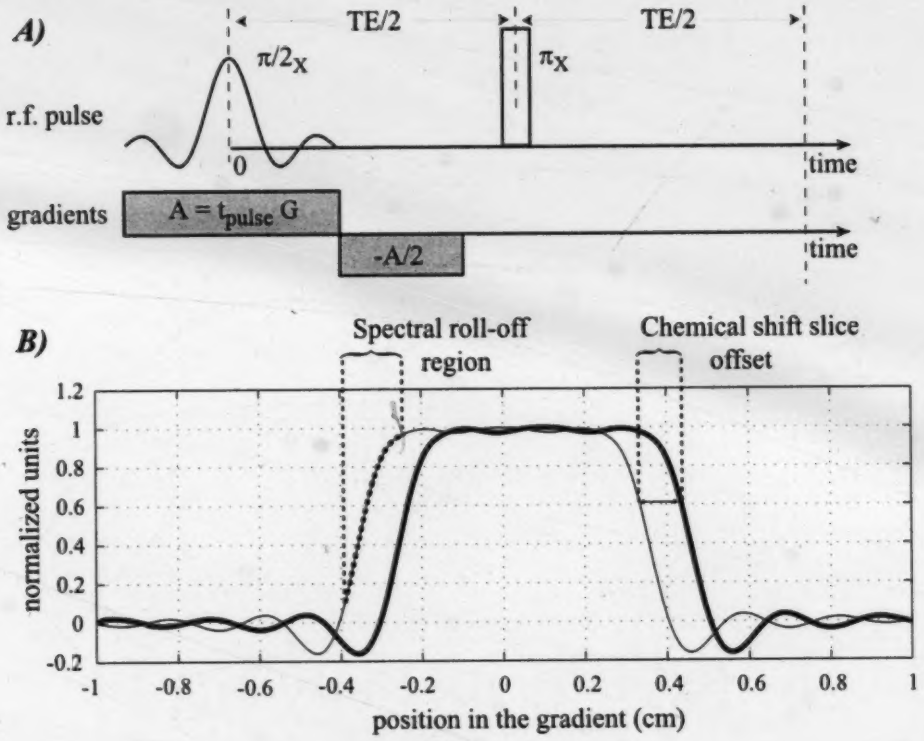

Figure 2-9 A) A spin-echo pulse sequence with a spatially selective sinc $\pi/2$ excitation pulse and a hard refocusing pulse. B) The spatial distribution of I_Y magnetization excited by the sequence in A) for two uncoupled spin systems with different chemical shifts (the source of the slice offset) is illustrated.

The slice offset originates from the chemical shift contribution, ω_a, to the total Hamiltonian during the r.f. pulse and gradient application. The field produced at a given location, x, in an x-directed gradient, G_x, can be expressed $\mathbf{B}(x) = \mathbf{B}_o + G_x \cdot x + \omega_a/\gamma$, or $\mathbf{B}(x) = \mathbf{B}_o + G_x \cdot (x + \omega_a/(G_x\gamma))$, where the slice offset is given by $\omega_a/(G_x\gamma)$.

Figure 2-10 displays the spatial distribution of coherences excited by a spatially selective refocusing pulse applied to a weakly coupled two-spin system in a spin echo experiment.

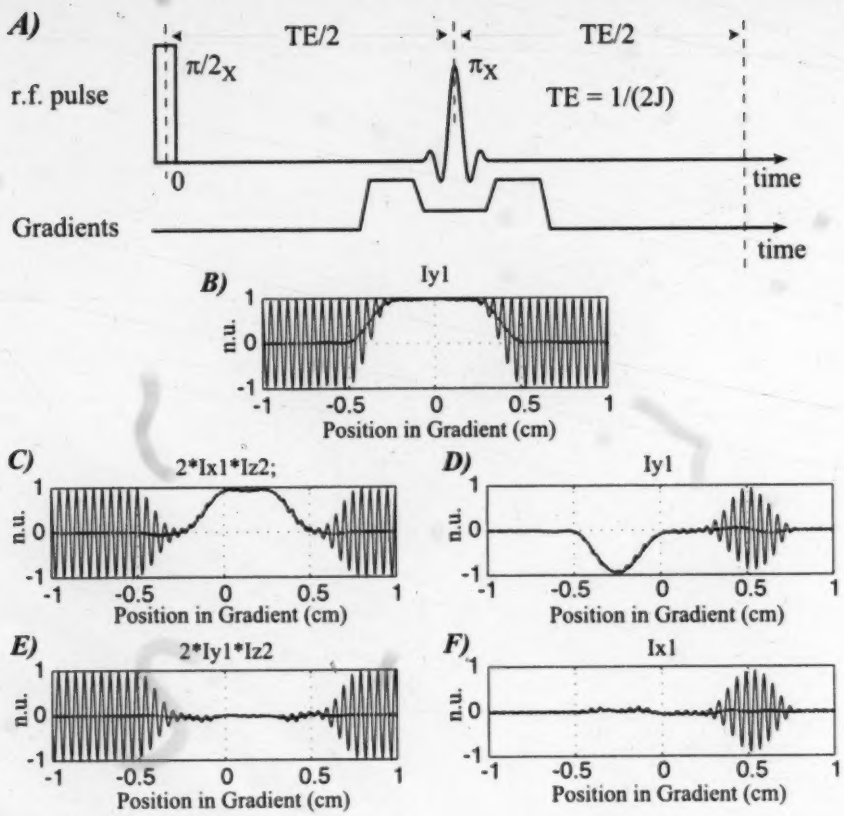

Figure 2-10 A) A spin-echo pulse sequence with a spatially selective sinc refocusing pulse and a hard excitation pulse. B) The spatial distribution of I_Y magnetization excited by the sequence in A) for an uncoupled spin system, $\omega_1 = 0$ ppm. In C) to F), the spatial distribution of $spin_1$ transverse magnetization excited by the sequence in A) for a coupled spin system, J = 10 Hz, $\omega_1 = 0$ ppm, $\omega_2 = 3$ ppm, is displayed. The echo length is set at 1/2J to optimize the generation of anti-phase coherence. For each profile a local average filter has been applied to smooth the gradient-induced oscillations.

The refocusing spin-echo is the most commonly employed sequence component following excitation in in-vivo NMR spectroscopy, acting to refocus the evolutions arising from both the chemical shielding interaction as well as from the main field inhomogeneities. The slice profiles from Fig. 2-10 C) to F) display an alteration of the distribution of coherences from the expected distribution, where the integrated signal from each profile represents the contribution from the corresponding coherence term. For example, from Fig. 2-10 C), the slice anomalies reduce the contribution from the only term predicted, from hard pulse theory, to be non-zero following the 1/2J spin echo, the

anti-phase term, $2I_{1_X}I_{2_Z}$, while creating an unexpected contribution from the in-phase term, I_{1_Y}, shown in D). Although not displayed in Fig. 2-10, there is also a coherence transfer associated with the slice artifacts, from $spin_1$ anti-phase coherence to $spin_2$ anti-phase coherence. Section 2.4.1.2 presents the selective pulse anomalies, such as signal loss and coherence transfer, as an integrated effect, to eliminate the spatial dimension from the already complex problem.

In both the PRESS and MQF sequences (Fig. 2-8), two refocusing pulses are employed to generate echoes, to optimize the phase coherence at the acquisition onset, and to limit the region of excitation in two spatial dimensions. Modeling even two dimensions of space requires a tremendous additional number of simulations beyond the hard pulse model, a factor of N_{points}^2 more if N_{points} positions in space are modeled in each spatial dimension. Because the influence of each slice is a function of the distribution of the coherences at the pulse onset, ρ_{pulse_onset}, the N_{points}^2 simulations need to be repeated for each variation of the echo times surrounding the π pulses, each variation giving rise to a unique ρ_{pulse_onset} for each of the two pulses. As was illustrated in Fig. 2-10, the existence of anti-phase coherences at the pulse onset creates the conditions necessary for slice anomalies. In order to efficiently simulate the distribution of *effective* r.f. pulse tip angles and phases experienced over space, a time-saving algorithm with direct application in the numerical simulation framework developed thus far is presented in the following section.

2.4.1.2 Shaped R.F Pulses – The Integrated Effect – The Transformation Matrix

In order to reduce the number of calculations required to model the realistic slice selective refocusing pulses, an alternate approach was developed. When the desired information is in the form of the integrated signal rather than it's spatial distribution, it is possible to model the slice selective pulse as a *black box* transfer function, transforming the input coherence to a distribution of output coherences. Such a *black box* should be a function of the r.f. pulse envelope and spin system properties (shifts and couplings), but not of the distribution of coherences (the density matrix) at the application of the transfer function, so it should be linear.

In order to derive the transfer function, consider first the general description of a density matrix at the onset of the slice selective pulse as a linear combination of basis operators,

$$\rho(0) = a_1 I_1 + a_2 I_2 + a_3 I_3 + \ldots + a_n I_n + \ldots = \sum_{n=1}^{M} a_n I_n, \qquad (2\text{-}13)$$

where $M = 2^{2N_{spins}}$. The set 'I_n' is assumed to be a complete set, which for a system of N_{spins} consists of $2^{2N_{spins}}$ components. It has been demonstrated that each point, P, in the gradient field must be simulated separately, giving rise to a final density matrix that is given by the sum of independent solutions, as shown in Eq. (2-14).

$$\rho_{total} = V_1^{-1}\rho(0)V_1 + V_2^{-1}\rho(0)V_2 + V_3^{-1}\rho(0)V_3 + \ldots V_\alpha^{-1}\rho(0)V_\alpha + \ldots = \sum_{\alpha=1}^{P} V_\alpha^{-1}\rho(0)V_\alpha \qquad (2\text{-}14)$$

Each element in the sum in this equation is equivalent to Eq. (2-6), where V_α is the evolution operator representing the evolution over the course of the entire r.f. pulse length, at a position in space ($\mathbf{r}$ in $\gamma\mathbf{G}\cdot\mathbf{r}$) indexed by α, from a total of P positions.

Each of these P terms, representing a separate density matrix, can be expanded using Eq. (2-13),

$$V_\alpha^{-1}\rho(0)V_\alpha = V_\alpha^{-1}(a_1 I_1 + a_2 I_2 + a_3 I_3 + \ldots + a_n I_n + \ldots)V_\alpha \qquad (2\text{-}15)$$

which can be rewritten

$$V_\alpha^{-1}\rho(0)V_\alpha = a_1 V_\alpha^{-1} I_1 V_\alpha + a_2 V_\alpha^{-1} I_2 V_\alpha + a_3 V_\alpha^{-1} I_3 V_\alpha + \ldots + a_n V_\alpha^{-1} I_n V_\alpha + \ldots \qquad (2\text{-}16)$$

Inserting Eq. (2-16) into Eq. (2-14), and grouping the 'a' coefficients, the density matrix following the slice selective pulse can be expressed as

$$\rho_{total} = a_1 \sum_{\alpha=1}^{P} V_\alpha^{-1} I_1 V_\alpha + a_2 \sum_{\alpha=1}^{P} V_\alpha^{-1} I_2 V_\alpha + \ldots + a_n \sum_{\alpha=1}^{P} V_\alpha^{-1} I_n V_\alpha \,. \tag{2-17}$$

Each of the sums in Eq. (2-17), if evaluated, results again in a single density matrix, which can also be expanded in terms of the basis I's, from Eq. (2-13), as

$$\sum_{\alpha=1}^{P} V_\alpha^{-1} I_m V_\alpha = \sum_{n=1}^{M} b_{nm} I_n \,. \tag{2-18}$$

Inserting Eq. (2-18) into Eq. (2-17) and grouping the coefficients of the basis I's, the contribution of each of the M terms to the total density matrix, now termed s_n, can be expressed

$$s_n = \sum_{m=1}^{M} b_{nm} a_m \,, \tag{2-19}$$

which can be expanded to reveal a series of equations, shown in Eq. (2-20).

$$\begin{aligned} s_1 &= b_{11}a_1 + b_{12}a_2 + \ldots + b_{1m}a_m \\ s_2 &= b_{21}a_1 + b_{22}a_2 + \ldots + b_{2m}a_m \\ &\vdots \\ s_n &= b_{n1}a_1 + b_{n1}a_2 + \ldots + b_{nm}a_m \end{aligned} \tag{2-20}$$

Figure 2-11 displays the matrix form of the series of equations.

Output — Transformation Matrix — Input

$$\rho_{total} = \sum_{n=1}^{M} s_n I_n \qquad \begin{pmatrix} s_1 \\ s_2 \\ \vdots \\ s_n \end{pmatrix} = \begin{pmatrix} b_{11} & b_{12} & \cdots & b_{1n} \\ b_{21} & b_{22} & & \\ \vdots & & \ddots & \\ b_{n1} & & & b_{nn} \end{pmatrix} \begin{pmatrix} a_1 \\ a_2 \\ \vdots \\ a_n \end{pmatrix} \qquad \rho(0) = \sum_{n=1}^{M} a_n I_n$$

Figure 2-11 The mathematical representation of the transformation matrix.

To determine the elements of the transformation matrix for a given pulse and spin system, the unit response to each of the input elements, a_1 to a_n, must be calculated. For example, setting $a_1 = 1$, and a_2 to $a_n = 0$, the first column of the transformation matrix is equivalent to the output 's' vector, with $b_{11} = s_1$, $b_{21} = s_2$ etc., as shown generally by Eq. (2-19). The s's are extracted from the density matrix, ρ_{total}, which is the sum (average) of the individual density matrices excited across the slice (the α locations in space), after setting $\rho(0) = a_1 I_1$.

Figure 2-10 illustrated that the slice profile must be calculated as a local average of the magnetization, due to the role of dephasing gradients in defining the slice, which was extracted by applying a local average filter to smooth the oscillations. To capture the signal cancellation arising from the dephasing, and simultaneously avoid the large number of separate simulations needed to model the rapid oscillations, a single step of phase-cycling can be incorporated to simplify the profile. This two-step subtractive procedure, shown in Fig. 2-12, is routinely applied in the actual in-vivo experiments to reduce unwanted out of slice signal contributions resulting from incomplete dephasing, and can be incorporated into the calculation of the transformation matrix without any loss of generality.

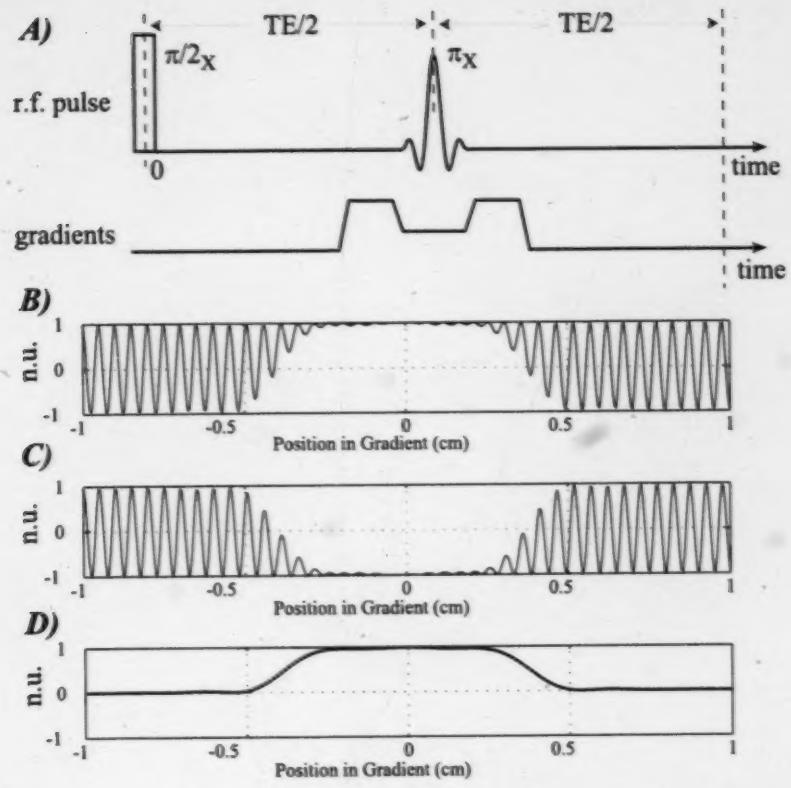

Figure 2-12 A two-step subtractive phase-cycling scheme is commonly employed for each refocusing pulse, such as the slice-selective π-pulse shown in A). The distribution of I_Y magnetization, from an uncoupled spin group, excited by the spin-echo sequence is shown in B) and C) for refocusing pulse phases of +x (0°) and +y (90°), respectively. The difference is shown in D).

The choice of basis operators in Eq. (2-13), I_n, is determined by the proposed use of the transformation matrix. For example, to compare the quality of different r.f. pulse designs, the use of the Cartesian operator basis for the calculation of the transformation matrix provides a measure of anomalous signal loss and coherence transfer in terms of the familiar I_X, I_Y and I_Z operators. Figure 2-13 provides an illustrative example for this scenario, for the AX spin system considered in Fig. 2-10, for which $\omega_1 = 0$ ppm, $\omega_2 = 3$ ppm, and $J = 10$ Hz.

Ignoring the identity matrix contribution, the coupled two-spin (spin ½) system is described by fifteen Cartesian basis product operator terms, listed below. The matrix forms of these operators are listed in Appendix II.

$$I_1 = 2I_{1X}I_{2Z},\ I_2 = 2I_{1Y}I_{2Z},\ I_3 = I_{1Y},\ I_4 = I_{1X},\ I_5 = 2I_{1Z}I_{2X},\ I_6 = 2I_{1Z}I_{2Y},\ I_7 = I_{2Y},\ I_8 = I_{2X},\ I_9 = I_{1Z},$$
$$I_{10} = I_{2Z},\ I_{11} = 2I_{1X}I_{2X},\ I_{12} = 2I_{1X}I_{2Y}\ \ I_{13} = 2I_{1Y}I_{2Y},\ I_{14} = 2I_{1Y}I_{2X},\ I_{15} = 2I_{1Z}I_{2Z} \quad (2\text{-}21)$$

The Cartesian transformation matrix shown in Fig. 2-13 was calculated for a 3 ms optimized sinc-like refocusing pulse (bandwidth*length = 4.19). A single step of phase cycling, illustrated in Fig. 2-12, was incorporated into the calculation. The r.f. pulse envelope is segmented into 250 rectangular components, and 201 locations in space (in the gradient field) are modeled for the each of the fifteen input coherence terms.

$$\begin{pmatrix} s_1 \\ s_2 \\ s_3 \\ s_4 \\ s_5 \\ s_6 \\ s_7 \\ s_8 \\ s_9 \\ s_{10} \\ s_{11} \\ s_{12} \\ s_{13} \\ s_{14} \\ s_{15} \end{pmatrix} = \begin{pmatrix} 42 & -1 & 7 & 0 & 2 & 5 & 1 & 4 & 0 & 0 & 0 & 0 & 0 & 0 & 0 \\ -1 & -42 & 0 & 7 & 5 & -2 & -4 & 1 & 0 & 0 & 0 & 0 & 0 & 0 & 0 \\ -7 & 0 & 99 & 0 & -1 & 4 & 0 & 0 & 0 & 0 & 0 & 0 & 0 & 0 & 0 \\ 0 & -7 & 0 & -99 & -4 & -1 & 0 & 0 & 0 & 0 & 0 & 0 & 0 & 0 & 0 \\ 2 & -5 & 1 & -4 & 42 & 0 & 7 & 0 & 0 & 0 & 0 & 0 & 0 & 0 & 0 \\ -5 & -2 & 4 & 1 & 1 & -42 & 0 & 7 & 0 & 0 & 0 & 0 & 0 & 0 & 0 \\ -1 & -4 & 0 & 0 & -7 & 0 & 99 & 0 & 0 & 0 & 0 & 0 & 0 & 0 & 0 \\ 4 & -4 & 0 & 0 & 0 & -7 & 0 & -99 & 0 & 0 & 0 & 0 & 0 & 0 & 0 \\ 0 & 0 & 0 & 0 & 0 & 0 & 0 & 0 & 0 & 0 & 0 & 0 & 0 & 0 & 0 \\ 0 & 0 & 0 & 0 & 0 & 0 & 0 & 0 & 0 & 0 & 0 & 0 & 0 & 0 & 0 \\ 0 & 0 & 0 & 0 & 0 & 0 & 0 & 0 & 0 & 0 & 0 & 0 & 0 & 0 & 0 \\ 0 & 0 & 0 & 0 & 0 & 0 & 0 & 0 & 0 & 0 & 0 & 0 & 0 & 0 & 0 \\ 0 & 0 & 0 & 0 & 0 & 0 & 0 & 0 & 0 & 0 & 0 & 0 & 0 & 0 & 0 \\ 0 & 0 & 0 & 0 & 0 & 0 & 0 & 0 & 0 & 0 & 0 & 0 & 0 & 0 & 0 \\ 0 & 0 & 0 & 0 & 0 & 0 & 0 & 0 & 0 & 0 & 0 & 0 & 0 & 0 & 0 \end{pmatrix} \begin{pmatrix} a_1 \\ a_2 \\ a_3 \\ a_4 \\ a_5 \\ a_6 \\ a_7 \\ a_8 \\ a_9 \\ a_{10} \\ a_{11} \\ a_{12} \\ a_{13} \\ a_{14} \\ a_{15} \end{pmatrix}$$

Figure 2-13 A Cartesian product operator transformation matrix for a two-spin system, J = 10 Hz, ω_1 = 0 ppm, ω_2 = 3 ppm, and a 3 ms optimized sinc-like refocusing pulse.

What is immediately clear from this matrix is that the in-phase coherences, terms 3, 4, 7 and 8, are virtually unchanged by this refocusing pulse, returning over 99% of the input magnetization to the same term (All values are normalized to the uncoupled single spin response). On the other hand, the anti-phase coherences, terms 1, 2, 5, and 6, experience a drastic reduction in intensity, to only 42% if the input term. This loss in signal is treated in detail in Chapter 5, *A Demonstration of the Sources of Variability in the Response of Coupled Spins to the PRESS Sequence and their Potential Impact on*

Metabolite Quantification. Terms 9 to 15 are the longitudinal and remaining two-term coherences, representing the DQCs, ZQCs and longitudinal Z order term. The two-step phase cycling incorporated tends to cancel out the contributions from these terms, although, in general, higher odd order coherences (such as TQC) will not be average out. The circled elements from Fig. 2-13 represent coherence transfer from $spin_1$ to $spin_2$, which for this optimized pulse are not significant. The transfer is a consequence of sub-180° tip angles from the spectral roll-off region of the slices (see Fig. 2-9) (11-16).

As an illustrative example, the transformation matrix for a poor quality refocusing pulse, a 2 ms Gaussian pulse with the same bandwidth as the optimized pulse just considered (1400 Hz), but a much more gradual slice roll-off, is calculated, shown in Fig. 2-14.

$$\begin{pmatrix} s_1 \\ s_2 \\ s_3 \\ s_4 \\ s_5 \\ s_6 \\ s_7 \\ s_8 \\ s_9 \\ s_{10} \\ s_{11} \\ s_{12} \\ s_{13} \\ s_{14} \\ s_{15} \end{pmatrix} = \begin{pmatrix} 24 & -3 & 5 & -1 & 21 & -36 & 0 & 4 & 0 & 0 & 0 & 0 & 0 & 0 & 0 \\ -3 & -24 & 1 & 5 & -36 & -21 & -4 & 0 & 0 & 0 & 0 & 0 & 0 & 0 & 0 \\ -5 & 1 & 99 & 0 & 0 & 4 & 0 & 0 & 0 & 0 & 0 & 0 & 0 & 0 & 0 \\ -1 & -5 & 0 & -99 & -4 & 0 & 0 & 0 & 0 & 0 & 0 & 0 & 0 & 0 & 0 \\ 21 & 36 & 0 & -4 & 24 & 3 & 5 & 1 & 0 & 0 & 0 & 0 & 0 & 0 & 0 \\ 36 & -21 & 4 & 0 & 3 & -24 & -1 & 5 & 0 & 0 & 0 & 0 & 0 & 0 & 0 \\ 0 & -4 & 0 & 0 & -5 & -1 & 99 & 0 & 0 & 0 & 0 & 0 & 0 & 0 & 0 \\ 4 & 0 & 0 & 0 & 1 & -5 & 0 & -99 & 0 & 0 & 0 & 0 & 0 & 0 & 0 \\ 0 & 0 & 0 & 0 & 0 & 0 & 0 & 0 & 0 & 0 & 0 & 0 & 0 & 0 & 0 \\ 0 & 0 & 0 & 0 & 0 & 0 & 0 & 0 & 0 & 0 & 0 & 0 & 0 & 0 & 0 \\ 0 & 0 & 0 & 0 & 0 & 0 & 0 & 0 & 0 & 0 & 0 & 0 & 0 & 0 & 0 \\ 0 & 0 & 0 & 0 & 0 & 0 & 0 & 0 & 0 & 0 & 0 & 0 & 0 & 0 & 0 \\ 0 & 0 & 0 & 0 & 0 & 0 & 0 & 0 & 0 & 0 & 0 & 0 & 0 & 0 & 0 \\ 0 & 0 & 0 & 0 & 0 & 0 & 0 & 0 & 0 & 0 & 0 & 0 & 0 & 0 & 0 \\ 0 & 0 & 0 & 0 & 0 & 0 & 0 & 0 & 0 & 0 & 0 & 0 & 0 & 0 & 0 \end{pmatrix} \begin{pmatrix} a_1 \\ a_2 \\ a_3 \\ a_4 \\ a_5 \\ a_6 \\ a_7 \\ a_8 \\ a_9 \\ a_{10} \\ a_{11} \\ a_{12} \\ a_{13} \\ a_{14} \\ a_{15} \end{pmatrix}$$

Figure 2-14 A Cartesian product operator transformation matrix for a two-spin system, $J = 10$ Hz, $\omega_1 = 0$ ppm, $\omega_2 = 3$ ppm, and a 2 ms Gaussian refocusing pulse.

Like the higher quality optimized sinc pulse, the Gaussian pulse returns over 99% of the in-phase coherences, of course with a Gaussian distribution of excitation across the slice. The poor quality of the pulse is reflected by the increased loss of signal for the input anti-phase coherences, terms 1, 2, 5, and 6, as well as by the significant coherence transfers, for example, from $spin_1$ to $spin_2$, indicated by the circled elements.

If the transformation matrix is being used purely as a time saving numerical tool, a basis set whose components consist of individual density matrix elements, shown in Eq. (2-22), will be shown to have the optimal utility.

$$I_1 = \begin{pmatrix} 0 & 1 & 0 & 0 \\ 0 & 0 & 0 & 0 \\ 0 & 0 & 0 & 0 \\ 0 & 0 & 0 & 0 \end{pmatrix}, \quad I_2 = \begin{pmatrix} 0 & 0 & 1 & 0 \\ 0 & 0 & 0 & 0 \\ 0 & 0 & 0 & 0 \\ 0 & 0 & 0 & 0 \end{pmatrix}, \quad I_3 = \begin{pmatrix} 0 & 0 & 0 & 1 \\ 0 & 0 & 0 & 0 \\ 0 & 0 & 0 & 0 \\ 0 & 0 & 0 & 0 \end{pmatrix}$$

$$I_4 = \begin{pmatrix} 0 & 0 & 0 & 0 \\ 0 & 0 & 1 & 0 \\ 0 & 0 & 0 & 0 \\ 0 & 0 & 0 & 0 \end{pmatrix}, \quad I_5 = \begin{pmatrix} 0 & 0 & 0 & 0 \\ 0 & 0 & 0 & 1 \\ 0 & 0 & 0 & 0 \\ 0 & 0 & 0 & 0 \end{pmatrix}, \quad I_6 = \begin{pmatrix} 0 & 0 & 0 & 0 \\ 0 & 0 & 0 & 0 \\ 0 & 0 & 0 & 1 \\ 0 & 0 & 0 & 0 \end{pmatrix} \qquad (2\text{-}22)$$

Figure 2-15 displays a transformation matrix calculated for the basis set shown in Eq. (2-22), for the same two-spin system treated in previous examples, and the optimized sinc refocusing pulse.

$$\begin{pmatrix} s_1 \\ s_2 \\ s_3 \\ s_4 \\ s_5 \\ s_6 \end{pmatrix} = \begin{pmatrix} -29-1i & 1+3i & 0 & 0 & -5-4i & -71-6i \\ 1-2i & -29+1i & 0 & 0 & -71-8i & 3+2i \\ 0 & 0 & 0 & 0 & 0 & 0 \\ 0 & 0 & 0 & 0 & 0 & 0 \\ -5+4i & -71+6i & 0 & 0 & -29+1i & 1-3i \\ -71+8i & 3-2i & 0 & 0 & 1+2i & -29-1i \end{pmatrix} \begin{pmatrix} a_1 \\ a_2 \\ a_3 \\ a_4 \\ a_5 \\ a_6 \end{pmatrix}$$

Figure 2-15 A single element basis set transformation matrix for a two-spin system, J = 10 Hz, $\omega_1 = 0$ ppm, $\omega_2 = 3$ ppm, and a 3 ms optimized sinc-like refocusing pulse.

Figure 2-16 displays a transformation matrix calculated for the basis set shown in Eq. (2-22), for the same two-spin system treated in previous examples, and the 2 ms Gaussian pulse.

$$\begin{pmatrix} s_1 \\ s_2 \\ s_3 \\ s_4 \\ s_5 \\ s_6 \end{pmatrix} = \begin{pmatrix} -37-1i & 11+18i & 0 & 0 & -15-18i & -62+6i \\ 11-18i & -39+2i & 0 & 0 & -62+3i & -7+17i \\ 0 & 0 & 0 & 0 & 0 & 0 \\ 0 & 0 & 0 & 0 & 0 & 0 \\ -15+18i & -62-6i & 0 & 0 & -37+1i & 11-18i \\ -62-3i & -7-17i & 0 & 0 & 11+18i & -38-1i \end{pmatrix} \begin{pmatrix} a_1 \\ a_2 \\ a_3 \\ a_4 \\ a_5 \\ a_6 \end{pmatrix}$$

Figure 2-16 A single element basis set transformation matrix for a two-spin system, J = 10 Hz, $\omega_1 = 0$ ppm, $\omega_2 = 3$ ppm, and a 2 ms Gaussian refocusing pulse.

The advantage of the single element basis matrices over the Cartesian set is both a saving of time, due to the reduction in the number of terms, as well as the ease of the calculation of the basis weightings, the a's and s's, from the density matrix. For the Cartesian set, each a and s must be calculated as an expectation value, $a_1 = Tr(\rho I_1)$, requiring a matrix multiplication and a sum, while they can be extracted directly from the density matrix when using the single element basis, $a_1 = \rho(1,2)$, $a_2 = \rho(1,3)$, ... etc. The density matrix following the application of the transformation matrix can be re-formed from the s-vector using the same protocol, $\rho(1,2) = s_1$, $\rho(1,3) = s_2$, ... etc. The lower diagonal elements are the complex conjugates of their Hermitian partner in the upper triangular region, $\rho(2,1) = s_1^*$, $\rho(3,1) = s_2^*$, ... etc.

Table 2-1 compares the simulation times required using the transformation matrix method versus the direct calculation method. The spin system considered is the three-spin ABX aspartyl group of NAA, whose response to the PRESS pulse sequence (Fig. 2-8B) is calculated. Two dimensions of spatial localization are simulated, excited by the two refocusing 180° optimized sinc pulses, the same pulse considered in Fig. 2-13 and Fig. 2-15, applied with orthogonal gradients. The spatial localization is modeled with 201 points across the slice in each dimension.

Table 2-1 The Transformation Matrix Efficiency – The ABX Spin-System

	Transformation Matrix	Direct Calculation
Overhead (Trans. Matrix Calculation)	60 secs	None
Simulation time per PRESS timing (one set of TE_1 and TE_2)	0.03 secs	77 secs
Simulation time per N PRESS timings	(60 + 0.03*N) secs	77*N secs

From Table 2-1, to calculate the response of the NAA ABX spin group to the PRESS sequence for 100 values of both of TE_1 and TE_2, the Transformation Matrix method will require 60 + 10,000*0.03 = 360 seconds[1]. To generate an identical result, the direct calculation approach would require 770,000 seconds = 8.9 days[1], about 2000 times longer.

[1]Pentium II 400 MHz PC running MATLAB 5

As a verification of the transformation matrix approach, consider the calculation of a single illustrative NAA spectrum (ABX group), for a single PRESS (TE_1, TE_2) combination, using both the direct calculation method and the transformation matrix approach. The direct calculation incorporated 201 locations in space for each of the two refocusing pulses, requiring over 40,401 separate PRESS simulations to model the two dimensions of localization. The 40,401 resulting spectra are summed and normalized to the volume of interest excited to model the total signal as acquired in practical single voxel experiments. The transformation matrix approach incorporates the spatial integration into the matrix itself, so requires only a single PRESS simulation. Note that the same transformation matrix can be applied twice in the same sequence if the slice selective gradients are orthogonal, which is always the case for the single voxel PRESS sequence. The single element basis set, exemplified in Eq. (2-22) and Figs. 2-15 and 2-16, is employed in this example. Both approaches utilized the 3 ms (1400 Hz bandwidth) optimized sinc-like refocusing pulse previously considered. Figures 2-17A) and B) display the NAA ABX spectra calculated for PRESS timings (TE_1, TE_2) = (112 ms, 24 ms) using the direct and transformation matrix methods, respectively.

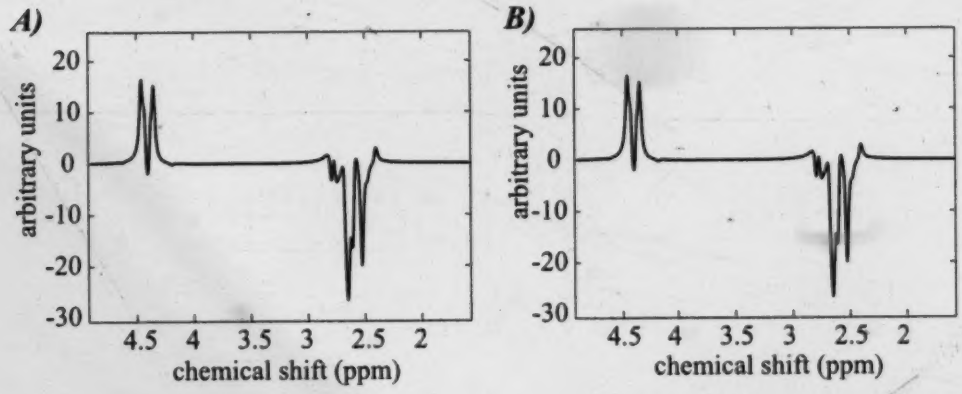

Figure 2-17 Calculated PRESS (112 ms, 24 ms) NAA ABX spectra (4 Hz line-broadening), with two dimensions of spatial localization provided by the refocusing pulses, calculated using A) direct methods and B) the transformation matrix approach. The spectra are identical to 1 part in 10^6.

The influence of the realistic slice selective pulses, as indicated in Fig. 2-13 for a weakly-coupled two-spin system, is primarily a loss of signal, exacerbated by the

existence of anti-phase coherence at the pulse onset. For the particular PRESS timings modeled (112 ms, 24 ms), the loss of signal induced by the slices is significant, as shown by a comparison of Figs. 2-17 and Fig. 2-18, where the response of the NAA ABX group to the equivalent hard-pulse sequence is displayed in the later. The full slice-selective model produced only 37% of the peak AB multiplet intensity excited with the hard-pulse model, although with only a small change in the line-shape. A pulse of poorer quality (a more gradual roll-off), such as the Gaussian pulse treated in Fig. 2-14, will result in significant coherence transfer and thus produce a change in line-shape as well as a reduction of peak intensity. Figure 2-19 displays the response of the NAA ABX group to the PRESS sequence including the 2 ms 1400 Hz bandwidth Gaussian pulse. For this low quality pulse, the peak intensity of the NAA AB multiplet is reduced to less than 10% of hard-pulse yield. In Chapter 4, *The Role of the N-actylaspartate Multiplet in the Quantification of Brain Metabolites*, the complete response of the N-actylaspartate AB multiplet to the PRESS sequence is calculated.

As illustrated in Table 2-1, the utility of the transformation matrix

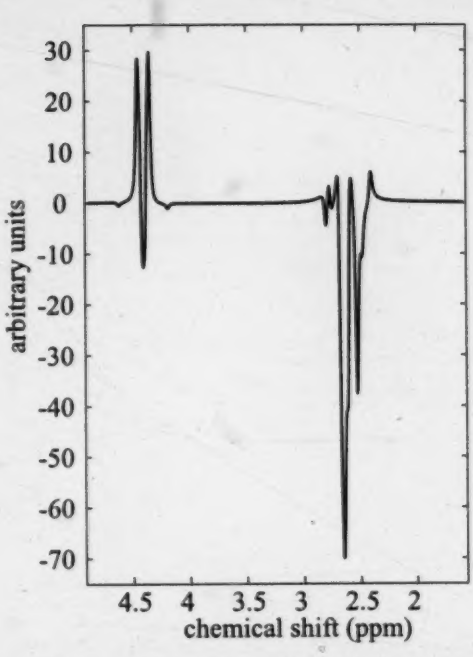

Figure 2-18 Calculated hard-pulse PRESS (112 ms, 24 ms) NAA ABX spectra (4 Hz line-broadening).

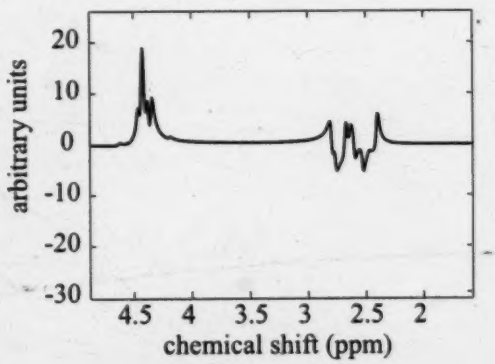

Figure 2-19 Calculated PRESS (112 ms, 24 ms) NAA ABX spectra (4 Hz line-broadening), incorporating 2 ms, 1400 Hz bandwidth Gaussian refocusing pulses.

approach lies in it's efficiency, allowing multiple sequence parameters to be varied even for pulse sequences incorporating multiple dimensions of spatial localization, as is the case with single-voxel techniques.

Generally speaking, the slice anomalies are exacerbated by an increase in main field strength, via two separate mechanisms. Firstly, the increase in the chemical shift difference, associated with the rise in field strength, results in an increase in the relative voxel shifts, for a given pulse bandwidth. Recall that the voxel shift is the primary source of the reduction of the diagonal elements of the transformation matrix, from Figs. 2-13 and 2-14. Secondly, the increased power deposition at higher frequencies reduces the B_1 amplitude generated with a given driving current (17). The result is either a reduction in the maximum pulse bandwidth (lower intensity results in longer pulses), as compared with lower field strengths, or a reduction in pulse quality (increase in roll-off) to retain the bandwidth (pulse quality $\propto$ bandwidth x length). For these reasons, the influence of realistic slice-selective pulses will probably be increasingly significant in the future, given the persistent demands for increasing field strengths to increase signal to noise and improve spectral discrimination.

Section 2.5 briefly outlines the general approaches employed in the remaining chapters for characterization and optimization of the coupled spin response to the PRESS, STEAM and MQF sequences.

2.5 Pulse Sequence Optimization

Figure 2-3 displays the evolution operator storage matrix utilized in all numerical simulations in this thesis. Section 2.2 describes how the variation in any sequence parameter, such as an inter-pulse delay or position in a gradient, is equivalent to a variation in the Hamiltonian, represented mathematically by multiple evolution operators. To characterize or optimize the response of a given spin system to a pulse sequence the density matrix following the sequence, for multiple values of the sequence parameters of interest, most commonly delay times, is calculated using the evolution operator storage matrix as the primary tool. The resulting density matrices are evaluated to form vectors or matrices of a desired result, be that the expectation value of an operator or the ultimate transverse magnetization. For example, consider the response of an ABC spin system to the PRESS sequence, assuming ideal hard pulses. Figure 2-20 displays the pulse acquire spectrum for this fictitious spin system (ω_A = 1 ppm, ω_B = 1.2 ppm and ω_C = 1.25 ppm, with J_{AB} = 20 Hz, J_{AC} = 12 Hz and J_{BC} = 15 Hz, for a field strength of 3 T).

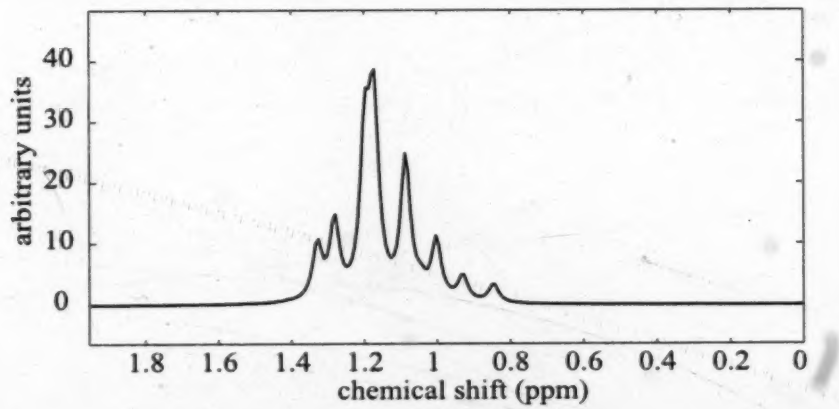

Figure 2-20 A pulse acquire spectrum from an ABC spin system (ω_A = 1 ppm, ω_B = 1.2 ppm and ω_C = 1.25 ppm, with J_{AB} = 20 Hz, J_{AC} = 12 Hz and J_{BC} = 15 Hz), at a field strength of 3 T. A 4 Hz exponential line-broadening was applied.

Consider now the response of this system to the PRESS pulse sequence (Fig. 2-8B) assuming ideal hard pulses. The PRESS sequence comprises two echoes, both of which influence the density matrix at the acquisition onset if the coupling is not weak. To characterize the response of the ABC system to the PRESS sequence, the resulting spectrum (FID) is calculated for multiple values of both TE_1 and TE_2, the PRESS echo

times. Figure 2-21 displays a filled contour plot that illustrates the peak value of the ABC multiplet as a function of these two timings. The PRESS sequence was simulated for echo times ranging from 0 ms to 120 ms, in 2 ms steps for both echo times, requiring a total of 3,721 separate simulations. The total simulation time was only ~ 9 seconds[1] to calculate the 3,721 density matrices, including the 3,721 FIDs. Because the density matrix is calculated for each timing pair, any property of the spin system can be plotted as was the peak value of the spectrum, including any of the spin operator terms, or even the amplitude or phase of any of the individual spectral lines.

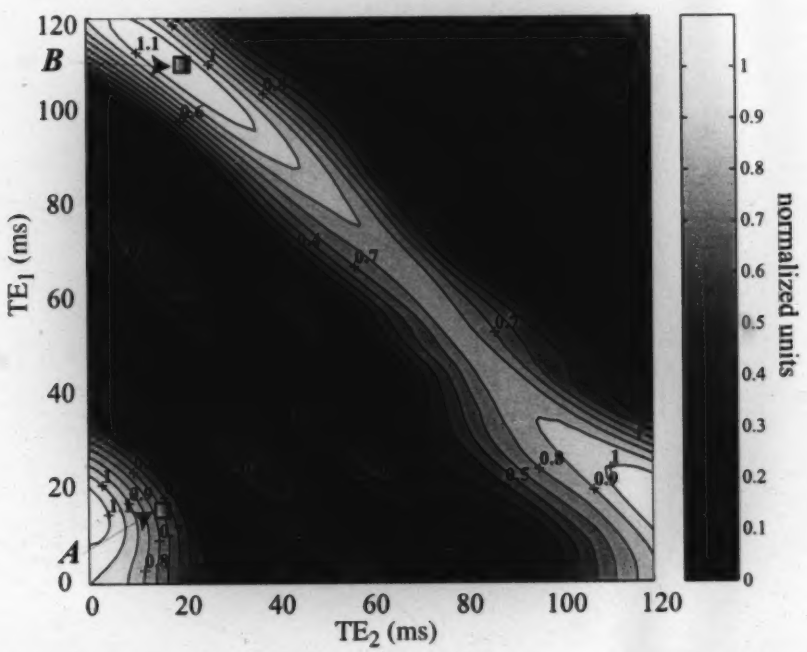

Figure 2-21 A filled contour plot displays the peak value of an ABC spin system as a function of the PRESS timings (TE_1, TE_2), normalized to the peak value of the pulse acquire spectrum, shown in Fig 2-20. Individual spectra a timings indicated by ***A*** and ***B*** as displayed in Fig. 2-22.

Two of the 3,721calculated spectra used to generate the contour are displayed in Fig. 2-22, for PRESS timings (16 ms, 16 ms), a poor choice of timings, and for (110 ms. 20 ms) a favorable set of timings.

[1]Pentium II 400 MHz PC running MATLAB 5

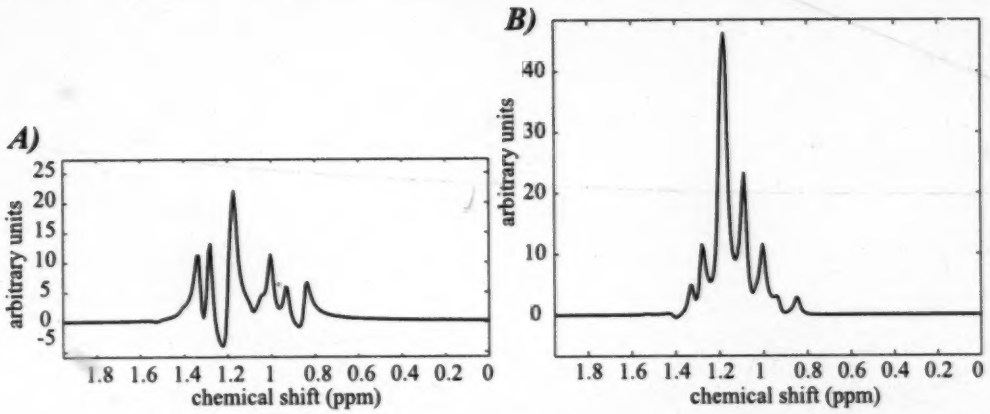

Figure 2-22 Calculated ABC PRESS spectra for timings A) (16 ms, 16 ms) and B) (110 ms, 20 ms). The spectrum in B) is ~ 110% of the peak amplitude of the pulse acquire spectrum from Fig. 2-20.

The transformation matrix methodology, outlined in section 2.4.1.2, can be applied to the previous calculations to incorporate the influence of realistic slice selective pulses into the PRESS sequence.

The numerical methodology outlined in chapters 1 and 2 is implemented in the following chapters, to optimize the response of several of the coupled-spin groups found in vivo to the STEAM, PRESS and DQF sequences. While the spin-systems considered in detail are a small sampling of the collection found in the human brain, the simulation software (see Appendix V) is general and can be applied to any target spin group of up to six spins.

2.6 References

1. S. A. Smith, T. O. Levante, B. H. Meier, R. R. Ernst, Computer simulations magnetic resonance. An object-oriented programming approach. *J. Magn. Reson.*, A **106**, 75-105 (1994).
2. T. Allman, A. D. Bain and J. R. Garbow, SIMPLTN, a program for the simulation of pulse NMR spectra, *J.Magn Reson.* **A 123**, 26-31 (1996).
3. H. Geen, S. Wimperis and R. Freeman, Band-selective pulses without phase distortion. A simulated annealing approach. *J. Magn. Reson.* **85**, 620 (1990).
4. G. B. Matson, An integrated program for amplitude-modulated RF pulse generation and re-mapping with shaped gradients, *Magn. Reson. Imag.*, **12**, 1205-25, (1994).
5. S. Conolly, J. Pauly, D. Nishimura and A. Macovski, Two-dimensional selective adiabatic pulses, *Magn. Reson. Med.* **24**, 302-13 (1992).
6. L. N. Ryner, Y. Ke, and M. A. Thomas. Flip angle effects in STEAM and PRESS-optimized versus sinc RF pulses. *J. Magn. Reson.* **131**, 118-125, (1998).
7. J. Slotboom, J. H. Creyghton,D. Korbee,A. F. Mehlkopf and W. M. Bovee, Spatially selective RF pulses and the effects of digitization on their performance. *Magn. Reson. Med.* **30**, 732-40 (1993).
8. J. Shen and D. L. Rothman, Adiabatic slice-selective excitation for surface coils. *J. Magn. Reson.* **124**, 72-9 (1997).
9. P. Sodano, C. Landon, M. Ptak, A novel composite 90 degrees pulse sequence which provides distortionless NMR spectra and suppresses without destroying the water magnetization. *J. Magn. Reson.* **133**, 194-9 (1998).
10. D. Rosenfeld, S. L. Panfil and Y. Zur, Design of selective adiabatic inversion pulses using the adiabatic condition. *J. Magn. Reson.*, **129**, 115-24 (1997).
11. W-I. Jung, and O. Lutz, Localized double-spin-echo proton spectroscopy of weakly coupled homonuclear spin systems. *J. Magn. Reson.* **96**, 237-251 (1992).
12. J. Slotboom, A. F. Mehlkopf and W. M. M. J. Bovee, The effects of frequency-selective RF pulses on J-coupled spin-1/2 systems. *J. Magn. Reson.* A **108**, 38-50 (1994).
13. F. Schick, T. Nagele, U. Klose and O. Lutz, Lactate quantification by means of PRESS spectroscopy influence of refocusing pulses and timing scheme. *Magn. Reson. Imag.* **13**, 309-319 (1995).
14. M. Bunse, W-I. Jung, O. Lutz, K. Kuper, and G. Dietze, Polarization-transfer effects in localized double-spin-echo spectroscopy of weakly coupled homonuclear spin systems. *J. Magn. Reson.* A **114**, 230-237 (1995).
15. I. Marshall and J. Wild, Calculations and experimental studies of the lineshape of the lactate doublet in PRESS-localized ^{1}H MRS. *Magn. Reson. Med.* **38**, 415-419 (1997).

16. I. Marshall and J. Wild, A systematic study of the lactate lineshape in PRESS-localized proton spectroscopy. *Magn. Reson. Med.* 40, 72-78 (1998).

17. P. M. Robitaille, A. M. Abduljalil, A. Kangarlu, X. Zhang,Y. Yu, R. Burgess, S. Bair, P. Noa, L. Yang ,H. Zhu, B. Palmer, Z. Jiang,D. M. Chakeres and D. Spigos, Human magnetic resonance imaging at 8 T. *NMR Biomed.* 11, 263-5 (1998).

CHAPTER 3

A New Multiple Quantum Filter Design Procedure for Use on Strongly Coupled Spin Systems Found In Vivo: Its Application to Glutamate[1]

3.1 Introduction

Although the observation of the uncoupled methyl singlets of choline (Cho), creatine (Cr) and N-acetyl-aspartate (NAA) has provided a significant impetus to the use of in-vivo proton spectroscopy for detecting biochemical abnormalities in brain (1), further substantial progress requires the ability to observe and quantify at will, several metabolites with coupled spins, most notably the amino acids (2-6). To quantify these metabolites one must be able to deal with their having similar chemical structures (and therefore similar chemical shift distributions); with a scalar coupling between their spins (and therefore multiplets that can overlap when several similar chemical structures are present together); with spin systems of five and six spins that are not always weakly coupled; and sometimes with signal intensities relative to background resonances and noise that approach unity. Methods for dealing with these issues seem to fall into four broad categories, namely, spectral modeling (7), spectral editing (2,6,8), 2D spectroscopy (9), and increasing the field strength (3,5). In this paper we present a spectral editing procedure, based on multiple quantum coherence (MQC) filtering, designed to accommodate the more challenging of the amino-acid-specific editing problems, including that of glutamate (Glu) and glutamine (Gln) (collectively referred to as Glx).

The procedure described below uses numerical methods in the design and optimization of the MQC filter sequence. Although in the past we have used the analytical approach of product operator calculations to evaluate filter performance (for example, for weakly coupled systems such as lactate (10) and γ-aminobutyric acid (GABA) (8), as well as in strongly coupled systems with a very limited number of spins (11,12) such as citrate and the aspartate group), the need to accommodate both

---

[1] A version of this chapter was published. R.B. Thompson and P.S. Allen, *Magn. Reson. Med.*, **39**, 762-771 (1998).

strong coupling and an increasing number of spins necessitated the combination of an analytical understanding with a numerical optimization to approach a solution to this problem. The sequence design procedure concurrently incorporates into a composite sequence the functions of spatial localization and coherence manipulation (13-15), optimises sequence timings in relation to the overall spin system and eliminates the solvent-dipolar-magnetization signals from water in brain (16-18). No weak coupling approximations were made. In the filter design procedure both Glu and Gln were treated as AMNPQ spin systems reflecting their strong scalar couplings at 3 T. The proton designated A is that bonded to the C2 carbon of Glx and the MN and PQ designations refer to the methylene protons that are bonded respectively to carbons C4 and C3. Strong coupling calculations were also included for the background signals from the AB multiplet of the ABX spin system of the aspartate groups of aspartic acid (Asp) and NAA. Moreover, when a full calculation of the GABA background was evaluated quite minor, but nevertheless quantifiable, deviations from the weak coupling limit were also found. These deviations will be more pronounced at 1.5 T. The efficacy of the resulting design procedure is demonstrated at 3 T, first, by the response of aqueous solution phantoms to the Glu filter, and secondly by the response of the human brain. A preliminary account of this work has been previously presented (19).

3.2 Composite Double Quantum Filter Design

A diagram illustrating the MQC filter sequence is shown in Fig. 1. At issue in the design of a composite sequence to target a single metabolite and incorporate spatial localization and coherence manipulation concurrently, are the design of the pulses and the optimization of the timings between them. These issues affect primarily the metabolite specificity but to a lesser extent the spatial resolution. Below they are discussed separately.

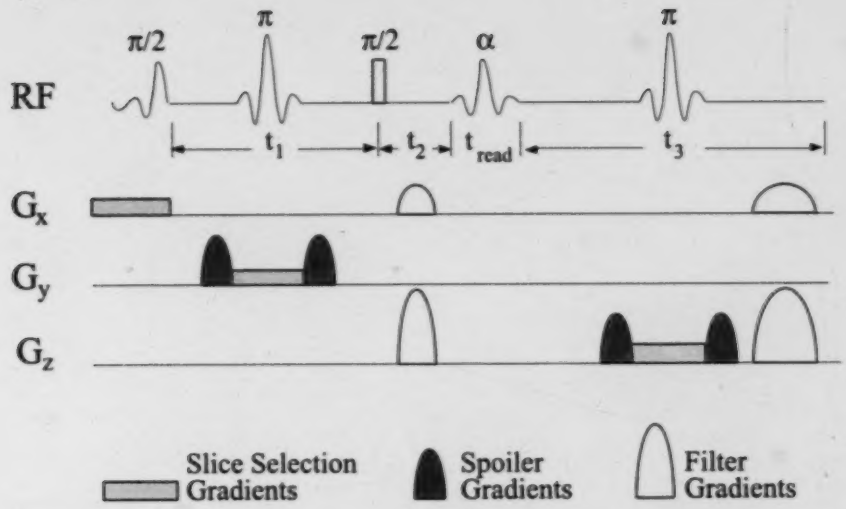

Figure 3-1 A schematic diagram of the double quantum filter pulse sequence localized for a single voxel. The $\pi/2$ excitation pulse was a 4ms BURP pulse (23); the π refocussing pulses were 4msec sinc pulses, modified to fine tune the slice profile; the $\pi/2$ double quantum generating pulse was a 250 μs rectangular pulse and the final $\pi/2$ "read" pulse was a 5 ms two-lobe sinc gaussian. The spoiler gradients were 2 ms long and 20 mTm^{-1} maximum amplitude, whereas the filter gradients, oriented at the 'magic angle', were 2 ms and 4 ms in length, also with a strength of 20 mTm^{-1}.

3.2.1 The Pulses

The incorporation of spatial selectivity into one or more of the pulses of an in-vivo editing acquisition sequence was originally explored several years ago (20,21), but has only recently begun to show more promise as both the conflicting demands of localization and coherence manipulation, as well as the consequences of strong scalar couplings have become better understood. Between the earliest and the most recent (6) reports of editing sequences, in addition to hard pulses, gaussian, sinc or even binomial 90° and 180° pulses have been employed in MQC filters, often in conjunction with gradients to fulfill both the filtering and localizing roles. However, as demonstrated by Slotboom et. al. (22), the presence of a chemical shift distribution and of the scalar coupling interaction complicates the response of the nuclear spin system to soft pulses (particularly if the scalar coupling is strong) and renders soft pulses specifically designed for the imaging of uncoupled water protons not always the most appropriate for localized

spectral editing. For example, for an initial spatially selective excitation pulse, chemical shift dephasing as well as gradient dephasing needs to be removed if one is to begin the preparation period (t_1 in Fig. 1) with spins that are all in phase. This can be done using self-refocussing pulses (13,19,22,23), although several authors (6,14,15) have chosen to relax this condition and use *sinc-like* excitation pulses together with the incorporation of a phase correction later in the sequence. The self-refocussing methodology of Geen and Freeman (23) was adopted here because of the need to control the post-pulse phase distribution of terms in the density operator. It took account of evolutions under gradient, chemical shift and the slice positioning frequency offsets. Soft 90° pulses later in the sequence can, if sufficient care is not taken, also give rise to unwanted distributions of coherence at the end of the pulses. The coherence distributions can be quite different from those which would have been produced by the very short, rectangular pulses of the same tip angles which are usually assumed in product operator analyses.

At least three of the five pulses normally used in a single voxel DQC filter must be made spatially selective. The most appropriate, because of their null role in transferring coherences, are the 90° excitation pulse and the two 180° pulses used to refocus chemical shift and field inhomogeneity dispersions (13-15). The remaining 90° pulses, namely, the producer of multiple quantum coherence (second 90° pulse) and the read pulse (third 90° pulse) can then be designed to satisfy filtering considerations alone. The 90° excitation pulse, which is required to produce in-phase transverse magnetization for a range of multiplet resonance frequencies, was provided by a *BURP* self-refocussing pulse (23). If, within the excitation slice, the spins are not all in phase at the beginning of the preparation period, t_1, the transfer of coherences later in the sequence will be compromised. Because 180° *sinc* pulses are self-refocussing, the refocussing of chemical shift dephasing and field inhomogeneities in the time periods t_1 and t_3 was carried out using spatially selective, modified *sinc* pulses. To minimize the mixing of coherences during the second 90° pulse (and hence modification of the filtered lineshape or yield) a rectangular shaped (250 μs) wideband (full width half height = 37.5 ppm) pulse was used. The importance of a short pulse for producing the desired combination of MQC at the beginning of the period, t_2, accentuates with increasing strength of B_o, because of the increase in chemical shift difference between the MN and PQ spins of Glx, and to a lesser extent on the strong coupling regime of the scalar coupling. For the read pulse a

spectrally selective *sinc* pulse was used, whose tip angle and ability to promote the mixing of coherences during the pulse were used to advantage (as described below) to tailor the filtered lineshape.

3.2.1 The Timings

Manipulation of both the preparation interval, t_1, between the first two 90° pulses, and the signal acquisition delay, t_3, can have a significant effect on the filter throughput (inherent yield and relaxation loss) as well as on the signal lineshape. For example, in systems more complex than the AX spin system, adjustment of t_1 from the conventional *1/2J* (usually a reduction) may not only increase the productions of DQC and hence the inherent filter yield, but it can also reduce the length of the filter and hence reduce the transverse relaxation losses (24,8,25). Furthermore, as demonstrated for GABA (8), waiving the demand for a fully in-phase output multiplet and accepting antiphase multiplets (where adjacent peak cancellation is not a problem) enables one to reduce t_3 and therefore reduce even further the transverse relaxation loss, thereby optimizing the output signal strength. The timing calculations for t_1 and t_3 made in references (24,8,25) were carried out for spin systems assumed to be weakly coupled (including Glu in reference 25) and excited by hard rectangular pulses. Although these calculations may well provide a good starting approximation for localized filter design in the weak coupling limit, when the coupling deviates from that limit, as in the Glx cases, and when coherence evolution begins to take place during soft pulses, numerical optimization becomes the only practical method for providing the framework within which pulse shapes can be optimized, the sequence timings can be chosen and the output lineshapes evaluated. In the present case, as is described below, contour plots of a performance index or figure of merit, ξ, were produced numerically as a function of the critical sequence parameters, in order to provide the means to optimize the filter sequence.

3.2.3 The Procedure

The starting points for the numerical optimization of the Glu filter sequence were as follows. First, the conventional MQC filter of three 90° pulses, but incorporating two 180° pulses to refocus chemical shielding and field inhomogeneity dispersions, was

assumed. Secondly, the chemical shift and *J*-coupling data of the metabolite in question, be it the target or the background, were incorporated into the mathematical model (see below). For the AMNPQ spin systems of Glx these are given in Table 3-1, where the experimental values derived in this laboratory (27) were acquired from 500 MHz spectra of either Glu or Gln in D_2O solution (pH ~ 7.2), again using the full coupling calculation to model each 500 MHz spectrum. Similar independent measurements of Glx couplings have been reported recently by Govindaraju et. al. (28).

Table 3-1 Chemical Shifts, δ ppm, and Scalar Couplings, J Hz, for the AMNPQ Spin Systems of Glu and Gln.

Chemical Shift		δ_A	δ_M	δ_N	δ_P	δ_Q
Metabolite						
Glu	(27)	3.75	2.13	2.05	2.36	2.34
Glu	(22)	3.76	2.12	2.04	2.35	2.34
Glu	(26)	3.76	2.10	2.06	2.36	2.36
Glu	(28)	3.743	2.120	2.042	2.349	2.334
Gln	(27)	3.77	2.14	2.13	2.46	2.44
Gln	(26)	3.78	2.14	2.14	2.46	2.46
Gln	(28)	3.757	2.135	2.115	2.456	2.434

J-Coupling		J_{AM}	J_{AN}	J_{MN}	J_{MP}	J_{MQ}	J_{NP}	J_{NQ}	J_{PQ}
Metabolite									
Glu	(27)	4.67	7.35	-14.7	6.63	8.86	8.83	6.16	-16.22
Glu	(22)	4.5	7.2	-15.2	6.0	9.5	8.0	6.8	-15.7
Glu	(26)	4.9	7.3	-	-	-	-	-	-
Glu	(28)	4.65	7.33	-14.85	6.43	8.47	8.39	6.89	-15.89
Gln	(27)	5.8	6.5	-14.0	6.0	9.8	9.5	5.8	-16.4
Gln	(26)	-	-	-	3.6	7.6	7.9	7.9	-
Gln	(28)	5.84	6.53	-14.45	6.33	9.25	9.16	6.35	-15.55

The numerical calculations carried out to optimize the sequence timings used the density matrix representation of the metabolite spin system outlined in Chapters 1 and 2. The Hamiltonian used included, in addition to the Zeeman interaction, the rf pulses, the gradient pulses for both spatial encoding and for encoding the orders of MQC, the chemical shielding interaction and the scalar coupling interactions.

The principal goal of the sequence optimization procedure was to produce as sharp a separation of Glu from Gln as possible in-vivo at 3T. The discriminate of Glx

from other background signals was a secondary objective. In Fig. 2 we illustrate the calculated MNPQ multiplets of both Glu and Gln at 3T as 1 Hz broadened spectra, where the 1 Hz line broadening was chosen for clarity.

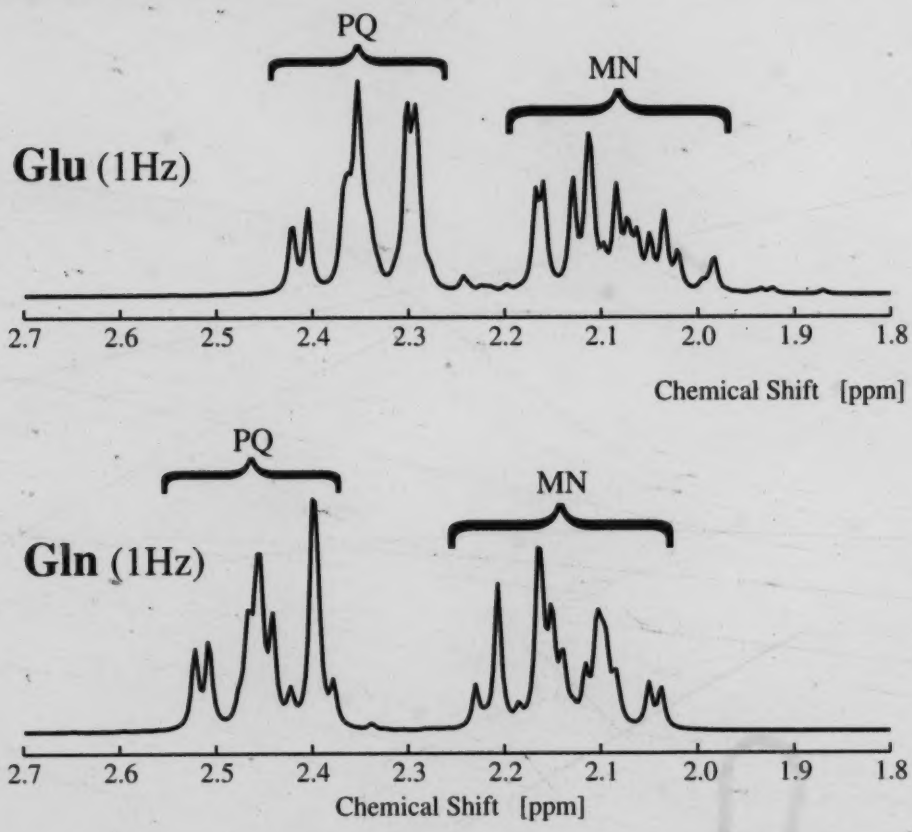

Figure 3-2 Calculated multiplet spectra for the MNPQ spins of both Glu and Gln at a field strength of 3T. The chemical shift and scalar couplings used in the calculations were obtained in this laboratory and are listed in Table 1. The linewidth was set at 1Hz in order to provide resolution of the major multiplet peaks and demonstrate the lack of overlap between Glu and Gln in the 2.3 ppm region of the spectrum.

It is clear from Fig. 2 that for successful resolution of Glu from Gln at 3T the filter design should focus on separating the PQ multiplets and should attempt to restrict the lineshape of the Glu PQ multiplet to its 2.3 ppm (downfield) component. That such a tailoring of the multiplet lineshape might be possible is suggested by previous experience (8) with the lineshape of the A_2 multiplet of GABA and from the fact that far more component terms contribute to the strongly coupled PQ multiplet lineshape of Glx, than

contribute to the A_2 multiplet of GABA. For example, with the GABA A_2 multiplet, the lineshape was shown (8) to be any one of an in-phase triplet, an anti-phase triplet, an anti-phase doublet, or a combination thereof, depending on the value of t_1 and t_3. The assumption was therefore made here, that because of the greater flexibility stemming from the multitude of contributing terms in the Glu case, the evolution of the various coherences could be adjusted to give a PQ multiplet lineshape that was predominantly its 2.3 ppm component.

To quantify our ability to target the 2.3 ppm Glu resonance by numerical simulation, a figure of merit, ξ, was defined for the 2.2 ppm to 2.5 ppm region of the filtered spectrum. The figure of merit, ξ, is defined below,

$$\xi = \{A_{2.3}\,\Delta_{singlet}/\Delta_{2.3}\} / B_{rms}$$

where $A_{2.3}$ and $\Delta_{2.3}$ are respectively the peak amplitude and width of the 2.3 ppm component of the Glu response to the filter, $\Delta_{singlet}$ is the width of a singlet resonance characterizing the pre-defined shim value, and B_{rms} is the root mean square amplitude of the positive and negative excursions from the baseline (not including the 2.3 ppm target peak) between 2.2 ppm and 2.5 ppm. The sequence adjustments to optimize ξ were made primarily by varying both t_1 and t_3, but were refined by varying the tip angle and length of the read pulse and further by adjustment of t_2. The read pulse refinements provided some control over the mixture of coherences produced during that pulse. To evaluate the optimum conditions the read pulse was initially set non-optimally with a tip angle of 90° and a length of 5 ms, and the filtered spectrum sampled over t_1 and t_3 to produce a contour plot similar to that of Fig. 3. In Fig. 3, the contour magnitudes are normalized to the maximum value of ξ derived in this (t_1, t_3) space. At the quasi-optimal t_1 and t_3, values derived from this plot, the read pulse tip angle and length were adjusted to provide the contour plot of Fig. 4, from which the optimal read pulse was derived. The optimal value of t_2, as illustrated in Fig. 5, was determined after the read pulse had been chosen. The final optimization of t_1 and t_3 was then carried out, subsequent to the optimization of the read pulse and t_2, by generating Fig. 3, which, together with Fig. 4, illustrates the sensitivity of the optimum conditions for a Glu filter.

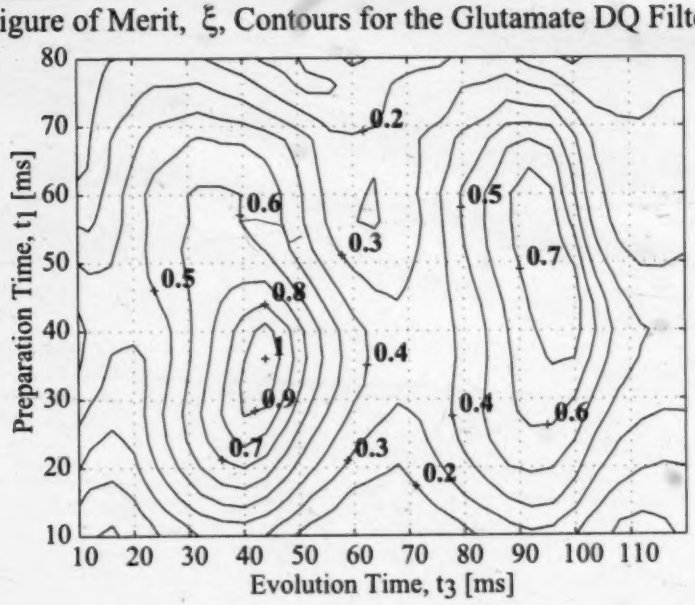

Figure 3-3 A contour plot of the calculated figure of merit, ξ, of the glutamate double quantum filter as a function of the times t_1 and t_3 in the filter sequence of Fig. 1. The numerical contour values are normalized to the maximum value which was observed in the region of (t_1, t_3) = (36ms, 43ms). The step interval was 1ms in each dimension.

Although MQC filters provide excellent suppression of single quantum coherences from uncoupled spins, as well as of the MQC from coupled spin systems whose multiplets are not excited by the read pulse, the similarity of chemical shift locations and *J* values of Glu, Gln, NAA, Asp and GABA, makes the leakage of some neighbouring coupled spin metabolite signals inevitable. Filter response signal calculations were therefore also carried out for the Glu filter sequence acting on all known spectrally neighbouring metabolites that might produce a background artifact, namely, Gln, NAA, Asp and GABA. From such calculations it was clear that the GABA contribution was quite small and it was consequently omitted from the subsequent phantom tests. Because discrimination from neighbouring metabolites was a key criterion in the final optimization of the filter sequence, the ultimate timings etc., for the Glu filter at a field strength of 3T were chosen once all target metabolite and background signals had been accumulated. It should not be forgotten however, that due to the strong coupling of Glu, Gln and Asp spin systems, the optimal solution is field dependent and the values derived here are only optimal at 3T.

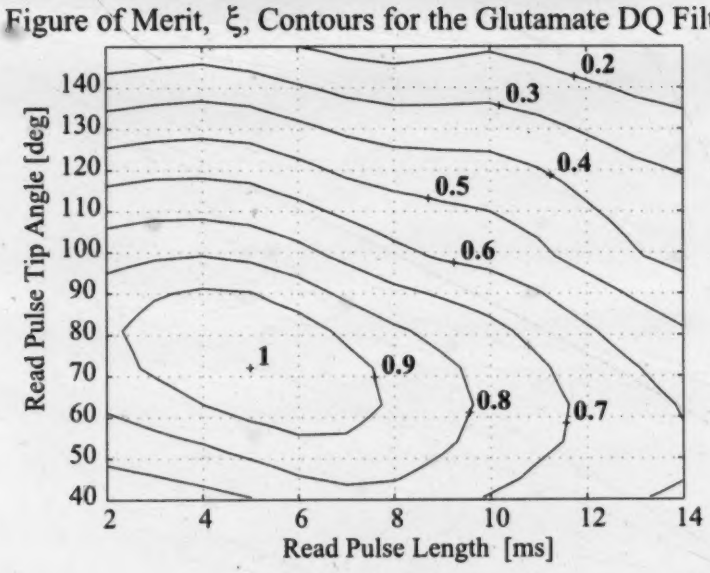

Figure 3-4 A contour plot of the calculated figure of merit, ξ, of the glutamate double quantum filter as a function of the read pulse tip angle and read pulse length in the sequence of Fig.1, while a constant read pulse shape was maintained. The numerical contour values are normalized to the maximum value which was observed at 72° and a pulse length of 5 ms. The step intervals were 2° in tip angle and 0.5 ms in pulse length.

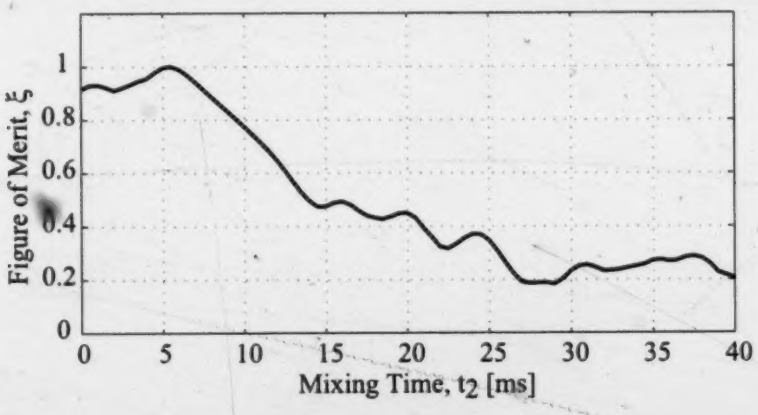

Figure 3-5 The dependence of the calculated figure of merit, ξ, of the glutamate double quantum filter as a function of the time, t_2, in the sequence of Fig. 1. The numerical amplitude is normalized to its maximum value at t_2 = 5.5 ms. The stepping interval in t_2 was 0.25 ms.

3.3 Testing of the Composite DQF Design

The composite DQC filter design for Glu was initially tested on small (5 cm and 8 cm diameter) spherical phantoms of aqueous solutions before being evaluated in-vivo on a single 2.5x2.5x2.5 cm^3 (15.6 ml) voxel in the region of the motor cortex. Using the phantoms the filter was evaluated for its spatial integrity, as well as for its ability to filter the 2.3 ppm component of the Glu PQ multiplet from a background of Gln, NAA and Asp signals, each of which was represented at a relative concentration corresponding to that in normal brain. These performance tests were carried out at 3T in an 80cm bore magnet (Magnex Scientific PLC, Abingdon, UK), using a home-built 28cm diameter quadrature birdcage coil for both transmission and reception. The gradient coils were actively shielded (access diameter 32cm) and spectrometer control was provided by an SMIS console (Surrey Medical Imaging Systems PCL, Guilford, UK). The validity of the numerical calculations was checked by comparing the calculated filtered Glu signal, broadened by 2.5Hz, with the experimental filter output from a phantom of Glu in aqueous solution. The agreement, shown in Fig. 6, also demonstrates the filter's ability to suppress all components of the MN and PQ multiplets relative to the 2.3 ppm peak of the PQ multiplet.

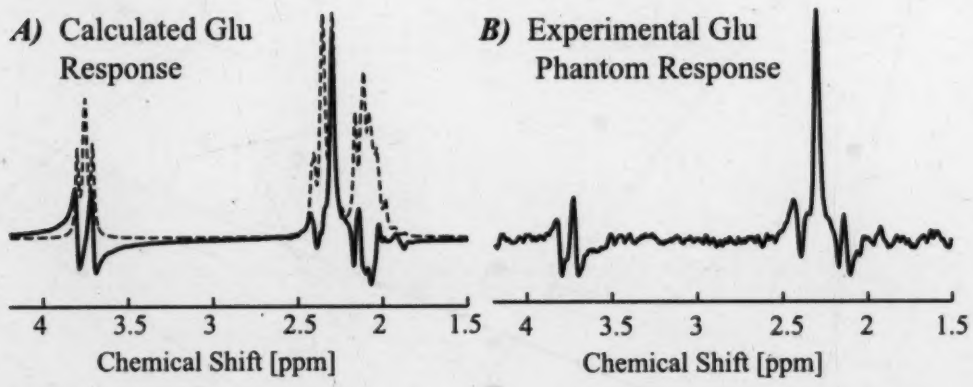

Figure 3-6 A comparison of the calculated (A) and experimental (B) response of Glu to the optimized Glu filter. Also included in panel (A), as the dashed curve, is a reproduction of the unfiltered Glu spectrum at 3T. Although both Glu signals are normalized to the same peak height to emphasise the isolation of the 2.3ppm peak, the filtered Glu peak is ~33% of its maximum value in the unfiltered Glu spectrum,. Both of the calculated spectra were broadened to 2.5 Hz to correspond to the linewidths in the experimental phantom response.

The phantom for the spectral discrimination test comprised Glu (36mM), Gln (12mM), NAA (27mM) and Asp (9mM) in aqueous solution in the central 5cm diameter sphere of a concentric spherical structure of which the outer 8cm diameter spherical compartment contained water. The results of this test are shown in Fig. 7, where the calculated response (A), a concentration weighted sum of the calculated metabolite responses to the optimized Glu filter, is compared to the experimental, filtered, phantom response (B). Also shown, in Fig. 7(C), is an in-vivo spectrum for comparison with the other two. The strong singlet peaks of NAA, Cr and Cho are clearly eliminated by this filter and other than the 2.3 ppm peak of Glu, the signals from coupled spins are markedly suppressed.

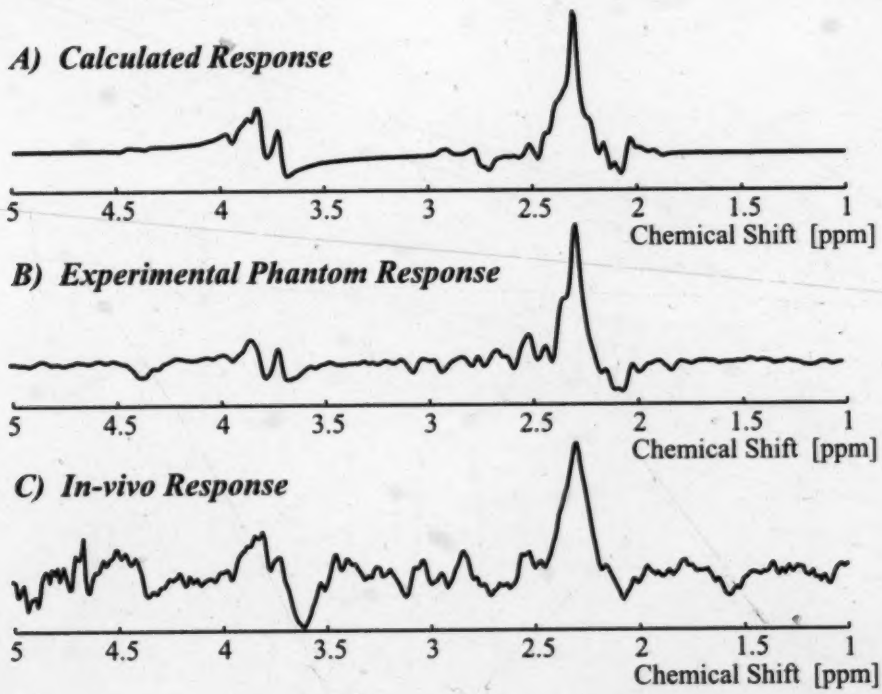

Figure 3-7 A comparison of the calculated (A), mixed phantom (B) and human brain (C) response to the optimized Glu filter. The calculation was a weighted sum of the calculated responses of Glu, Gln, NAA and Asp at normal physiological concentrations. The mixed solution phantom contained solutions of Glu, Gln, NAA and Asp also in normal physiological proportions. Both the calculated and phantom responses were artificially broadened to 7Hz linewidth in order to be comparable with the in-vivo spectrum.

To demonstrate the spatial integrity of the filter, we chose to construct a phantom from the two metabolites that are most difficult to separate spectroscopically, namely Glu and Gln. The spectral resolution of the Glu and Gln responses to the Glu filter is illustrated in Fig.8, where the metabolites are represented in normal physiological proportions and where the line broadening has been increased to the value we regard as limiting for such resolution with this filter at 3T, namely, 4 Hz.

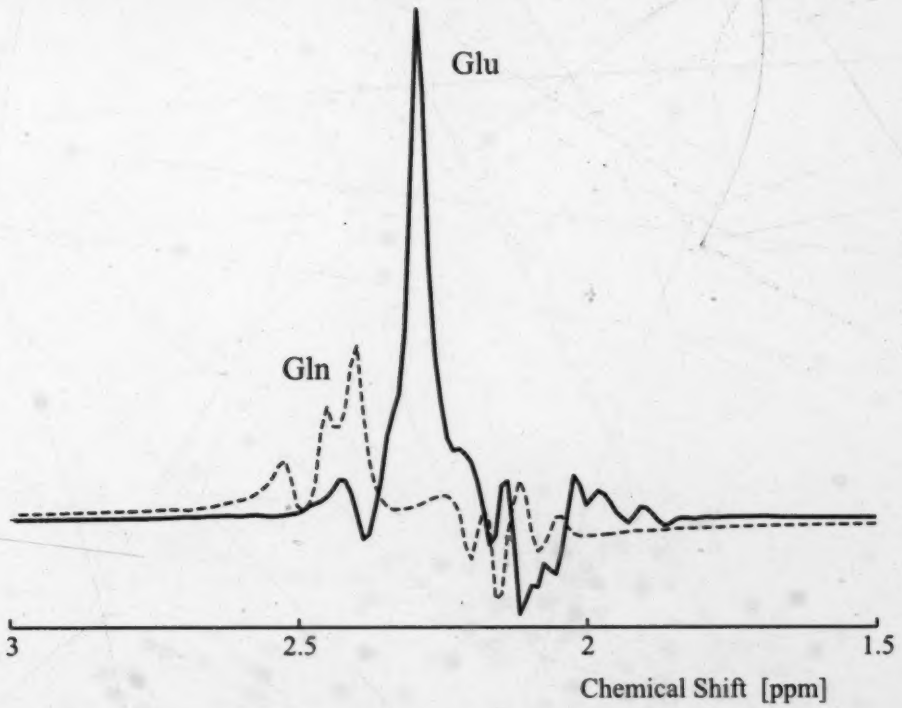

Figure 3-8 A comparison of the calculated responses, broadened to a linewidth of 4Hz, of both Glu and Gln to the optimized Glu filter and presented on the same axis to illustrate the limiting nature of the resolution at 4Hz. Glu and Gln are assumed to be in a concentration ratio of 12:4, representing relative physiological concentrations.

For the spatial integrity test we chose to use these metabolites not in physiological proportions but in equal 20mM concentrations. Each of the chambers of the concentric spherical structure was filled with one or other of the Glu or Gln solutions and the Glu filter applied to each chamber in turn. The spatial discrimination is illustrated in Fig. 9.

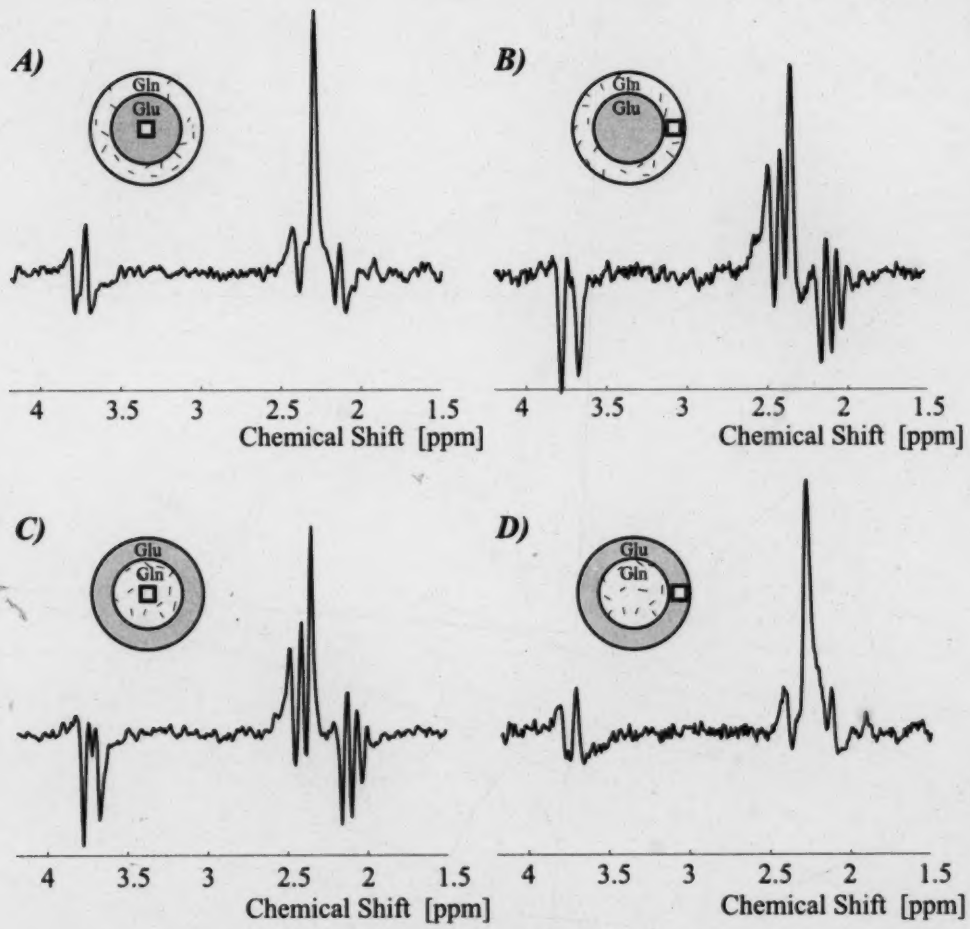

Figure 3-9 A demonstration of the spatial integrity of a 1.5 x 1.5 x 1.5 cm^3 single voxel filtered response at both the isocentre and 3cm from the isocentre in a pair of concentric spheres. Each of the spheres contained either Glu or Gln as indicated in each of the four panels, (A) to (D). For each configuration of Glu and Gln, namely, (A) and (B) on the one hand and (C) and (D) on the other, the response of the metabolite in each of the spheres was interrogated, i.e.(A) versus (B) on the one hand and (C) versus (D) on the other. The linewidth is ~ 3 Hz

Notwithstanding the excellent, localized, editing performance of the DQC filter sequence with spherical aqueous phantom solutions of metabolites, when the sequence was initially applied to human brain in-vivo it was found that signals could be returned by the filter whose characteristics appeared to match those of solvent, dipolar-demagnetizing field signals, known to very high field spectroscopists (17,18,29-31), but

not previously reported from in-vivo experiments. In the present work these signals have been assigned to water protons, although they do not necessarily always occur at 4.75 ppm and they do not result from water proton magnetization excited by the initial 90° pulse. Their source was initially suspected because of their sharp sensitivity to the ratio of the filter gradients (they peaked sharply when G_2/G_1 was set precisely to an integral value) and by their $(3\cos^2\theta\text{-}1)$ dependence on the angle, θ, between the static field, B_o, and the filter gradient direction. In later experiments the intensity of these signals was found to depend on the tip angle, ϕ, of the read pulse according to the $\sin\phi(1\text{-}\cos\phi)$ dependence predicted by Bowtell (17) for the dipolar demagnetizing field signals of solvent nuclei at very high field. Although these signals are not novel in high field NMR, we believe that this is the first report of their interference at low fields with the operation of localizing MRS sequences, although magic angle gradient settings to inhibit their appearance have been reported (32,33). In the DQF sequence presented here the dipolar demagnetizing field signals are generated by the second and third 90° pulses of the DQF, together with the filter gradients. Although they are detectable in a two pulse experiment at a low level from irregularly shaped samples when the filter gradients are not present, they are dramatically increased when the filter gradients are applied with an integral ratio of their amplitudes. To ensure their elimination from the DQC Glu filter response, we found that phase cycling was required (34) as well as the magic angle setting of the gradients. A more detailed discussion of the characteristics, origin and elimination of these signals is provided in chapter 7.

3.4 Summary and Conclusions

The objectives of the paper have been, first, to outline a procedure that is appropriate for the design of MQC filter sequences targeted for the strongly coupled, multiple spin systems that occur in the metabolites of the brain and, secondly, to provide an evaluation of the performance of such a sequence designed for Glu, both in a phantom and in-vivo. For spin systems that are not weakly coupled, the number of significant terms in the density operator (even over the course of the simplest pulse sequence) greatly exceeds that for the same number of weakly coupled spins (compare for example the AB multiplet of the ABX spin system of the aspartate group of NAA (12,35) with the standard text book example of an AX spin system). As the number of spins in the coupled groups increases, the problem of evaluating the response of the spin system

analytically using product operator methods becomes intractable. The design procedure proposed here uses numerical methods of solution for the density matrix equations in order to establish first, the most suitable target multiplet for editing, to provide secondly a set of contour plots of a performance index of the filter, ξ, in terms of the critical parameters in the DQC filter sequence, and to produce thirdly the response of the target and background metabolites to that filter sequence. Without both the numerical solution of the strongly coupled problem and the complete set of coupling parameters measured in this laboratory, our choice of a target peak at 2.3 ppm in the mixed Glx 3T spectrum, as depicted by Fig.2, would have been very difficult to establish. The performance index, ξ, embodies this spectral design objective of the filter, and the calculated contour plots of Figs. 3 and 4 illustrate what, for us, is not obtainable analytically, namely, that under the right circumstances a component peak can indeed be isolated from within a particular multiplet of a strongly coupled spin system. It would, however, be wrong to extrapolate too far from this success and assume that a suitable peak for editing can always be identified and isolated. The juxtaposition, that is shown in Fig.2, of the Glu spectrum against its principal interfering background spectrum from Gln, is valid only at ~ 3T. At different field strengths not only does the multiplet separation change relative to multiplet splittings, but for strongly coupled systems the multiplet band shapes themselves also change substantially. Realization of this emphasises the importance of the initial targeting procedure, prior to the filter sequence design. When coupled spins are involved in both target and background metabolites, the targeting procedure becomes somewhat more sophisticated than for the weakly coupled GABA multiplet obscured by the singlet Cr resonance (36).

That a practical filter can be optimized to return primarily the 2.3 ppm peak of the Glu PQ multiplet is demonstrated in Fig.6, where not only are the unfiltered and filtered multiplets compared, but where an experimental phantom response clearly verifies the calculated response. The sensitivity of this response to the sequence parameters is clearly evident in Figs.3 through 5. The advantageous shortening of t_1 and t_3 from 1/2J, previously demonstrated for the weakly coupled GABA (8), is reaffirmed. The importance of t_2 and read pulse adjustments are also clear, although it is impractical to list the optimal distribution of coherences (amongst the 160 terms of the density operator which we tracked) brought about by these adjustments.

Although the response of all possible background metabolites to the Glu-optimized filter have been calculated (27), only their concentration-weighted sum has been shown in Fig.7 in the interests of brevity. In Fig.7, the calculated overall response and the experimental phantom response have been artificially broadened to correspond to the broader 7Hz linewidth of the experimental in-vivo spectrum, all of which show clearly the dominance of the 2.3 ppm Glu peak. The line broadening in-vivo was determined from the NAA singlet at 2.02 ppm of an unfiltered proton spectrum of brain. At ~ 7Hz line broadening, even though the response is dominated by the 2.3 ppm peak of Glu, we cannot say that Glu and Gln are fully resolvable at 3T with this filter. We estimate that to resolve Glu fully from Gln with this filter we need to shim to 4Hz or better, as is illustrated in the 4Hz broadened calculated responses shown in Fig.8. Nevertheless, relative to concentration estimates taken from unfiltered proton spectra acquired with PRESS or STEAM, the credibility of quantitative in-vivo measures of Glu are likely to be significantly enhanced by this filter design procedure, because of efficient background suppression. Even at 7 Hz linewidth, the 2.3 ppm peak amplitude (used by some) is ~95% Glu and the signal to noise ratio in-vivo is ~10:1. Moreover, the detailed numerical access to the sequence-dependent response lineshapes of the strongly coupled metabolite spins underscores any interpretation by allowing a modelled decomposition of the experimental filter response to take place, thereby allowing the actual magnitude of the suppressed components to be determined.

Finally the spatial integrity of the single voxel defined by the filter is very well demonstrated by Fig.9, taken in conjunction with the response lineshapes of Glu and Gln shown in Fig.8. Because of the very close spectral similarity of Glu and Gln, no confusion arises between spatial and spectral discrimination in this phantom test. The narrow solution linewidths (~3 Hz) provide a clear spectral separation of the two metabolites, so that the discrimination demonstrated in Fig.9 is entirely spatial. The volume demands of an in vivo application are unlikely to be so great as in this phantom test.

3.5 References

1 J. Vion-Dury, D.J. Neyerhoff, P.J. Cozzone and M.W. Weiner, What Might Be the Impact on Neurology of the Analysis of Brain Metabolism by In Vivo Magnetic Resonance Spectroscopy ?, *J. Neurol.*, **241**, 354-371 (1994)

2. D.L. Rothman, O.A.C. Petroff, K.L. Behar, and R.H. Mattson. Localized ^{1}H NMR Measurements of γ-Aminobutyric Acid in Human Brain In Vivo *Proc. Natl. Acad. Sci. USA*, **90.** pp. 5662-5666 (1993).

3 G. F. Mason, J. W. Pan, S. L. Ponder, D. B. Twieg, G. M. Pohost and H. P. Hetherington, Detection of Brain Glutamate and Glutamine in Spectroscopic Images at 4.1T, *Magn. Reson. Med.*, **32**, 142-145 (1994)

4. H.K. Lee, A Yaman and O Nalcioglu, Homonuclear J-Refocussed Spectral Editing Technique for Quantification of Glutamine and Glutamate by 1H NMR Spectroscopy, *Magn. Reson. Med.*, **34**, 253-259 (1995).

5. J. W. Pan, G. F. Mason, G. M. Pohost and H. P. Hetherington, Spectroscopic Imaging of Human Brain Glutamate by Water supressed J-Refocussed Coherence Transfer at 4.1T, *Magn. Reson. Med.*, **36**, 7-12 (1996)

6. J.R. Keltner, L.L. Wald, B. de B. Frederick, and P.F. Renshaw, In Vivo Detection of GABA in Human Brain Using a Localized Double Quantum Filter Technique, *Magn. Reson. Med.*, **37**, 366-371 (1997)

7. S.W. Provencher, Estimation of Metabolite Concentrations from Localized In Vivo Proton NMR Spectra *Magn. Reson. Med.*, **30**, 672-679 (1993).

8. A.H. Wilman and P.S. Allen. Yield enhancement of the double quantum filter sequence designed for the detection of GABA in proton spectroscopy of brain, *J. Magn. Reson.*, **109**, 169-174 (195).

9. L. N. Ryner, J. A. Sorenson and M. A. Thomas, 3D Localized 2D NMR Spectroscopy on an MRI Scanner, *J. Magn. Reson.*, **B107**, 126-137 (1995)

10. L.A. Trimble, J.F. Shen, A.H. Wilman and P.S. Allen. Lactate Editing by means of Selective Pulse Filtering of Both Zero and Double Quantum Coherences, *J. Magn. Reson.*, **86**, 191-198 (1990).

11. A.H. Wilman and P.S. Allen, The response of the strongly coupled AB system of Citrate to typical ^{1}H MRS Localization Sequences, *J. Magn. Reson.*, **107B**, 25-33 (1995)

12. A.H. Wilman and P.S. Allen, Observing N-Acetyl Aspartate Via Both Its N-Acetyl and Its Strongly Coupled Aspartate Groups in In Vivo Proton Magnetic Resonance Spectroscopy, *J. Magn. Reson.*, **113B**, 203-213 (1996)

13. R.B. Thompson and P.S. Allen. An Integrated Volume Localization and Spectral Editing Pulse Sequence, *Proc. of SMR 3rd Ann. Mtg., Nice.*, **p1909**, (1995).

14. L. Jouvensal, P.G. Carlier and G. Bloch, Double Quantum Proton Editing of Lactate in the Human Calf During Excercise, *Proc. of SMR 3rd Ann. Mtg., Nice.*, **p427**, (1995).

15. L. Jouvensal, P.G. Carlier and G. Bloch, Practical Implementation of Single Voxel Double Quantum Editing on a Whole-Body NMR Spectrometer: Localized Monitoring of Lactate in the Human Leg During Exercise, *Magn. Reson. Med.*, **36**, 487-490 (1996).

16. R.B. Thompson and P.S. Allen. The Penetration of In Vivo Multiple Quantum Filters by "Dipolar Field Effect Signals" from Water, *Proc. of ISMRM 5th Ann. Mtg., Vancouver.*, **p1351**, (1997)

17. R. Bowtell, R.M. Bowley, and P. Glover, Multiple Spin Echoes in Liquids in a High Magnetic Field, *J. Magn Reson.*, **88**, 643-651 (1990).

18. W.S. Warren, W. Richter, A.H. Andreotti and B.T. Farmer II, Generation of Impossible cross peaks between Bulk Water and Biomolecules in Solution NMR, *Science*, **262**, 2005-2009 (1993)

19. R.B. Thompson and P.S. Allen. In Vivo Double Quantum Filtering of Glutamate, *Proc. of ISMRM 5th Ann. Mtg., Vancouver.*, **p1350**, (1997)

20. A. Knuettel and R. Kimmich. A Phase Sensitive Single Scan Method for Volume Selective Editing of NMR Signals using Cyclic Polarization Transfer. In Vivo Determination of Lactate, *J. Magn. Reson.*, **86**, 253-263 (1990).

21. R.E. Hurd and D. Freeman, Proton Editing and Imaging of Lactate, *NMR in Biomed.*, **4**, 73-80 (1991).

22. J. Slotboom, A.F. Mehlkopf and W.M.M.J. Bovee. The Effects of Frequency Selective RF Pulses on J-Coupled Spin-1/2 Systems, *J. Magn. Reson.*, **108A**, 38-50 (1994).

23. H. Geen and R. Freeman. Band-Selective Radio Frequency Pulses, *J. Magn. Reson.*, **93**, 93-141 (1991).

24. J.F. Shen and P.S. Allen, Reduced length for double quantum filtering sequences, *J. Magn. Reson.*, **92**, 398-403 (1991).

25. A. Ziegler, M. Izquierdo, C. Remy, M. Decorps, Optimization of Homonuclear Two Dimensional Correlation Methods for In Vivo and Ex Vivo NMR, *J. Magn. Reson.*, **B107**, 10-18 (1995)

26. K. L. Behar and T. Ogino Assignment of Resonances in the 1H Spectrum of Rat Brain by Two-Dimensional Shift Correlated and J-Resolved NMR Spectroscopy, *Magn. Reson. Med.*, **17**, 285-303 (1991).

27. P.S. Allen, R.B. Thompson and A.H. Wilman, Metabolite Specific NMR Spectroscopy In-Vivo, *NMR in Biomed.*, Accepted for Publication (1997).

28. V. Govindaraju, V.J. Basus, G.B. Matson and A.A. Maudsley. Measurement of Chemical Shifts and Coupling Constants for Glutamate and Glutamine, Submitted to *Magn Reson Med*, (1997)

29. G. Deville, M. Bernier and J.M. Delrieux, NMR Multiple Echos Observed in Solid 3He, *Phys. Rev.* **B19**, 5666-5688 (1979)

30. R. Bowtell, Indirect Detection via the Dipolar Demagnetizing Field, *J. Magn Reson.*, **100**, 1-17 (1992)

31. R. Richter, S. Lee, W.S. Warren and Q. He, Imaging with Intermolecular Multiple Quantum Coherences in Solution Nuclear Magnetic Resonance, *Science*, **276**, 654-657 (1995)

32. Q. He, Z.M. Bhujwalla and J.D. Glickson, Proton Detection of Choline and Lactate in EMT6 Tumors by Spin Echo-Enhanced Selective Multiple Quantum Coherence Transfer, *J. Magn. Reson.*, **B112**, 18-25 (1996).

33. Q. He, Z.M. Bhujwalla, R.J. Maxwell, J.R. Griffiths and J.D. Glickson, Proton NMR Observation of the Antineoplastic Agent Iproplatin In Vivo by Selective Multiple Quantum Coherence Trasnfer (Sel-MQC), *Magn. Reson. Med.*, **33**, 414-416 (1995).

34. J. Hennig, The Application of Phase Rotation for Localized In Vivo Proton Spectroscopy with Short Echo Times, *J. Magn Reson.*, **96**, 40-49 (1992)

35. L. Kay and R.E. McClung, Product Operator Description of AB and ABX Spin Systems, *J. Magn. Reson.*, **77**, 258-273 (1988).

36. A.H. Wilman and P.S. Allen, In-vivo NMR Detection Strategies for γ-aminobutyric Acid, Utilizing Proton Spectrosocpy and Coherences Pathway Filtering with Gradients, *J. Magn. Reson.*, **101**, 165-171 (1993).

CHAPTER 4

The Role of the N-Acetyl-Aspartate Multiplet in the Quantification of Brain Metabolites[1]

4.1 Introduction

The goal of this manuscript is to clarify the influential role of a major brain metabolite, namely, N-acetyl-aspartate (NAA), in the accurate quantification of other lower concentration metabolites that are no less important in understanding the metabolic status of regions of the central nervous system (CNS). NAA has evolved (Vion-Dury et al. 1994) as the primary marker of neuronal dysfunction and loss as measured by proton magnetic resonance spectroscopy (MRS) of the CNS. It is found in significant concentration (8-11mM) in normal brain (Pouwels et al., 1998). Numerous in-vivo MRS studies have correlated changes in measured NAA levels with specific sources of neuronal loss, including chronic infarcts (Graham et al., 1993; Gideon et al., 1994; Hetherington et al., 1994), tumours (Usenius et al., 1994; Negendank et al., 1996; Preul et al., 1996), chronic MS plaques (Koopmans et al., 1993; Arnold et al., 1994; Davie et al., 1994; Husted et al., 1994; Pan et al., 1996), ALS (Jones et al., 1995; Gredal et al., 1997; Cwik et al., 1998) and several other cerebral disorders (Kreis et al., 1993; Chang et al., 1996; Ashwal et al., 1997). NAA is also thought to play a role in the metabolism of N-acetyl aspartyl glutamate (NAAG), an excitatory dipeptide which co-resonates with one of the NAA peaks.

The spectrum of NAA is characterized by an acetyl singlet, resonating at 2.02 ppm and by means of which it is most commonly quantified, together with an ABX spin group contributing an AB multiplet at 2.60 ppm and an X multiplet at 4.40 ppm. Under in-vivo conditions, where one has no control over overlapping background metabolites, the AB multiplet of NAA contributes to the crowded spectral region between 2 and 3 ppm occupied by other strongly coupled multiplets from, for example, the aspartate (Asp) AB group at 2.76 ppm and the PQ and MN spins of the AMNPQ spin systems of

---

[1] A version of this chapter was published. R.B. Thompson and P.S. Allen, *Bioch. and Cell Biol.*, **76**, 497-502 (1998).

glutamate (Glu) and glutamine (Gln) extending from 2.0 ppm to 2.5 ppm. The X resonance of NAA in most studies falls under the wings of the larger water signal and is therefore neglected, while the acetyl singlet dominates the acetyl resonance of NAAG at 2.05 ppm, as well as partially obscuring neighbouring multiplets of Glu, Gln, and γ-amino butyric acid (GABA). Fig. 4-1 shows a calculation of the contributions of 1 mM of each of these metabolites at a field strength of 3T, assuming a typical in-vivo linewidth of 5 Hz.

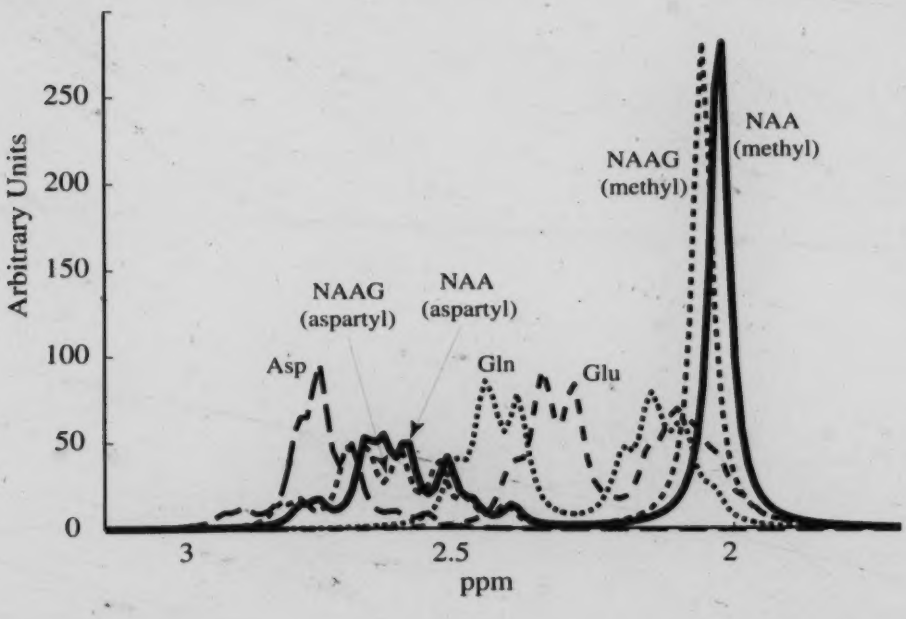

Figure 4-1 Numerically calculated 90° pulse response spectra for the significantly contributing metabolites in the 2.0 ppm to 2.8 ppm spectral band. Each metabolite is assumed to be of 1 mM concentration, and is broadened to a line width of 5 Hz to simulate in-vivo conditions.

The subject of this paper is the marked variability of the strongly coupled aspartate group in NAA which can significantly affect the quantification of other metabolites through their strongly coupled multiplets in the 2.0 to 3.0 ppm spectral band. This follows from the popular quantification procedure (Provencher 1993) of fitting the measured spectrum to a linear combination of individual metabolite basis spectra, in order to identify the linear coefficients as metabolite concentrations. Such a procedure requires that the spectral line shapes and relaxation times are known for all potential contributors throughout the full window of the observed spectrum. In this paper we

neglect relaxation time differences between metabolites in the physiological milieu, which is one source of artifact, and focus on the line shape issue, demonstrating the marked sensitivity of coupled spin multiplets to characteristics of the pulse sequence, namely, the pulse type, the pulse design and the inter-pulse intervals.

The PRESS sequence (Bottomley 1987), shown in chapter 2 (Fig. 2-8B), has recently enjoyed widespread application in in-vivo MRS because it provides the maximum signal available from the uncoupled resonances, specifically, the singlets of NAA, creatine (Cr) and choline (Cho). However, strongly-coupled spins, e.g., the ABX portion of NAA, experience complex echo-time and pulse shape dependent coherence evolutions that give rise to a variability in the lineshape and the spectral yield of the PRESS sequence, which are not well documented for NAA. A previous analytical, product operator, treatment of the AB multiplet of NAA (Wilman and Allen 1996) demonstrated an irregular echo-time dependence at a number of field strengths. However, this analysis assumed sharp pulses with no intra-pulse evolution of coherences and it also neglected the edge effects of selective in-vivo pulses, both of which can have a substantial effect on the distribution of coherences at the start of inter-pulse evolution periods. By means of a numerical approach, we demonstrate here a dependence of the AB multiplet yield on the individual echo times, TE_1 and TE_2, (not previously acknowledged in the literature), as well as on the total PRESS length, TE. Furthermore, it will be shown that this variability is exacerbated by evolutions occurring during the spatially selective 180° pulses, an effect previously considered by Slotboom et. al (1994) in the weakly coupled limit of an AX spin system. For a particular field strength and a given pulse design, the numerical evaluation of the response of the coupled spins of NAA to PRESS enables the changes in multiplet amplitude and lineshape to be determined for all combinations of echo times, demonstrating the striking difference from the behaviour of the uncoupled NAA singlet.

4.2 The Response to PRESS (TE_1 and TE_2 Dependence)

To calculate the response to the PRESS sequence numerically, the density matrix representation of the metabolite spin system outlined in Chapters 1 and 2 was employed. The Hamiltonian used in the present calculations included, in addition to the Zeeman

interaction, the r.f. pulses, the gradient pulses for spatial encoding, the chemical shielding interaction and the strong scalar coupling interactions.

4.2.1 Hard Pulse Limit

The previous product operator calculation of the response of the NAA ABX spin group to PRESS (Wilman and Allen 1996) (which assumes hard pulses) only provided the signal dependence on the total echo time, TE. However, because the chemical shift and scalar coupling Hamiltonians do not commute when the coupling is strong, the individual echo times, TE_1 and TE_2, independently contribute to the overall response, even for the idealized, hard pulse, PRESS sequence. A sole dependence on the total echo time occurs only in the weak coupling limit. Furthermore, strong coupling evolutions give rise to complex and changing line shapes, making a simple area measurement an inappropriate assessment of the echo-time dependence of the response. A more meaningful assessment requires some multiplet simplification, e.g., a peak height. Figure 4-2 represents, as a contour plot, the numerical evaluation of the peak value response of the 2.60 ppm multiplet, calculated in terms of TE_1 and TE_2.

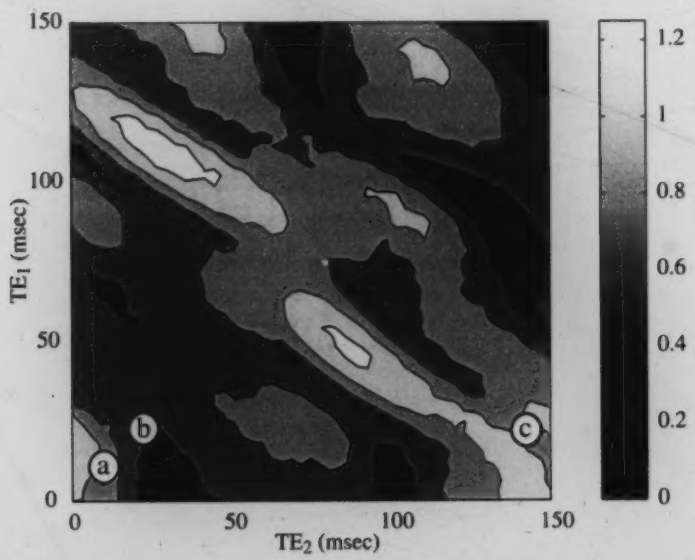

Figure 4-2 A contour representation of the peak value of the NAA AB multiplet as a function of the PRESS echo times, TE_1 and TE_2, in which all r.f. pulses are hard pulses. The contour values are normalized to the AB multiplet peak intensity corresponding to a PRESS sequence of minimum length. Calculated and experimental spectra are produced for echo times corresponding to the points labeled a, b, and c are given if Fig. 4-3.

What is immediately clear from Fig. 4-2 is the prediction that the full peak intensity of this multiplet can be recovered at several echo time combinations displaced from the TE_1=TE_2 diagonal. Although the integrated area under the multiplet cannot exceed unity, the transfer of coherences within the spin system can enhance peak intensity, as is illustrated for example at echo time combinations (TE_1, TE_2) of (112 ms, 24 ms) and (45 ms, 90 ms). At these PRESS timings the peak of the AB multiplet is inverted to more than 120% of the "90°-response" peak intensity. To illustrate the sensitivity of the AB line shape to both echo times, some representative calculated and experimental spectra are plotted in Fig. 4-3, corresponding to the variety of echo time combinations annotated on Fig. 4-2. The experimental spectra were acquired from an 8 ml sphere containing a solution of 20 mM NAA, balanced to a pH of 7.2.

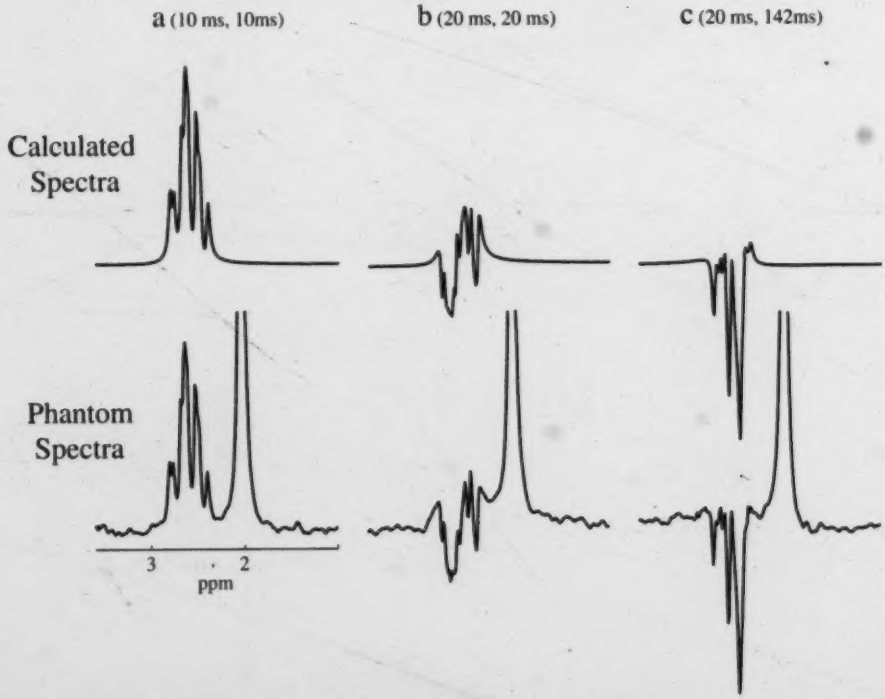

Figure 4-3 Calculated and experimental phantom spectra for three PRESS echo-time combinations corresponding to the timings of locations a, b, and c in Fig. 4-2. The numerical calculations exclude the NAA acetyl singlet at 2.02 ppm. The experimental and calculated spectra were line broadened to a width of 5 Hz to be consistent with in-vivo conditions. The phantom spectra are normalized to the intensity of the NAA methyl singlet, to correct for T_2 losses.

4.2.2 Selective Pulses Inducing Slice Effects

Limitations on peak r.f. power, pulse length and gradient strength give rise to the bandwidth limitations and spectral roll-off characteristics for the refocussing pulses of a practical PRESS sequence, which make them less than ideal. Although previously recognized (Slotboom et al., 1994), the incorporation of a realistic pulse design into full spectral response calculation has not been reported in the literature. Incorporating 3.5 msec 180° sinc refocussing pulses into the PRESS sequence Hamiltonian, the echo-time dependence of the spectral response of the NAA 2.60 ppm multiplet was again calculated numerically. The modified contour plot illustrating multiplet peak value variations is shown in Fig. 4-4. The sinc pulse design was optimized to maximize the rectangular slice profile and provide a bandwidth of 1.2 kHz.

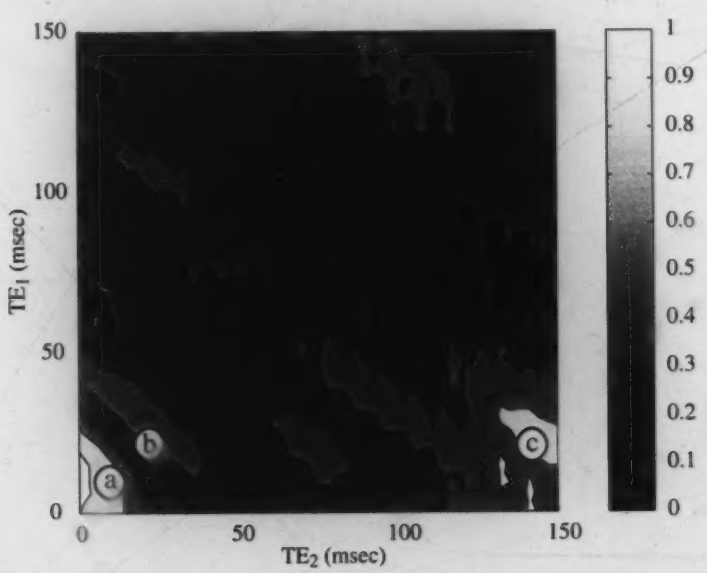

Figure 4-4 A contour representation of the peak value of the NAA AB multiplet as a function of the PRESS echo times, TE_1 and TE_2, in which realistic slice selective refocusing pulses are included. The contour values are normalized to the AB multiplet peak intensity corresponding to a PRESS sequence of minimum length. Calculated and experimental spectra are shown in Fig. 4-6 for echo times corresponding to the points labeled a, b, and c.

What is most apparent from Fig. 4-4 is the drastic reduction in yield compared with that obtained for the hard pulse PRESS response, for all echo times larger than a few milliseconds. In addition to the coherence evolutions during the long selective pulses,

this signal loss stems from a spatial variation of tip-angle due to the roll-off characteristics of the pulses and to the relative slice shifts of the coupled spins, ~ 20% in the present case. The collective action of these mechanisms following localization by the two refocussing 180° pulses is illustrated in Fig. 4-5 for the y component of the A spin transverse magnetization, A_y, and for an antiphase coherence term, $2A_yB_z$, which contributes significantly to the line shape at longer echo-times. To emphasize this action, Fig. 4-5 illustrates first, a spatial distribution at ultra short echo-times which minimize the evolution of the transverse terms into antiphase coherences, and secondly, at an echo-time combination (112 ms, 24 ms) which was optimal for the hard pulse PRESS sequence but which degraded as slice selective pulses introduced sub-180° refocussing due to roll-off and slice shifts.

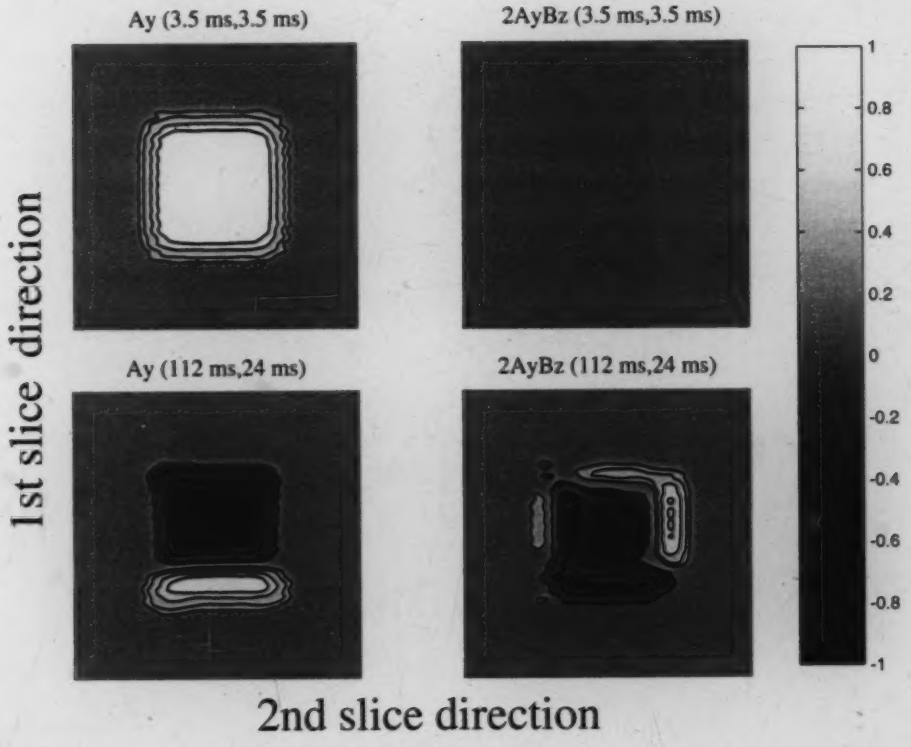

Figure 4-5 The spatial distribution calculated for two coherence terms, A_y and $2A_yB_z$, following a PRESS sequence incorporating slice selective refocusing pulses. Two echo time combinations are compared, a sequence of minimum length (3.5 ms, 3.5 ms), limited only by the pulse length of 3.5 ms, and a longer echo time combination (112 ms, 24 ms), which produced the maximum AB multiplet intensity in the case of PRESS employing hard pulses.

Jung and Lutz, (Bunse et al., 1995) first pointed out that refocussing tip angles of less than 180° readily caused coherence transfers of anti-phase coherences. It is the existence of the anti-phase coherences at the onset of the refocussing pulses which exacerbates the slice effects, e.g., the inversion of the coherence terms in regions proximal to the slice edges shown in Fig. 4-5, resulting in destructive interference and a loss of signal. The echo time dependence of AB line shape is illustrated in Fig. 4-6, where a good choice of echo times (20 msec, 142 msec) is contrasted with a poor symmetric (20 ms, 20 ms) choice. The phantom spectra were acquired from a $2x2x2cm^3$ voxel centered in a 1 litre flask containing 20 mM NAA, balanced to a pH of 7.2.

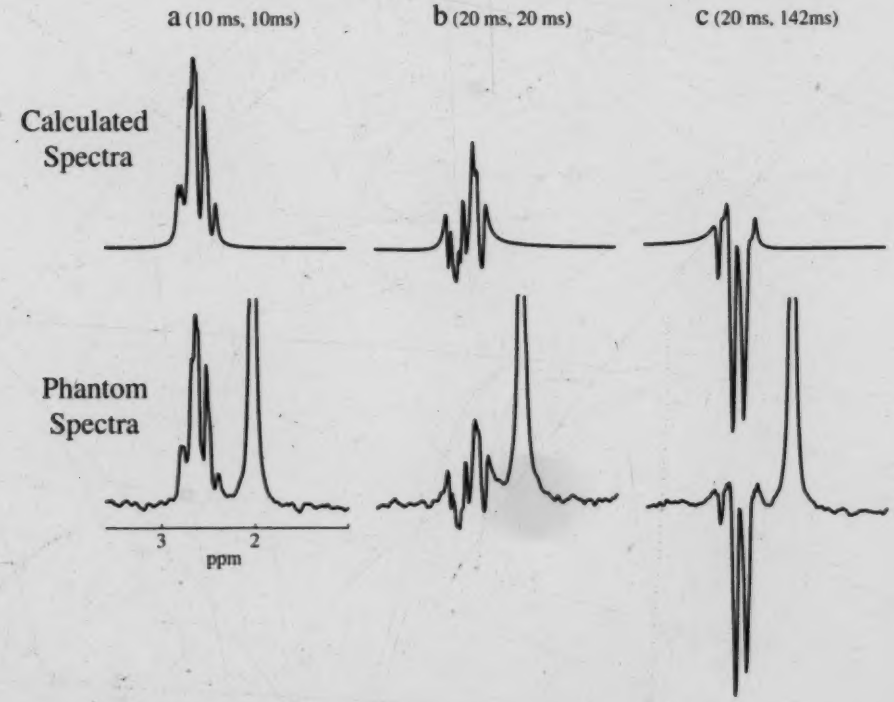

Figure 4-6 Calculated and experimental phantom spectra plotted for three slice-selective PRESS echo combinations, corresponding to the contour diagram locations a, b, and c in Fig. 4-4. In contrast to the experimental phantom spectra the numerical calculations include only the ABX spin group, and so do not produce the NAA acetyl singlet at 2.02 ppm. The experimental and calculated spectra were line broadened to a width of 5 Hz to be consistent with in-vivo conditions. The phantom spectra are normalized to the intensity of the NAA methyl singlet, to correct for T_2 losses.

4.3 Discussion

The use of the PRESS sequence in in-vivo proton MRS is well established for the observation of the uncoupled spins, and possibly the weakly coupled methyl doublet of lactate. The wealth of overlapping signals from strongly-coupled spins, representing many important metabolites, is often allowed to decay through the use of long PRESS echo times to clean up the singlet spectrum from a number of shorter lived signals and phenomena, such as macromolecules, water and eddy currents. At the echo time combinations where the strongly-coupled multiplets can be observed, a fitting routine is often employed for modeling the observed PRESS spectrum as a linear combination of individual metabolite basis spectra, each one obtained from a single metabolite phantom using an identical PRESS sequence. Neglecting relaxation time differences between phantoms and tissue, this fitting strategy has substantial merit. However, such strategies are sensitive to errors in the basis spectra over the whole fitting range and not just at the spectral location of the target metabolite. For this reason, knowledge of the NAA aspartate multiplet is significant for estimating several other coupled spin metabolites whose resonances occur between 2.0 ppm and 3.0 ppm.

By means of Figs 4-2 to 4-6 we have demonstrated that the dependence on the individual TE_1 and on the pulse design is so variable, that the use of basis spectra from any other echo time combination or pulse design can lead to significant differences in metabolite estimation using the fitting algorithm. Moreover, because different metabolites have different echo time and pulse design dependencies, comparison of relative peak heights will also be very pulse design and echo time dependent. These points, together with the strong field dependence of the strong coupling evolutions, suggest that when making field to field or laboratory to laboratory comparisons of metabolite concentrations or concentration differences obtained by means of a modelling methodology a degree of caution should be exercised. Nevertheless, numerical methods as suggested here provide a detailed knowledge of this spectral variability that is otherwise difficult to anticipate. They can, for example, be used to design experiments which not only optimize the yield of a target metabolite, but also predict the best TE compromise between signal strength, lineshape, and background interference contingent as always upon estimates of relaxation times also being known.

4.4 References

1. Arnold, D.L., Riess, G.T., Matthews, P.M., Francis, G.S., Collins, D.L., Wolfson, C. and Antel, J.P. 1994. Use of proton magnetic resonance spectroscopy for monitoring disease progression in multiple sclerosis. Ann. Neurol. **36**:76-82.
2. Ashwal, S., Holshouser, B.A., Tomasi, L.G., Shu, S., Perkin, R.M., Nystrom, G.A. and Hinshaw, D.B. 1997. ^{1}H-Magnetic resonance spectroscopy-determined cerebral lactate and poor neurological outcome in children with central nervous system disease. Ann. Neurol. **41**:470-481.
3. Bottomley, P.A. 1987. Spatial localization in NMR spectroscopy in vivo. Ann. N.Y. Acad. of Sci. **508**:333-348.
4. Bunse, M., Jung, W.I., Lutz, O., Kuper, K. and Dietze, G. 1995. Polarization-transfer effects in localized double-spin-ehco spectroscopy of weakly coupled homonuclear spin systems. J. Magn. Reson. **A114**:230-237.
5. Chang, L., Ernst, T., Poland, R.E. and Jenden, D.J. 1996. In vivo proton magnetic resonance spectroscopy of the normal aging human brain. Life Sciences. **58**:2049-2056.
6. Cwik, V.A., Hanstock, C.C., Allen, P.S. and Martin, W.R.W. 1998. Estimation of brainstem neuronal loss in amyotrophic lateral sclerosis with in vivo proton magnetic resonance spectroscopy. Neurol. **50**:72-77.
7. Davie, C.A., Hawkins, C.P., Barker, G.J., Brennan, A., Tofts, P.S., Miller, D.H. and McDonald, W.I. 1994. Serial proton magnetic resonance spectroscopy in acute multiple sclerosis lesions. Brain. **117**:49-58.
8. Duyn, J.H., Frank, J.A. and Moonen, C.T.W. 1995. Incorporation of lactate measurement in multi-spin-echo proton spectroscopic imaging. Magn. Reson. Med. **33**:101-107.
9. Gideon, P., Sperling, B., Arlien-Soborg, P., Olsen, T.S. and Henriksen, O. 1994. Long-term follow-up of cerebral infarction patients with proton magnetic resonance spectroscopy. Stroke **25**:967-973.
10. Graham, G.D., Blamire, A.M., Rothman, D.L., Brass, L. M., Fayad, P.B., Petroff, O.A. and Prichard, J.W. 1993. Early temporal variation of cerebral metabolites after human stroke. A proton magnetic resonance spectroscopic study. Stroke **24**:1891-1896.
11. Gredal, O., Rosenbaum, S., Topp, S., Karlsborg, M., Strange, P. and Werdelin, L. 1997. Quantification of brain metabolites in amyotrophic lateral sclerosis by localised magnetic resonance spectroscopy. Neurol. **48**:878-881.
12. Hetherington, H.P., Pan, J.W., Mason, G.F., Ponder, S.L., Tweig, D.B., Deutsch, G., Mountz, J. and Pohost, G.M. 1994. 2D ^{1}H spectroscopic imaging of the human brain at 4.1T. Magn. Reson. Med. **32**:530-534.

13. Husted, C.A., Goodin, D.S., Hugg, J.W., Maudsley, A.A., Tsuruda, J.S., DeBie, S.H., Fein, G., Matson, G.D. and Weiner, M.W. 1994. Biochemical alterations in multiple sclerosis lesions and normal appearing white matter detected by in vivo ^{31}P and ^{1}H spectroscopic imaging. Ann. Neurol. **36**:157-165.

14. Jones, A.P., Gunawardena, W.J., Coutinho, C. M.A., Gatt, J.A., Shaw, I.C. and Mitchell, J.D. 1995. Preliminary results of proton magnetic resonance spectroscopy in motor neuron disease (amyotrophic lateral sclerosis). Neurol. Sci. **129 (Suppl)**:85-89.

15. Koopmans, R.A., Li, D.K.B., Zhu, G., Allen, P.S., Penn, A. and Paty, D.W. 1993. Magnetic Resonance Spectroscopy of Multiple Sclerosis - In-vivo Detection of Myelin Breakdown Products. Lancet **341**:631-632.

16. Kreis, R., Ernst, T. and Ross, B.D. 1993. Development of the human brain: In vivo quantification of metabolite and water content with proton magnetic resonance spectroscopy. Magn. Reson. Med. **30**:424-437.

17. Negendank, W.G., Sauter, R., Brown, T.R., Evalhoch, J.L., Falini, A., Gotsis, E.D., Heerschap, A., Kamada, K., Lee, B.C.P., Mengeot, M.M., Moser, E., Padavic-Shaller, K.A., Sanders, J.A., Spragins, T.A., Stillman, A.E., Ternney, B., Vogl, T.J., Wickloq, K. and Zimmerman, R.A. 1996. Proton magnetic resonance spectroscopy in pateints with glial tumors: a multicentre study. J. Neurosurg. **84**:449-458.

18. Pan, J.W., Hetherington, H.P., Vaughn, J.T., Mitchell, G., Pohost, G.M. and Whitaker, J.N. 1996. Evaluation of multiple sclerosis by ^{1}H spectroscopic imaging at 4.1T. Magn. Reson. Med. **36**:72-77.

19. Pouwels, J.W. and Frahm, J. (1998). Regional metabolite concentrations in human brain as determined by quantitative localized proton MRS. Magn. Reson. Med. **39**, 53-60.

20. Preul, M., Caramanos, Z., Collins, D., Villemure, J., leblanc, R., Olivier, A., Pokrupa, R. and Arnold, D. 1996. Accurate, noninvasive diagnosis of human brain tumors by using proton magnetic resonance spectroscopy. Nature Medicine **2**:323-325.

21. Provencher, S.W. 1993. Estimation of metabolite concentrations from localized in vivo proton NMR spectra. Magn. Reson. Med. **30**:672-679.

22. Schick, F., Nagele, T., Klose, U. and Lutz, 0. 1995. Lactate quantification by means of PRESS spectroscopy - Influence of refocusing pulses and timing scheme. Magn. Reson. Imag. **13**:309-319.

23. Slotboom, J., Mehlkopf, A.F. and Bovee, W.M.M. 1994. The effects of frequency selective RF pulses on J-coupled spin-1/2 systems. J. Magn. Reson. **A108**:38-50.

24. Usenius, J.P., Vainio, P., Hernesniemi, J. and Kauppinen, R.A. 1994. Choline-containing compounds in human astrocytomas studied by ^{1}H NMR spectroscopy in vivo and in vitro. J. Neurochem. **63**:1538-1543.

25. Vion-Dury, J., Meyerhoff, D.J., Cozzone, P.J. and Weiner, M.W. 1994. What might be the impact on neurology of the analysis of brain metabolism by in-vivo magnetic resonance spectroscopy? J. Neurol. **241**:354-371.

26. Wilman, A.H. and Allen P.S. 1996. Observing N-Acetyl Aspartate via both its N-Acetyl and its strongly coupled aspartate groups in In Vivo proton magnetic resonance spectroscopy. J. Magn. Reson. **B113**:203-213.

27. Wilman, A.H. and Allen P.S. 1995. The response of the strongly coupled AB system of citrate to typical ^{1}H MRS localization sequences. J. Magn. Reson. **B107**:25-33.

CHAPTER 5

A Demonstration of the Sources of Variability in the Response of Coupled Spins to the PRESS Sequence and their Potential Impact on Metabolite Quantification[1]

5.1 Introduction

Metabolite quantification has increased in reliability due to the recent adoption of segmentation techniques (1-3) and the appreciation of magnetization transfer effects (4). Nevertheless, when coupled spins are involved the potential for quantification errors due to the action of the pulse sequence seems to have been largely overlooked. It is true that in the majority of past in-vivo studies the action of the sequence has not been an issue, since these studies have confined their attention to the uncoupled singlet resonances of N-acetylaspartate (NAA) at 2.02 ppm, of creatine (Cr) at 3.05 ppm and of choline (Cho) at 3.2 ppm, for which the spin dynamics are straightforward. However, the majority of metabolites contain only coupled spins, and if metabolite quantification is to go beyond the uncoupled singlets, the modifications of the line shape and the loss in integrated signal intensity of the coupled-spin multiplets must be quantitatively understood. In the coupled spin case the intuitive vector model no longer applies and, in principle, it is necessary to calculate the evolutions taking place under chemical shielding and scalar coupling Hamiltonians both between and within the radio frequency (r.f.) pulses. Even for weakly-coupled spins, selective pulses can elicit a response that is substantially different from that predicted for ideal hard pulses (5-12). The situation for strongly-coupled spins is significantly more complex because the chemical shielding and scalar coupling Hamiltonians no longer commute, and antiphase coherences proliferate in comparison to those in a weakly coupled system of the same number of spins. The purpose of this paper is to demonstrate, by means of a full numerical solution of the equation of motion of the density matrix, that the response of coupled spins to a localizing MRS pulse sequence is sufficiently variable to give rise first, to misleading comparisons with the response of uncoupled spins and secondly, to be a potential source of error in comparisons between different sites using different pulse designs. The

---

[1] A version of this chapter was published. R.B. Thompson and P.S. Allen, *Magn Reson Med.*, **41**, 1162-9 (1999).

numerical methods employed enable the theoretical envelope to encompass both the selective r.f. pulse design and to increase the number of strongly coupled spins beyond the two already treated by product operator techniques (13-16), and in particular, to accommodate five or more spins as is found in the important amino acids glutamate (Glu) and glutamine (Gln).

Because it provides the maximum signal obtainable from uncoupled singlet resonances, PRESS (17-19) has emerged as the sequence of choice for many in-vivo spectroscopy laboratories. The coupled-spin response to the PRESS sequence (Fig. 2-8B), is substantially more variable than that of uncoupled spins for two reasons. The first, to which detailed reference was initially made by Slotboom et. al. (7), is a dependence on the length (bandwidth) and on the spectral roll-off characteristics of the r.f. pulses. These both manifest themselves as slice selection anomalies that can significantly affect the echo time dependence of both line shape and integrated signal intensity. The second, which is the consequence of strong coupling and which can arise independently of the pulses, is a discordant dependence on the individual evolutions taking place during each of the TE_1 and TE_2 intervals. These two mechanisms make the response to PRESS deviate significantly from a single dependence on the total echo time $TE = TE_1 + TE_2$, found for uncoupled spins (and weakly coupled spins with ideal pulses). Although the principal objective of this paper is to demonstrate these effects for the strongly-coupled five spin AMNPQ system of Glu, the consequences of providing alternative coherence pathways and signal loss mechanisms through the slice selection procedures do not seem to have been fully clarified even in the weak-coupling limit. The AX_3 spin system of lactate is therefore used to characterize the intra-pulse effects.

The variability of the response to PRESS, namely, the echo time dependence of the line shape and integrated intensities, is calculated using a numerical solution of the equation of motion of the density matrix that has been described previously (20) and that incorporates the r.f. pulse design as well as all scalar couplings. The tip-angle aspect of the pulse design has been treated by others for weakly coupled spins using product operator techniques (6,9,10,11). However, the incorporation of either a complete pulse profile, and/or the strong coupling for five spins, required a numerical approach. For any given pulse design and spin system, numerical simulation enables the optimum PRESS echo times to be identified in combinations that result in the optimum yield (when

relaxation is also included) and desirable line shapes. Moreover, from the point of view of relative quantification, it enables the signal loss to be quantified relative to uncoupled spin performance.

5.2 Intra-180°-Pulse Effects in the PRESS Sequence (Weak Coupling Illustration)

Lactate signal loss resulting from non-rectangular soft pulses in the PRESS sequence has been noted for some time (5,6) and empirical evaluations of the signal dependence on pulse quality and on sequence timings have also been reported (8). However, some previous publications on the lactate response (6,9,11) attribute to the PRESS sequence (see below) phenomena that are a consequence of the 180° pulse design rather than of the sequence itself. With proper design these are avoidable. Nevertheless, other intra-pulse effects, some of which were also reported previously (6,9,11), are inevitable in view of the power capabilities of current hardware. The weak-coupling lactate example is an excellent vehicle for demonstrating the origins of these intra-pulse effects. Using a product operator analysis one may either neglect the pulse characteristics altogether (21), or model a selective pulse as a spatial distribution of hard-pulse tip angles at the edges of the selective pulse bandwidth (6,9,11). However, the tip-angle distribution is only one of the causes of intra-pulse effects. Others are (i) the spatial displacement of the excitation band of the different coupled species under the influence of a linear gradient (12), and (ii) the chemical shift evolution taking place within the duration of the pulse (7). The numerical approach taken here, including all details of the excitation process, is to our knowledge the first to accommodate all of these effects in lactate.

The action of each 180° pulse of the PRESS sequence can be characterized by a transformation matrix which itemizes the effect of the pulse on each term of the density operator for the spin system in question. Section 2.4.1.2 of chapter 2 provides a detailed derivation of the transformation matrix method. To clarify the action of slice-selective 180° pulses, the truncated transformation matrices (of eight representative coherences of the AX_3 system) corresponding to several variants of a 180° pulse are shown in Figs. 5-1A to E. Figures 5-1A to C demonstrate the three intra-pulse effects mentioned above.

$1 \equiv A_x$
$2 \equiv 2A_xX_{1z}$
$3 \equiv A_y$
$4 \equiv 2A_yX_{1z}$
$5 \equiv X_{1x}$
$6 \equiv 2A_zX_{1x}$
$7 \equiv X_{1y}$
$8 \equiv 2A_zX_{1y}$

A) *(Hard Pulses)*

Input \ Output	1	2	3	4	5	6	7	8
1	100	0	0	0	0	0	0	0
2	0	-100	0	0	0	0	0	0
3	0	0	-100	0	0	0	0	0
4	0	0	0	100	0	0	0	0
5	0	0	0	0	100	0	0	0
6	0	0	0	0	0	-100	0	0
7	0	0	0	0	0	0	-100	0
8	0	0	0	0	0	0	0	100

B) *(Optimized Sinc Pulse Δ = 1.2 MHz)*

Input \ Output	1	2	3	4	5	6	7	8
1	100	0	0	0	0	0	0	0
2	0	-76	0	0	0	24	0	0
3	0	0	-100	0	0	0	0	0
4	0	0	0	76	0	0	0	-24
5	0	0	0	0	100	0	0	0
6	0	24	0	0	0	-76	0	0
7	0	0	0	0	0	0	-100	0
8	0	0	0	-24	0	0	0	76

C) *(Optimized Sinc Pulse Δ = 1.2 kHz)*

Input \ Output	1	2	3	4	5	6	7	8
1	98	0	0	5	0	-2	0	1
2	0	-38	-5	3	2	1	-1	6
3	0	5	-98	0	0	1	0	2
4	-5	3	0	38	-1	6	-2	-1
5	0	2	0	1	98	0	0	5
6	-2	1	-1	-6	0	-38	-5	-3
7	0	1	0	-2	0	5	-98	0
8	-1	-6	2	-1	-5	-3	0	38

D) *(Sinc-Hamming Pulse Δ = 1.2 kHz)*

Input \ Output	1	2	3	4	5	6	7	8
1	99	0	0	5	0	-2	0	2
2	0	-33	-5	-4	2	-19	-2	5
3	0	5	-99	0	0	2	0	2
4	-5	-4	0	33	-2	5	-2	19
5	0	2	0	2	100	0	0	5
6	-2	-19	-2	-5	0	-33	-5	4
7	0	2	0	-2	0	5	-100	0
8	-2	-5	2	19	-5	4	0	33

E) *(Gaussian Pulse Δ = 1.2 kHz)*

Input \ Output	1	2	3	4	5	6	7	8
1	100	-1	0	3	0	-3	0	0
2	0	-25	-3	-3	3	-18	1	-39
3	0	3	-100	1	0	0	0	3
4	-3	-3	0	25	1	-39	-3	18
5	0	3	0	0	100	1	0	3
6	-3	-18	1	39	0	-25	-3	3
7	0	0	0	-3	0	3	-100	-1
8	1	39	3	18	-3	3	0	25

Figure 5-1 Transformation matrices of a representative set of lactate coherences for five variants of a 180° refocusing pulse, specifically, an ideal hard refocusing pulse (A), an artificially wide-band selective pulse (B), and three pulses with realistic bandwidths of 1.2 kHz, namely, an optimized sinc (C), a sinc-Hamming pulse (D) and a Gaussian pulse (E). The highlighted elements represent the non-zero contributions and illustrate that the off diagonal terms increase in both number and magnitude with worsening of pulse quality from (A) to (E)

The first pulse variant, an ideally sharp, rectangular pulse with an infinitely wide bandwidth and applied without a concurrent magnetic field gradient, eliminates the edge distribution of tip angles, the excitation band shift, and the evolutions occurring during a selective pulse. This variant is equivalent to the hard pulse assumed in product operator mathematics (21) and its transformation matrix, Fig. 5-1A, reflects its ideal nature, since 100% of each input coherence term is recovered following the pulse. A sign change in the transformation matrix denotes inversion of the input. A second variant, designed to prevent the spatial shift of the excitation band, as well as the intra-pulse chemical shift or scalar coupling evolutions (mechanisms neglected in references 6 and 9), can still be made to produce tip-angle edge effects by scaling a selective pulse to an artificial extreme. This variant was a 3-lobe optimized sinc pulse of length 3.5 μs applied in conjunction with a 1.7 Tm^{-1} gradient pulse to refocus a slice ~ 1.66 cm thick. Its transformation matrix, Fig. 5-1B, demonstrates that the anti-phase coherence inputs (even input elements) are now transformed to a mixture of anti-phase terms following the slice-selective 180° pulse, as disclosed originally by Jung et al (6). The third variant, a realistic unscaled selective pulse, was also a 3 lobe optimized sinc pulse but of length 3.5 ms and applied in conjunction with a 1.7 mTm^{-1} gradient, so that it again refocused a slice of thickness ~ 1.66 cm. The transformation matrix for the third variant (Fig. 5-1C) shows considerably more redistribution of the input anti-phase coherence terms, as the two additional intra-pulse mechanisms compound the coherence transfer due to tip-angle edge effects. Although these transformation matrices (which are integrals across the slice) clearly demonstrate the new transfer pathways provided by the pulse, the full impact of the additional mechanisms (in terms of line shape modification and significant signal loss) is more clearly seen from the actual distribution of a coherence across the slice rather than from its integral. Such a distribution is shown in Fig. 5-2, where only a representative input anti-phase coherence term (A_zX_{1x}) is included because the in-phase coherences are relatively insensitive to pulse characteristics, a feature which they have in common with the behavior of uncoupled spins. While the off diagonal terms are kept to a minimum by the pulse design employed for Fig. 5-2, the marked bipolar variation of the diagonal term (A_zX_{1x}) across the slice (arising primarily from the excitation band shift) will contribute significantly to the ultimate lineshape and signal loss. Such behavior is strongly influenced by the slice bandwidth, Δ, relative to the chemical shift difference, δω, of the coupled spin species. Other pulse designs can be less successful at reducing the off-diagonal terms and hence lead to a greater degradation of the signal.

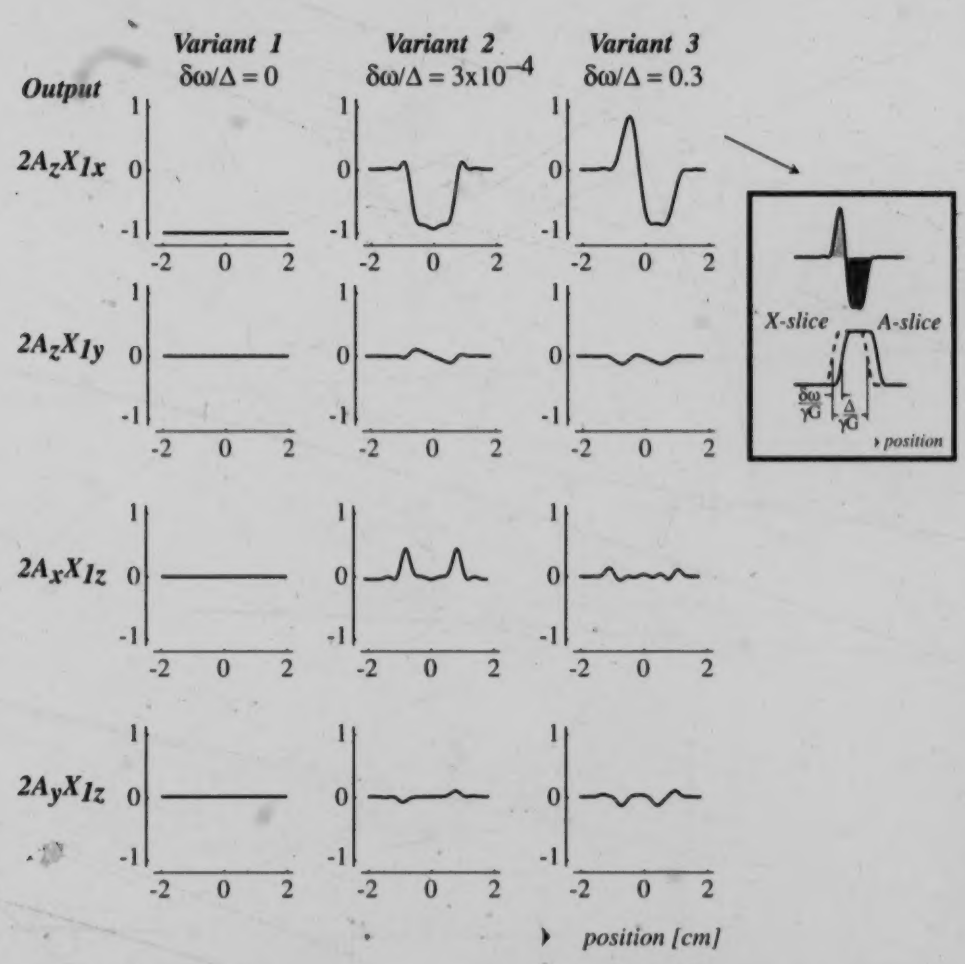

Figure 5-2 An illustration of the slice distribution of four antiphase coherence output terms resulting from a single input term, $2A_zX_{1x}$, and following the application of each of the first three variants of a refocusing pulse. Their integrals give rise to the corresponding elements in Figs. 5-1A, B and C. The excitation band shift effect is clarified by an inset for the diagonal term under pulse variant 3.

Tailoring the shape of the r.f. pulse can reduce edge effects by making the edges sharper. This increase in pulse quality demands a corresponding increase in pulse length for a given bandwidth. Moreover, to reduce the relative excitation band shift by increasing the pulse bandwidth, and at the same time retain the same pulse quality, requires an increase in the sharpness of the time domain waveform e.g., the sinc waveform. Such an increase in sharpness reduces the area under the r.f. modulation envelope unless the B_1 amplitude is increased, and this area must be maintained to

maintain tip angle. Limited by the peak pulse power available, this usually necessitates a trade off between pulse quality and bandwidth in the design of the pulse. The transformation matrices of Figs. 5-1C to E show that for three designs common to the literature, the perturbation of anti-phase diagonal terms increases, and the number and amplitude of off-diagonal terms also increases in going from the optimized-sinc, through the sinc-Hamming pulse to the Gaussian pulse.

For the full PRESS sequence, the ultimate line shape and signal intensity are governed by the distribution of coherences in the signal acquisition period, a distribution that is determined by both the transformation matrices of the pulses and the evolutions taking place during the inter-pulse intervals. The full solution for the response of lactate is reflected in the variation of the integrated doublet intensity contours in (TE_1, TE_2) space, as shown in Fig. 5-3 (c.f. Fig 2C of reference 11). The absence of any high frequency oscillations in the echo time dependence of the intensity (178 Hz at 1.5T, 356 Hz at 3T) previously reported by Schick et al (8), Bunse et al (9) and by Marshall and Wild (11), is due to the optimization of the r.f. pulse design used here. These high frequency oscillations can easily introduce unwanted variations in intensity of up to 40 % and need to be removed. Nonetheless, it is still clear from Fig. 5-3 that within the constraints of the typically available hardware power, even optimized selective pulses cause the response of lactate to PRESS to deviate significantly from the cosinusoidal dependence on total TE that is predicted by ideal hard pulses (21). It cannot be emphasized too strongly that the predictions of hard pulse models can be significantly in error over the proportion of the lactate signal returned by a PRESS sequence, leading therefore to significant errors in lactate concentrations when comparisons are made to the uncoupled spin performance. For example, what is conventionally thought to be a good choice of sequence timings for lactate, namely, $TE_1 = TE_2$ with TE = 2/J = 280 ms, can be a surprisingly poor choice, giving rise to less than 25% of the integrated signal intensity predicted by idealized pulse calculations. Moreover, Fig. 5-3 emphasizes that the maintenance of a good lactate yield at the longer TE used for macromolecular signal suppression, requires a PRESS sequence that is quite asymmetric.

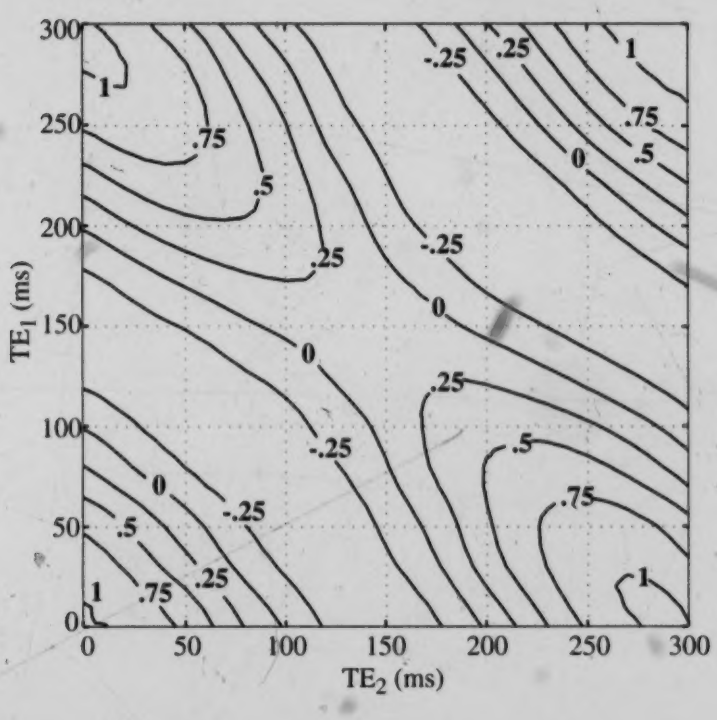

Figure 5-3 A contour plot illustrating the integrated lactate doublet intensity as a function of PRESS echo times TE_1 and TE_2. An optimized sinc refocusing pulse (see Fig. 5-1C) was used in the calculation of this response.

5.3 Strong Coupling Effects in the PRESS Sequence (Glu Illustration)

Several important brain metabolites are strongly coupled at in-vivo field strengths (1.5 T to 4 T), e.g., Glu, Gln, aspartate (Asp), NAA and NAAGlu, taurine (Tau) and myo-inositol (m-Ins). Although the response of the simplest of these, namely, the AB part of the ABX spin system of Asp, NAA and NAAGlu, has been explored using both the product operator formalisms (16) and a full numerical solution (22), the treatment of larger strongly-coupled spin systems has yet to be reported. To illustrate the outcome in such cases, we chose to evaluate the Glu response to PRESS. Focusing on the 2.0 ppm to 2.45 ppm range of the proton spectrum, we have calculated the MN (2.08 ppm) and PQ (2.34 ppm) multiplets of the five spin, strongly coupled (AMNPQ) system (see reference 20 for an illustration). The irregular positive and negative excursions of the PQ and MN multiplets, coupled to their complex evolution with echo time, can make a simple area

measurement a somewhat misleading measure of the spectral yield. Although peak height is not entirely reliable for quantification either, the principal peak of the Glu PQ multiplet centered at 2.34 ppm is a stable feature of this multiplet evolution, and so it was used to reflect the variability of Glu yield from PRESS.

In the (TE_1, TE_2) plane the variation in the Glu PQ multiplet response, in contrast to that of the lactate doublet, exhibits no striking difference in *contour shape* between sequences with ideal hard pulses and sequences with realistic selective pulses (Fig. 5-4). Neither pulse type gives rise to a response that is dependent only on the sum of TE_1 and TE_2. This stems from the strong coupling. Specifically, when spins are strongly coupled the chemical shift and the scalar coupling Hamiltonians do not commute, thereby providing a pathway for polarization transfer (15) that exists independently of and additional to that provided by the non-ideal r.f. pulses. In contrast to the weak-coupling limit therefore, coherence transfer takes place even when ideal hard 180° pulses are employed. During the strongly-coupled evolution, the coherence terms proliferate and substantial polarization transfer takes place between the M, N, P and Q spins. This is demonstrated in Fig. 5-5. Bearing in mind that in practice the initial state comprises the x magnetization of the A, M, N, P and Q spins, Fig. 5-5A assumes an initial state consisting exclusively of P_x spin magnetization and emphasizes the proliferation by providing a snapshot (at a single TE_1 = 30 ms) of the amplitudes of all the 160 single-quantum terms that were tracked for Glu. Figure 5-5B on the other hand illustrates how several representative in-phase and anti-phase coherences have evolved at TE_1 in a hard-pulse PRESS sequence (equivalent to a spin-echo experiment), where $0 < TE_1 < 100$ ms. Some of the terms illustrated have no P spin operator involved, emphasizing the polarization transfer.

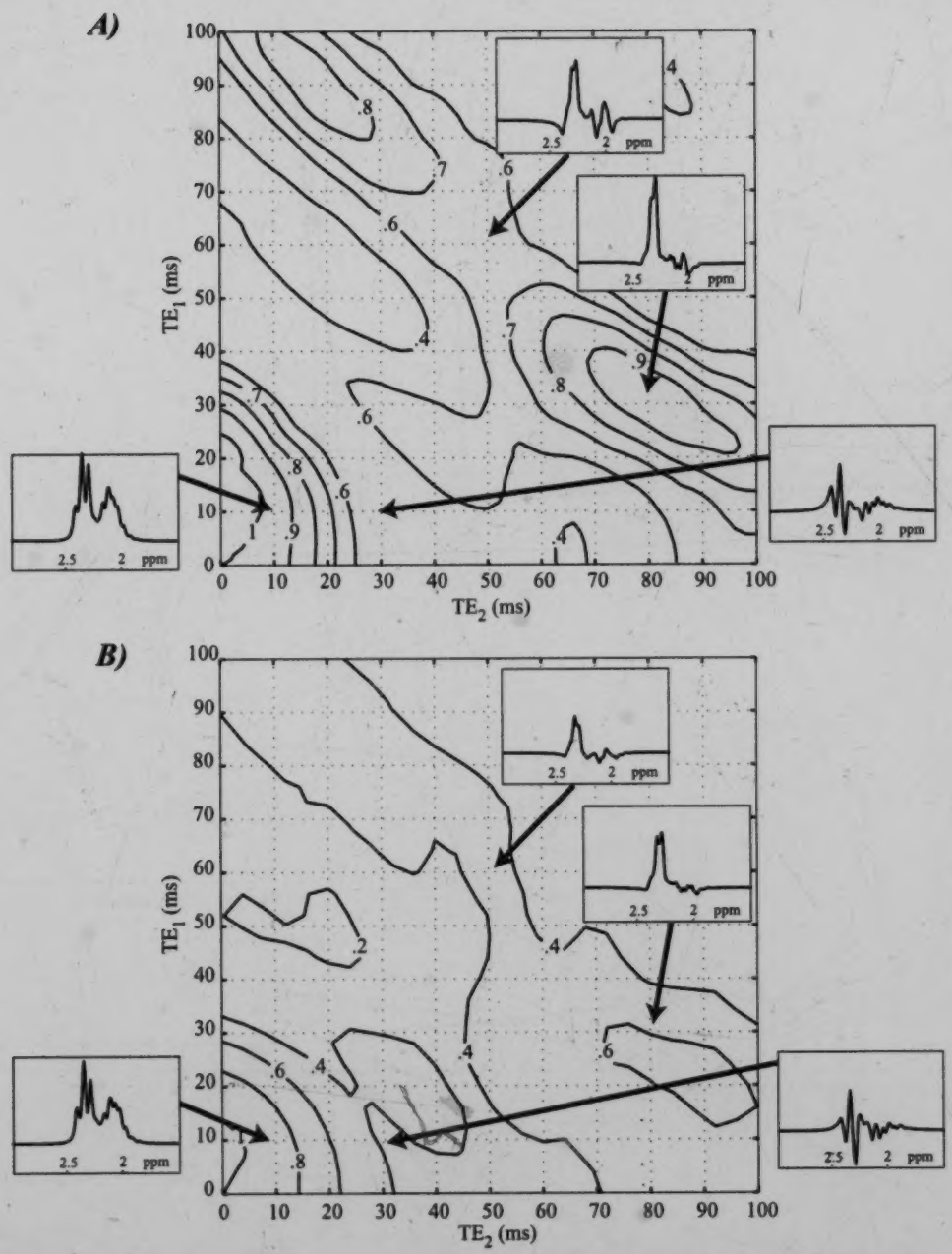

Figure 5-4 Contour diagrams of the peak value of the Glu PQ 2.34 ppm multiplet as a function of PRESS echo times TE_1 and TE_2 for the case of ideal refocusing pulses (A) and realistic slice selective refocusing pulses (B). The optimized sinc pulse (see Fig. 2C) was used in calculation of B. The calculated spectra used to generate the contours were broadened to a linewidth of 5.0 Hz, appropriate for in-vivo comparisons. For each contour plot, four of these calculated spectra are displayed.

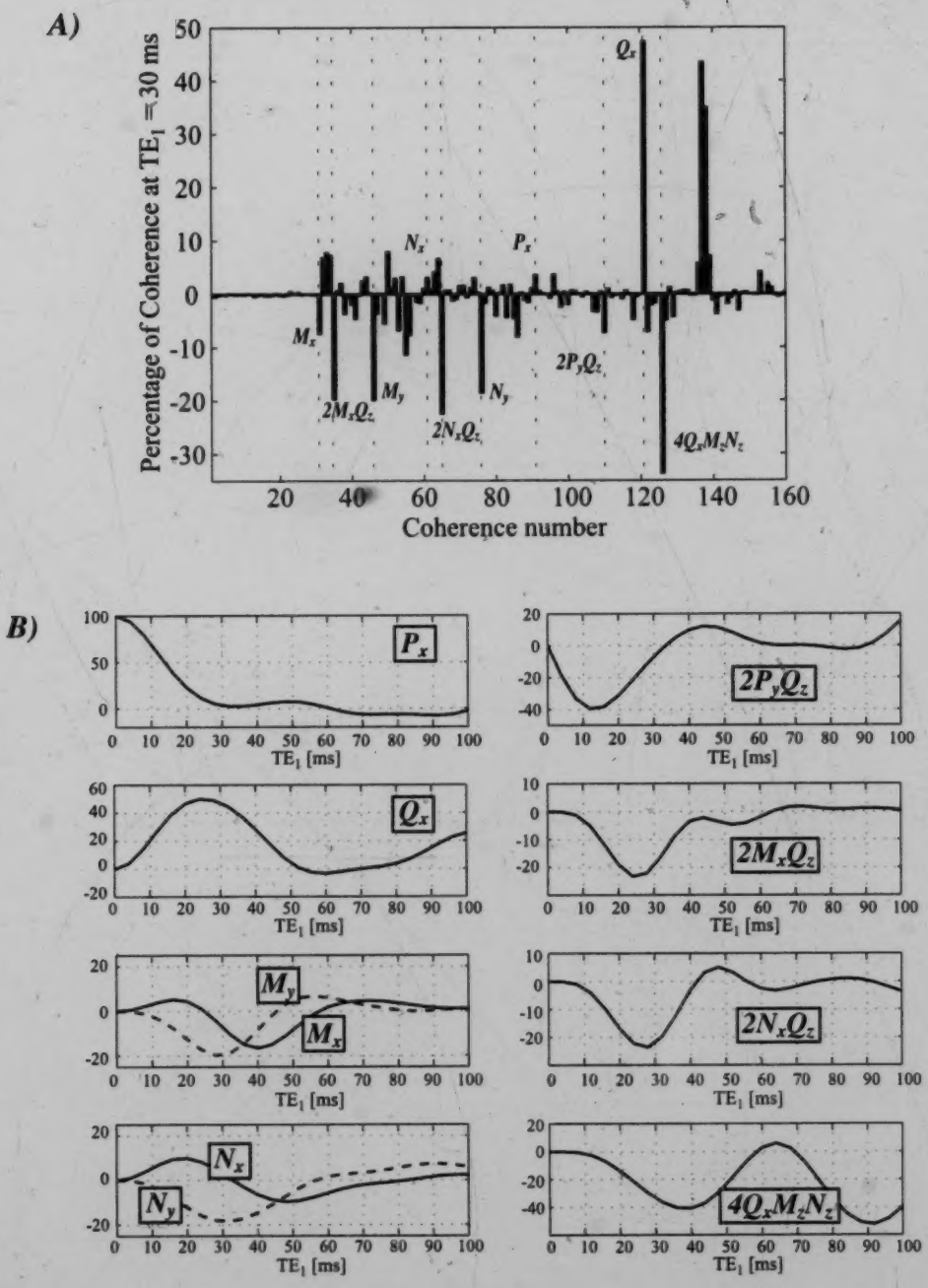

Figure 5-5 (A) A snapshot at TE_1 = 30ms of the distribution across 160 single quantum terms of the AMNPQ spin system of Glu. (B) The variation of several of these terms at TE_1 as TE_1 is varied from 0 to 100 ms, showing the evolution of Glu P-spin magnetization into the coherences of the M, N and Q spins.

For the full PRESS sequence the response of the Glu PQ multiplet in the (TE_1, TE_2) plane, even as shown in Fig. 5-4B, is dominated by the inter-pulse evolution. Although the inclusion of realistic slice-selective refocusing pulses still redistributes the anti-phase coherences, that redistribution does not create significantly more anti-phase terms, as it does for lactate after the first 180° pulse. Instead, in Glu, pulses redistribute anti-phase coherences amongst the large number of terms that have already evolved under the strong coupling and are already finite. The multiplet lineshape (also shown in Fig 5-4) arises from the component lineshapes of an array of coherence terms evolving through the signal acquisition period, some of which yield a net positive intensity while others have negative areas. The proportionately smaller contribution to the line shape from any one of the large number of terms means that the redistribution resulting from the action of selective pulses does not have a dramatic effect on the response. The redistribution evens positive and negative contributions and leads to a loss of intensity. The ultimate influence of slice-selection pulse design is therefore to mitigate the reduction in the intensity of the PQ multiplet by minimizing the redistribution, c.f. Figs. 5-1C to E. The loss of signal from excitation band shifts will also be much less for Glu than for lactate (see Fig. 5-2), since the chemical shift difference between the PQ spins and their coupling partners, the MN spins, is quite small (~30 Hz at 3 T), in contrast to the A and X spins of lactate which are separated by 356 Hz at 3T. Unlike the MN spins, the PQ spins are not coupled to the A spin, 182 Hz upfield at 3.75 ppm (23,24).

Previous product operator treatments of Glu, in which a weak-coupling (A_2M_2 or AM_2X_2) approximation was made (25,26), were unable to predict either the polarization transfers or the proliferation of coherence terms included here with the complete strong-coupling model.

5.4 Experimental Results

Experimental verification of the PRESS calculations was carried out using an aqueous metabolite solution, balanced to a pH of 7.2 and comprising 30 mM Glu and 10 mM creatine (Cr). The solution was placed in either a 1 ℓ flask (for volume selective experiments) or an 8ml sphere for measurements without spatial localization. All experiments were carried out at 3 T in an 80-cm bore magnet (Magnex Scientific PLC, Abingdon, UK), using a home-built 28-cm diameter quadrature birdcage coil for both

transmission and reception. The gradient coils were actively shielded and spectrometer control was provided by a SMIS console (Surrey Medical Imaging Systems PCL, Guilford, UK).

To verify the hard-pulse calculations, rectangular 180° pulses of length 200 μs were employed accompanied by 2 ms spoiler gradients of amplitude 10 mTm^{-1}. Verification of selective-pulse calculations reproduced the optimized sinc pulse of the model with a length 3.5 ms, giving a bandwidth of 1.2 kHz. Concurrent gradients of 1.7 $mT\ m^{-1}$ enabled a 5 ml cubic volume to be selected. The same spoilers were also used in the selective PRESS sequence. Using the Cr 3.05 ppm line as the intensity standard, the experimental and calculated results were compared for both the MNPQ multiplet shape and the peak amplitude of the 2.34 ppm peak across 45° cuts through {TE_1, TE_2} space that (i) maintained TE_1=TE_2 (symmetric PRESS) and (ii) maintained constant TE. On no occasion (36 measurements) did experiments and calculations differ by more than 2%. Figure 5-6 displays the calculated and measured Glu lineshapes following a localized PRESS experiment with timings {TE_1, TE_2} equal to {24 ms, 24 ms} and {30 ms, 78 ms}, where the excellent agreement between calculated and measured lineshape and yield is illustrated.

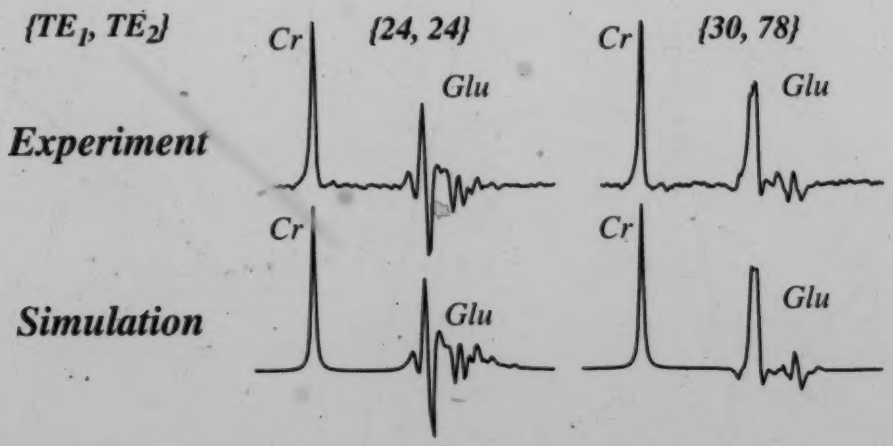

Figure 5-6 Two illustrations of the experimental and calculated Glu response to a localizing PRESS sequence, incorporating the optimized sinc refocusing pulses. The experimental solution spectra were also broadened to 5 Hz through post processing with an exponential multiplication in the time domain. For both timing examples, the measured PQ multiplet peak value is within 2% of the numerically predicted value.

5.5 Summary and Discussion

In general, the temporal modulation of a coupled-spin response to a localizing pulse sequence, e.g., PRESS, will depend on the characteristics of that spin system and on the design of the r.f.pulses. The nature of these modulations (which can be far from intuitive for strongly-coupled spins) determines the shape and intensity of the individual metabolite spectrum, which in turn is used to quantify the metabolite in question. However, the spin-system dependence of these modulations leads to a timing dependence of the total spectrum (which is made up from many spin systems) in which the relative intensities of unit concentration of different metabolites (neglecting all other factors) is quite variable. This is particularly relevant when the intensity of a coupled-spin multiplet is compared with that of an uncoupled singlet for quantification purposes, and it is also very important not to assume that as the timings are changed the intensity of a target metabolite will remain in the same proportion to the background metabolites in the same spectral region. Moreover, the spectral variability arising from the nature of the spin systems can be exacerbated by the design of the selective pulses, leading to the potential for inter-laboratory variability as well. Although it has been shown (27) that in principle an empirical approach of modeling the spectrum should give reliable quantification (if all the multiplet lineshapes, acquired with identical pulse sequences, are known for all possible metabolites across the total extent of the observed spectrum), the modeling approach does not advise the experimenter before the experiment which experimental parameters are the most appropriate for obtaining the optimum spectral yield to background of the target metabolite. The numerical approach provides all this information.

It has been known empirically for some time (8) that weakly-coupled spin systems are not immune from pulse sequence induced effects that are additional to the inter-pulse scalar-coupled evolution. Earlier reports (6,9,11) have outlined some of these effects using product operator methods, but the full numerical solution presented here enables the roll-off characteristics of the pulse, the excitation band shift and the chemical shift evolution during the pulse, all to be included in the response prediction. Focusing on the lactate example, we have demonstrated with the numerical approach (i) the value of introducing a transformation matrix to characterize the action of each selective r.f.pulse design, (ii) the elimination of the high frequency oscillations previously reported

for lactate when observed using PRESS without numerically optimized refocusing pulses (8,9,11) and (iii) the value of the (TE_1, TE_2) plane contour plots to identify when intuition derived from ideal hard pulse experience can seriously undermine performance, namely, the choice of symmetric PRESS sequence with total TE = 2/J.

The majority of metabolites of interest in brain however, contain spin systems that are strongly, not weakly, coupled. Moreover their spin systems often contain five or more spins. Under these conditions a numerical method of solution is the only way to accommodate both the spin system and the pulse design. Focusing on the Glu example, intra-pulse effects are shown to be less of a perturbation for strongly-coupled spins because of the dominating influence of the strong coupling, which drives the proliferation of coherences and the polarization transfer. Previous product operator treatments of Glu, in which a weak-coupling (A_2M_2 or AM_2X_2) approximation was made (25,26), were not capable of predicting either the polarization transfers or the proliferation of coherence terms included here with the complete strong-coupling model. From the full solution, selective pulses clearly reduce the yield (Fig. 5-4), but possibly a more important aspect of the (TE_1, TE_2) plane analysis is the ability to predict the nature of the lineshape (as well as that of the background metabolites) so that the yield and observability can be optimized. From Fig. 5-4 (c.f. Fig.2 of reference 20) it is clear that the MN spin contribution is suppressed in the region of {30 ms, 78 ms} leaving a much simpler spectrum without a penal reduction in yield (to ~ 60%), in practical cases.

Notwithstanding the restriction of this paper to a simple PRESS sequence, it must also be borne in mind the several other localizing sequences also make use of selective 180° refocusing pulses and are therefore affected by the intra-pulse mechanisms. Sequences such as the single voxel *J*-resolved experiment using PRESS (28-30), localized multiple quantum filters (31-33,20), *J*-refocused sequences with even a single refocusing slice selection (25,26), etc., are all sensitive to the effects outlined in this paper. To deal with this, as well as the field strength variation, it is advantageous to apply numerical methods to determine the optimum sequence design for each target metabolite, field strength and localizing sequence. Individual voxels in spectroscopic imaging sequences incorporating PRESS localization (to limit the image ROI) experience, essentially, the hard pulse sequence, if the voxel location is sufficiently distant from the

slice edges. In such cases the timings and yields correspond to the hard pulse model predictions.

5.6 References

1. R. Kreis, T. Ernst, and B. D. Ross, Absolute quantification of water and metabolites in the human brain. II Metabolite concentrations. *J. Magn. Reson.* B **102**, 9-19 (1993).
2. H. P. Hetherington, J. W. Pan, G. F. Mason, D. Adams, M. J. Vaughn, D. B. Twieg and G. M. Pohost, Quantitative ^{1}H spectroscopic imaging of human brain at 4.1 T using image segmentation. *Magn. Reson. Med.* **36**, 21-29 (1996).
3. Y. Wang, S. J. Li, Differentiation of metabolic concentrations between gray matter and white matter of human brain by in vivo ^{1}H magnetic resonance spectroscopy. *Magn. Reson. Med.* **39**, 28-33 (1998).
4. W. Dreher, D. G. Norris and D. Leibfritz, Magnetization transfer affects the proton creatine/phosphocreatine signal intensity: in vivo demonstration in the rat brain. *Magn. Reson. Med.* **31**, 81-84 (1994).
5. T. H. Ernst, and J. Hennig, Coupling effects in volume selective H-1 spectroscopy of major brain metabolites. *Magn. Reson. Med.* **21**, 82-87 (1991).
6. W-I. Jung, and O. Lutz, Localized double-spin-echo proton spectroscopy of weakly coupled homonuclear spin systems. *J. Magn. Reson.* **96**, 237-251 (1992).
7. J. Slotboom, A. F. Mehlkopf and W. M. M. J. Bovee, The effects of frequency-selective RF pulses on J-coupled spin-1/2 systems. *J. Magn. Reson.* A **108**, 38-50 (1994).
8. F. Schick, T. Nagele, U. Klose and O. Lutz, Lactate quantification by means of PRESS spectroscopy influence of refocusing pulses and timing scheme. *Magn. Reson. Imag.* **13**, 309-319 (1995).
9. M. Bunse, W-I. Jung, O. Lutz, K. Kuper, and G. Dietze, Polarization-transfer effects in localized double-spin-echo spectroscopy of weakly coupled homonuclear spin systems. *J. Magn. Reson.* A **114**, 230-237 (1995).
10. I. Marshall and J. Wild, Calculations and experimental studies of the lineshape of the lactate doublet in PRESS-localized ^{1}H MRS. *Magn. Reson. Med.* **38**, 415-419 (1997).
11. I. Marshall and J. Wild, A systematic study of the lactate lineshape in PRESS-localized proton spectroscopy. *Magn. Reson. Med.* **40**, 72-78 (1998).
12. D. A. Yablonskiy, J. J. Neil, M. E. Raichle and J. J. Ackerman, Homonuclear J coupling effects in volume localized NMR spectroscopy: pitfalls and solutions. *Magn. Reson. Med.* **39**, 169-78 (1998).
13. L. Kay and R.E. McClung, Product operator description of AB and ABX spin systems. *J. Magn. Reson.* **77**, 258-273 (1988).
14. T. Nakai, and C. A. McDowell, Product operator theory for ABX spin systems and its application to H-C-C INEPT NMR experiments. *Mol. Phys.* **81**, 337-358 (1994).

15. A. H. Wilman and P. S. Allen, The response of the strongly coupled AB system of citrate to typical ^{1}H MRS localization sequences. *J. Magn. Reson.* B **107**, 25-33 (1995).

16. A. H. Wilman and P. S. Allen, Observing N-acetyl aspartate via both its N-acetyl and its strongly coupled aspartate groups in in vivo proton magnetic resonance spectroscopy. *J. Magn. Reson.* B **113**, 203-213 (1996).

17. R. E. Gordon and R. J. Ordidge, Volume selection for high resolution NMR studies. Abstracts of the Society of Magnetic Resonance in Medicine, 3rd Annual Meeting, New York, p. 272, 1984.

18 P. A. Bottomly, Selective volume method for performing localized NMR spectroscopy. US Patent 4,480,228 (1984).

19. R. J. Ordidge, M. R. Bendall, R. E. Gordon and A. Connelly, Magnetic Resonance in Biology and Medicine (G. Govil, C. L. Khetraplal and A. Saran, Eds.), pp. 387-397, McGraw-Hill, New Dehli, 1985.

20. R. B. Thompson and P. S. Allen, A new multiple quantum filter design procedure for use on strongly coupled spin systems found in vivo: its application to glutamate. *Magn. Reson. Med.* **39**, 762-771 (1998).

21. A. H. Wilman and P. S. Allen, An analytical and experimental evaluation of STEAM versus PRESS for the observation of the lactate doublet. *J. Magn. Reson.* **101**, 102-105 (1993).

22. R. B. Thompson and P. S. Allen, The role of the N-acetyl-aspartate multiplet in the quantification of brain metabolites. Accepted by *Bioch. and Cell Biol.*

23. P. S. Allen, R. B. Thompson and A. H. Wilman, Metabolite-specific NMR spectroscopy in vivo. *NMR in Biomed.* **10**, 435-444 (1997).

24. V. Govindaraju, V. J. Basus, G. B. Matson and A. A. Maudsley, Measurement of chemical shifts and coupling constants for glutamate and glutamine. *Magn. Reson. Med.* **39**, 1011-1013 (1998).

25. J. W. Pan, G. F. Mason, G. M. Pohost and H. P. Hetherington, Spectroscopic imaging of human brain glutamate by water suppressed J-refocused coherence transfer at 4.1 T. *Magn. Reson. Med.* **36**, 7-12 (1996).

26. H. K. Lee, A. Yaman and O. Nalcioglu, Homonuclear J-refocused spectral editing technique for quantification of glutamine and glutamate by ^{1}H NMR spectroscopy. *Magn. Reson. Med.* **34**, 253-259 (1995).

27. S. W. Provencher, Estimation of Metabolite Concentrations from Localized In Vivo Proton NMR Spectra. *Magn. Reson. Med.* **30**, 672-679 (1993).

28. W. Dreher and D. Leibfritz, On the use of two-dimensional-J NMR measurements for in vivo proton MRS: Measurement of homonuclear decoupled spectra without the need for short echo times. *Magn. Reson. Med.* **34**, 331-337 (1995).

29. L. N. Ryner, J.A. Sorenson and M.A. Thomas, Localized 2D J-resolved ^{1}H MR spectroscopy: Strong coupling effects in vitro and in vivo. *Magn. Reson. Imag.* **13**, 853-869 (1995).

30. M. A. Thomas, L. N. Ryner, M. P. Mehta, P. A. Turski and J. A. Sorenson, Localized 2D J-resolved ^{1}H MR spectroscopy of human brain tumors in vivo. *J. Magn. Reson. Imag.* **6** 453-459 (1996).

31. L. Jouvensal, P. G. Carlier and G. Bloch, Practical implementation of single voxel double quantum editing on a whole-body NMR spectrometer: Localized monitoring of lactate in the human leg during exercise. *Magn. Reson. Med.* **36**, 487-490 (1996).

32. J. R. Keltner, L. L. Wald, B. de B. Frederick, and P. F. Renshaw, In vivo detection of GABA in human brain using a localized double quantum filter technique. *Magn. Reson. Med.* **37**, 366-371 (1997).

33. J. R. Keltner, L. L. Wald, P. J. Ledden, Y-C. I. Chen, R. T. Matthews, E. H. G. K. Kuestermann, J. R. Baker, B. R. Rosen, B. G. Jenkins, A localized double quantum filter for the in vivo detection of brain glucose. *Magn. Reson. Med.* **39**, 651-656 (1998).

CHAPTER 6

The Response of Metabolites with Coupled Spins to the STEAM Sequence

6.1 Introduction

Metabolite detection and quantification in vivo with proton spectroscopic methods is most commonly carried out using the spatial localization provided either by the single voxel PRESS (point resolved spectroscopy) (1,2) or STEAM (stimulated echo acquisition mode) (3,4) sequences. The sequence of choice is often determined by the metabolite target. For example, the observation of uncoupled singlet resonances in brain, namely N-acetylaspartate (NAA) at 2.02 ppm, creatine (Cr) at 3.05 ppm and choline (Cho) at 3.2 ppm, are routinely observed with a long-echo PRESS sequence. This stems from the factor of two advantage in signal yield over STEAM and the relatively long T_2 of these resonances compared with either the macromolecular signals or the *J*-modulation envelopes of coupled spins. However, when the target metabolites contain coupled spin systems, short-echo STEAM spectroscopy has gained popularity in the clinical setting, due principally to its robustness at echo times from ~10 ms to ~ 50 ms. Nonetheless, the response of certain key, coupled-spin metabolites to the STEAM sequence, not to mention the background metabolite spectrum, exhibit significant variability. The purpose of this paper is to demonstrate the efficacy of numerical calculations in the determination of the sources of that variability. The range of echo and mixing times considered (TE and TM respectively) is that which is typically regarded as falling into the short-echo experimental range, namely, TE and TM less than ~ 50 ms.

The short-echo-time limit is regarded as desirable for the observation of coupled spins because the longer echo-time modulations of the metabolite line shapes lead, more often than not, to a reduction in intensity accompanied by the appearance of undesirable, oppositely-phased peaks. The mitigation of transverse relaxation losses is a bonus of the shorter echo times. Nevertheless, there are limitations to the minimum sequence lengths attainable with any practical sequence. For example, finite radiofrequency (r.f.) pulse lengths, the time required to play out all the spoiler gradients, and the time allotted for eddy current decay, all contribute to the minimum length. Moreover, unwanted contributions from broad, but short T_2, macromolecular resonances that can affect

quantification are reduced if the short-echo-time limit is not pursued too vigorously. As a result of these competing factors, the shorter echo-time applications of STEAM have been reported over a range of echo and mixing times between 10 and 50 ms.

The variability in the coupled-spin response to STEAM arises from the creation and evolution, in various parts of the sequence, of time dependent anti-phase coherences and zero quantum coherences (ZQCs), both of which influence the magnitude of components that ultimately contribute to the observable line shape. The amplitude of each of these coherence types can be significantly influenced by elements of the sequence, such as r.f. and gradient pulse characteristics and inter-pulse timings, giving rise to pulse design, TE and TM dependent variations in the measured line shape and intensity. Using numerical techniques (5) which employ the density matrix representation of nuclear spin systems (see chapters 1 and 2), we have evaluated the production and evolution of all coherence terms for several spin systems as a function of pulse design, TE and TM. This knowledge enables a TE-TM contour plot of signal intensity to be generated for any pulse design, so that the sequence elements can be optimised for the best yield and background discrimination. The same knowledge can also provide the prior information needed by non-parametric spectral fitting methods (6-8). These fitting methods employ as basis functions the full-width spectra of each metabolite, and although these basis spectra could be obtained experimentally from a collection of individual phantoms (9), it is far more efficient to derive them numerically.

In a PRESS sequence, the coupled-spin response predicted by a hard-pulse model (reflecting manual, product-operator calculations) can differ substantially from the predictions of a full numerical solution that accommodates a selective 180° pulse design (5). In contrast to PRESS, the influence of the selective 90° pulse design of a practical STEAM sequence is not so great, it is however, finite, particularly when higher field strengths are used (>1.5 T). With STEAM therefore, the efficacy of numerical methods stems largely from the need to clarify the substantial effects of the coupling rather than the need to deal with pulse design. A full determination of the response to STEAM for the weakly-coupled example, lactate (AX_3), is compared below to the previously published product operator analyses (10), which assume rectangular pulses and non-concurrent gradients. To illustrate the strongly-coupled regime, the sequence

dependence of the aspartyl signal from the ABX group of NAA is quantified, as is that of the PQ and MN multiplets of the AMNPQ spin system of glutamate (Glu).

6.2 Numerical Methods

When spins are not coupled, their response to the STEAM sequence is well represented by a vector model, leading to the well known 50% yield of the sequence (3,4,11). For spins that are coupled, product operator analyses of STEAM have been undertaken. However, these anlayses have been confined to simple examples of coupled-spin systems, i.e., the weakly coupled AX_2 system of lactate (10), the strongly-coupled AB system of citrate (12-14), and the AB spins of the NAA aspartyl ABX group (15). In brain, many key metabolites have the more demanding strongly-coupled spin systems, and, apart from some qualitative considerations over a limited range of echo and mixing times (16), their response to STEAM has not been evaluated. To calculate this response, it is necessary to solve the Liouville-von Neumann equation for the time-dependent density operator of the spin system, outlined in chapters 1 and 2. The Hamiltonian used in our calculations included, in addition to the Zeeman interaction, the r.f. pulses, the gradient pulses, the different chemical shielding interactions and the several scalar coupling interactions. No approximations were made for weak coupling.

6.3 The STEAM Sequence

Modeling of the STEAM sequence, shown in chapter 2, Fig. 2-8, requires, in addition to the r.f. pulses, the incorporation of three independent sets of gradients, namely, slice selection, echo and mixing gradients. Schematically, the inter-pulse evolution of coherence types that are influential in causing the STEAM output variability is illustrated in Fig. 6-1. The first of these, arising after the first 90° pulse, is the mixture of in-phase and anti-phase coherences which evolves from in-phase transverse magnetization during the first TE/2 period. The evolution is governed primarily by the scalar coupling but is also influenced by the field-strength-dependent chemical shift difference. The chemical shift (and field inhomogeneity) dephasing is ultimately recovered for the spins of the target voxel through the action of the pair of echo gradients and the second and third selective 90° pulses.

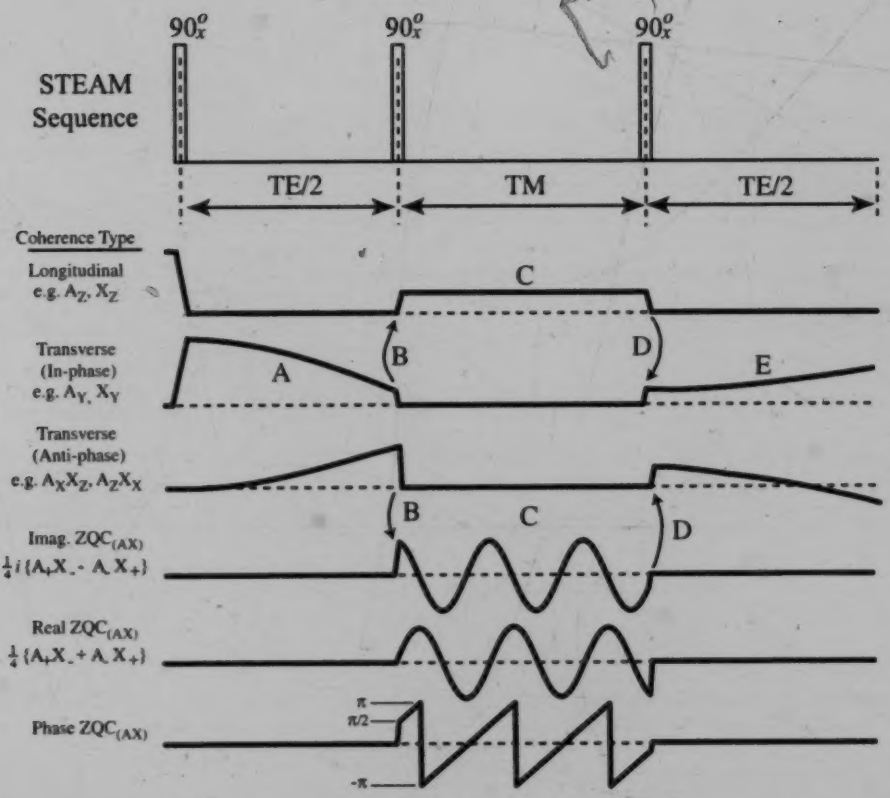

Figure 6-1 A schematic diagram of the evolution of the coherence types which are significant in determining the coupled-spin response to the STEAM sequence. The spoiler gradients commonly applied in both the echo and mixing periods are not shown in this qualitative diagram. A) Following excitation, the transverse magnetization evolves into a mixture of in-phase and anti-phase coherence. B) The second 90° pulse tips the in-phase coherences to the longitudinal plane and the anti-phase coherences to a mixture of zero quantum coherence (ZQC) and higher order coherences. C) A spoiler gradient (not shown) applied in the mixing section dephases all coherences save for the gradient insensitive terms, namely, the longitudinal and zero quantum terms. The ZQCs evolve between real and imaginary states while the longitudinal terms are static. D) The final 90° pulse tips the longitudinal magnetization back to the transverse plane, but tips only a portion of the ZQC back to anti-phase coherence because of the phase-sensitivity of this process. This phase-sensitivity results in a time dependent (TM) production of anti-phase coherences immediately following the last 90° pulse. E) In the final TE/2 evolution period the in-phase coherence evolve into a final mixture of transverse coherences which will determine the metabolite line shape and yield.

The second influential coherence type is the zero quantum coherence (ZQC) group, which is generated by the second 90° pulse and which exhibits an oscillatory

evolution during the mixing period, TM, as shown in Fig. 6-1. The magnitude of the antiphase terms (at the end of the first TE/2) that are convertable to multiple quantum coherences by this second pulse (this includes ZQC), is governed by the choice of TE. In the subsequent TM the mixing gradient, a filter mechanism designed to destroy all gradient sensitive magnetization, does not affect either the ZQC or the longitudinal magnetization. However, it radically dephases the transverse magnetization and higher orders of multiple quantum coherence. The evolution of ZQC during TM (to be described more fully below) determines the magnitude and character of an important set of antiphase coherence terms produced by the third 90° pulse. That set evolves to contribute to the signal during the acquisition period.

6.3.1 R.F. Pulse Design Effects

To isolate the effects of r.f. pulse design from those of inter-pulse evolution is not as straight forward in STEAM as it is in PRESS (5). In contrast to PRESS, where the selective 180° refocusing pulses can be treated independently, the second and third selective 90° pulses of STEAM, together with the echo and mixing time gradients, act in concert to generate the stimulated echo. To demonstrate the difference between a selective-r.f.-pulse-gradient-pulse package, and a hard-pulse-gradient-pulse package with the same 90° tip angles, it is necessary to artificially reduce TM in order to eliminate inter-pulse evolutions and hence isolate the effects of the pulses. In Fig. 6-2 the difference between these packages is summarized in transformation matrices, where the elements of each row of a matrix reflect the ability of the r.f.-gradient package to convert a particular density operator component either into itself or into another component (5). Comparing Figs. 6-2A) and 6-2B) it is evident that practical selective pulses have effects comparable to those predicted with a hard-pulse model. In both cases, the generation of the unexpected off-diagonal elements is due primarily to the coupled spin evolutions arising from the scalar coupling and chemical shift interactions, although the differences between the transformation matrices do reflect a measurable selective pulse influence as compared to the hard pulse model.

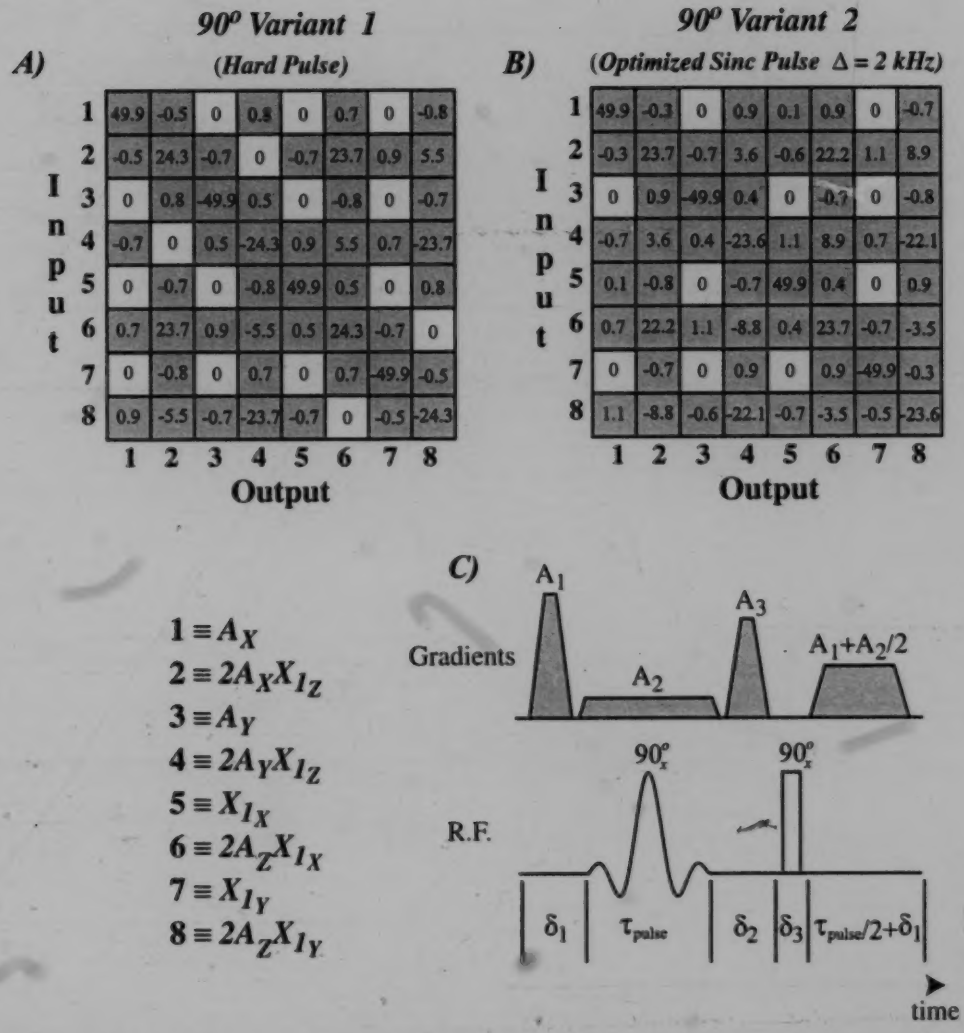

Figure 6-2 A) and B) display lactate transformation matrices for the 2nd STEAM pulse, both for a hard pulse and a realistic sinc-like pulse (A numerically optimized 2 kHz $\pi/2$ pulse, generated with the SLR algorithm in MATPULSE (17)). The matrices display the influence of the STEAM refocusing pulse pair, shown in C), as the transformation of each of the eight input SQ coherences to a mixture of same eight terms following the pulse pair. To validate the direct comparison between these very different pulses, δ_1 and δ_2 are set to infinitesimal for B), and τ_{pulse} to 3.675 ms, while δ_1 and δ_2 are set to 3.675/2 ms in A), keeping the total sequence length identical for both cases. The in-phase SQC terms (odd) return ~ 50% as expected, while the anti-phase SQC terms (even) return a maximum of 25% to the input term, as well as a maximum of 25% to the coupled spin term, for example, term 2 and term 6, respectively. The small differences between the matrices in A) and B) reflect the validity of the hard pulse model in predicting the complete slice-selective pulse response.

Another consequence of the selective pulse design which needs to be considered is its effect on the voxel size and shape for each of the coherence terms, because this affects the ultimate metabolite yield (and lineshape). It is the second and third pulses of the STEAM sequence which act on a distribution of coherences, and Fig. 6-3 illustrates the degradation of the uncoupled spin voxel shape (Fig. 6-3A), when an in-phase coherence (Fig. 6-3B) and an anti-phase coherence (Fig. 6-3C) are followed from the first TE/2 period through to acquisition.

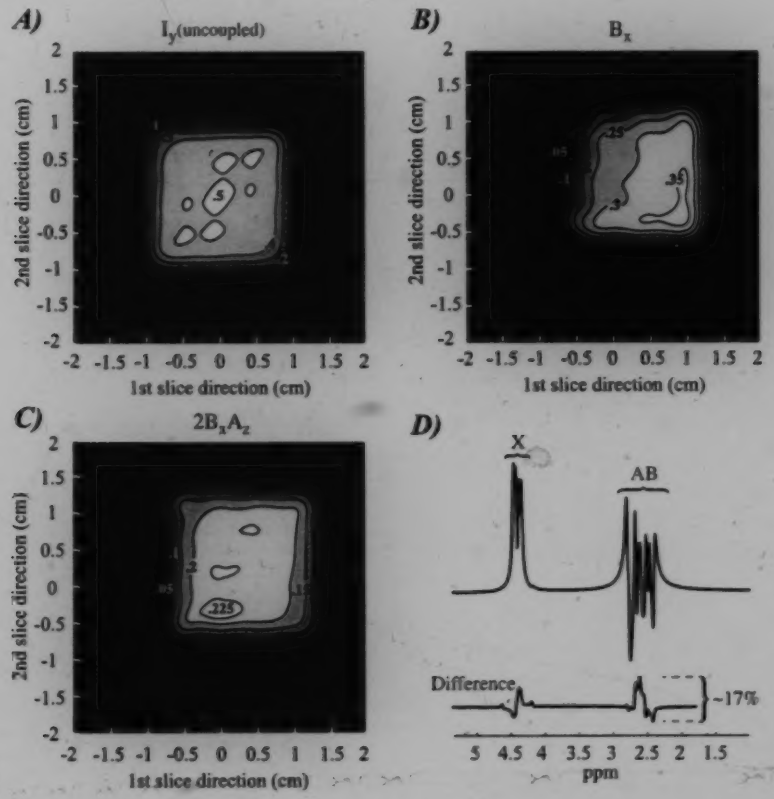

Figure 6-3 An illustration of selective pulse 2D definition effects for strongly-coupled spins responding to STEAM with TE = 30 ms and TM = 35 ms. Panel (A) shows the spatial distribution of transverse magnetization, I_y, for an uncoupled spins resonating at the transmitter frequency. Shallow modulations in the excitation plateau give rise to the spotty 50% level of excitation. Panel (B) shows the spatial distribution of the in-phase NAA term B_x while (C) shows that of the anti-phase B_xA_z. The volume-integrated aspartyl multiplet resulting from the selective pulse sequence is shown in (D), together with its difference from the predictions of the hard-pulse model. This difference is quantified relative to 50% of the pulse-acquire signal amplitude.

6.3.2 ZQC Effects in TM

A potentially larger influence on the ultimate lineshape is the evolution of ZQC terms in TM. For example, in the simplest weak coupling example of an AX spin system, the chemical shift Hamiltonian causes an oscillation between real, $\frac{1}{4}\{A_+X_- + A_-X_+\}$, and imaginary, $\frac{1}{4}i\{A_+X_- - A_-X_+\}$, components of $ZQC_{(AX)}$ at a frequency, $\delta\omega$, that is equal to the chemical shift difference between the coupled spin species. When more than two spins are involved in the weak coupling between two spin species, e.g., the AX_3 system of lactate, additional terms can evolve from a single component of $ZQC_{(AX_3)}$ due to the scalar coupling Hamiltonian. Such evolutions that occur for lactate are illustrated in Figs. 6-4A to 6-4C. If the coupling is strong, the frequency of ZQC oscillation falls below $\delta\omega$ and the scalar coupling also facilitates coherence transfer between ZQC terms that involve different spins. For example, in an ABX system such as the aspartyl group of NAA, components of $ZQC_{(AX)}$ will evolve into components of $ZQC_{(BX)}$. Figures 6-4D to 6-4G illustrate how a single initial component, namely, the imaginary term of $ZQC_{(AX)}$, will evolve over a mixing period of 50 ms, into several other zero order terms.

As illustrated in Fig. 6-1, the density matrix comprises longitudinal and ZQC terms, exclusively, during the STEAM mixing period. The remaining terms are gradient sensitive, and are dephased by the mixing gradient. For a weak-coupling model (for example, the lactate AX_3 group), the TM dependence of the STEAM signal arises exclusively from the ZQC evolutions, while, on the other hand, the existence of strong coupling (for example, the NAA ABX group) facilitates the generation of ZQC and DQC terms directly from longitudinal magnetization (15). The numerical approach incorporated in this report includes this coherence pathway, but the contributions to the STEAM signal variability are insignificant for the strongly coupled spin groups found in-vivo, so are not presented explicity.

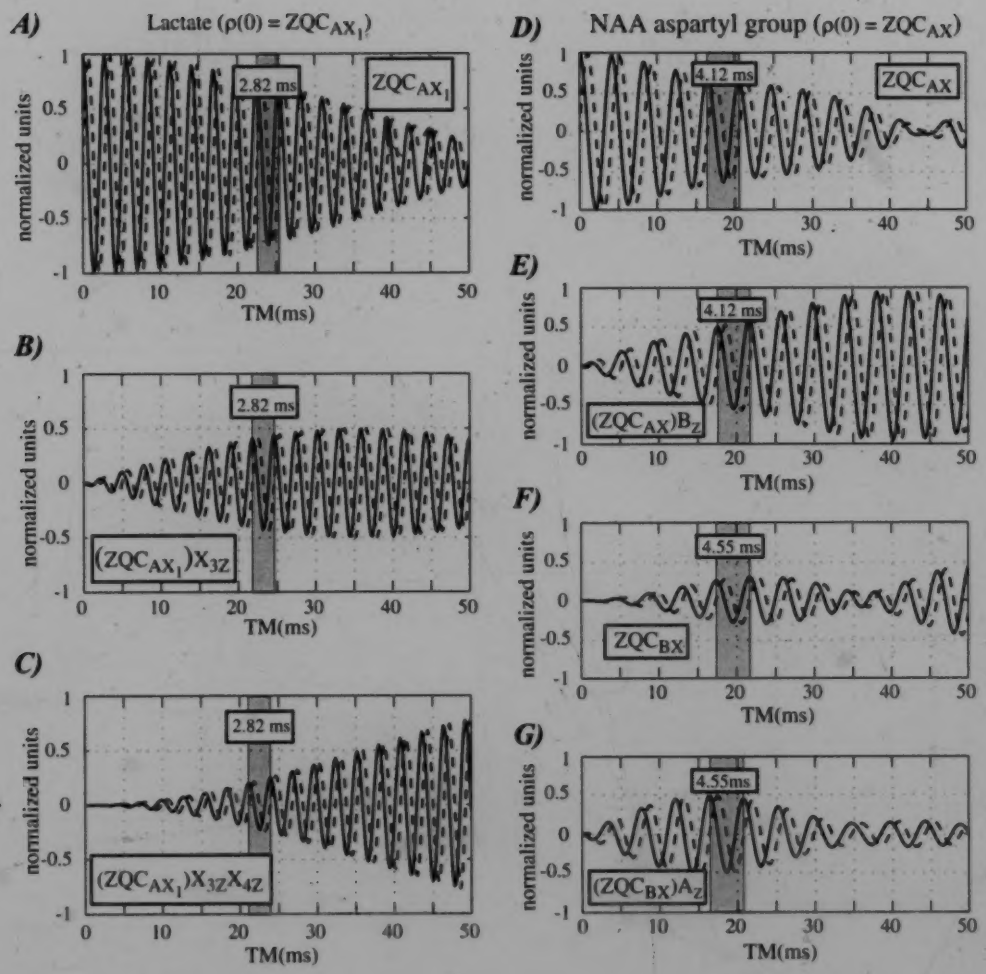

Figure 6-4 Panels (A) to (G) display the evolution of zero order terms over a period of 50 ms. The full lines denote imaginary components and the dashed lines, the real components. From an initial state of a lactate spin system, AX_3, that comprises only the imaginary component of $ZQC_{AX_1} = \{A_X X_{1_Y} - A_Y X_{1_X}\} = \frac{1}{4} i \{A_+ X_- - A_- X_+\}$, the two term ZQC's shown in (A) evolve to three term ZQC's, (B), as well as four term ZQC's, (C), through the scalar coupling interaction. Panels (D) to (G) display similar evolutions for the ABX spin system of NAA. The initial state again comprises a single imaginary component, namely, ZQC_{AX}. Like the AX_3 system of lactate, the two term ZQC's of NAA evolve into three term ZQC's, as shown in (E). Unlike lactate however, the strong coupling of the AB group results in coherence transfer, giving rise to ZQC_{BX}, as shown in (F). The ZQC_{BX}, like ZQC_{AX}, evolves under the scalar coupling Hamiltonian to produce three term ZQC's as shown in (G). In the interest of brevity, the contributions from the ZQC_{AB} terms are not displayed.

6.3.3 The Acquisition Period

Notwithstanding the fact that only in-phase transverse magnetization terms are detectable, the evolution between terms predetermines that a metabolite yield and line shape will be governed by the distribution over anti-phase, as well as in-phase, transverse coherences at the onset of the signal acquisition period. Stated mathematically, the response of an N spin, I = 1/2, system is determined by the density operator at the start of acquisition, $\sigma(TE,TM)$, which can be expressed as a weighted sum of the complete set of product operator basis terms. Of these 2^{2N} terms, there are $Nx2^N$ that will give rise to observable magnetization, the T_k, and others which do not lead to observable signals, i.e.,

$$\sigma(TE,TM) = \sum_{k=1}^{N2^N} a_k(TE,TM)T_k \; + \; \text{non-observable terms,} \qquad (6\text{-}1)$$

where the weighting coefficients, a_k, are in general functions of trigonometric terms whose arguments depend on scalar coupling coefficients and chemical shifts, as well as on TE and TM. Although each of the $Nx2^N$ single quantum (transverse) terms will evolve during acquisition, that evolution produces line shape components characteristic of the originating coherence. The overall lineshape can therefore be determined from the onset coherence distribution as a weighted sum of these characteristic lineshape components, the weighting being governed by the magnitude of the coherence term from which the component originated.

The coherence distribution at the onset of acquisition arises from the action of the third 90° pulse followed by evolution during the final TE/2 period. The action of the third 90° pulse is to generate in-phase coherence from the stored longitudinal magnetization and to transform imaginary components of the ZQCs of the coupled spins back into anti-phase coherences. The magnitude of the anti-phase coherences is critically dependent upon the ZQC phase evolution and the coherence transfer occurring during TM. In the case of the lactate doublet, although the three categories of ZQC, shown in Figs. 6-4A to 6-4C, give rise, in principle, to three corresponding varieties of anti-phase coherence, only one of these (A_xX_y, etc) can evolve into observable doublet magnetization in the weak-coupling limit. Nevertheless, its magnitude is modified by the

growth of the other terms. Even in this simple case, the numerical approach facilitates, by means of a contour plot (Fig. 6-5) a clear overview of the influence of TE and TM on the intensity of the lactate doublet for a realistic localizing STEAM sequence.

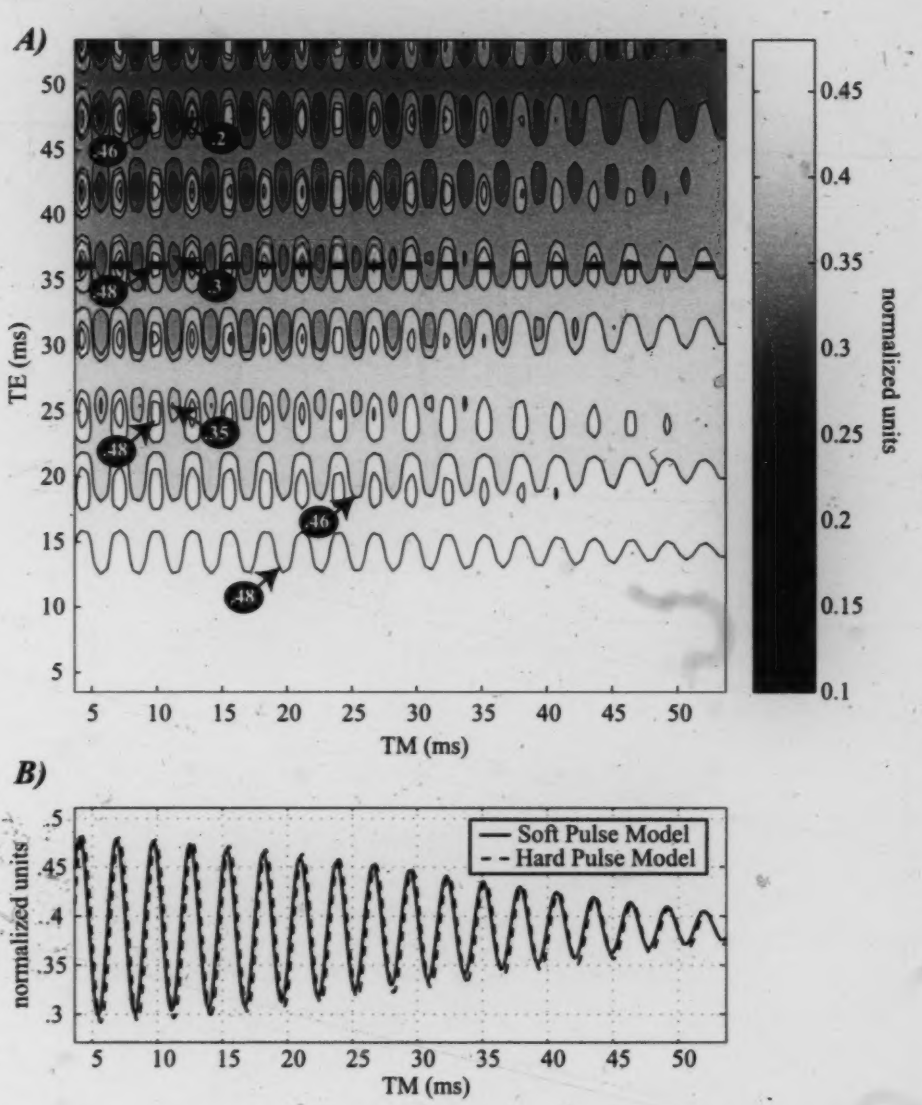

Figure 6-5 The lactate X_3 yield (area) is displayed in panel (A) as a contour plot in TE-TM space. In panel (B) a contour profile along a cut at a constant TE of 36.8 ms emphasizes the sensitivity of the doublet area to small variations in TM. The influence of including optimized spatially selective $\pi/2$ pulses (17) is indicated by the comparison with the hard pulse product operator predictions provided by the dashed line.

Cuts through the contours at specific TE or TM display a very similar oscillatory behavior to that originally calculated for such cuts using product operator techniques (11). When 3.675 ms optimized (17) sinc 90° pulses are used (bandwidth 2 kHz), the amplitudes and frequencies shown in Fig. 6-4 differ by less than 5% from the hard pulse predictions of references (11).

For the strongly-coupled NAA aspartyl ABX group, coherence transfer during TM, from $ZQC_{(AX)}$ (Fig 6-4D) into $ZQC_{(BX)}$ (Fig 6-4F) for example, gives rise to the possibility of eight zero-order components evolving from the single imaginary $ZQC_{(AX)}$, four of which transform to antiphase coherence that can evolve into observable signal following the third 90° pulse. The other initial ZQC terms will clearly give rise to additional components at the end of TM. This proliferation of ZQC terms for strongly-coupled groups of spins significantly complicates the dependence of the metabolite response to changes in TM. To illustrate this, the acquisition onset contours of two representative single-quantum transverse terms that contribute to the AB multiplet centred at ~ 2.6 ppm are shown in TE-TM space in Fig. 6-6. Contributions to each of these terms arise from several component sources. The sources are reflected in the complexity of the contour plots (Figs 6-6A, 6-6B) but seen most easily in the cuts along TM shown in Figs 6-6C and 6-6D. For example, the representative in-phase term, B_x, receives contributions from the longitudinal magnetization stored in TM, as well as the $ZQC_{(AB)}$ and $ZQC_{(BX)}$ that evolved during TM and were converted to anti-phase coherence by the third 90° pulse. The relative influence of the two ZQC contributors can be gleaned from the oscillation periods, 4.12 ms for $ZQC_{(BX)}$ and 35.6 ms for $ZQC_{(AB)}$. The difference in period arises from the chemical shift difference at 3T between the coupled spins of each ZQC. The anti-phase example, $2B_xX_z$, shows its $ZQC_{(BX)}$ source, oscillating in TM with a period of 4.12 ms, most clearly.

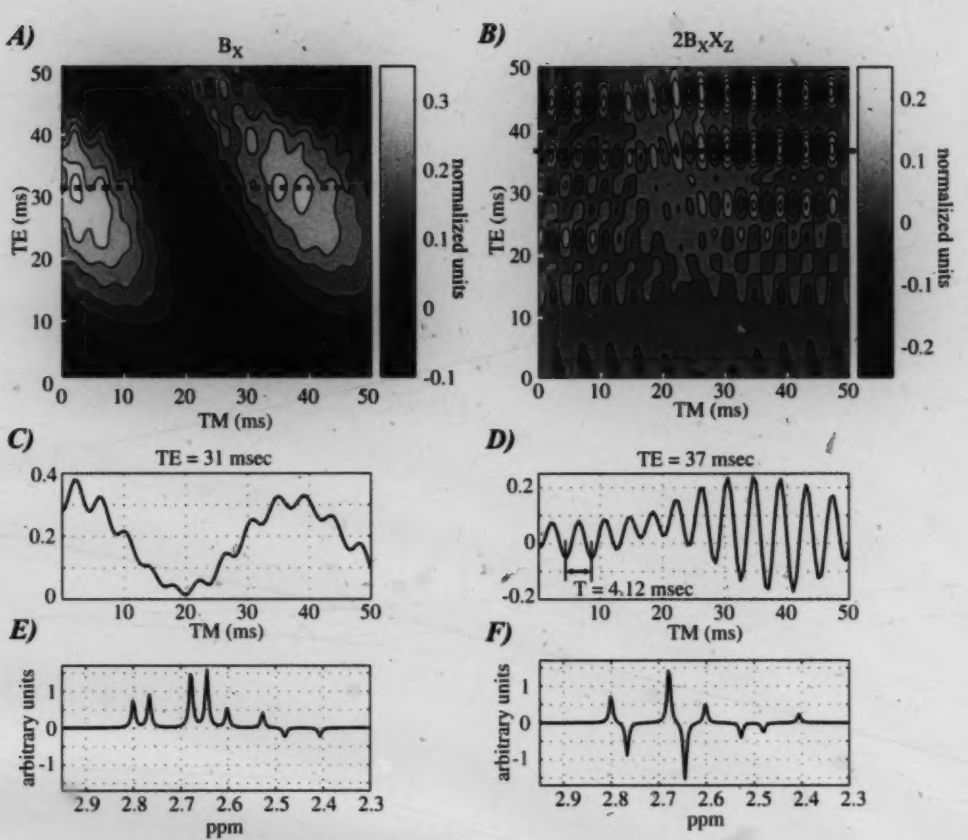

Figure 6-6 The TE and TM dependence of two representative NAA aspartyl product operator terms at the onset of the acquisition period of a STEAM sequence. The in-phase term, B_x, is shown in panel (A) and the anti-phase term, $2B_xX_z$, is shown in (B). They are displayed over TE-TM time intervals of 0 to 50 ms. In panel (C) the variation of B_x along the TE=32 ms cut, shows the dominance of $ZQC_{(AB)}$ as its source through the 35.6 ms period. The lineshape component associated with the B_x term is shown in (E). The more rapid variation of the $2B_xX_z$ term with changes in TM is illustrated in (D) at TE = 37 ms, where the $ZQC_{(AX)}$ and $ZQC_{(AB)}$ oscillation frequencies are both apparent. The B_xX_z lineshape component is shown in (F).

Besides having a unique TE and TM dependence, each of the $N \times 2^N = 24$, transverse ABX terms in NAA also has a characteristic line shape contribution, weighted by the acquisition-onset value of the coherence. The B_x and B_xX_z lineshape contributions are shown in Figs. 6-6E and 6-6F. The overall lineshape and yield therefore exhibit a complex dependence on TE and TM. This is illustrated in Fig. 6-7A, where a map of the peak value of the NAA aspartyl AB multiplet is displayed in TE-TM space.

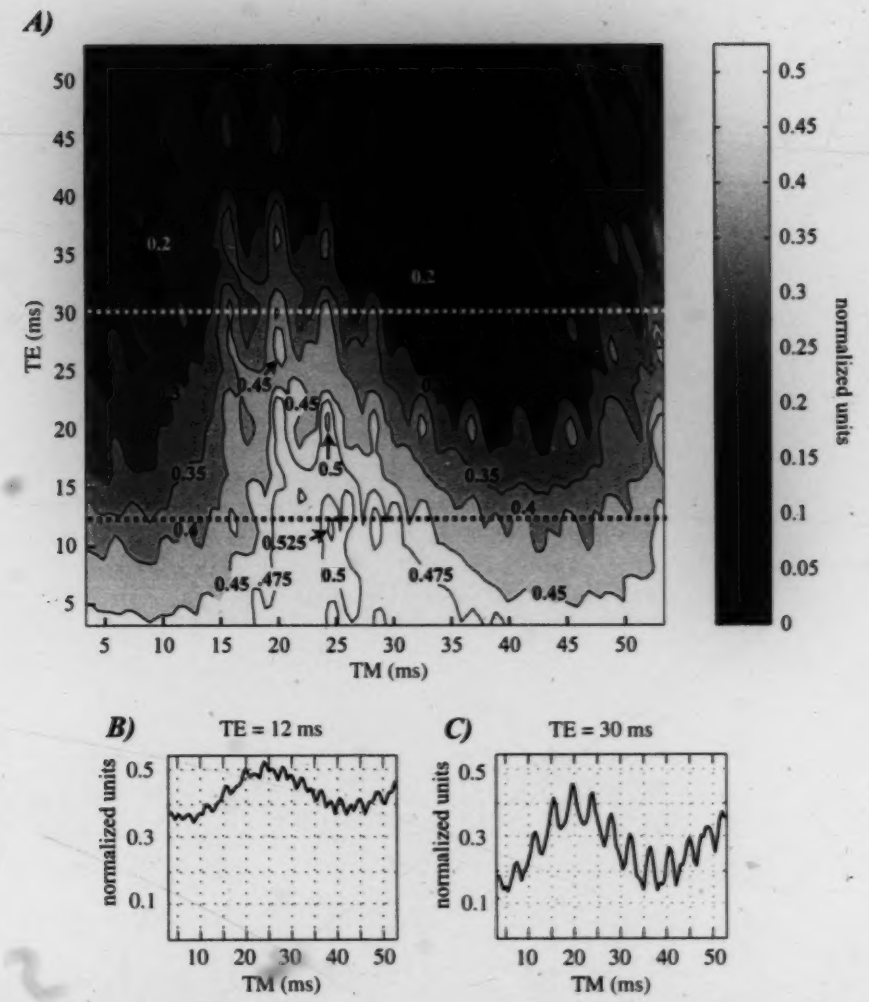

Figure 6-7 Panel (A) shows a contour plot of the peak value (at ~ 2.6 ppm) of the NAA AB multiplet in TE-TM space. All values are normalized to the peak value of the pulse-acquire spectrum. An exponential linewidth of 5 Hz was incorporated to approximate in-vivo conditions. Cuts through the contours at constant TEs of 12 ms in panel (B), and 30 ms in panel (C), emphasize the rapid modulation of the NAA AB yield with changes in the mixing time TM.

Because of the significant changes in lineshape, (see Fig. 6-8), the spectral location of this peak value is not unique, but remains in close proximity to 2.6 ppm. The contour data were generated from the calculated spectra at intervals of 0.5 ms along each of the TE and TM axes from 0 ms to 50 ms, for a total of 10201 spectra. Cuts along TM

at constant TE (Figs 6-7B and 6-7C) demonstrate two points. First, both the high frequency ($ZQC_{(AX)}$ and $ZQC_{(BX)}$) and the low frequency ($ZQC_{(AB)}$) modulations in TM are clearly reflected in the AB multiplet yield. Secondly, even at very short echo times, TE = 12 ms, the large scalar coupling between the A and B spins (15.5 Hz) results in the production of AB anti-phase coherence in the first TE/2 period, giving rise to a significant amount of $ZQC_{(AB)}$ in TM, and a reduction in yield (See Fig. 6-7B) to ~ 65% of that seen for uncoupled spins. At longer echo times, e.g., TE = 30 ms in Fig. 6-7C, the yield is further suppressed relative to uncoupled spins and the increased amplitude of the $ZQC_{(AX)}$ and $ZQC_{(BX)}$ components makes the yield significantly more variable with TM. Although the numerical and experimental phantom spectra, shown in Fig. 6-8, demonstrate, the agreement between calculation and experiment, they also demonstrate quite strikingly, the variability of the lineshape and yield of the strongly-coupled AB multiplet relative to the singlet resonance of NAA falling at 2.02 ppm.

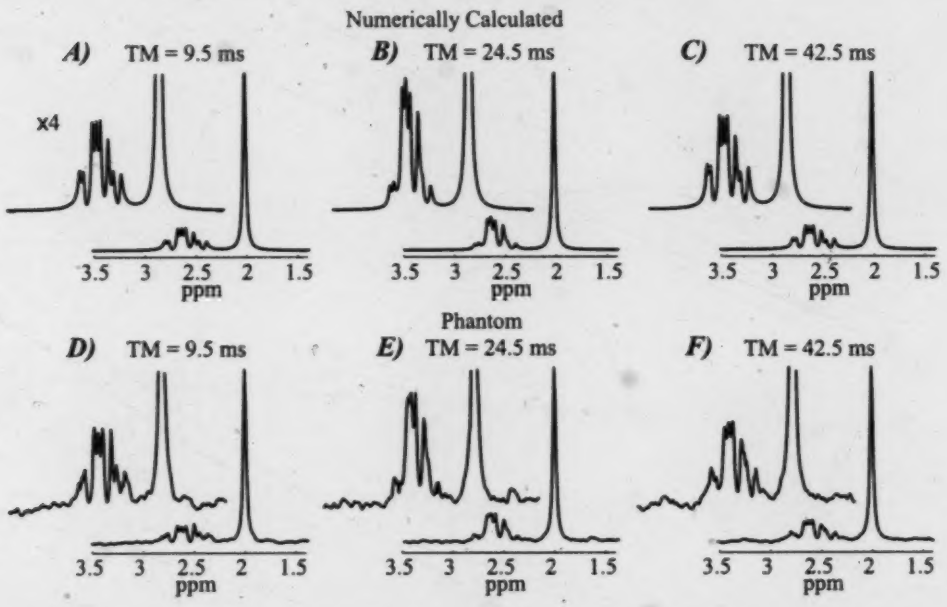

Figure 6-8 (A-F) Calculated and experimental phantom NAA spectra illustrating the TM dependence of the AB multiplet for a TE of 12 ms in panels A to F. Neglecting relaxation, the peak value of the NAA singlet at 2.02 ppm remains fixed at 1.0, independent of changes in TE or TM. For all spectra a linewidth of 5 Hz was incorporated to approximate in-vivo conditions.

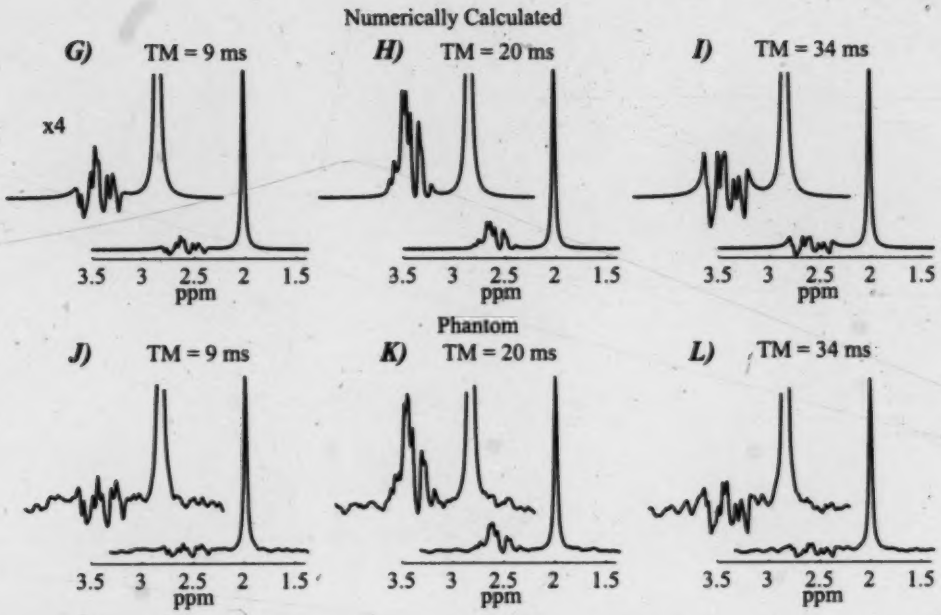

Figure 6-8 (G-L) Calculated and experimental phantom NAA spectra illustrating the TM dependence of the AB multiplet for a TE of 30 ms in panels G to L. Neglecting relaxation, the peak value of the NAA singlet at 2.02 ppm remains fixed at 1.0, independent of changes in TE or TM. For all spectra a linewidth of 5 Hz was incorporated to approximate in-vivo conditions.

For the strongly-coupled AMNPQ system of Glu, there can exist as many as 220 zero-order components during TM. Relatively speaking, this makes each of the individual contributions less significant than was the case for each ZQC terms of the ABX group of NAA. The outcome is a smoother response in TE-TM space. For example, if we omit a term by term discussion in the interests of brevity and focus on the resulting spectral response, we find that at 3 T and a 5 Hz linewidth the dominant PQ multiplet (5,18) appearing between 2.25 ppm and 2.45 ppm (~ 25Hz at 3T), maintains a relatively stable triple-peak character (see Fig. 6-10). Relative to Cr there is gradual loss in intensity with increasing TE, and slow oscillations with changes in TM. The TM modulation of the outer PQ peaks is significantly greater than that of the central peak and this is demonstrated in Fig. 6-10, which displays both numerically calculated and phantom Glu STEAM spectra, measured at an echo-time of 18 ms. In Fig. 6-9, the calculated area of the upfield Glu PQ peak (identified in Fig. 6-9A), is displayed as a cut along TM at a constant TE = 18 ms in Fig. 6-9B and as a TE-TM contour plot in Fig. 6-

9C. The contour data was generated in a manner identical to that for NAA. Both Figs. 6-9B and 6-9C demonstrate a characteristic evolution period of ~ 28 ms. This period arises from an averaged chemical shift difference between the PQ and MN groups (18,19), i.e. ~ 0.266 ppm (~ 34 Hz at 3T).

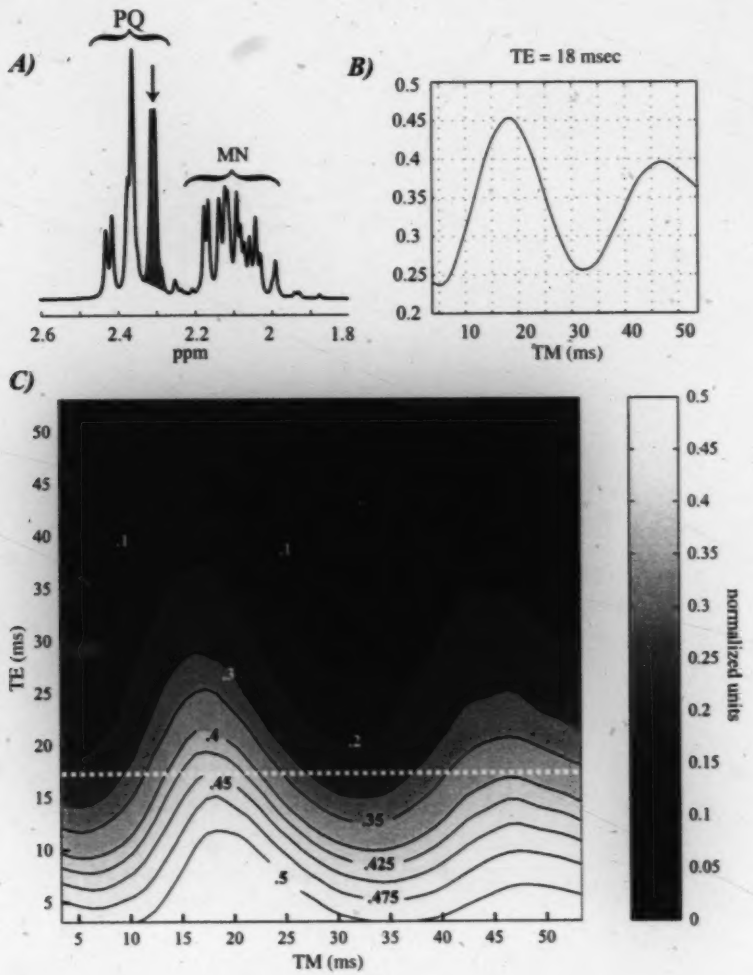

Figure 6-9 An illustration of the TE-TM space dependence of the upfield peak of the PQ multiplet at 2.31 ppm. Panel (A) identifies the upfield peak and panel (B) illustrates the variation in its amplitude at TE = 18 ms as TM is varied. Panel (C) shows the contours of this peak area in TE-TM space. The contours are normalized to the 2.31 ppm peak area from a pulse-acquire spectrum.

Numerical and experimental phantom spectra, shown in Fig. 6-10, demonstrate the agreement between calculation and experiment, highlighting the variability of the upfield PQ resonance with changes in the STEAM mixing time, TM.

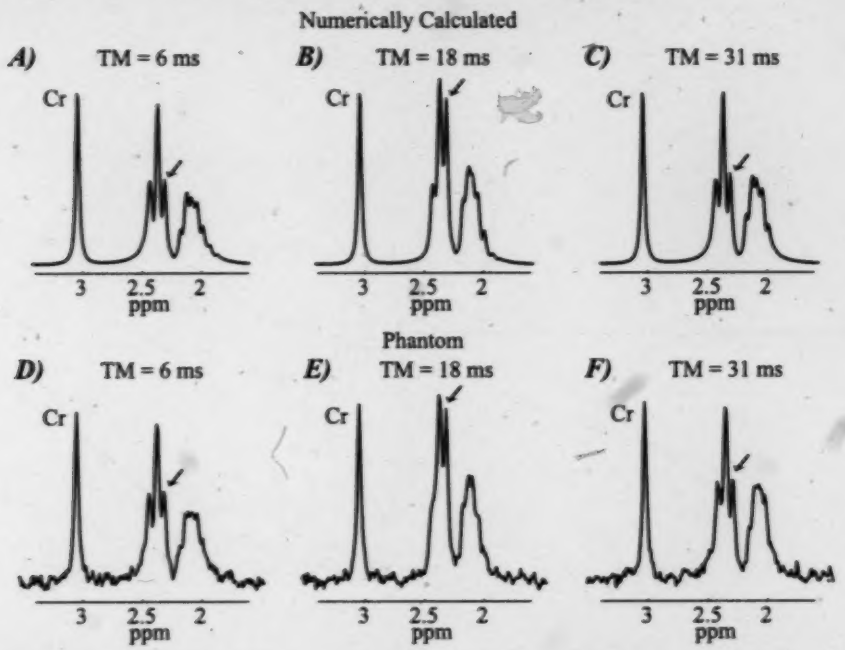

Figure 6-10 A comparison of calculated and experimental phantom spectra for the MNPQ multiplets of Glu together with the 3.05 ppm Cr singlet resonance (TE = 20 ms). The phantom solution contained 30 mM Glu together with 10 mM creatine (Cr). A 5 Hz linewidth was incorporated in all spectra to approximate in-vivo conditions.

6.4 In-Vivo Validation

In the spectral region between 2 ppm and 3 ppm more metabolites contribute to the in-vivo proton spectrum than the strongly coupled NAA and Glu treated in detail above. They include aspartate (Asp) which behaves similarly to the aspartate group of NAA, glutamine (Gln) which behaves similarly to Glu, as well as γ-aminobutyric acid (GABA). Additionally, NAAG contains both aspartate and glutamate groups. In-vivo spectra, acquired at 3 T from a 2.5x2.5x2.5 cm^3 volume located in the temporal lobe of a healthy volunteer are shown in Fig. 6-11A. As expected, the uncoupled methyl singlets of NAA (2.02 ppm), Cr (3.05 ppm) and Cho (3.24 ppm) are essentially unchanged by the increment in mixing time from 20 ms to 34 ms at the constant echo time of 30 ms. However, considerable spectral differences are produced by the TM change in the

coupled-spin resonances between 2.02 ppm to 2.8 ppm. To interpret these spectra either the calculated metabolite spectra can be used to model the in-vivo spectrum and extract the concentrations as unknowns, or the literature values for normal concentrations can be used to generate a normal in-vivo spectrum from the calculated metabolite spectra. The former procedure was adopted, giving rise to the best fit calculated spectra shown in Fig. 6-11B.

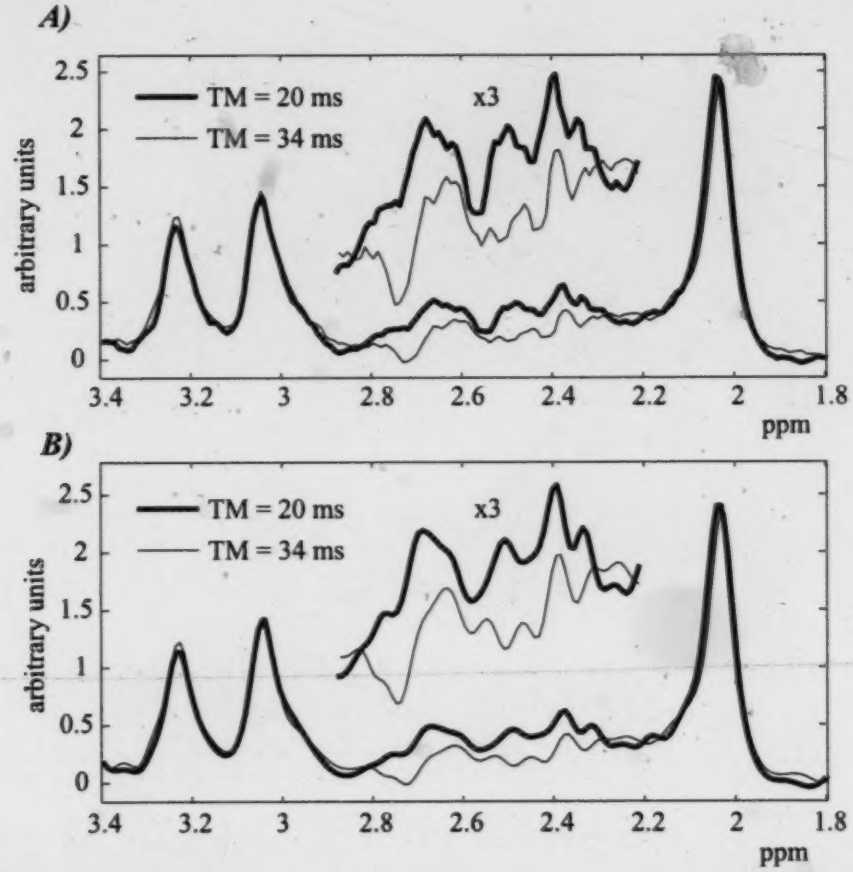

Figure 6-11 A demonstration of the fitting of two in-vivo, proton, brain spectra acquired at 3 T using pulses identical to those used in the numerical simulations. The heavier lines in both the experimental (A) and fitted (B) spectra correspond to (TE, TM) timings of (30 ms, 20 ms), whereas the lighter lines correspond to (30 ms, 34 ms). The in-vivo spectra were acquired from a 15.6 cm^3 volume of the temporal lobe in 256 scans with TR = 2.5 ms. A line broadening of 1.5 Hz was added to the calculated spectra.

The fitting method used to exploit the calculated metabolite spectra employs the full-width basis spectrum for each metabolite as well as several macromolecular and baseline fitting terms (6-9).

6.5 Summary and Discussion

In view of the fact that the majority of proton observable metabolites have strongly-coupled spins and in view of the popularity of the short TE/TM STEAM sequence for observing such metabolites, it is essential not only to understand how this coupling might lead to errors in metabolite quantification by STEAM, but also to have a means of predicting the optimum STEAM sequence design for quantifying any particularly target metabolite. The purpose of this paper has been to demonstrate that a numerical solution of the quantum mechanical equations is an excellent means to deal with each of these issues. We have shown that because the STEAM sequence uses only 90° selective pulses, the provision of alternative coherence pathways by the selective pulses is much less significant in modifying the ultimate lineshape response to STEAM than it is in the PRESS case (5), where selective 180° pulses are used. As a result, r.f. pulse design differences are usually no greater than a few percent. The critical sequence-dependent spectral variability resulting from the STEAM sequence arises from the TE and TM combination, which modifies the coherence evolution between the pulses and changes the responses of coupled spins relative to the uncoupled singlets often used as standards, and also relative to each other. Using both the weakly-coupled lactate and the strongly-coupled aspartyl group of NAA we have demonstrated that significant coupled-spin evolution occurs even in short-echo experiments and that small changes in timings, particularly TM, can produce marked changes in the overall lineshape and yield that are spin system (i.e. metabolite) dependent. Although the first TE/2 period sets the stage by governing the degree to which evolution and coherence transfer enlarge the portfolio of coherences, particularly anti-phase coherences, immediately prior to the second 90° pulse, it is the oscillatory evolution and coherence transfer within the cohort of ZQCs that makes the ultimate lineshape so sensitive to TM. Comparison of the ABX group of NAA with the 5 spin AMNPQ spin system of Glu, indicates that a greater the number of coupled spins (and hence ZQC terms) tends to smear the dependency on TM. Expressing a peak-amplitude (or some other chosen measure of the response) as a contour plot in

TE-TM space enables one to select optimal timings for the maximization of a target metabolite and/or the minimization of a co-resonant background peak.

The quantification of a target metabolite depends on knowing (i) the exact lineshape the target metabolite produces in response to the localizing sequence, (ii) the intensity of those lineshapes relative to that of an uncoupled singlet produced by the same sequence, and (iii) lineshape response of all background metabolites. Errors in quantification, or misleading comparisons between laboratories using different timing parameters, might arise if these conditions are not met. Although, in principle, experimental phantom spectra can provide the data base of information, and although pulse design does not seem to be an significant issue with STEAM, the subtle sensitivities of the spectrum to small changes in TM are not always appreciated. We propose that it is much more convenient and possibly more reliable to use a numerical approach for the planning of optimal pulse sequence timings and generation of the resulting metabolite responses. Finally, it is important to note that the sensitivity of the coupled-spin response to small changes in TM increases with an increase in main field strength due to role of chemical shift differences (in Hz) in determining the TM modulation frequencies.

6.6 References

1. P.A. Bottomley, Selective volume method for performing localized NMR spectroscopy. US Patent 4,480,228 (1984).
2. R.J. Ordidge, M.R. Bendall, R.E. Gordon and A. Connelly, Magnetic Resonance in Biology and Medicine (G. Govil, C.L. Khetraplal and A. Saran, Eds.), pp. 387-397, McGraw-Hill, New Dehli, (1985).
3. J. Frahm, K.D. Merboldt and W. Hanicke, *J. Magn. Reson.* **72**, 502 (1987).
4. J. Frahm, H. Bruhn, M.L. Gyngell, K.D. Merboldt, W. Hanicke and R. Kaptein, Localized High-Resolution Proton NMR Spectroscopy using Stimulated Echoes: Initial Applications to Human Brain In Vivo. *Magn. Reson. Med.* **9**, 79 (1989).
5. R.B. Thompson and P.S. Allen, A Demonstration of the Sources of Variability in the Response of Coupled Spins to the PRESS Sequence and their Potential Impact on Metabolite Quantification, *Magn. Reson. Med.* **41**, 1162-9 (1999).
6. B.J. Soher, K. Young, V. Govindaraju, and A. A. Maudsley. Automated Spectral Analysis III: Application to In Vivo Proton MR Spectroscopy and Spectroscopic Imaging. *Magn. Reson. Med.* **40**, 822-831 (1998).
7. K. Young, B. J. Soher, and A. A. Maudsley. Automated Spectral Analysis II: Application of Wavelet Shrinkage for Characterization of Non-Parameterized Signals. *Magn. Reson. Med.* **40**, 816-821 (1998).
8. K. Young, V. Govindaraju, B. J. Soher, and A. A. Maudsley. Automated Spectral Analysis I: Formation of a Priori Information by Spectral Simulation. *Magn. Reson. Med.* **40**, 812-815 (1998).
9. S.W. Provencher, Estimation of Metabolite Concentrations from Localized In Vivo Proton NMR Spectra *Magn. Reson. Med.* **30**, 672-679 (1993).
10. A. H. Wilam and P. S. Allen, An Analytical and Experimental Evaluation of STEAM Versus PRESS for the Observation of the Lactate Doublet, *J. Magn. Reson.* B **101**, 102 (1993).
11. E.L. Hahn, *Phys. Rev.* **80**, 590 (1950).
12. H. Wilman and P. S. Allen. The Response of the Strongly Coupled AB System of Citrate to Typical 1H MRS Localization Sequences. *J. Magn. Reson.* B **107**, 25-33 (1995).
13. R. V. Mulkern, J. L. Bowers, S. Peled, R. A. Kraft, and D. S. Williamson. Citrate Signal Enhancement with a Homonuclear J-Refocusing Modification to Double-Echo PRESS Sequences [published erratum appears in *Magn. Reson. Med.* **37**, 477 (1997)]. *Magn. Reson. Med.* **36**, 775-780 (1996).
14. K. Straubinger, F. Schick, and O. Lutz. Influence of Pulse Angle Variations on Stimulated Echo Acquisition Mode Proton Nuclear Magnetic Resonance Spectra of AB Spin Systems: Theory and Experiments with Citrate. *MAGMA* **7**, 88-94 (1998).

15. A. H. Wilman and P. S. Allen, Observing N-Acetyl Aspartate Via Both its N-Acetyl and its Strongly Coupled Aspartate Groups in In-Vivo Proton Magnetic Resonance Spectroscopy, *J. Magn. Reson.* B **113**, 203-213 (1996).

16. T. Ernst and J. Hennig. Coupling Effects in Volume Selective 1H Spectroscopy of Major Brain Metabolites. *Magn. Reson. Med.* **21**, 82-96 (1991).

17. G. B. Matson, An Integrated Program for Amplitude-Modulated RF Pulse Generation and Re-Mapping with Shaped Gradients, *Magn. Reson. Imag.* **12**, 1205-25, (1994).

18. R.B. Thompson and P.S. Allen, A New Multiple Quantum Filter Design Procedure for Use on Strongly Coupled Spin Systems Found In Vivo: Its Application to Glutamate *Magn. Reson. Med.* **39**, 762-771 (1998).

19. V. Govindaraju, V. J. Basus, G. B. Matson, and A. A. Maudsley. Measurement of Chemical Shifts and Coupling Constants for Glutamate and Glutamine. *Magn. Reson. Med.* **39**, 1011-1013 (1998).

CHAPTER 7

The Residual Intra-molecular Dipolar Coupling of the Cr / PCr Methyl Resonance in Resting Human Medial Gastrocnemius Muscle[1] and the Influence of Inter-molecular Dipolar Coupling of Water in In-Vivo Multiple Quantum Filters

This chapter is divided into two sections, both of which focus on the dipolar coupling of proton systems found in-vivo. Section 7.1 describes the influence of the residual intra-molecular dipolar coupling of the protons within Cr / PCr methyl group, paying particular attention to the resulting line shape and echo time modulations of that line shape. Section 7.2 describes the generation of an unexpected contamination water signal generated by an in-vivo double quantum filter, a sequence described in detail in Chapter 3. The passage of water through the filter is accommodated by inter-molecular dipolar coupling between neighboring water molecules. The dipolar coupled water coherence pathways through the multiple quantum filter sequence are displayed, as are methods to minimize the unwanted signal.

7.1 Intra-Molecular Dipolar Coupling (Cr / PCr)

7.1.1 Introduction

In many studies using magnetic resonance spectroscopy (MRS) the observation of creatine (Cr) plays a significant role, either in standardizing changes in various other metabolite concentrations or as a metabolite of interest in its own right. In most instances it is assumed that Cr and phosphocreatine (PCr) coexist in a single rapidly equilibrating pool (t-Cr). Nonetheless, in skeletal muscle a body of opinion exists that questions this assumption (1). Moreover, the interpretation of recent MRS experiments showing an unexpected behaviour of the co-resonant methylene peaks of Cr and PCr at 3.9 ppm (2, 3) is also at variance with this assumption. Specifically, Kreis et al (2) conclude that the methylene proton signal observed from the anterior tibialis is a dipolar doublet (frequency separation, Δf = 14.7 Hz) that arises solely from PCr. This assignment to PCr and not to Cr is derived from the temporal evolution of the peak height following

[1] A version of this chapter was published. Hanstock, C.C., Thompson, R.B., Trump, M.E., Gheorghiu, D., Hochachka, P.W., and Allen, P.S., *Magn. Reson. Med.*, **42**, 421-4 (1999).

exercise. The corollary of this assignment is that in vivo, under typical acquisition conditions, a significant proportion of the t-Cr pool in muscle is not NMR-visible, possibly due to it having a very short transverse relaxation time, T_2. Such a conclusion would be consistent with a slow interchange of Cr between these two metabolic states, and a partially restricted accessibility of Cr to the intracellular milieu (2). This conclusion is also supported by measurements in which the specific activity of ^{14}C-labelled Cr became incorporated into PCr to a much higher degree than into Cr (4).

To shed light on the creatine pool issue through MRS requires first of all that the mechanisms giving rise to the spectrum be fully understood. In the past, the methylene proton multiplet has been the focus of study, while in most investigations it is the t-Cr methyl signal at 3.02 ppm that must be understood, since it is this peak that is used to quantify t-Cr or to be an internal standard. In this paper we report that the t-Cr methyl protons also manifest a residual dipolar coupling. Our observation in the medial gastrocnemius muscle (MGM) demonstrates a methyl triplet rather than a singlet. The existence of the triplet has not always been recognized in practice. For example, in reporting two exponential components for the transverse decay of the methyl signal, Styles et. al (5) assumed a singlet. Taken at face value the two components might appear to reflect two slowly exchanging Cr pools. Some of our own results (6,7), also showing two transverse components in resting muscle, were similarly ambiguous in their interpretation without a clear understanding of the triplet behaviour.

To explain the TE dependence of the methyl signal we present the results of a numerical solution of the equation of motion of the density matrix (8) incorporating not only the residual dipolar coupling effects, but also the effects of the slice selective pulses used in the PRESS localisation scheme (9). This solution has enabled us to interpret the time dependence of the transverse methyl magnetization in terms of a single pool. It does not however, identify what constitutes that pool.

To account for an apparent residual dipolar coupling of the protons of Cr and PCr in skeletal muscle (2,3) several explanations have been proposed. These include the possibility of binding to creatine kinase (CK) which resides within ordered structures (2).

However, the limited number of binding sites on CK would restrict this mechanism to a small fraction of the available t-Cr pool. A further proposal, by the same authors (2), postulates that the elongated spaces between the actin and myosin chains hinder the t-Cr molecule/hydration sphere entities, and prevented them from tumbling isotropically. The hindered motion hypothesis is supported by previous reports from striated muscle of residual dipolar interactions resulting from the orientation of water (10), and of finite quadrupolar interactions being observed when D_2O is substituted. Furthermore, electron paramagnetic resonance spectroscopy (EPR) has shown small molecules such as spin-labelled ADP to be highly oriented relative to the muscle fiber axis when myosin is bound to actin (11).

7.1.2 Methods

Experimental data were acquired in vivo at 3T (magnet from Magnex Scientific PCL and spectrometer from Surrey Medical Imaging Systems Ltd.) using a 28 cm diameter quadrature birdcage resonator for transmission and signal reception. Normal volunteers were positioned supine in the magnet with the thickest portion of the right MGM centred at the isocentre of the static field, B_o. In order to minimise the susceptibility difference effects, a bag containing Kaopectate solution was located immediately adjacent to the interrogated region. A typical linewidth of the central methyl peak of the t-Cr triplet was ~ 0.05 ppm (~ 6 Hz). Multi-slice gradient-echo imaging in the transverse, sagittal and coronal planes was used to register the 2 x 2 x 3 cm PRESS selected volume precisely to the MGM. In addition to the voxel placement, the angular orientation of the tibia relative to B_o was also estimated. This estimate enabled the variation in muscle orientation between subjects to be minimised and at the same time the angular factor in the dipolar Hamiltonian estimated. To establish the TE dependence of the methyl triplet experimentally, a series of water-suppressed spectra were acquired at rest on eleven subjects using a symmetric PRESS pulse sequence (12,13) with inversion-null water suppression (14). The sequence parameters were TR = 2s, and TE = 20 ms to 300 ms (in progressively increasing increments between 4 ms to 20 ms). 1024 data points were acquired per scan, as were 128 averages. The radio-frequency (r.f.) pulses were 90° sinc-Gauss and 180° optimised-sinc shapes. Following zero-filling (to 2048 data points), filtering (2 Hz exponential), and an FFT of the time

domain data, the spectra were deconvoluted using the PERCH analysis package (15), where each peak was fitted to a Gaussian lineshape. To decompose the transverse decay into component exponentials, a non-negative-least-squares (NNLS) algorithm (16), that requires no *a priori* assumption of the number of components was employed. Both peak areas and peak heights were evaluated as inputs to the NNLS algorithm.

To account for modulations in the methyl lineshape that are distinct from the effects of transverse relaxation, the TE dependence of a dipolar-coupled triplet was evaluated numerically. The triplet character of the methyl resonance arises if the molecular motion at the individual molecule, and/or individual muscle fiber level, fails to average the dipolar interaction completely. When the C_3 axis of a rapidly rotating methyl group is not itself isotropically averaged by rapid tumbling motion, the geometric term of the truncated dipolar interaction between the equilateral protons reduces to a form in which the angle ϕ between the C_3 axis and the magnetic field B_o, appears as the factor $(3\cos^2\phi - 1)$(17). The three dipolar interactions of a methyl group then give rise to a triplet whose ϕ dependent splitting $f(\phi)$ also varies as the factor $(3\cos^2\phi - 1)$, and with an amplitude f_{max}, such that,

$$f(\phi) = f_{max}(3\cos^2\phi - 1) \qquad (7\text{-}1)$$

Under the influence of a Hamiltonian that contained the residual dipolar interaction, in addition to the Zeeman terms, together with the r.f. and gradient waveforms of the slice selective pulses, the evolution of the density matrix of the methyl spins enabled the TE dependence to be calculated. This model allowed us to include an angular distribution in the residual dipolar coupling whose mean angle, shape, and bandwidth could be varied. By assuming, as was previously proposed for spin-labelled ADP bound in the actin-myosin-ADP (A-M-ADP) complex (11), that the distribution was Gaussian, the mean angle, θ_m, and the bandwidth, G_{bw}, could be adjusted to provide the best agreement with experiment. The linewidth was set to equal that measured in vivo. Calculated and experimental spectra were compared at each echo time to establish the robustness of the model. The TE dependence of the central peak calculated from the model was used to isolate an estimate of the true transverse decay from the experimental

TE dependence. This true transverse decay was then analysed using the NNLS algorithm described above.

7.1.3 Results and Discussion

In the resting MGM the dipolar coupled methyl triplet was readily resolved at 3T as shown in Fig. 7-1. A mean satellite peak separation ($2f$) of 22.4 Hz was measured for the triplet at TE = 20 ms. A TE-dependent modulation of the height of both the central peak and the satellite pair was also observed. However, despite the maintenance of significant signal intensity by the central peak, the satellite pair could not be observed at TE's above 60 ms. These observations can only be fully accounted for if one assumes in the numerical model a distribution of residual dipolar-coupling strengths and if one also includes the actual slice-selective pulse design in the Hamiltonian.

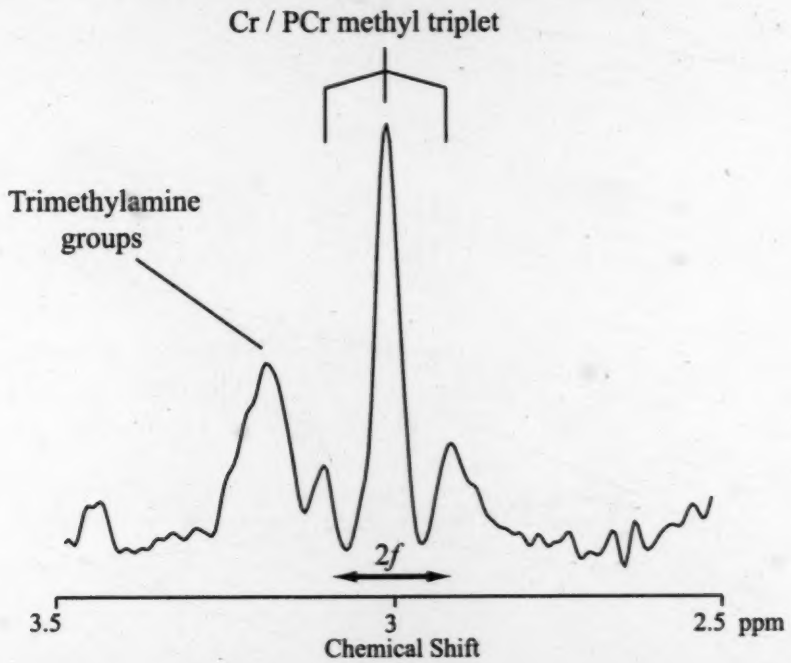

Figure 7-1 A typical PRESS-localised proton spectrum obtained from 2x2x3 cm^3 of resting medial gastrocnemius muscle at 3T. The total echo time ($TE_1 + TE_2$) = TE = 40 ms for the symmetric PRESS sequence. This spectrum demonstrates the Cr/PCr methyl triplet at 3.02 ppm (with satellites separated by $2f$ = 22.4 Hz), and also shows the broad signal at 3.2 ppm from trimethylamine groups.

To demonstrate the effects of these inclusions, we begin by illustrating, in Fig. 7-2A, the TE dependence of the triplet lineshape resulting from a PRESS sequence with ideal, non-selective, pulses acting on a volume containing fibers of identical orientation, with f =11.2 Hz, and in a field distribution corresponding to a linewidth of 6 Hz. In Fig. 7-2A both the satellites and the central peak are seen to be modulated. Without the local field distribution only the satellites would be modulated, fully refocusing at TE = n/f, where n is an integer. Nonetheless, the behaviour displayed in Fig. 7-2A is inconsistent with the rate of disappearance of the satellite peaks in the experimental spectra. Including the influence of the slice-selective pulses reduces the heights of the central and satellite peaks, as shown in Fig. 7-2B, but still not sufficiently to agree with experiment. The key to explaining the rapid satellite decay is to recognize the existence of anti-phase coherences at the onset of the slice selective pulses. These anti-phase terms evolve from the in-phase coherences under the influence of the residual dipolar coupling. They are particularly vulnerable to polarization transfer in the region of space which corresponds to the edge of any selective 180°-pulse slice profile. Such polarisation transfer due to the tip-angle distributions associated with practical selective pulses has been shown to give rise to significant modifications of scalar-coupled line shapes in response to a PRESS pulse sequence (9,18,19).

The final refinement (illustrated in Fig. 7-2C) incorporates a distribution within the selected volume of the individual muscle fiber orientations relative to B_o. Small variations in the bandwidth and mean angle of the Gaussian distribution affect the decay of the central peak and it's attendant satellites. The patterns of decay observed in-vivo were very consistent from one subject to another, indicating a consistency in the distribution of fiber orientations among the subjects studied. Through a systematic variation of the bandwidth, G_{bw} , and its mean value, θ_m, the numerical model was adjusted to fit the temporal evolution of the experimental t-Cr triplet shape over the entire 300 ms of the decay. Inclusion of the appropriate line width and the experimental selective pulse design were also essential to this fit. The best fitting parameters were θ_m = 18° and G_{bw} = 26°, in conjunction with a line width of 6 Hz, and a splitting of f = 11.2 Hz, which corresponds to f_{max} = 13.0 Hz. These values are close, but not identical to the mean angular offset of the tibia (not the fibers) from the B_o axis measured from the sagittal images, namely, 10°, and to the bandwidth reported for the Gaussian distribution

of spin-labeled ADP, namely, 15° (11). The dominant cause of the enhanced disappearance of the satellite peak is the range of phases that arises from the distribution of dipolar coupling strengths. Summation of the consequent range of signals results in their destructive interference. The longer the TE value, the more the phase differences have evolved and the greater the destructive interference.

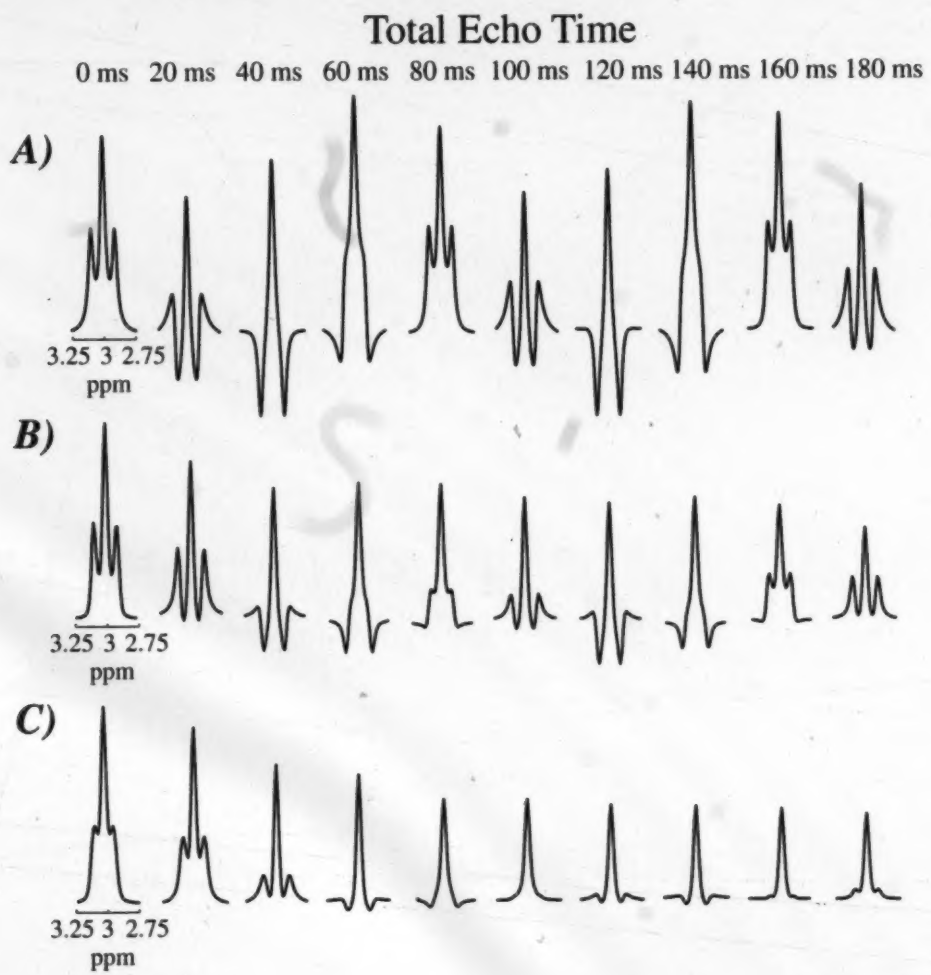

Figure 7-2 A series of numerical spectra illustrating the predicted dipolar evolution of the Cr/PCr triplet as a function of TE for a symmetric PRESS sequence, (A) with ideal, non-selective pulses, and assuming a single fiber orientation to B_o (θ_m= 18°), and a linewidth of 6 Hz, (B) with the actual slice-selective pulses, and assuming a single fiber orientation to B_o (θ_m= 18°), and a linewidth of 6 Hz, and, (C) with the actual slice-selective pulses, and assuming a Gaussian distribution (G_{bw} = 26°) of fiber orientation to B_0, centred θ_m= 18°, and a linewidth of 6 Hz. These series neglect transverse relaxation.

The issue of different creatine pools in skeletal muscle can often be addressed in terms of separable components of the transverse magnetization decay. Moreover, two decay components have already been reported for the t-Cr methyl signal from muscle, namely, ~ 23 ms and ~ 212 ms (5). If the TE dependence of the t-Cr methyl lineshape is to contribute to an understanding of separable pool signals, the effects of the dipolar modulation and the selective 180° pulses must be separated from the transverse relaxation decay. In particular these effects must be separated from the decay of the central peak, because it is upon this that which experimental measurements focus. Figure 7-3A displays the calculated TE dependence of the normalized central peak height, S_{peak} (TE), obtained from the numerically-acquired spectra of Fig. 7-2C. An NNLS analysis of this evolution indicates a single decay term (with a characteristic time of 34.3 ms), and a residual constant term. An analysis of the transverse decay of the experimental data therefore requires that each experimental data point be divided by the corresponding relative amplitude of the dipolar-evolution, in order to obtain a decay arising entirely from transverse relaxation. When the separated experimental transverse decays from all of the subjects were analyzed using the NNLS algorithm, only single exponential components were obtained. The mean value of their decay times was 162.5 ± 4.6 ms. This leads us to conclude that observations of multiple creatine T_2's in muscle, such as those reported previously by Styles et al (5) and ourselves (6), are the result of a shorter dipolar-evolution decay and a longer transverse relaxation decay. A comparison of a typical set of experimental data points with a calculated decay that takes account of all mechanisms is displayed in Fig. 7-3B.

It is important to note that if the distribution of fiber orientations is changed, for example, by going from one muscle to another, the line shape will change. In particular, the splitting may disappear if θ_m approaches the magic angle, or alternatively, if G_{bw} is broadened. Nevertheless, the rapid dipolar evolution will still contribute a decaying term to the overall TE dependence of the central peak. In the soleus for example, there is no apparent residual dipolar splitting but it is still possible to extract two apparent components from the transverse decay using NNLS analysis. The differences that exist between muscles means that imprecise localization techniques using surface coils are likely to give rise to a mixture of line shapes and a composite TE dependence.

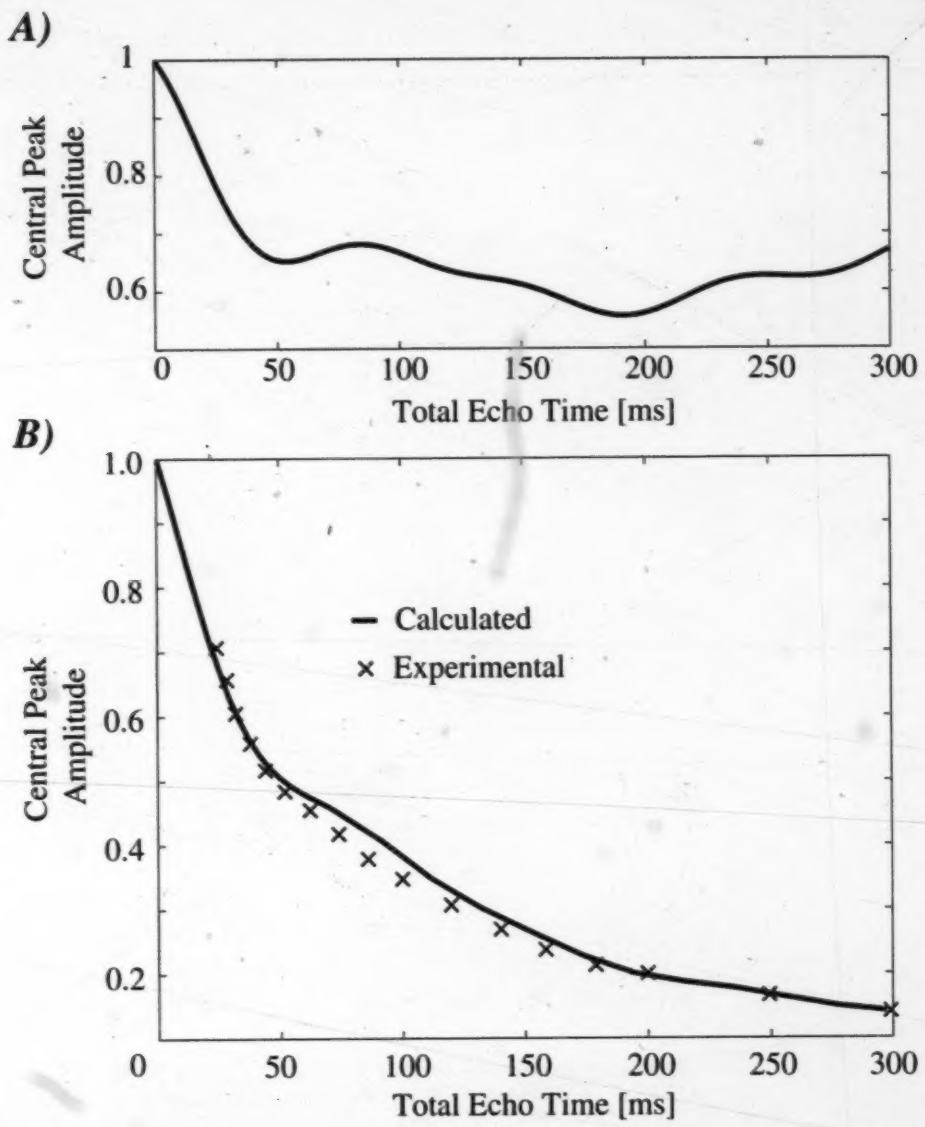

Figure 7-3 Two illustrations of the TE evolution of the central peak of the Cr/PCr methyl triplet. (A) The predicted variation in central peak amplitude of the PCr/Cr triplet using the model employed for Figure 2(C) which neglects transverse relaxation. (B) A comparison of the experimental data (represented by the symbols *x*) and the predictions of the model, when the predicted dipolar evolution is combined with a single transverse relaxation decay of time constant 162.5 ms. The experimental data were acquired from a 2x2x3 cm^3 volume of the medial gastrocnemius muscle, at 3T using a symmetric PRESS sequence.

In conclusion, the numerical model proposed here predicts methyl proton spectra for t-Cr, that are a close approximation to those observed in vivo. The predictions are sensitive to the distribution of dipolar couplings arising from the orientations of the muscle fibers, and to the r.f. pulse characteristics, which together give rise to an enhanced decay of the dipolar satellite peaks of the methyl triplet. The numerical model also predicts a unique and unexpected modulation pattern in the TE dependence of central peak of the triplet. This modulation is characterised by a short decay over a time of ~34 ms, to a residual plateau of between 60% and 70% of its value at TE ≒ 0. By combining transverse relaxation with this numerical solution, we conclude that although two decay coefficients may be apparent from the experimental TE dependence, the shortest of these (characteristic time = 34.3 ms) arises from the evolution under the dipolar coupling and the longest from a single transverse relaxation component, T_2 = 162.5 ms. In presenting this model of the data we have regarded the mechanism giving rise to the single transverse decay component as beyond its scope. However, it should not be forgotten that if that mechanism is dipolar in origin, then it too will depend on the angle, ϕ, (20,21) and different distributions of ϕ can give rise to different relaxation times. These observations emphasise that interpretation of the TE dependence of the t-Cr methyl signal in resting human muscle cannot be made solely in terms of differently relaxing pools. It is also important to recognize that because of dipolar coupling, the relationship between the concentration and the intensity of the central peak is no longer the simple exponential function of TE. This could have significant implications in applications that require precise t-Cr concentrations.

7.2 Inter-Molecular Dipolar Coupling (Water)

7.2.1 Introduction

For several years researchers using high field strengths (>11T) have reported signals that have been variously ascribed to the dipolar demagnetizing field of the solvent nuclei using a Bloch equation model (22-25) or to long range inter-molecular multiple quantum coherences (26-30). These signals display surprising characteristics and the mechanism from which they arise is still the subject of some controversy. The principal requirement for the observation of such signals seems to be a substantial nuclear magnetization vector and a spatial symmetry that is less than isotropic. The substantial

net magnetization has, in previous published work has been achieved by using field strengths greater than 11 T. The reduction of spatial symmetry has been brought about using linear magnetic field gradients during evolution and acquisition periods, although asymmetries caused by structural boundaries are sufficient to give rise to dipolar demagnetizing field-induced signals. The observable manifestation of the phenomenon has been an effectively infinite train of echoes resulting from just two pulses (23,25). More recently, there have been reports of the use of the dipolar coupled water signal as an additional contrast mechanism for use in MRI (31,32).

At the high end of the in-vivo field strength range (3 T), we have found that there is ample net magnetization present to produce dipolar demagnetizing field-induced signals if the pulse sequence is appropriate. In the vast majority of in-vivo experiments, e.g. conventional MRI or MRS using STEAM or PRESS, the configuration of r.f. and gradient pulses are inappropriate for causing large dipolar demagnetizing field effect signals. However, the single voxel multiple quantum (MQ) filter incorporates a configuration of r.f. and magnetic field gradients that can provide the necessary conditions for generating such signals from the water pool. These signals exhibit all the characteristics of those previously described as dipolar demagnetizing field effects using the Bloch equation model (22-25) or intermolecular multiple quantum coherences (26-30). Traditionally, the appeal of MQ filters applied in-vivo is the prospect of the elimination of those signals arising from uncoupled spin species, including those of water and the methyl singlets of several metabolites. However, it will be shown that, if not carefully applied, the in-vivo MQ filter can generate significant contaminant water signal, not necessarily at the expected shift of 4.7 ppm, via the demagnetizing field of the water itself.

7.2.2 The Multiple Quantum Filter

The single voxel double quantum filter (DQF), shown in chapter 3 in Fig. 3-1, has been previously demonstrated (33-39). To localize the experiment to a single voxel, at least three of the five pulses normally used in a DQC filter must be made spatially selective. The most appropriate, because of their null role in transferring coherences, are the 90° excitation pulse and the two 180° pulses used to refocus chemical shift and field

inhomogeneity dispersions. The PRESS style localization leaves the 2nd and 3rd 90° pulses free to be optimized for filtering, playing no role in the spatial localization. The objective of the spatially selective excitation is to ensure that only spins within the single voxel ROI produce DQ filtered, refocused magnetization from the targeted scalar-coupled metabolites. Spins outside this region of interest, depending on their position in space, experience different combinations of pulses, which, in all cases, would result in no observable signal from either scalar-coupled or uncoupled spins if the mechanism of the dipolar demagnetizing field was not present. However, several of the outer voxel regions experience a sequence of pulses very similar to that used to demonstrate dipole demagnetizing field effects. Fig. 7-4 illustrates the simplest pulse sequence that can generate observable transverse magnetization via the mechanism of the inter-molecular dipolar coupling, termed the CRAZED sequence by Warren (26).

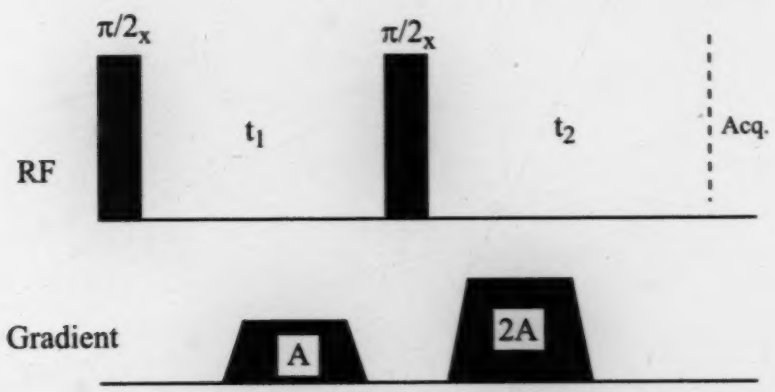

Figure 7-4 The CRAZED pulse sequence (COSY revamped with asymmetric z-gradient echo detection), named so because standard density matrix theory would predict a null signal from this experiment. The gradient pair selects for two-quantum coherences during t_1, which require a minimum of *two* pulses to generate under normal conditions.

Figure 7-5A displays the sequence of pulses and gradients experienced by the region of space excited by the 2nd and 3rd π/2 pulses and the final refocusing pulse. Apart from the refocusing pulse, this sequence is identical to the CRAZED pulse sequence.

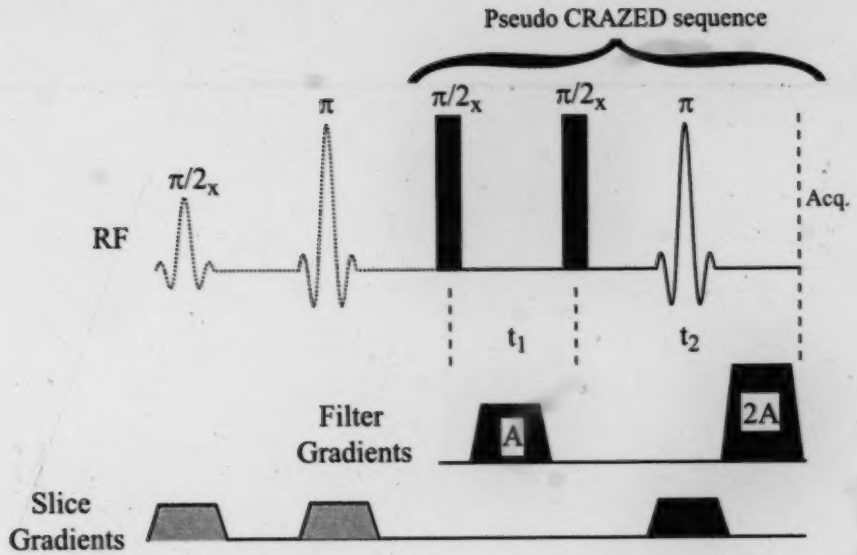

Figure 7-5 The single voxel double quantum filter pulse sequence is displayed. The slice gradients are applied in orthogonal axes (not shown) to define the volume of interest. Regions of space that do not experience the first two slice selective pulses experience a pseudo CRAZED pulse sequence (see Fig. 7-4).

The following section briefly outlines the coherence pathways followed throughout the CRAZED pulse sequence, allowing transverse magnetization to be generated from the two-pulse gradient filtered sequence.

7.2.3 Theory

To describe the generation of the contaminant solvent signal from a CRAZED-like sequence, a density matrix approach is desirable, to remain consistent with the methodology developed throughout the thesis. An excellent description utilizing density matrix techniques has been provided by Warren et. al. (26-30), as well, a Bloch equation description has also been published (23). Although, it has been noted that the Bloch equation approach, while agreeing with experimental results for the two-pulse CRAZED experiment, does not appear to agree with experimental results for more than two pulses (27). The theory that follows is a brief summary of the quantum mechanical description of the generation of the CRAZED signal, provided by Warren (26).

To incorporate the methods of Warren, the only required modification of the density matrix approach developed in Chapters 1 and 2 is an alteration of the thermal equilibrium density matrix. For a sample of N spins, the thermal equilibrium density matrix is most commonly represented by a power series expansion, shown in Eq. (7-2).

$$\rho_{eq} = \exp(-\beta\mathcal{H})/\mathrm{Tr}[\exp(-\beta\mathcal{H})] \approx 2^{-N}\,((1-\beta\hbar\omega_o\textstyle\sum_{i=1}^{N} I_{Z_i}) + \tfrac{1}{2}\,(\beta\hbar\omega_o)^2\textstyle\sum_{i=1}^{N}\sum_{j=1}^{N} I_{Z_i} I_{Z_j} + \ldots), \text{ where } \beta = 1/kT. \qquad (7\text{-}2)$$

The operator coefficient, $\beta\hbar\omega_o$, is very small even for high field spectrometers, ~ 10^{-4} for 800 MHz machines operating at room temperature, apparently justifying the truncation of the higher order (order > 1) terms from Eq. (7-2). However, Warren argues that each spin is coupled to N other spins when the dipolar Hamiltonian is incorporated, the result being a total contribution from higher order terms that is not insignificant over the double sum in Eq. (7-2) (or triple sum for the third order term ... etc). Following excitation, the free evolution rotating frame Hamiltonian for the dipolar coupled system, shown in Eq. (7-3), includes the chemical shielding and gradient terms (Eq. 1-91)), as well as the A and B terms of the dipolar Hamiltonian (Eq. (1-101)).

$$\mathcal{H} = [\hbar\,(\omega_i + \gamma Gr)\textstyle\sum_{i=1}^{N} I_{Z_i} + \frac{\gamma^2\hbar^2}{4}\sum_{j,k}^{N}\frac{(1-3\cos^2\theta_{jk})}{r_{jk}^3}(3I_{jZ}I_{kZ} - \mathbf{I}_j\cdot\mathbf{I}_k)] \qquad (7\text{-}3)$$

In (26), Warren calculated the observable transverse magnetization following the CRAZED pulse sequence by incorporating the Hamiltonian from Eq. (7-3) between ideal hard r.f. pulses, utilizing only the 2nd order term from Eq. (7-2) as the thermal equilibrium density matrix, and a gradient pair in ratio of 1:2, as shown in Fig, 7-4. The derivation is lengthy and complete in (26) so is not included here. To verify the theoretical predictions for a field strength of 3 T, as compared to 14 T in (26), the results from several phantom experiments are presented for the CRAZED experiment as well as for the in-vivo MQF sequence.

7.2.4 Results

To verify that the CRAZED pulse sequence is capable of generating gradient filtered transverse magnetization at a field strength of 3 T, the sequence was applied to a spherical phantom (8 ml) of water and copper-sulfate, and the ratio of the gradient pair (z-directed) was varied from 1:0 to 1:3.33. The first gradient pulse had a length of 7 ms and an amplitude of 0.6 G/cm, and the amplitude of the second, also of length 7 ms, was varied from 0 G/cm to 2 G /cm. The inter-pulse interval was kept constant at 10 ms, and the gradients were applied directly prior to and following the second pulse to minimize diffusion signal loss. Figure 7-6 displays the filtered signal dependence, following application of the CRAZED pulse sequence, on the ratio of the second to first gradient areas.

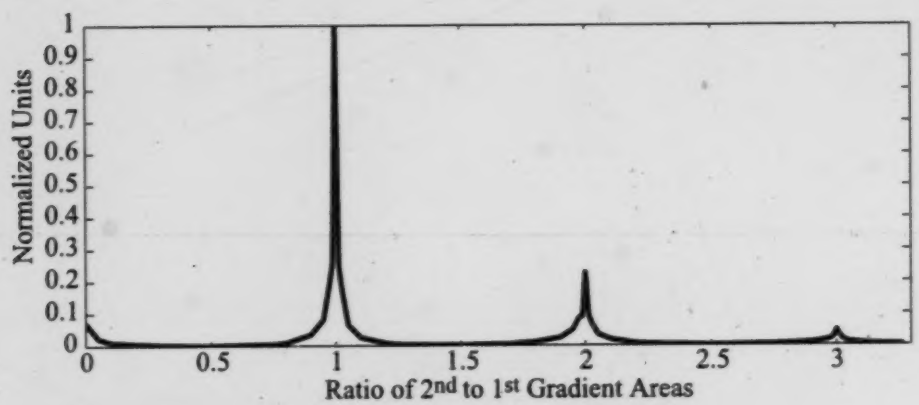

Figure 7-6 The measured CRAZED signal amplitude dependence on the ratio of the second to first filter gradient areas.

The series of peaks in Fig. 7-6 indicates the existence of zero, one, two and three-quantum coherences following the first CRAZED pulse. Figure 7-7 displays the free induction decay acquired for the gradient pair in a ratio of 1:2. The envelope of the echo is a function of the efficiency of the generation of observable in-phase transverse magnetization, from the anti-phase coherence generated by the second CRAZED pulse, by the dipolar fields. The envelope is also influenced by the T_2^* signal losses and the refocusing of chemical shifts and main field inhomogeneities.

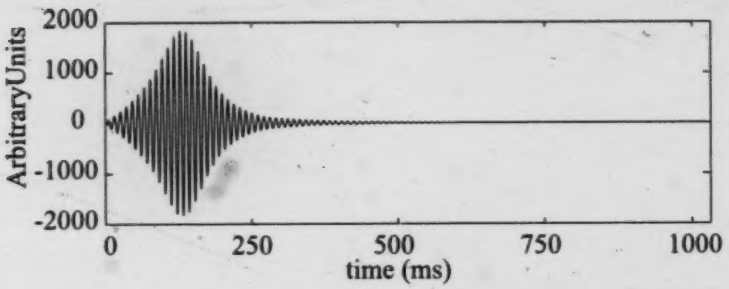

Figure 7-7 The measured free induction decay excited by the CRAZED pulse sequence for the double quantum filter gradient ratio, 1:2. The signal acquisition began 20 ms after the second $\pi/2$ pulse.

To confirm the 'dipolar field' origin of the observed signal, the dependence of the double quantum signal (gradient ratio of 1:2) on the gradient angle (to the main field) was measured for angles from 0° (z-directed) to 90° (x-directed). The well known $\left(3\cos^2\phi - 1\right)$ dependence of the dipolar field amplitude on the angle, ϕ, between the gradient vector and the magnetic field is exploited to confirm the influence of the dipolar field. Figure 7-8 displays the measured double quantum CRAZED signal as a function of the gradient angle, along with theoretical predictions.

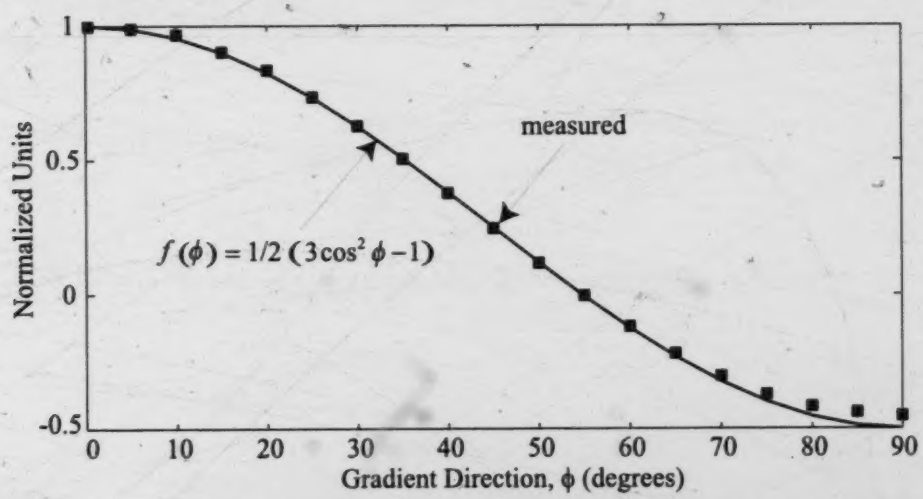

Figure 7-8 The measured double quantum filtered CRAZED signal (black squares) is plotted as a function of the gradient angle to the main field. The theoretical $\left(3\cos^2\phi - 1\right)$dependence is plotted (solid line) to illustrate excellent agreement to theory.

In his treatment of the CRAZED experiment, Warren included a second pulse tip angle of 90°. As further verification of the density matrix approach, the signal yield can be calculated as a function of this tip angle. Assuming a thermal equilibrium density matrix with an operator component $I_{1Z}I_{2Z}$, it is a simple calculation (see appendix IV) to derive a sin(β)(1-cos(β)) dependence of the resulting single quantum coherence directly following the CRAZED experiment on the second pulse tip angle, β. This tip angle dependence was derived previously by Bowtell (23) using a Bloch equation model incorporating the bulk dipolar demagnetizing field. Figure 7-9 displays the measured double quantum CRAZED signal as a function of the second pulse tip angle, along with theoretical predictions.

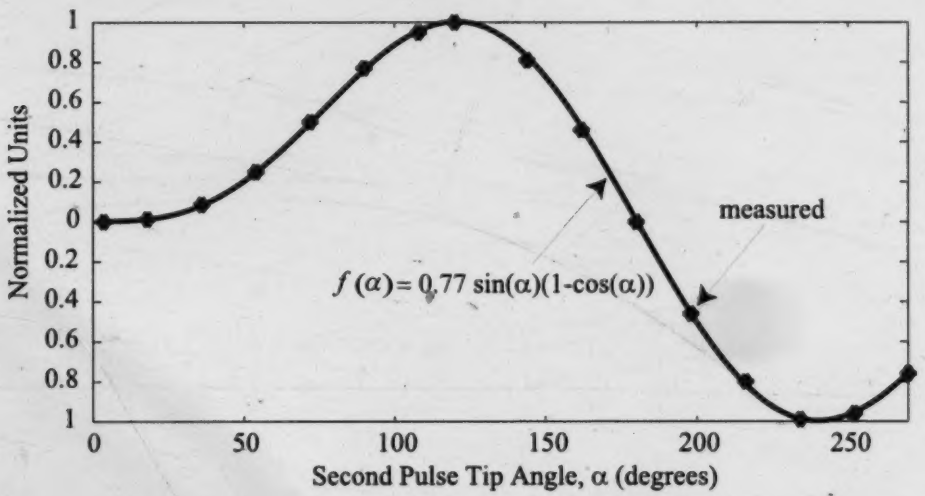

Figure 7-9 The measured double quantum filtered CRAZED signal (black points) is plotted as a function of the tip angle, β°, of the second pulse. The theoretical sin(β)(1-cos(β)) dependence is plotted (solid line) to illustrate excellent agreement to theory. The weighting of 0.77 is a normalization factor.

Because the generation of the CRAZED signal requires the action of both pulses, if either one is spectrally selective, the signal will be generated only within the bandwidth of that pulse. This effect is of particular importance for MQF sequences, which commonly employ a spectrally selective read pulse to improve filter yield, as was shown in Chapter 3. To illustrate this phenomenon, the second pulse of the CRAZED sequence is replaced with a spectrally selective sinc-Gaussian pulse (bandwidth = 200 Hz), and applied to a phantom with an extremely inhomogeneous field distribution. Figure 7-10

displays the frequencies excited from the phantom using a hard pulse CRAZED sequence, as well as the spectrally selective pulse version, both with no frequency offset, and with a 300 Hz offset.

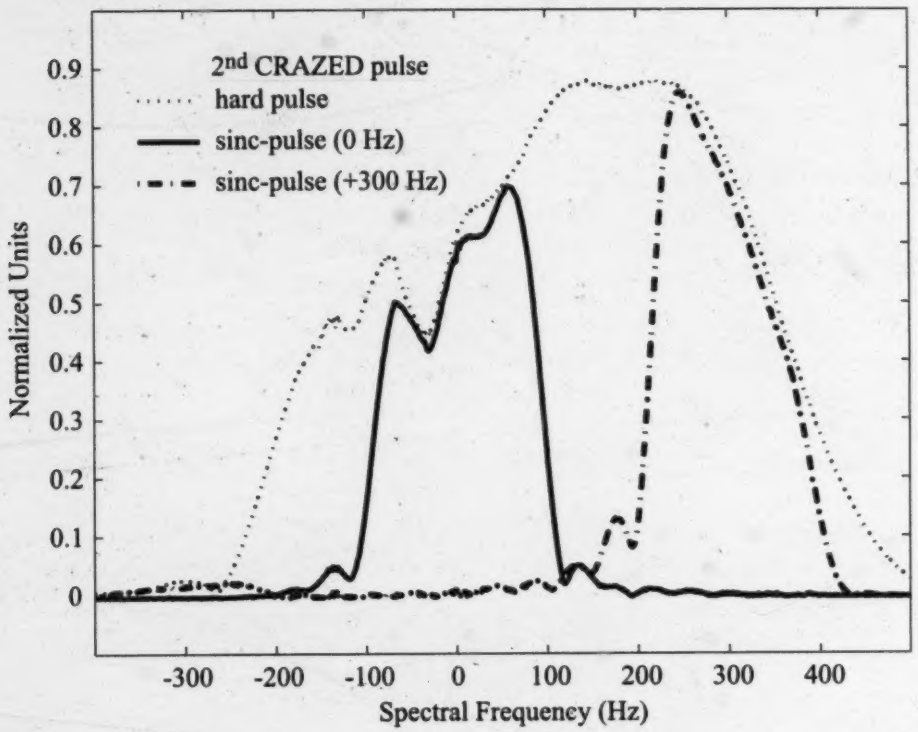

Figure 7-10 The measured distribution of frequencies excited with the CRAZED sequence from a phantom in an inhomogeneous static field. Three variations of the second pulse of the CRAZED sequence are employed, a hard pulse, and a 200 Hz bandwidth sinc-Gaussian pulse applied on resonance, and 300 Hz off resonance.

Application of the single voxel DQF sequence to a water phantom gave rise to a water signal with properties identical to those generated with the CRAZED pulse sequence, including the gradient angle effects and read pulse tip angle influence. These results were presented previously at the 5th Annual meeting of the ISMRM in Vancouver (40). To evaluate the origin, in space, of the DQ water signal, read and phase encoding was added to the DQF sequence. Figure 7-11 displays a transverse image acquired using the DQF imaging sequence.

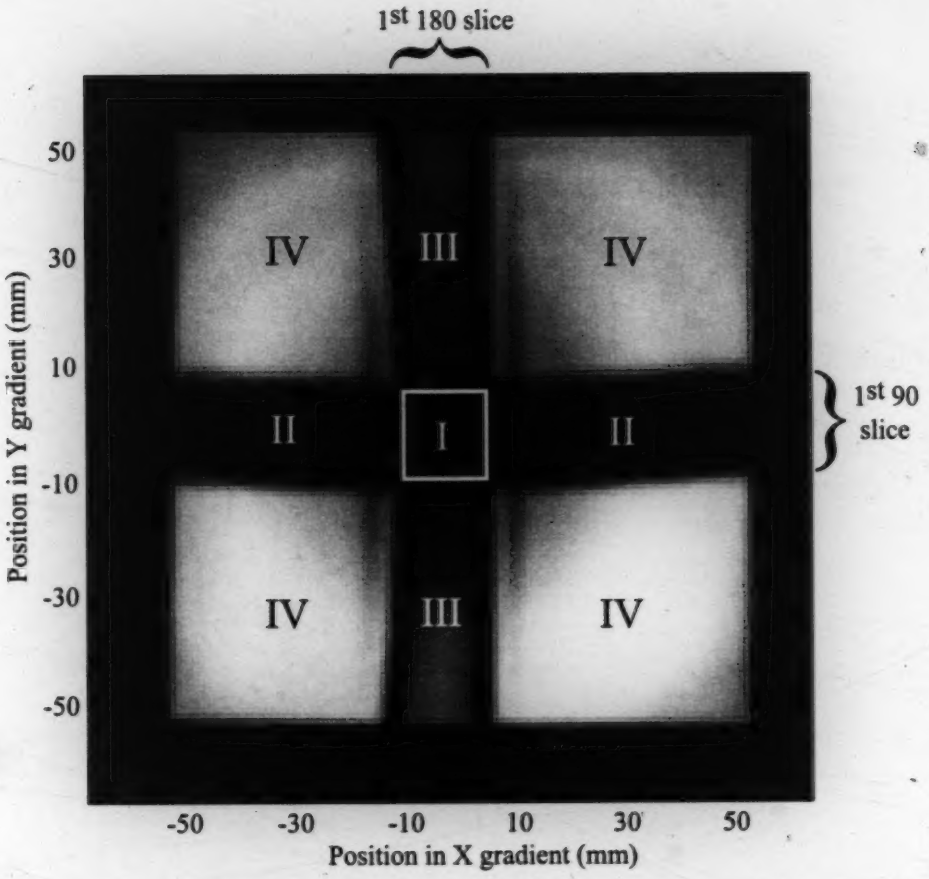

Figure 7-11 An imaging evaluation of the single voxel double quantum filter sequence, applied to a 10 x 10 x 10 cm^3 cubic phantom comprising water and copper sulfate. The read and phase encoding gradients were employed in the transverse (x-y) plane, and the single voxel (I) was placed in the center of the cube. The slice selective 90° pulse gradient was oriented along the y-axis, and the first 180° pulse gradient was oriented along the x-axis, while the second 180° pulse gradient was oriented along the z-axis, acing as the imaging slice selective pulse. Each of the four regions, I to IV, experience a different sequence of pulses.

As illustrated in Fig. 7-11, the majority of the water signal passing through the single voxel DQF sequence originates from outside the volume of interest, in region IV. The spins in region IV experience the pulse sequence termed the pseudo CRAZED sequence, shown in Fig. 7-5. The spins in region III also experience the Pseudo CRAZED sequence, following an inversion by the second the slice selective refocusing pulse. The reduction in signal as compared to region IV reflects the poor inversion

properties of sinc-shaped refocusing pulses. Regions I and II are excited by the first slice selective (90°) pulse, preparing the two-term thermal equilibrium terms, the $I_{1Z}I_{2Z}$, to two-quantum coherences *prior* to the second (hard) 90° pulse (see Fig. 7-5). Because the pseudo CRAZED sequence (see Fig. 7-5) produces observable signal only from the longitudinal term, $I_{1Z}I_{2Z}$, spins that encounter the first slice selective (90°) pulse will not pass through the filter, as shown in Fig, 7-11. To verify the dipolar origin of the signal generated by the DQ imaging experiment, the $3\cos^2\phi - 1$ dependence of the image intensity on the filter gradient orientation was observed.

7.2.3 Discussion

The appeal of the multiple quantum filter sequence is its ability to eliminate unwanted resonances, particularly from the uncoupled spin groups, including the large water signal. Unfortunately, the imaging evaluation of the double quantum filter, shown in Fig, 7-11, clearly displays that water does pass through the filter, primarily from regions of space not experiencing the complete series of r.f. pulses. Because the contaminant signal arises from outside the volume of interest, where the local field homogeneity is necessarily reduced, the resonant frequency of the water is more likely to overlap with the target metabolite resonances, away from the 4.7 ppm peak. To minimize the intensity of the contaminant signal, a combination of phase cycling and magic angle filter gradients ($3\cos^2\phi - 1 = 0$) can be incorporated. It is important to note that the magic angle gradient criteria cannot be met, exactly, at all locations in space due to unavoidable imperfections in gradient linearity, particularly with increasing distance from the gradient iso-center. Relying on phase-cycling to destroy out of volume signal, unfortunately, diminishes the allure of the gradient filtering approach, whose claim to fame is single-shot elimination of unwanted resonances. Nevertheless, the coupled spin response to the single voxel filter is not influenced by the anomalous dipolar coupled water, which can be effectively eliminated if effective phase-cycling and magic angle filter gradient orientations are applied with care. Figure 7-12 displays a series of double quantum filtered Glu phantom spectra, incorporating the optimized single voxel filter sequence detailed in chapter 3. The phantom comprised a 1 liter jug of 20 mM glutamate, doped with copper sulfate, balanced to pH of ~ 7.2.

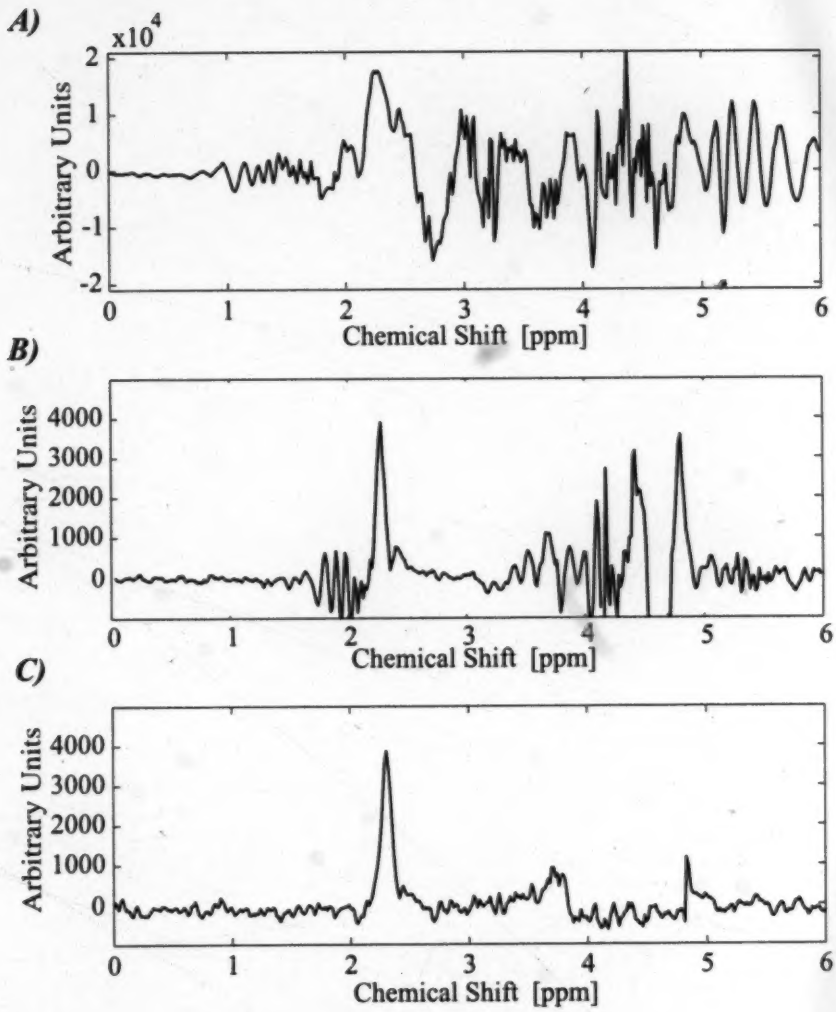

Figure 7-12 A) A single voxel DQ filtered Glu spectrum, acquired without phase cycling and with filter gradients oriented parallel to the main field, from a 1 liter jug containing a 20 mM Glu solution. B) The experiment from A) is repeated with filter gradients oriented at the magic angle to the main field (54.74°). C) The experiment from A) is again repeated, with magic angle gradients and a 16 step phase cycling routine similar to that reported in (39). No additional water suppression is applied in the above experiments. The peaks at 2.3 ppm and 3.75 ppm belong to Glu.

Chapter 3 displays results for the application of the Glu DQ filter sequence in-vivo, in all cases incorporating the magic angle gradients and phase cycling.

7.3 References

1. Wallimann T, Wyss M, Brdiczka D, Nicolay K and. Eppenberger HM. Intracellular compartmentation, structure and function of creatine kinase isoenzymes in tissues with high and fluctuating energy demands: the 'phosphocreatine circuit' for cellular energy homeostasis. Biochem. J. **281**, 21-40 (1992).
2. Kreis R and Boesch C. Liquid-crystal-like structures of human muscle demonstrated by in vivo observation of direct dipolar coupling in localized proton magnetic resonance spectroscopy. J. Magn. Reson. **104B**(2), 189-192 (1994)
3. Kreis R, Slotboom J, Felblinger J, Jung B and Boesch C. Can proton MRS detect changes in phosphocreatine? *in* "Proc., ISMRM, 5th Annual Meeting, Vancouver, 1997," p. 1338.
4. Hochachka PW and Mossey MK. Does muscle creatine phosphokinase have access to the total pool of phosphocreatine plus creatine? Am. J. Physiol. **274**, R868-872 (1998).
5. Styles P, Dixon RM, and Radda GK. Unexpected heterogeneity in the ^{1}H creatine signal from human skeletal muscle, *in* "Proc., SMR, 3rd Annual Meeting , Nice, 1995," p. 1890.
6. Trump ME, Hochachka PW, Gheorghiu D, Hanstock C and Allen PS. ^{1}H-MRS Evaluation of the phosphocreatine-creatine (PCr/Cr) pool in human muscle, *in* "Proc., ISMRM, 5th Annual Meeting, Vancouver, 1997,"p. 1337.
7. Hanstock CC, Thompson RB, Gheorghiu D, Trump ME, Hochachka PW and Allen PS. The unusual properties of the methyl resonance of PCr / Cr in muscle at rest, *in* "Proc., ISMRM, 6th Annual Meeting, Sydney, 1998," p. 1780.
8. Ernst RR, Bodenhausen B and Wokaun A. Principles of Nuclear Magnetic Resonance in one and two dimensions. Oxford University Press, Oxford, UK. (1987).
9. Thompson RB and Allen PS. A demonstration of the sources of variability in the response of coupled spins to the PRESS sequence and their potential impact on metabolite quantification. Magn. Reson. Med., **41**, 1162-70 (1999).
10. Fung BM. Orientation of water in striated frog muscle. Science **190**(4216), 800-802 (1975).
11. Crowder MS and Cooke R. Orientation of spin-labeled nucleotides bound to myosin in glycerinated muscle fibers. Biophys. J. **51**, 323-333 (1987).
12. Gordon RE and Ordidge RJ. Volume selection for high resolution NMR studies, *in* "Proc., SMRM, 3rd Annual Meeting, New York, 1984,"p. 272.
13. Bottomley PA. Spatial localisation in NMR spectroscopy in vivo. Annals of the New York Academy of Science 1987, **508**, 333-348.
14. Patt SL and Sykes BD. Solvent suppression using the WEFT (water eliminated Fourier transform) method. J. Chem. Phys. **56**, 3182 (1972).

15. Software distributed by the PERCH Project, Department of Chemistry, University of Kuopio, Finland.

16. Whittall KP and MacKay AL. Quantitative interpretation of NMR relaxation data. J. Magn. Reson. **84**, 134-152 (1989).

17. Andrew ER and Bersohn R. Nuclear magnetic resonance line shape for a triangular configuration of nuclei. J. Chem. Phys. **18**(2), 159-161 (1950).

18. Jung W-I and Lutz O. Localised double-spin-echo proton spectroscopy of weakly coupled homonuclear spin systems. J. Magn. Reson. **96**, 237-251 (1992).

19. Bunse M, Jung W-I, Lutz O, Kuper K and Dietze G. Polarisation-transfer effects in localised double-spin-echo spectroscopy of weakly coupled homonuclear spin systems. J. Magn. Reson. **114B**, 230-237 (1995).

20. Gutowsky HS and Pake GE. Structural investigations by means of nuclear magnetism. II. Hindered rotation in solids. J. Chem. Phys. **18**(2), 162-170 (1950).

21. Allen PS. On nuclear spin-lattice relaxation due to hindered molecular reorientation. J. Phys. C: Solid State Phys. **6**, 3174-3186 (1973).

22. G. Deville, M. Bernier and J.M. Delrieux, NMR Multiple Echos Observed in Solid 3He, *Phys. Rev.* **B19**, 5666-5688 (1979)

23. R. Bowtell, R.M. Bowley, and P. Glover, Multiple Spin Echoes in Liquids in a High Magnetic Field, *J. Magn Reson.*, **88**, 643-651 (1990).

24. M. McCoy and W.S. Warren, Three-Quantum Nuclear Magnetic Resonance Spectroscopy of Liquid Water: Intermolecular Multiple-Quantum Coherence Generated by Spin-Cavity Coupling, *J. Chem. Phys.*, **93**, 858-860 (1990)

25. R. Bowtell, Indirect Detection via the Dipolar Demagnetizing Field, *J. Magn Reson.*, **100**, 1-17 (1992)

26. W.S. Warren, W. Richter, A.H. Andreotti and B.T. Farmer II, Generation of Impossible cross peaks between Bulk Water and Biomolecules in Solution NMR, *Science*, **262**, 2005-2009 (1993)

27. Q. He, W. Richter, S. Vathyam and W.S. Warren, Intermolecular Multiple-Quantum Coherences and Cross Correlations in Solution Nuclear Magnetic Resonance, *J. Chem. Phys.*, **98**, 6779-6800 (1990)

28. R. Richter, S. Lee, W.S. Warren and Q. He, Imaging with Intermolecular Multiple Quantum Coherences in Solution Nuclear Magnetic Resonance, *Science*, **276**, 654-657 (1995)

29. S. Ahn, W.S. Warren and S. Lee, Quantum treatment of intermolecular multiple-quantum coherences with intramolecular J coupling in solution NMR.*J. Magn. Reson.*, **128**, 14-29 (1997)

30. S. Ahn, N. Lisitza and W.S. Warren and, Intermolecular zero-quantum coherences of multi-component spin systems in solution NMR,.*J. Magn. Reson.*, **133**, 266-72 (1998)

31. S. Mori, R.E. Hurd and P.C. Van Zijl,. Imaging of shifted stimulated echoes and multiple spin echoes.. Magn. Reson. Med., **37**, 336-40 (1997).

32. W.S. Warren, S. Ahn, M. Mescher, M. Garwood, K. Ugurbil, W. Richter, R.R. Rizi, J. Hopkins and J.S. Leigh, MR imaging contrast enhancement based on intermolecular zero quantum coherences, *Science*, **281**, 247-51 (1998)

33. R.B. Thompson and P.S. Allen. An Integrated Volume Localization and Spectral Editing Pulse Sequence, *Proc. of SMR 3rd Ann. Mtg., Nice.*, **p1909**, (1995).

34. L. Jouvensal, P.G. Carlier and G. Bloch, Double Quantum Proton Editing of Lactate in the Human Calf During Excercise, *Proc. of SMR 3rd Ann. Mtg., Nice.*, **p427**, (1995).

35. L. Jouvensal, P.G. Carlier and G. Bloch, Practical Implementation of Single Voxel Double Quantum Editing on a Whole-Body NMR Spectrometer: Localized Monitoring of Lactate in the Human Leg During Exercise, *Magn. Reson. Med.*, **36**, 487-490 (1996).

36. J.R. Keltner, L.L. Wald, B. de B. Frederick, and P.F. Renshaw, In Vivo Detection of GABA in Human Brain Using a Localized Double Quantum Filter Technique, *Magn. Reson. Med.*, **37**, 366-371 (1997)

37. J.R. Keltner, L.L. Wald, P.J. Ledden, Y-C.I. Chen, R.T. Matthews, E.H.G.K. Kusestermann, J.R. Baker B.R. Posen and B.G. Jenkins, A Localized Double-Quantum Filter for the In-Vivo detection of Brain Glucose, *Magn. Reson. Med.*, **39**, 651-656 (1998)

38. R.B. Thompson and P.S. Allen. A New Multiple Quantum Filter Design Procedure for Use on Strongly Coupled Spin Systems Found In Vivo: Its Application to Glutamate, *Magn. Reson. Med.*, **39**, 762-771 (1998).

39. A. H. Trabesinger, .M. Weber, C.O. Duc and P. Boesiger, Detection of Glutathione in the Human Brain In Vivo by Means of Double Quantum Coherence Filtering, *Magn. Reson. Med.*, **42**, 283-289 (1999).

40. R.B. Thompson and P.S. Allen. The Penetration of In Vivo Multiple Quantum Filters by "Dipolar Field Effect Signals" from Water, *Proc. of ISMRM 5th Ann. Mtg., Vancouver.*, **p1351**, (1997)

CHAPTER 8

Concluding Remarks

The objective of this thesis was to evaluate and optimize the response of several of the metabolite proton spin systems found in-vivo to the realistic in-vivo NMR pulse sequences used to observe them. Detailed consideration was given to the widely used STEAM and PRESS sequences, as well to the multiple quantum filter approach. To avoid the limitations of the product operator approaches so heavily favored in the past, a numerical method of evaluation was developed that utilized the density matrix representation of the spin systems, allowing the most demanding strongly-coupled spin systems to be treated. Previous product operator investigations of *'in-vivo'* pulse sequences have most commonly incorporated hard pulse models, neglecting the influence of the realistic shaped r.f. pulses used to provide the spatial localization. The use of numerical methods allows *all* aspects of the in-vivo NMR pulse sequence to be included in the evaluation.

The numerical approach was used to evaluate the response of the strongly-coupled five spin system of glutamate to the STEAM (chapter 6), PRESS (chapter 5) and DQ filter sequences (chapter 3), including the influence of the realistic slice-selective pulses. The response of the ABX group of NAA to the STEAM (chapter 6) and PRESS (chapter 4) sequences was also considered, to exemplify the utility of the numerical approach, both to illustrate the sources of signal modulations and to optimize the yield of the resulting signal. As well, the response of the weakly coupled lactate system to the STEAM (chapter 6) and PRESS (chapter 5) sequences was calculated, to compare the numerical calculations with published product operator predictions, and illustrate the influence of the realistic slice-selective pulses on those responses. Finally, chapter 7 detailed the influence of the direct dipole-dipole interaction in-vivo for two interesting cases. *Intra*-molecular coupling, within the Cr / PCr methyl spin group, in the ordered muscle environment, was shown to give rise to drastic line shape modulation and signal loss, while *inter*-molecular coupling of the spins within a bulk water sample was shown to give rise to a contaminant water signal that unexpectedly passed through a single voxel

DQF sequence. Phantom and in-vivo results at a field strength of 3 T were a close match to all of the numerically calculated responses.

8.1 The Utility of a Numerical Approach in NMR Problem Solving

The density matrix (or equivalently, density operator) representation of the ^1H spin system is a powerful and comprehensive tool. The density matrix contains all of the spin system information, the energy level populations and the amplitudes and phases of the coherences that exist between the spin states, including the single quantum in-phase coherence that corresponds to the directly detectable transverse magnetization. If the system Hamiltonian is time-independent throughout the segments that make up the NMR experiment, the density matrix can be evolved throughout the experiment without approximation, even for the larger strongly coupled spin groups, as was outlined in chapter 2. Given the density matrix throughout the sequence, the expectation value of any of the spin operators could then be directly calculated during or following the experiment.

The observable magnetization collected by the experimentalist following the NMR experiment is a linear sum of sinusoids with *discrete* frequencies and complex weightings, as outlined in section 2.3. Given the density matrix at the onset of the signal acquisition period, the amplitude and phase of each of these discrete spectral lines could be directly extracted, or the total line shape calculated as the sum of the components. To extend the density matrix method to allow realistic single voxel experiments to be simulated, approximate methods were developed to allow time-dependent r.f. pulses (Hamiltonians) to be included (section 2.4). Additionally, efficient methods were developed that allowed multiple sequence parameters to be varied, to characterize and optimize the coupled spin response to the pulse sequence (section 2.2 and 2.5).

A cautionary note: While the numerical approaches have great utility for computation, the product operator method can provide insight into the underlying mechanisms and coherence pathways that are the essence of the NMR experiment. On several occasions, during the development and use of the numerical tools, sources of

signal variability that were misinterpreted or missed altogether were eventually clarified with basic product operator methods.

8.1.1 Time-Dependent Hamiltonians

Section 2.4 outlined approximate methods of evaluation for time-dependent Hamiltonians, particularly for time-dependent r.f. pulses used in conjunction with gradient fields to provide spatial localization. Realistic pulses, with finite bandwidths and a characteristic spectral roll-off, excite a distribution of coherences over space, effectively giving rise to a distribution of density matrices over space. To calculate the net influence of these pulses on the resulting metabolite line shape and yield for a voxel experiment, the transformation matrix approach was developed to alleviate the time restrictions of simulating multiple dimensions of space. Additionally, it was recognized that the transformation matrix could also provide a quantitative measure of the anomalies associated with a given pulse and spin system, exposing both signal loss and coherence transfer effects. As an alternative to simulating multiple points in space, the transformation matrix method was shown to be from hundreds to thousands of times more time efficient, particularly where sequence characterization and optimization is concerned (see table 2-1).

8.1.2 Pulse Sequence Optimization

The product operator methodology allows the response of a spin system to a sequence of pulses and delays to be optimized by expressing the resulting transverse magnetization as a function of the sequence parameters. The numerical approach, while lacking the elegance of the product operator algebra, was shown to be an effective tool for sequence optimization, whereby the sequence response was calculated for a range of each of the parameters considered to characterize that response. For example, a two-dimensional contour plot representation was commonly employed in chapters 3 to 6 to display the dependence of ; integrated peak area, maximum peak intensities, and spin operator expectation values, as a function of two sequence timings (STEAM, PRESS and MQF). Additionally, the contour plot was used to display the spatial distribution of coherences excited by the single voxel sequences.

8.2 Future Applications

While only a small sampling of the complete set of metabolite spin systems found in-vivo were considered in this thesis, the numerical tools developed provide a general method to calculate the responses of even the most demanding strongly coupled spin systems to virtually any NMR experiment, including the influence of spatial localization. For example, the optimization of sequences such as the Glu DQF, that target a single metabolite, can be developed for any target, given the properties (shifts, couplings and field strength) of that spin system, and those that obscure it (chapter 3). The simulation software can also be used for the generation of basis metabolite spectra, used increasingly for the fitting of the total spectral response, as was illustrated in chapter 6. In particular, the optimal sequence timings (e.g. STEAM (TE, TM) or PRESS (TE_1, TE_2)) used to acquire the spectrum to be fit can be determined for all metabolites, or a reduced set of target metabolites. Additionally, the response of the coupled-spin systems to two-dimensional sequences such as in-vivo COSY or J-resolved methods can be simulated, including the influence of r.f. pulses used to incorporate spatial localization, allowing 2-D basis spectra to be generated (for fitting in multiple dimensions) and optimal sequence parameters to be identified.

The simulation software should also be expanded to include the influence of time-dependent gradient fields, to allow spectral/spatial selective pulses and eddy current effects to be incorporated. Additionally, the relaxation phenomena (T_1 and T_2) were applied as simple exponential recoveries and decays throughout the thesis, without the incorporation of the relaxation superoperator mathematics into the density matrix. A complete description of the coupled spin dynamics requires an incorporation of the relaxation superoperator into the simulation framework.

APPENDIX I

The Weak Coupling Product Operator Transformation Rules for a Two Spin System

AI-1 Derivation

The dynamic equation describing the evolution of the density matrix for a spin system described by a time-independent Hamiltonian, $\mathcal{H}$, is given by Eq. (1-48), $\rho(t) = \exp(-i\mathcal{H}t/\hbar)\ \rho(0)\ \exp(i\mathcal{H}t/\hbar)$. The evaluation of this expression requires the assessment of the exponential form of the Hamiltonian, which is not, in general, simply the exponent of each element. The exponential can be expanded as a power series to remove the operator from the exponent, as follows.

$$\exp(i\alpha I) = Id + i\alpha I + (i\alpha)^2 I^2/2! + (i\alpha)^3 I^3/3! + \ldots \qquad \text{(AI-1)}$$

In the special case in which the Hamiltonian contains a single operator component, for example $\mathcal{H}t/\hbar = \alpha I_Z$, a simple operator property, shown below in (AI-2) and (AI-3), can be used to simplify the sum in (AI-1).

n = even

$$I_Z^n = (1/2)^n\, Id \qquad \text{(AI-2)}$$

n = odd

$$I_Z^n = (1/2)^n\, (2I_Z) \qquad \text{(AI-3)}$$

These expressions are true for a spin-½ system with any number of spins, for any of the Cartesian operators. Grouping (AI-1) into even and odd terms, and applying (AI-2) and (AI-3), two series can be defined

$$\exp(i\alpha I_Z) = \{1-(\alpha/2)^2/2!+(\alpha/2)^4/4!-\ldots\}Id + i\{\alpha/2-(\alpha/2)^3/3!+(\alpha/2)^5/5!-\ldots\}I_Z \quad \text{(AI-4)}$$

The component series are the sine and cosine series, which, unlike the exponential form, have the advantage of having a scalar argument, $\alpha/2$, that can be directly evaluated.

$$\exp(i\alpha I_Z) = \cos(\alpha/2)Id + i\sin(\alpha/2)(2I_Z). \quad \text{(AI-5)}$$

This equation holds for each of the Cartesian operators, I_X, I_Y and I_Z. As stated above, Eq. (AI-5) is valid only if the Hamiltonian contains a *single* operator component, such as a hard r.f. pulse (I_X or I_Y component), or a chemical shift evolution (I_Z component). Weak coupling evolutions, described by the truncated Hamiltonian, $\mathcal{H}_{truncated} = 2\pi J I_{1_Z} I_{2_Z}$, contain a product of the operators, $I_{1_Z}I_{2_Z}$, a term which has properties similar to the single Cartesian terms, as follows.

n = even

$$(I_{1_Z}I_{2_Z})^n = (1/4)^n Id \quad \text{(AI-6)}$$

n = odd

$$(I_{1_Z}I_{2_Z})^n = (1/4)^n (4I_{1_Z}I_{2_Z}) \quad \text{(AI-7)}$$

Expanding and grouping terms for the coupled spin Hamiltonian case and utilizing Eqs. (AI-6) and (AI-7), the weak coupling exponential operator expansion becomes

$$\exp(i2\pi Jt I_{1_Z}I_{2_Z}) = \cos(\pi Jt/2)\, Id + i\sin(\pi Jt/2)\,(4I_{1_Z}I_{2_Z}). \quad \text{(AI-8)}$$

Utilizing the evolution operator equations, from (AI-5) and (AI-8), a set of transformation equations, shown below, can be defined for the Cartesian operator set, for a two-spin system. The transformations are defined for an r.f. pulse of tip angle α radians, a chemical shift of ω radians, or a scalar coupling of J Hz.

AI-2 Radio-frequency Pulse Transformation

$$
\begin{aligned}
I_X &\xrightarrow{\alpha I_X} I_X \\
I_Y &\xrightarrow{\alpha I_X} I_Y\cos(\alpha) + I_Z\sin(\alpha) \\
I_Z &\xrightarrow{\alpha I_X} I_Z\cos(\alpha) - I_Y\sin(\alpha)
\end{aligned}
\qquad \text{(AI-9)}
$$

$$
\begin{aligned}
I_X &\xrightarrow{\alpha I_Y} I_X\cos(\alpha) - I_Z\sin(\alpha) \\
I_Y &\xrightarrow{\alpha I_Y} I_Y \\
I_Z &\xrightarrow{\alpha I_Y} I_Z\cos(\alpha) + I_X\sin(\alpha)
\end{aligned}
$$

AI-3 Chemical Shift Transformation

$$
\begin{aligned}
I_X &\xrightarrow{\omega t I_Z} I_X\cos(\omega t) + I_Y\sin(\omega t) \\
I_Y &\xrightarrow{\omega t I_Z} I_Y\cos(\omega t) - I_X\sin(\omega t) \\
I_Z &\xrightarrow{\omega t I_Z} I_Z
\end{aligned}
\qquad \text{(AI-10)}
$$

AI-4 Scalar Coupling Transformation (Weak-Coupling Approximation)

$$
\begin{aligned}
I_X &\xrightarrow{2\pi J I_{1Z} I_{2Z} t} I_X\cos(\pi J t) + 2I_{1_Y} I_{2_Z}\sin(\pi J t) \\
I_Y &\xrightarrow{2\pi J I_{1Z} I_{2Z} t} I_Y\cos(\pi J t) - 2I_{1_X} I_{2_Z}\sin(\pi J t) \\
I_Z &\xrightarrow{2\pi J I_{1Z} I_{2Z} t} I_Z
\end{aligned}
$$

$$
\begin{aligned}
2I_{1_X} I_{2_Z} &\xrightarrow{2\pi J I_{1Z} I_{2Z} t} 2I_{1_X} I_{2_Z}\cos(\pi J t) + I_{1_Y}\sin(\pi J t) \\
2I_{1_Y} I_{2_Z} &\xrightarrow{2\pi J I_{1Z} I_{2Z} t} 2I_{1_Y} I_{2_Z}\cos(\pi J t) - I_{1_X}\sin(\pi J t) \\
2I_{1_Z} I_{2_Z} &\xrightarrow{2\pi J I_{1Z} I_{2Z} t} 2I_{1_Z} I_{2_Z} \\
2I_{1_X} I_{2_X} &\xrightarrow{2\pi J I_{1Z} I_{2Z} t} 2I_{1_X} I_{2_X} \\
2I_{1_X} I_{2_Y} &\xrightarrow{2\pi J I_{1Z} I_{2Z} t} 2I_{1_X} I_{2_Y} \\
2I_{1_Y} I_{2_Y} &\xrightarrow{2\pi J I_{1Z} I_{2Z} t} 2I_{1_Y} I_{2_Y}
\end{aligned}
\qquad \text{(AI-11)}
$$

APPENDIX II

Matrix Representation of the Two-Spin Cartesian Basis Operators (Spin ½ System)

$$I_{1_X} = 1/2\begin{pmatrix} 0 & 1 & 0 & 0 \\ 1 & 0 & 0 & 0 \\ 0 & 0 & 0 & 1 \\ 0 & 0 & 1 & 0 \end{pmatrix} \quad I_{1_Y} = 1/2\begin{pmatrix} 0 & -i & 0 & 0 \\ i & 0 & 0 & 0 \\ 0 & 0 & 0 & -i \\ 0 & 0 & i & 0 \end{pmatrix} \quad I_{1_Z} = 1/2\begin{pmatrix} 1 & 0 & 0 & 0 \\ 0 & -1 & 0 & 0 \\ 0 & 0 & 1 & 0 \\ 0 & 0 & 0 & -1 \end{pmatrix}$$

$$I_{2_X} = 1/2\begin{pmatrix} 0 & 0 & 1 & 0 \\ 0 & 0 & 0 & 1 \\ 1 & 0 & 0 & 0 \\ 0 & 1 & 0 & 0 \end{pmatrix} \quad I_{1_Y} = 1/2\begin{pmatrix} 0 & 0 & -i & 0 \\ 0 & 0 & 0 & -i \\ i & 0 & 0 & 0 \\ 0 & i & 0 & 0 \end{pmatrix} \quad I_{1_Z} = 1/2\begin{pmatrix} 1 & 0 & 0 & 0 \\ 0 & 1 & 0 & 0 \\ 0 & 0 & -1 & 0 \\ 0 & 0 & 0 & -1 \end{pmatrix}$$

$$2I_{1_X}I_{2_Z} = 1/2\begin{pmatrix} 0 & 1 & 0 & 0 \\ 1 & 0 & 0 & 0 \\ 0 & 0 & 0 & -1 \\ 0 & 0 & -1 & 0 \end{pmatrix} \quad 2I_{1_Y}I_{2_Z} = 1/2\begin{pmatrix} 0 & -i & 0 & 0 \\ i & 0 & 0 & 0 \\ 0 & 0 & 0 & i \\ 0 & 0 & -i & 0 \end{pmatrix} \quad 2I_{1_Z}I_{2_X} = 1/2\begin{pmatrix} 0 & 0 & 1 & 0 \\ 0 & 0 & 0 & -1 \\ 1 & 0 & 0 & 0 \\ 0 & -1 & 0 & 0 \end{pmatrix}$$

$$2I_{1_Z}I_{2_Y} = 1/2\begin{pmatrix} 0 & 0 & -i & 0 \\ 0 & 0 & 0 & i \\ i & 0 & 0 & 0 \\ 0 & -i & 0 & 0 \end{pmatrix} \quad 2I_{1_X}I_{2_X} = 1/2\begin{pmatrix} 0 & 0 & 0 & 1 \\ 0 & 0 & 1 & 0 \\ 0 & 1 & 0 & 0 \\ 1 & 0 & 0 & 0 \end{pmatrix} \quad 2I_{1_X}I_{2_Y} = 1/2\begin{pmatrix} 0 & 0 & 0 & -i \\ 0 & 0 & -i & 0 \\ 0 & i & 0 & 0 \\ i & 0 & 0 & 0 \end{pmatrix}$$

$$2I_{1_Y}I_{2_X} = 1/2\begin{pmatrix} 0 & 0 & 0 & -i \\ 0 & 0 & i & 0 \\ 0 & -i & 0 & 0 \\ i & 0 & 0 & 0 \end{pmatrix} \quad 2I_{1_Y}I_{2_Y} = 1/2\begin{pmatrix} 0 & 0 & 0 & -1 \\ 0 & 0 & 1 & 0 \\ 0 & 1 & 0 & 0 \\ -1 & 0 & 0 & 0 \end{pmatrix} \quad 2I_{1_Z}I_{2_Z} = 1/2\begin{pmatrix} 1 & 0 & 0 & 0 \\ 0 & -1 & 0 & 0 \\ 0 & 0 & -1 & 0 \\ 0 & 0 & 0 & 1 \end{pmatrix}$$

APPENDIX III

The Calculation of Metabolite Chemical Shifts and Scalar Couplings (NAAG, Glu, Gln and Ino)

The following figures display 500 MHz pulse acquire spectra for the abundant brain metabolites NAAG, Glu, Gln and Inos. In all cases the metabolite solutions were measured at room temperature and balanced to a pH of ~ 7.2. The solution spectra were subsequently analyzed with fitting software (PERCH – see chapter 7, ref 15) to extract the chemical shifts and scalar coupling constants, used to generate the simulated spectra, plotted for comparison.

AIII-1 NAAG (N-Acetylaspartylglutamate)

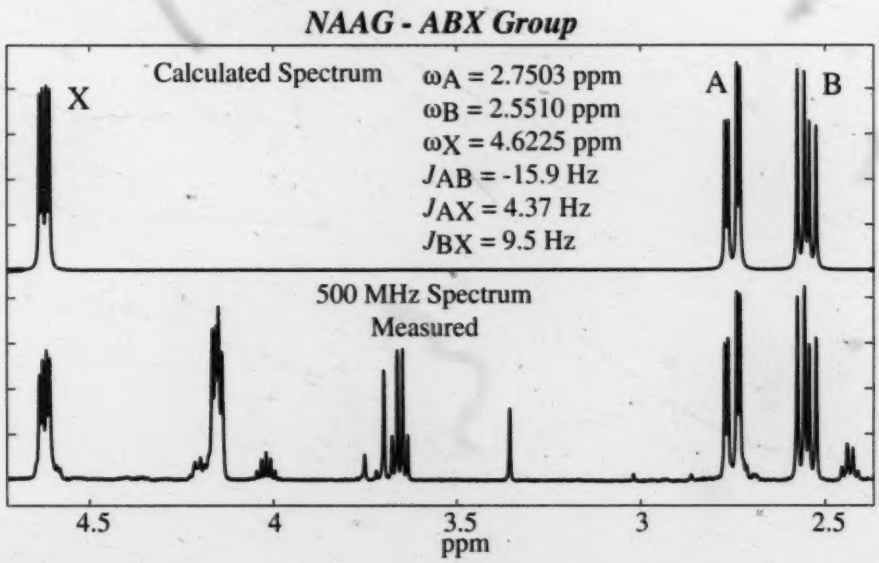

Figure AIII-1 A 500 MHz NAAG pulse acquire spectrum – ABX group characterization.

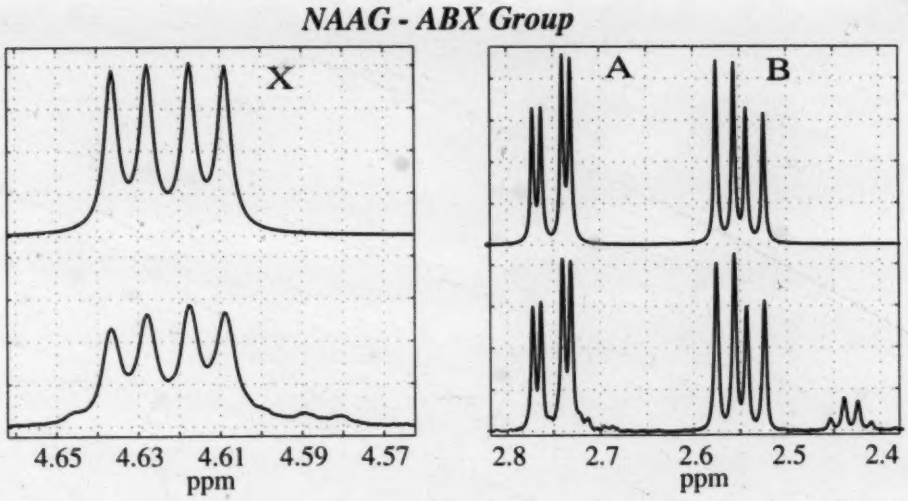

Figure AIII-2 A 500 MHz NAAG spectrum – ABX group characterization. A close-up of the A, B and X peaks. The solution X-multiplet most likely has a broader linewidth than the A and B peaks due to its proximity to an exchanging NH proton (See Fig. 1-15).

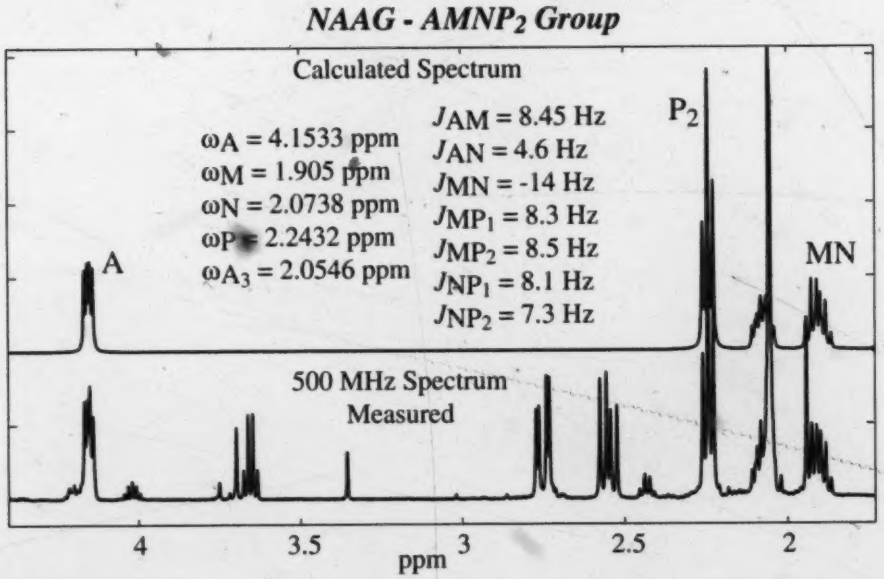

Figure AIII-3 A 500 MHz NAAG pulse acquire spectrum – $AMNP_2$ group characterization.

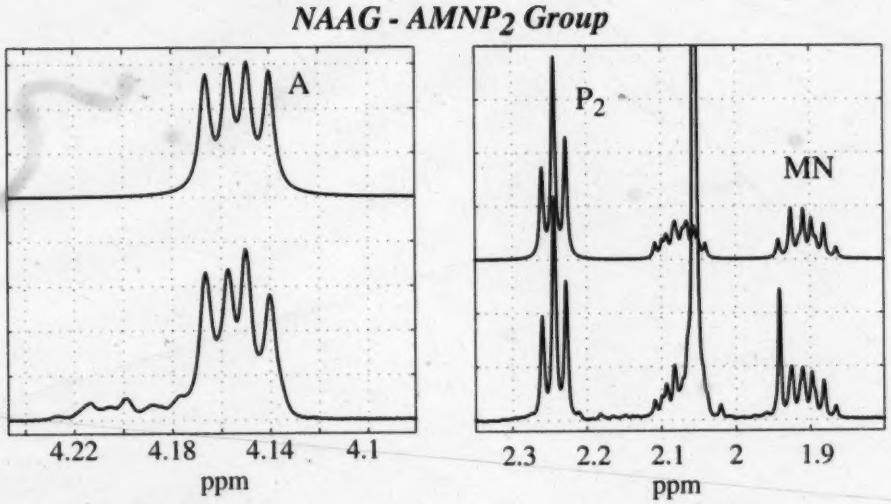

Figure AIII-4 A 500 MHz NAAG spectrum – $AMNP_2$ group characterization. A close-up of the A, MN and P_2 peaks.

AIII-2 Glu (Glutamate)

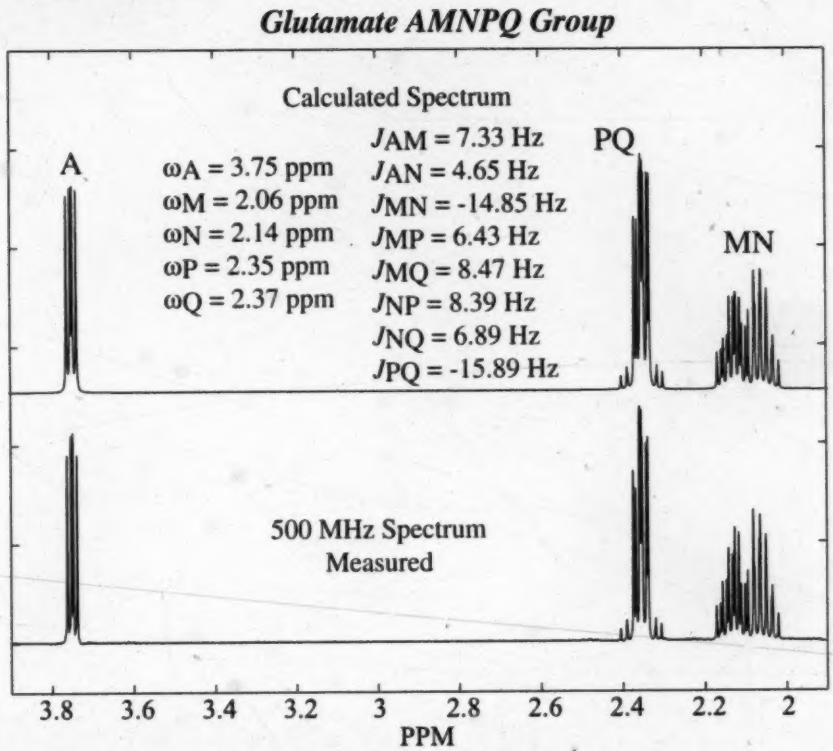

Figure AIII-5 A 500 MHz Glu spectrum – AMNPQ group characterization.

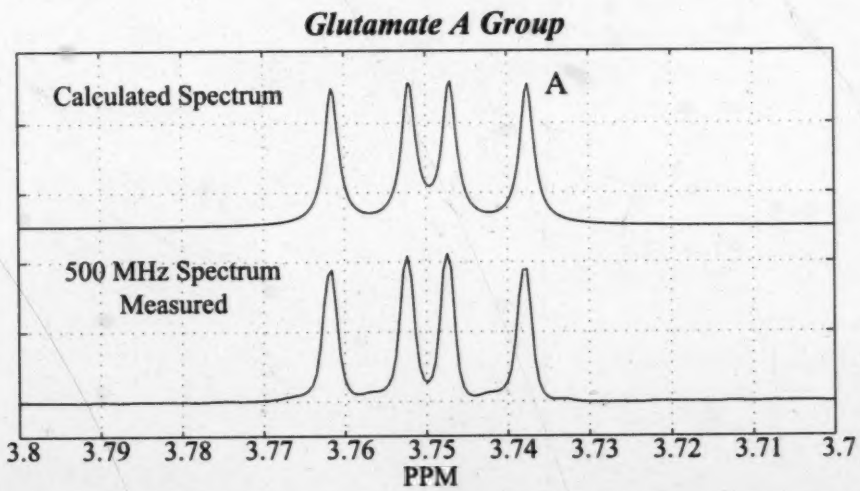

Figure AIII-6 A 500 MHz Glu spectrum – A group characterization. A close-up of the A peaks.

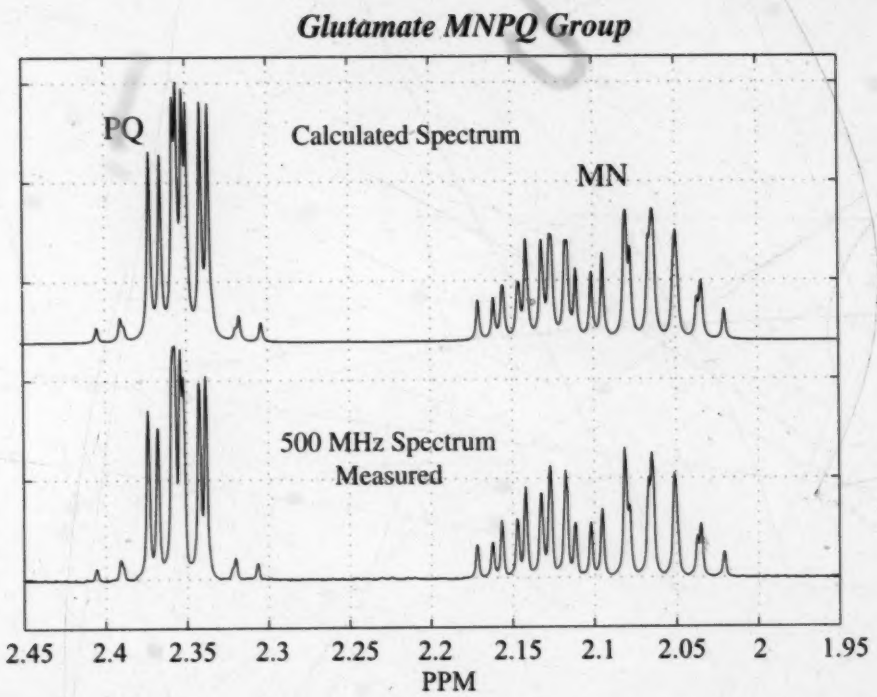

Figure AIII-7 A 500 MHz Glu spectrum – MNPQ group characterization. A close-up of the MNPQ peaks.

AIII-3 Gln (Glutamine)

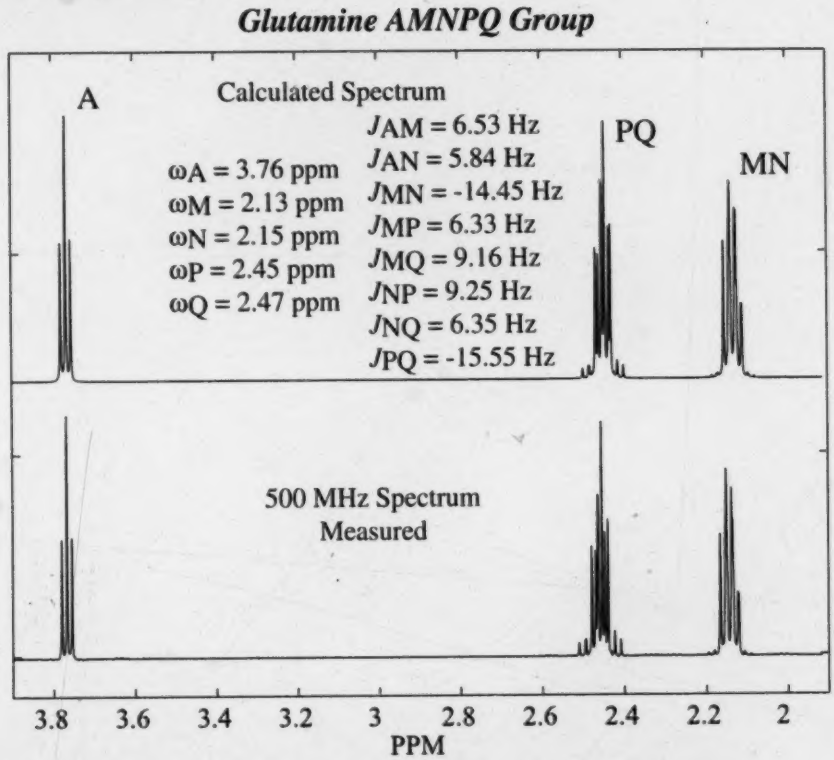

Figure AIII-8 A 500 MHz Gln spectrum – AMNPQ group characterization.

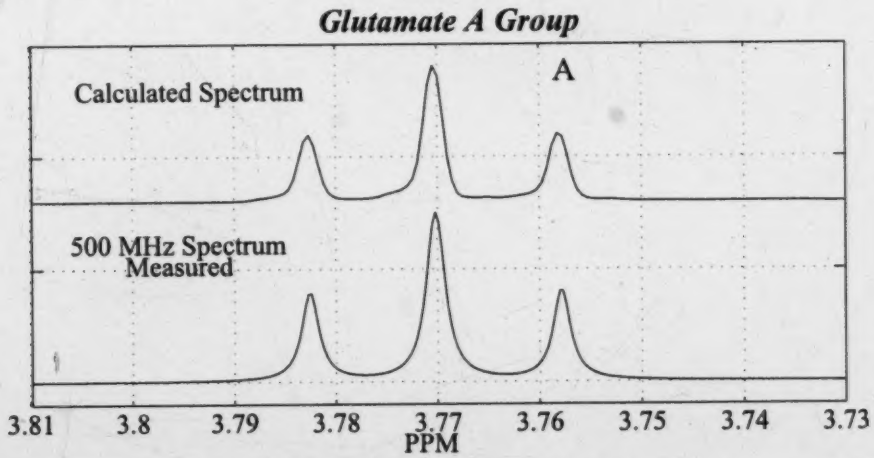

Figure AIII-9 A 500 MHz Glu spectrum – A group characterization. A close-up of the A peaks.

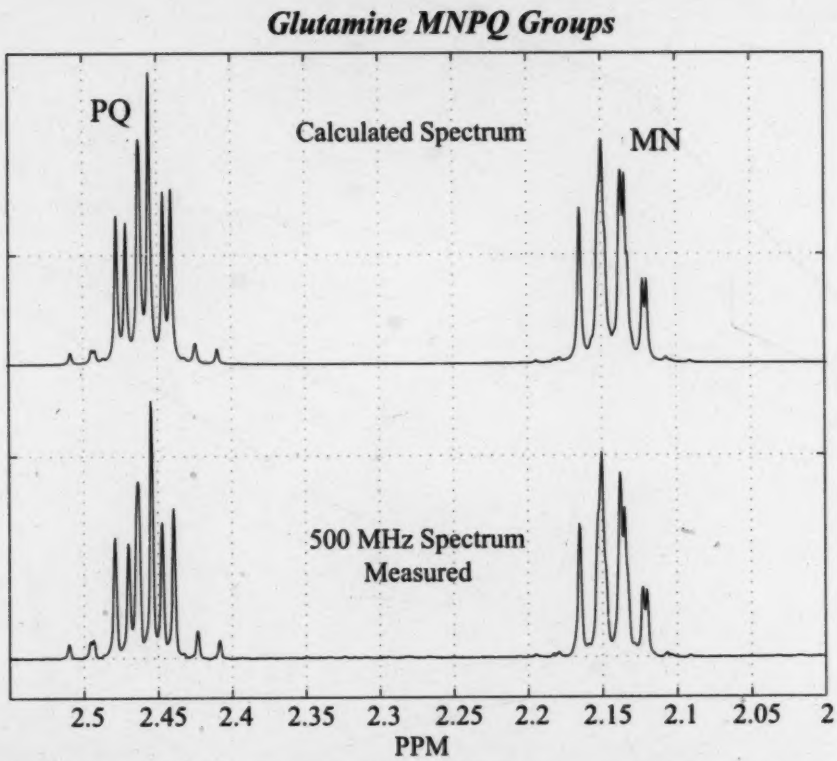

Figure AIII-10 A 500 MHz Glu spectrum – MNPQ group characterization. A close-up of the MNPQ peaks.

AIII-4 Ino (Myo-Inositol)

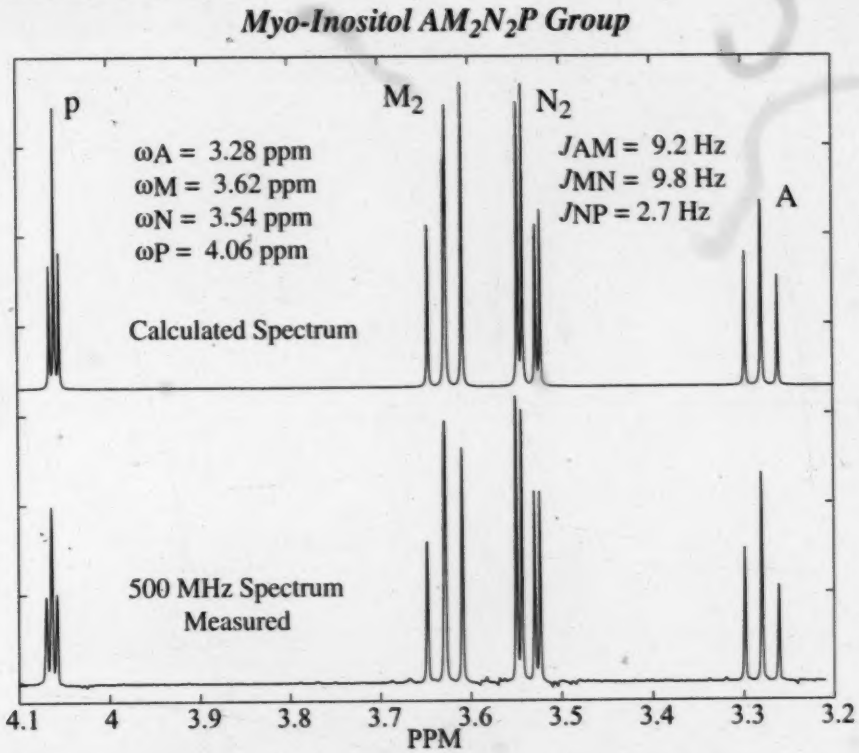

Figure AIII-11 A 500 MHz Ino spectrum – AM_2N_2P group characterization.

Appendix IV

The CRAZED Pulse Sequence – Product Operator Evaluation of the Tip Angle Signal Dependence

The CRAZED (COSY revamped with asymmetric z-gradient echo detection) pulse sequence, shown in chapter 7, Fig. 7-4, is known to pass multiple orders of gradient filtered coherences through a two-pulse experiment. The coherence pathways are outlined in chapter 7, and the associated references, using a product operator method, incorporating tip angles of $\pi/2$ for both of the CRAZED pulses. The calculations that follow generalize the product operator calculations to tip angles of $\alpha°$ (1^{st} pulse) and $\beta°$ (2^{nd} pulse), for the generation of signal through the two-quantum pathway.

The two-quantum pathway originates from the two-term longitudinal thermal equilibrium density operator,

$$\rho(0) = I_{1_z} I_{2_z}. \qquad \text{(AIV-1)}$$

Following excitation by an $\alpha°$ pulse (x-directed), the density operator becomes

$$\rho(1^{st}\ \text{pulse}) = \sin^2(\alpha) I_{1_y} I_{2_y} + \text{non-contributing terms}. \qquad \text{(AIV-2)}$$

The evolution of the density operator only need be calculated to directly following the second CRAZED pulse (including the 2^{nd} gradient) to determine first and second pulse tip angle dependencies. For simplicity, therefore, the chemical shift interaction will not be included in the following calculations (i.e. shift refocusing is not modeled).

The application of the first gradient pulse, of length τ ms, gives rise to four separate Cartesian product operator terms, shown in Eq. (AIV-3).

$$\begin{aligned}\rho(\tau) = \sin^2(\alpha)\{&\cos(\theta_1)\cos(\theta_2) I_{1_y} I_{2_y} - \cos(\theta_1)\sin(\theta_2) I_{1_y} I_{2_x} \\ &-\sin(\theta_1)\cos(\theta_2) I_{1_x} I_{2_y} + \sin(\theta_1)\sin(\theta_2) I_{1_x} I_{2_x}\}\end{aligned} \qquad \text{(AIV-3)}$$

The angles θ_1 and θ_2 are a function of the spin location in space, given generally by $\theta_n=\gamma \mathbf{G}\cdot\mathbf{r}_n\tau$. Because the spins are coupled though space via the indirect dipole-dipole interaction, the two spins can be assigned different locations in the gradient, and thus different phases.

Application of the 2nd, β° pulse, gives rise to several anti-phase coherence terms, shown in Eq. (AIV-4), that can evolve into observable in-phase magnetization under the influence of dipolar coupling.

$$\begin{aligned}\rho(\tau^+)=\sin^2(\alpha)\{&\sin(\beta)\cos(\beta)\cos(\theta_1)\cos(\theta_2)[I_{1_Y}I_{2_Z}-I_{1_Z}I_{2_Y}]\\&+\sin(\beta)[\cos(\theta_1)\sin(\theta_2)I_{1_Z}I_{2_X}+\sin(\theta_1)\cos(\theta_2)I_{1_X}I_{2_Z}]\}\end{aligned} \qquad \text{(AIV-4)}$$

The second gradient will have twice the amplitude of the first, to retain only those spins prepared to double quantum coherence following the 1st pulse. The phase angle induced by the second gradient is thus $\theta_n^{'}=2\gamma \mathbf{G}\cdot\mathbf{r}_n\tau$, giving rise to the following expressions for the four anti-phase terms from Eq. (AIV-4).

$$\begin{aligned}\rho(2\tau)=\sin^2(\alpha)\{&[-\sin(\beta)\cos(\beta)\cos(\theta_1^{'})\cos(\theta_1)\cos(\theta_2)+\sin(\beta)\sin(\theta_1^{'})\sin(\theta_1)\cos(\theta_2)]\,I_{1_Y}I_{2_Z}\\&+[\sin(\beta)\cos(\beta)\sin(\theta_1^{'})\cos(\theta_1)\cos(\theta_2)+\sin(\beta)\cos(\theta_1^{'})\sin(\theta_1)\cos(\theta_2)]\,I_{1_X}I_{2_Z}\\&+[-\sin(\beta)\cos(\beta)\cos(\theta_2^{'})\cos(\theta_1)\cos(\theta_2)+\sin(\beta)\sin(\theta_2^{'})\cos(\theta_1)\sin(\theta_2)]\,I_{1_Z}I_{2_Y}\\&+[\sin(\beta)\cos(\beta)\sin(\theta_2^{'})\cos(\theta_1)\cos(\theta_2)+\sin(\beta)\cos(\theta_2^{'})\cos(\theta_1)\sin(\theta_2)]\,I_{1_Z}^{*}I_{2_X}\}\end{aligned} \qquad \text{(AIV-5)}$$

As a simplifying approximation, assume $\theta = \theta_1 = \theta_2$, allowing trigonometric identities to be used to simplify Eq. (AIV-5), particularly, cos(a)cos(b)={cos(a+b)+cos(a-b)} and sin(a)cos(b)={sin(a+b)+sin(a-b)}. Note that the sin and cos product terms are composed of sums and differences of their arguments, corresponding to double quantum and zero quantum coherences, respectively. Incorporating the trig. identities and the gradient ratio of 1:2, or $\theta' = 2\theta$, Eq. (AIV-5) can be rewritten

$$\rho(2\tau)=\sin^2(\alpha)\{[-\sin(\beta)\cos(\beta)\cos(2\theta)(\cos(2\theta)+1)+\sin(\beta)\sin(2\theta)\sin(2\theta)]\, I_{1_Y} I_{2_Z}$$
$$+[\sin(\beta)\cos(\beta)\sin(2\theta)(\cos(2\theta)+1)+\sin(\beta)\cos(2\theta)\sin(2\theta)]\, I_{1_X} I_{2_Z}$$
$$+[-\sin(\beta)\cos(\beta)\cos(2\theta)(\cos(2\theta)+1)+\sin(\beta)\sin(2\theta)\sin(2\theta)]\, I_{1_Z} I_{2_Y} \qquad \text{(AIV-6)}$$
$$+[\sin(\beta)\cos(\beta)\sin(2\theta)(\cos(2\theta)+1)+\sin(\beta)\cos(2\theta)\sin(2\theta)]\, I_{1_Z} I_{2_X}\}.$$

Averaging each of the trig. products over an integer number of cycles, the expression in Eq. (AIV-6) can be further simplified to

$$\rho(2\tau)=\sin^2(\alpha)\{\sin(\beta)(1-\cos(\beta))/2)\,(I_{1_Y} I_{2_Z}+I_{1_Z} I_{2_Y})\} \qquad \text{(AIV-7)}$$

utilizing $\overline{\sin^2(\varphi)}=1/2$, $\overline{\cos^2(\varphi)}=1/2$, and $\overline{\sin(\varphi)\cos(\varphi)}=0$.

While by no means a complete expression for the gradient refocused single quantum signal generated by the CRAZED pulse sequence, Eq. (AIV-7) does display the $\sin(\beta)(1-\cos(\beta))$ signal dependence on the 2nd tip angle, as well as a $\sin^2(\alpha)$ dependence on the 1st tip angle.

APPENDIX V

MATLAB™ PROGRAMS

The numerical methods introduced in chapters 1 and 2 are implemented in the higher level programming language MATLAB™. The MATLAB™ graphic user interface (GUI) tools were used to generate a user friendly interface to accommodate the simple input of the complete NMR pulse sequence Hamiltonian, including the acquisition parameters (bandwidth and number of samples). To define the free evolution Hamiltonian, several parameters, including the main field strength, chemical shifts, scalar couplings and dipolar couplings for up to six spins can be entered. The shifts and couplings for several of the spin systems found in vivo are automatically loaded by selecting a metabolite of interest from the Metabolite list, shown below in the main simulation window, Fig. AV-1.

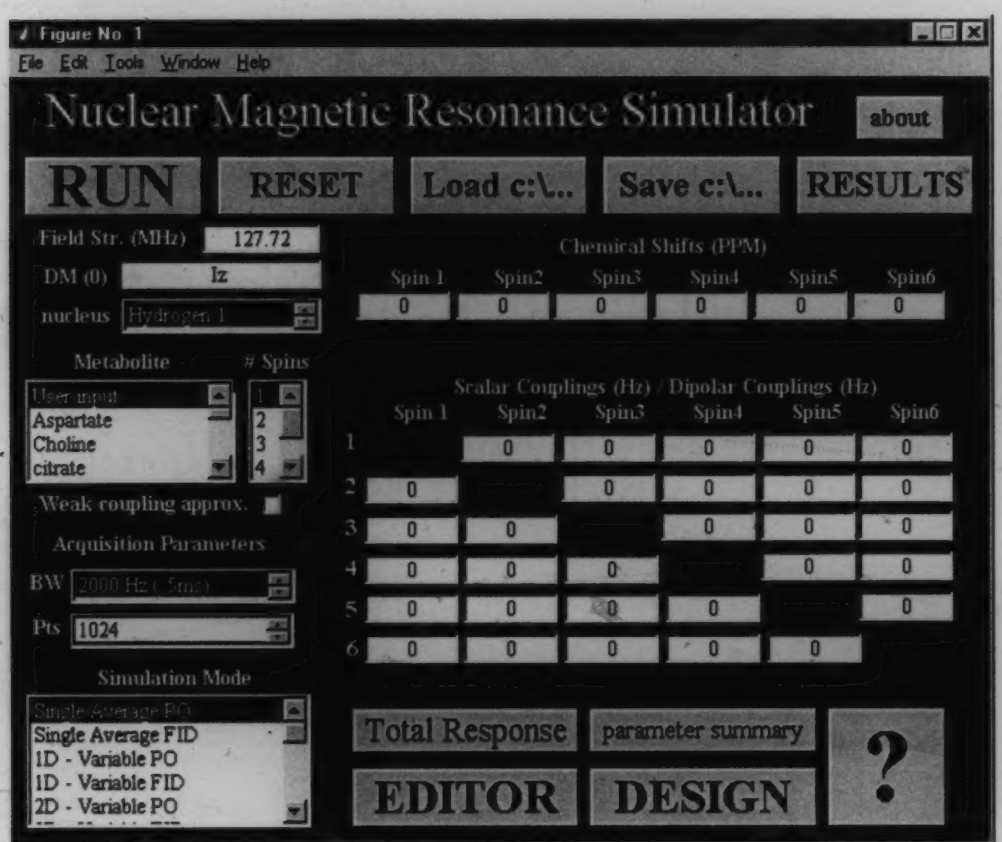

Figure AV-1 The main NMR simulation window.

Specifying a metabolite spin system, for example glutamate, as shown below in Fig. AV-2, loads the stored shifts and couplings, as well as the spin operator libraries appropriate for the number of spins, N_{spins}, in the system, five in the case of glutamate. (The library of spin operators comprise the Cartesian spin components for each of the N_{spins} spins, for example, I_{1_X}, I_{1_Y}, I_{1_Z} I_{2_X}, I_{2_Y}, and I_{2_Z} for an 'N_{spins} = 2' system).

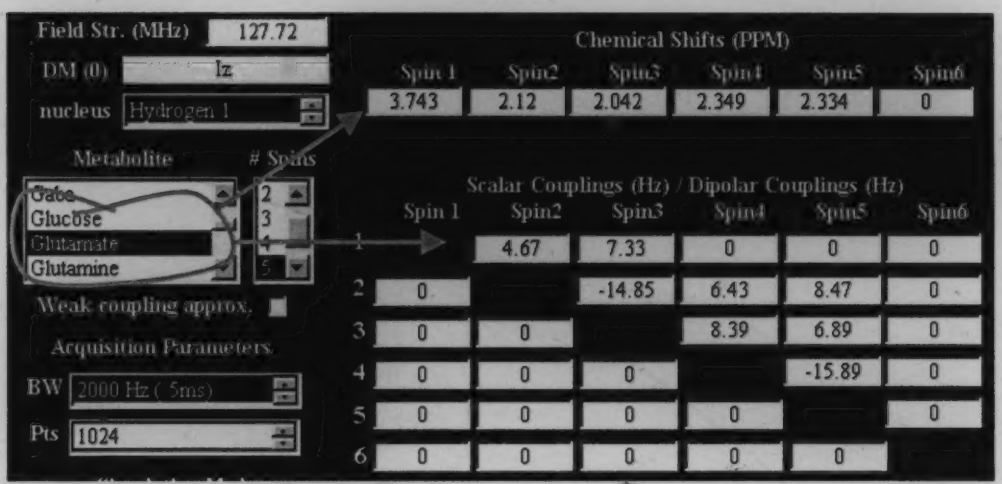

Figure AV-2 Specifying a metabolite spin system loads scalar coupling and chemical shift constants, shown here for glutamate, although user specified values can be manually entered. These constants, along with the field strength (MHz), completely define the free evolution Hamiltonian in a homogeneous main field.

A weak coupling approximation (i.e. $\mathcal{H}_{coup} = 2\pi J I_{1_Z} I_{2_Z}$) can be specified (see Fig. AV-2) to truncate the full strong coupling expression, $\mathcal{H}_{coup} = 2\pi J \mathbf{I_1} \cdot \mathbf{I_2}$, for all subsequent calculations. Specifying the nucleus defines the gyromagnetic ratio, γ, but does not alter the list of metabolites, although the infrastructure of the program supports an expansion to include heteronuclear systems of spins.

To define the Hamiltonian for the externally applied fields (r.f. and gradient pulses, and their associated delays) a pulse sequence editor (select **EDITOR** on the main window) allows up to 12 unique 'segments' (see chapter 2.2) to be defined. This seemingly arbitrary number of segments was selected to accommodate the representation of the in vivo MQF sequence, the most complex sequence considered in this thesis. Figure AV-3 displays the pulse sequence editor window.

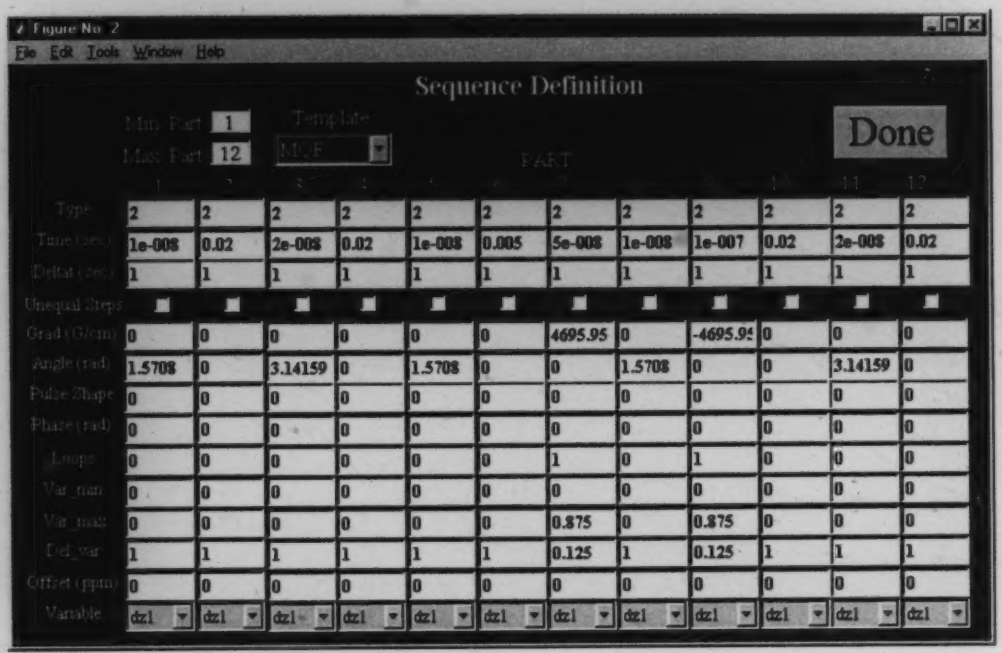

Figure AV-3 The pulse sequence editor window.

Each of the segments has an array of properties that define the Hamiltonian throughout that segment. The range of segments to be incorporated into the simulation is defined by *Min. part* and *Max. part*. Segment *type* (0, 1, or 2) corresponds, respectively, to a null segment (no evolutions), a time-dependent Hamiltonian and a time-independent Hamiltonian. Each segment has a total length, in seconds, defined by *Time*. A time increment (also in seconds) must be specified for time-dependent Hamiltonians (*Deltat*). If the steps throughout the time-dependent segment (i.e. *type* = 1) are unequal, *Unequal steps* must be indicated. In this case, the step sizes throughout the segment must be specified in a separate file. Presently, the simulator is equipped only for time-dependent r.f. pulse envelopes, specified with an index under *Pulse Shape*. A list of pulse shapes and corresponding indices is given at the end of the Appendix. The simulator automatically divides the pulse up into rectangular sub-segments (see chapter 2.4), according to the segment *Time* and *Deltat*. A magnetic field gradient can be specified (in G/cm) in the *Gradient* box. The tip angle of a time-independent (rectangular) pulse is specified in *Angle*, in radians, while the pulse phase (only constant phase pulses can presently be specified) for all pulses is entered in *Phase*, in radians. The frame of reference is always assumed to be the rotating frame (0 ppm) unless specified in *Offset*, in ppm. This option is useful primarily to offset spectrally selective pulses to excite target resonances, or offset slices in space (in the presence of a gradient).

To utilize the 'multiple value' option, to calculate multiple segment evolution operators, for a range of a segment property (see chapter 2.2), the *Loop* value must be set to 1 (otherwise 0). Presently, the segment *Time*, *Gradient* (dz1 on Fig.) or *Angle* can be

varied (specified in *Variable*), although this list of terms can readily be expanded to include any variable used to define a segment Hamiltonian. The range of values incorporated into the simulation are set with *Var_min*, *Var_max* and *Del_var*.

Several templates have been designed that when specified will load an array of segment properties that define standard pulse sequences, including the STEAM, PRESS and MQF experiments. For example, fig. AV-4 displays the specification of a double quantum filter in the editor window, along with the corresponding pulse sequence.

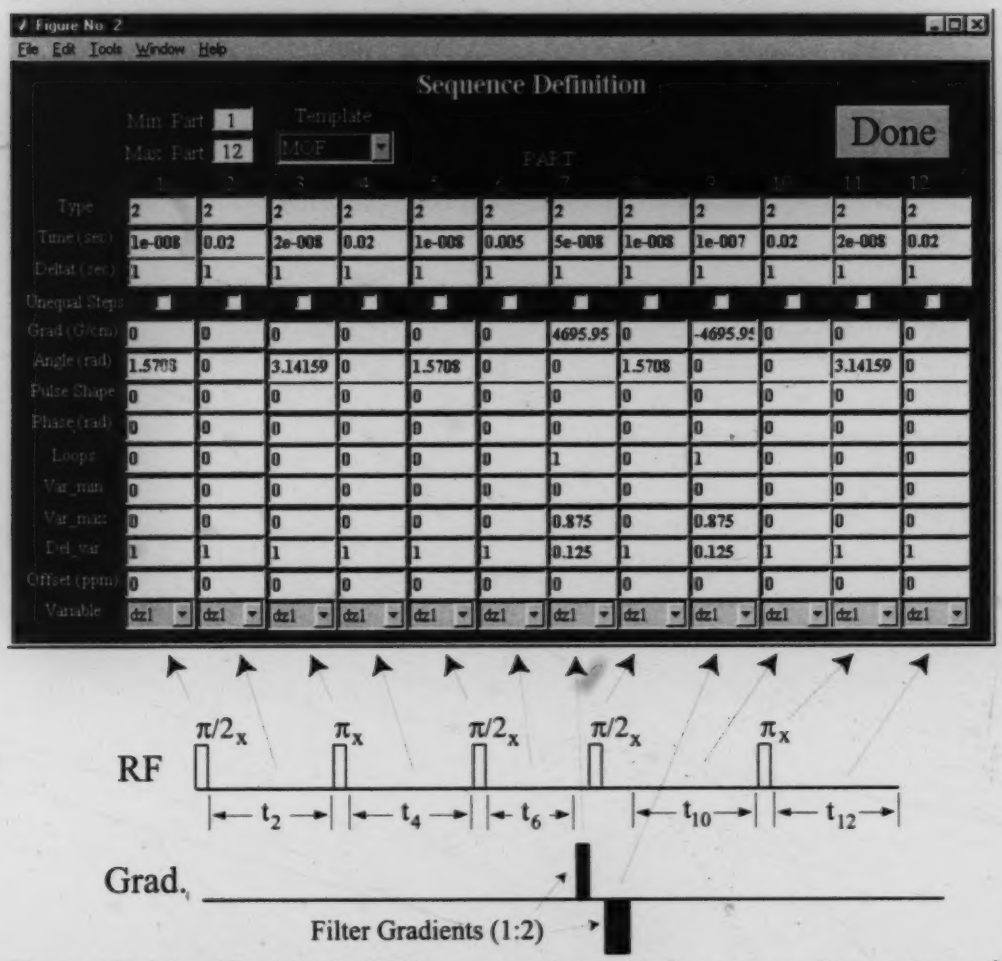
Figure No. 2
File Edit Tools Window Help
Sequence Definition
Min Part 1
Max Part 12
Template
MQF
Done
PART
Type 2 2 2 2 2 2 2 2 2 2 2 2
Time (sec) 1e-008 0.02 2e-008 0.02 1e-008 0.005 5e-008 1e-008 1e-007 0.02 2e-008 0.02
Deltat (sec) 1 1 1 1 1 1 1 1 1 1 1 1
Unequal Steps
Grad (G/cm) 0 0 0 0 0 0 4695.95 0 -4695.95 0 0 0
Angle (rad) 1.5708 0 3.14159 0 1.5708 0 0 1.5708 0 0 3.14159 0
Pulse Shape 0 0 0 0 0 0 0 0 0 0 0 0
Phase (rad) 0 0 0 0 0 0 0 0 0 0 0 0
Loops 0 0 0 0 0 0 1 0 1 0 0 0
Var_min 0 0 0 0 0 0 0 0 0 0 0 0
Var_max 0 0 0 0 0 0 0.875 0 0.875 0 0 0
Del_var 1 1 1 1 1 1 0.125 1 0.125 1 1 1
Offset (ppm) 0 0 0 0 0 0 0 0 0 0 0 0
Variable dz1 dz1 dz1 dz1 dz1 dz1 dz1 dz1 dz1 dz1 dz1 dz1
RF
π/2x
πx
π/2x
π/2x
πx
t2
t4
t6
t10
t12
Grad.
Filter Gradients (1:2)

Figure AV-4 Specification of a DQF sequence along with the corresponding sequence of r.f. pulses and gradients.

As shown in Fig. AV-4, to model the de-phasing and subsequent selective re-phasing of coherence orders selected by the filter gradient pair, several locations in space (8 individual points), over a complete cycle (2*pi radians), are included. In a field of ~4696 G/cm, applied for 5e-8 seconds, 8 points at 0.125 cm intervals (0:0.125:0.875) represent

one complete cycle (phase = γGrt = 2*pi*4259 radians/G/sec*4696 G/cm*1 cm*5e-8 sec = 2*pi radians).

Recall from chapter 2.2 that an evolution operator storage matrix is generated from the Hamiltonian(s) defined for each segment. For the previous example, that of the DQ filter, the evolution operator storage matrix will comprise 12 rows of operators (each of which has a dimension of 2^{Nspins} by 2^{Nspins}), for the 12 segments, and 8 columns of operators, for the 8 locations in space modeled in segments 7 and 9. The remaining segments (1,2,3,4,5,6,8,10,11 and 12) will each have a non-zero contribution only in the first of the eight columns. To combine these operators to generate the density matrix throughout and following the pulse sequence, a ***simulation mode***, selected on the main window, defines a set of instructions to be carried out following the generation of the storage matrix. These existing modes can be used, or the user can generate additional subroutines specific to a desired pulse sequence. The existing modes are listed below, and a few select modes are outlined in some detail to exemplify the general approach.

Simulation Modes – Combining the Evolution Operators

The evolution of the density matrix, from which the expectation values of the basis operators or the ultimate transverse magnetization are calculated, is evaluated using the following equation

$$\rho_n = V_n^{-1} \rho_{n-1} V_n. \qquad \text{(AV-1)}$$

The operator, V_n, is called the evolution operator, defined

$$V_n = U_n^{-1} \exp(1\mathcal{H}_{n_{diag}} t_n / \hbar) U_n, \qquad \text{(AV-2)}$$

where U_n and $\mathcal{H}_{n_{diag}}$ comprise the eigenvectors and eigenvalues, respectively, of the Hamiltonian of the n^{th} segment. These V_ns are calculated and stored in a larger matrix, and subsequently used to determine the density matrix throughout and following the pulse sequence. The *simulation mode* that is specified is a set of instructions for the calculation of either i) the expectation values of product operator basis terms or ii) the spin system FID, as a function of sequence properties such as inter-pulse timings or r.f pulse tip angles.

Presently, there exist 20 simulation modes, each described briefly below.

1) Single Average PO – This simulation mode is used to calculate a single density matrix and corresponding P.O. terms following a pulse sequence. The evolution operator storage matrix, Rtemp1, is reduced to a 2^{Nspins} by 2^{Nspins} matrix (Rtemp) for an N_{spins} system, or as large as a 2^{Nspins} by (2^{Nspins} x siz2) matrix if a variable parameter is specified

(with siz2 different values), the net response being the sum the 'siz2' density matrices following the pulse sequence. The sum of the multiple responses for the case of a specified variation (siz2>1) has application for the calculation of the integrated gradient response in one dimension, such as a spin-echo slice with spoilers and a slice gradient, or a gradient pair in a multiple quantum filter sequence.

Consider the response of a two-spin proton system (ω_1 = 1 ppm, ω_2 = 4 ppm, and J_{12} = 10 Hz) to a spin-echo pulse sequence with an ideal hard excitation pulse and a slice-selective refocusing pulse. Spoiler gradients are applied around the 180° pulse, and a slice gradient is applied concurrently with the shaped r.f. pulse, a numerically optimized sinc-like pulse (bandwidth =1500 Hz). The echo-time is set to $1/(2J_{12})$ = 50 ms to optimize the generation of anti-phase coherence.

Figure AV-5 Specification of a coupled two spin system, in an external field of strength 3 T.

The complete Hamiltonian is specified by defining the remaining external magnetic fields, including the r.f. pulses, gradients and associated delays, shown in Fig. AV-6.

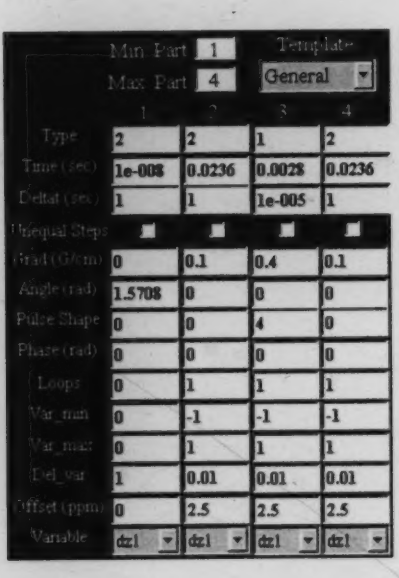

Figure AV-6 Specification of a spin-echo pulse sequence in the sequence editor window. The four segments include 1) a 10 ns hard $\pi/2$ excitation pulse, followed by 2) a 23.6 ms evolution in a 0.1 G/cm gradient. The position in the gradient, is calculated for –1 cm to 1 cm in 0.01 cm steps. (The *dz1* variable indicates that position in the gradient is the variable of choice). 3) The shaped refocusing pulse is 2.8 ms in length (sub-segmented in 280 rectangular components) and excites a 0.88 cm FWHM slice in the 0.4 G/cm slice gradient. The echo is completed with 4) a final 23.6 ms evolution, again in a 0.1 G/cm spoiler gradient. Note that all variable segments must have the same range of values, -1:0.01:1 cm in this case. The total echo length is 50 ms.

The density matrix calculated for this pulse sequence is the average of the individual density matrices calculated for the 201 locations in space –1:0.01:1 cm. The MATLAB™ code used to generate the density matrix and PO contributions is shown below. Rtemp1 is the evolution operator storage matrix of dimension (4 segements * 4) by (201 variations * 4) = 16 by 3216. Rtemp is a reduced for of Rtemp1, by combining the evolution operators for segments 1 to 4, but still with the 201 variations of the position in the gradient, giving rise to a 4 by 3216 matrix. Because the sum (average) of the resulting density matrices is the desired output, Eq. (AV-1) can be evaluated with a single matrix multiplication by changing the dimension of Rtemp with the routine flip.m.

```
Rtemp=dmform(Npartsmin,Nparts,Rtemp1,M,varsiz,siz2); % evolution operator matrix is combined to
form a condensed evolution matrix
b=flip(Rtemp,M); % change dimension of Rtemp
pold=b'*flip(poldenter*Rtemp,M)/siz2; % single density matrix following sequence is calculated
eval(resprogram(Nspins,:)) % P.O. response program is called
```

For the case of a hard pulse spin echo (TE =$1/2J_{12}$) and the spin system defined above, the PO term contributions following the pulse sequence shown below.

$$\begin{aligned} &\langle I_{1X}\rangle = -0.05 \ \langle I_{1Y}\rangle = 0.01 \ \langle I_{1Z}\rangle = 0.00 \ \langle 2I_{1X}I_{2Z}\rangle = 0.99 \ \langle 2I_{1Y}I_{2Z}\rangle = 0.00 \\ &\langle I_{2X}\rangle = 0.05 \ \langle I_{2Y}\rangle = 0.01 \ \langle I_{2Z}\rangle = 0.00 \ \langle 2I_{1Z}I_{2X}\rangle = 0.99 \ \langle 2I_{1Z}I_{2Y}\rangle = 0.00 \\ &\langle 2I_{1X}I_{2X}\rangle = 0.00 \ \langle 2I_{1X}I_{2Y}\rangle = 0.00 \ \langle 2I_{1Y}I_{2Y}\rangle = 0.00 \ \langle 2I_{1Y}I_{2X}\rangle 0.00 \ \langle 2I_{1Z}I_{2Z}\rangle = 0.00 \end{aligned} \quad \text{(AV-3)}$$

The influence of the slice selective refocusing pulse on a coupled spin system is a loss of signal and some coherence transfer, resulting from chemical shift induced voxel offsets and slice role-off. The PO term expectation values for the spin echo incorporating the slice-selective refocusing pulse are shown below, where all contributions are normalized to the signal excited from an uncoupled spin system with the same sequence.

$$\begin{aligned} &\langle I_{1X}\rangle = -0.03 \ \langle I_{1Y}\rangle = -0.23 \ \langle I_{1Z}\rangle = 0.00 \ \langle 2I_{1X}I_{2Z}\rangle = 0.72 \ \langle 2I_{1Y}I_{2Z}\rangle = 0.03 \\ &\langle I_{2X}\rangle = 0.03 \ \langle I_{2Y}\rangle = -0.23 \ \langle I_{2Z}\rangle = 0.00 \ \langle 2I_{1Z}I_{2X}\rangle = 0.72 \ \langle 2I_{1Z}I_{2Y}\rangle = 0.03 \\ &\langle 2I_{1X}I_{2X}\rangle = 0.00 \ \langle 2I_{1X}I_{2Y}\rangle = 0.00 \ \langle 2I_{1Y}I_{2Y}\rangle = 0.00 \ \langle 2I_{1Y}I_{2X}\rangle 0.00 \ \langle 2I_{1Z}I_{2Z}\rangle = 0.00 \end{aligned} \quad \text{(AV-4)}$$

The spatial origin of the coherence alteration caused by the slice selective pulse is displayed for simulation mode 3, **1D - Variable PO**, below.

2) **Single Average FID** – This simulation mode is identical to **Single Average PO**, expect the response is the free induction decay (FID), whose parameters are defined with a specified bandwidth and number of acquisition points. The FID is contained in the vector 'mag'.

3) **1D - Variable PO** – This simulation mode is very similar to the **Single Average PO** mode, the only difference is the discrete calculation of the PO expectation values versus the average value calculated with mode 1. The example previously considered using the **Single Average PO** mode is briefly re-visited using this multi-output mode.

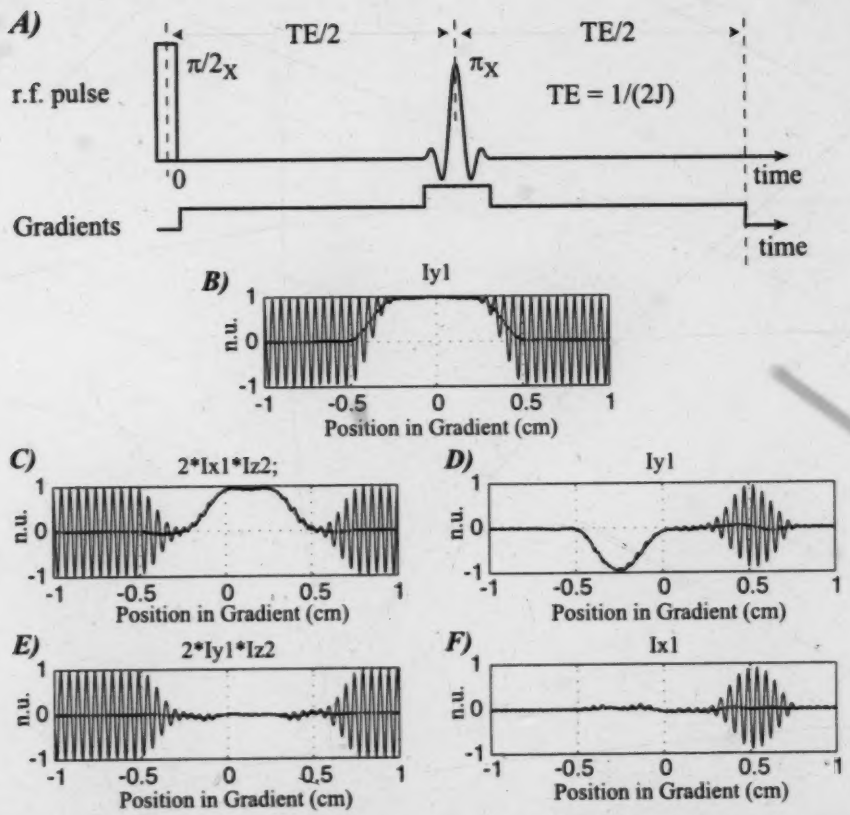

Figure AV-7 A) A spin-echo pulse sequence with a spatially selective optimized sinc refocusing pulse and a hard excitation pulse. B) The spatial distribution of I_Y magnetization excited by the sequence in A) for an uncoupled spin system, $\omega_1 = 0$ ppm. In C) to F), the spatial distribution of spin$_1$ transverse magnetization excited by the sequence in A) for a coupled spin system, J = 10 Hz, ω_1 = 1 ppm, ω_2 = 4 ppm, is displayed. The echo length is set at 1/2J to optimize the generation of anti-phase coherence. For each profile a local average filter has been applied to smooth the gradient-induced oscillations.

The alteration in the expectation values of the two-spin product operators, as a result of the slice-selective refocusing pulse (see Fig. AV-7), shown in Eqs. (AV-3) and (AV-4), are displayed above as a function of position in the gradient for a few select coherences. The expectation values calculated using simulation mode 1, **Single Average PO**, are identical the integrated values from the plots in Fig. AV-7 for each individual PO term.

4) **1D - Variable FID** - This simulation mode is identical to **1D - Variable PO**, expect the response is the free induction decay (FID), whose parameters are defined with a specified bandwidth and number of acquisition points. The FIDs are contained in the matrix 'mag'.

5) 2D - Variable PO - This simulation mode is identical to **1D - Variable PO**, expect two dimensions of variation in the basis PO terms can be calculated. The only limitation is that the variations must be sequential, for example, both the spin-echo timings and the refocusing pulse tip angle cannot be varied because the echo period *surrounds* the pulse in question. To group the simulation segments, to allow for the separation of the two sequential sets of segments to be varied, the file 'seqmode.m' must be edited to indicate the appropriate groupings. For example, consider the COSY pulse sequence, a two pulse experiment with an inter-pulse delay. It might be of interest to calculate the response of a coupled spin system to variations in both the inter-pulse delay, and the tip angle of the second r.f. pulse. The number of segment groupings is set with the variable 'seqgroup', equal to 2 in this case. Additionally, the vectors 'minpart' and 'maxpart' must contain the range of segments included in each of the' seqgroup' groupings. For the COSY sequence, setting minpart=[1 3 0 0 0] and maxpart=[2 3 0 0 0] indicates that the first group included segments 1 to 2 (excitation pulse and variable inter-pulse delay), and the second of the two groupings contains only the third segment (r.f. pulse of variable tip angle). The simulation output will be a matrix of expectation values for each of the PO terms. A third vector, called 'multiple', defines each of the 'seqgroup' groupings of segments as either a muli-variable grouping (value = 1), or a single-variable grouping (value = 0). For example, 'seqgroup' could have been set to 3 for this experiment, with minpart=[1 2 3 0 0] and maxpart=[1 2 3 0 0], with multiple=[0 1 1 0 0], while multiple must be set to [1 1 0 0 0] if only two seqgroup's are specified, as above.

6) **2D - Variable FID** - This simulation mode is identical to **2D - Variable PO**, expect the response is the free induction decay (FID), whose parameters are defined with a specified bandwidth and number of acquisition points. The FIDs are contained in the matrix 'mag'.

7) **PRESS 2D PO** - This simulation mode is identical to **2D - Variable PO**, with the minpart, maxpart and multiple vectors set up for the simulation of the PRESS sequence. The PRESS template, in the EDITOR window, is automatically loaded when this simulation mode is selected. The PRESS echo times, TE_1 and TE_2, or the position in the slice-selective refocusing pulse gradients can be varied. The later allows the distribution of coherences over two-dimensions of space to be calculated.

8) **PRESS 2D FID** – Identical to **PRESS 2D PO** expect FIDs instead of PO responses are calculated.

9) **PRESS 2D PO (slice)** - Identical to **PRESS 2D PO** expect a transformation matrix replaces each of the refocusing pulses. The transformation matrix must be loaded into the MATLAB™ workspace, and is then automatically utilized in the simulation.

10) **PRESS 2D FID (slice)** – Identical to **PRESS 2D PO (slices)** expect FIDs instead of PO responses are calculated.

11) **STEAM 2D PO –** The response of spin systems to variations in the STEAM mixing and echo times are calculated with this simulation mode. The influence of the echo spoiler gradients is automatically entered and need not be edited. The simulation output will be a matrix of expectation values for each of the PO terms.

12) **STEAM 2D FID** – Identical to **STEAM 2D PO** expect FIDs instead of PO responses are calculated.

13) **STEAM 2D PO (slice)** - - Identical to **STEAM 2D PO** expect a transformation matrix replaces the second and third $\pi/2$ pulses. The transformation matrices, a different one for each of these two pulses, must be loaded into the MATLAB™ workspace, and is then automatically utilized in the simulation.

14) **STEAM 2D FID (slice)** – Identical to **STEAM 2D PO (slices)** expect FIDs instead of PO responses are calculated.

15) **MQF 2D PO –** The response of spin systems to variations in the multiple quantum filter mixing and echo times are calculated with this simulation mode. The influence of the filter gradients is automatically entered and need not be edited, save to change to the order of the filter, which is done by varying the length of the second of the pair gradients to the desired order (multiple of the length of the first gradient). The default is a double quantum filter. Note that only one of the mixing time or the first echo time (preparation time) can be varied in a given simulation. The simulation output will be a matrix of expectation values for each of the PO terms.

16) **MQF 2D FID** – Identical to **MQF 2D PO** expect FIDs instead of PO responses are calculated.

17) **MQF 2D PO (slices)** - Identical to **MQF 2D PO** expect a transformation matrix replaces each of the refocusing pulses. The transformation matrix must be loaded into the MATLAB™ workspace, and is then automatically utilized in the simulation.

18) **MQF 2D FID (slices)** – Identical to **MQF 2D PO (slices)** expect FIDs instead of PO responses are calculated.

19) **COSY 2D PO** – The COSY sequence is a two pulse experiment with an inter-pulse delay. This simulation simply the **1D - Variable PO** mode set up to run the COSY experiment. The simulation output will be a vector of expectation values for each of the PO terms.

20) **COSY 2D FID** –This simulation simply the **1D - Variable FID** mode set up to run the COSY experiment. The simulation output will be a series of FIDs, stored in the matrix 'mag'. A two-dimensional Cosine transform of this matrix directly yields the 2D correlation spectrum.

Simulation Results – Spectra and Product Operators

The output of the simulations is either the expectation values of PO terms (i.e. the density matrix) or the resulting FID (spectrum). Figure AV-8 displays the RESULTS window, selected from the main simulation window following completion of the calculations, used to display the FIDs and expectation values of the spin operators.

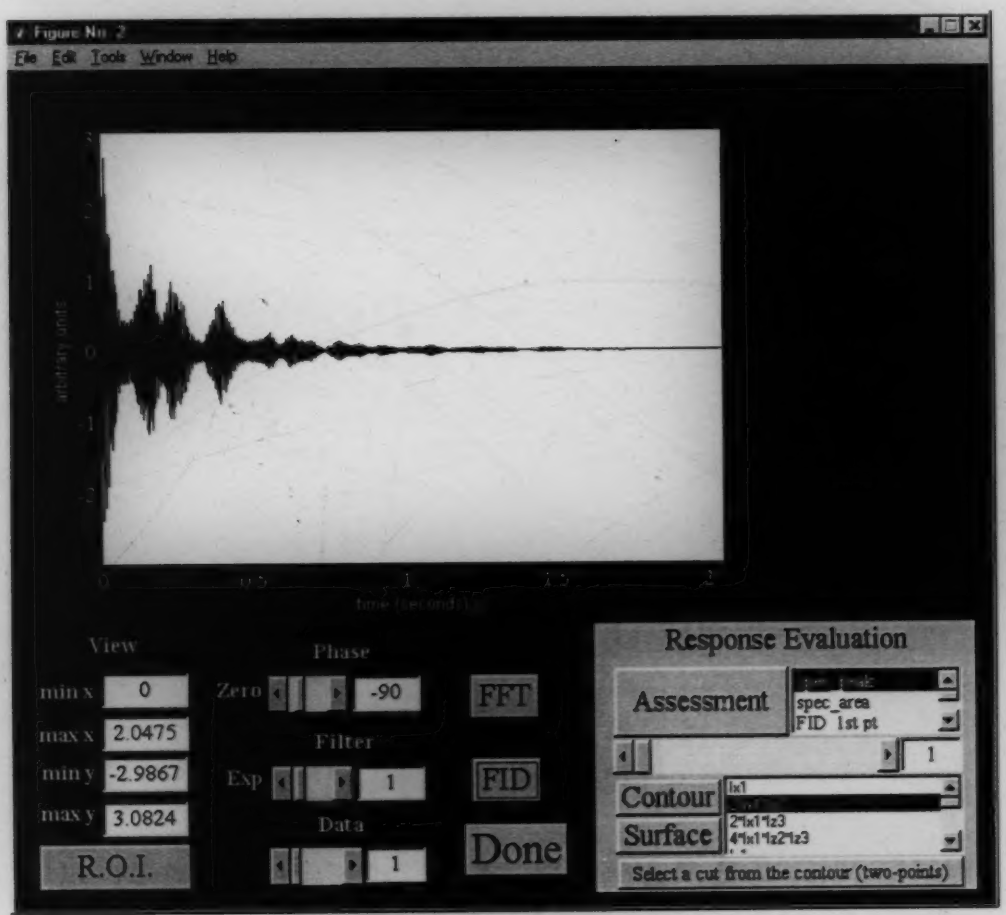

Figure AV-8 The simulation results window.

Figure AV-8 displays a pulse acquire free induction decay excited from the aspartate spin system, with 4096 acquisition points and a bandwidth of 2000 Hz ($\Delta t = 0.5$ ms), and a 1 Hz exponential line-broadening. The simulation output is either FIDs, as shown above, or PO expectation values. Treatment of these two output forms are described separately below.

Free Induction Decays - Spectral Evaluation

The RESULTS window will display the FID (select FID) or spectrum (select FFT) contained in the 'mag' vector/matrix. If more than one FID is collected, the DATA slider can be used scroll though the FIDs/spectra. An exponential line-broadening can be applied, as can a zero order phase variation. The results plot axes range can be varied with min/max values or by selecting a region of interest with the ROI pushbutton. There are three modes of assessment of the resulting spectra, using 1) peak value of the spectrum in the ppm range slected, 2) area under the spectrum in the ppm range selected, or 3) the first point in the FID (equal to total area under the spectrum). After selecting the mode of assessment, pressing the ASSESSMENT pushbutton will create a vector/matrix (depending on the simulation mode used to generate the results. i.e. 1D or 2D of variation) of values, and plot the vector/first row of the matrix. If the simulation resulted in a single spectrum, no assessment is required, for 1D of variation, the single vector is plotted on the results axis, and for 2D of variation, the individual vectors that comprise the matrix of results can be scrolled though (slider under the assessment pushbutton), or a contour or surface plot of the matrix can be plotted. If a contour is plotted, a cut between any two points can be plotted with the 'select a cut from the contour' pushbutton. For processing outside of the RESULTS window, the FIDs are always stored in the array 'mag', and the assessed data in the 'assessment' array.

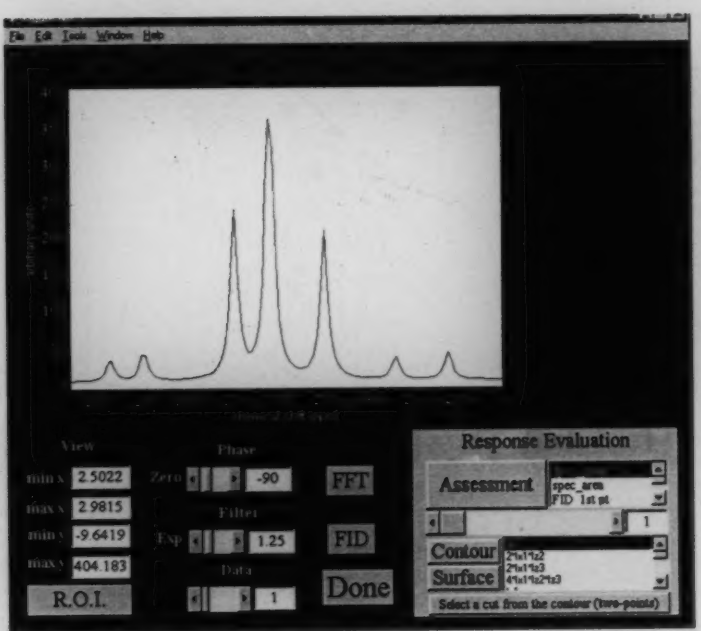

Figure AV-9 The Results window displays an aspartate spectrum, one of a 2D array of spectra acquired with excitation by the PRESS sequence, with variations in both echo times, TE_1 and TE_2. Viewing the spectrum allows a ppm range to be manually selected for assessment of the spectral response in that range, allowing single lines to assessed if desired.

Figure AV-9 displays an aspartate spectrum, and the ppm range to be used to assess the response, the peak value of the spectrum in the range of 2.5 to 2.98 ppm, to variations in the PRESS sequence timings, shown in Fig. AV-10.

Figure AV-10 The Results window displays a contour plot of the peak value of the aspartate AB multiplet, shown in Fig. AV-9, as a function of PRESS echo times, for TE_1 = 0:4:100 ms, and TE_2 = 0:4:100 ms. The contour is normalized to the peak value of the contour data.

Product Operator Evaluation

Half of the simulation modes provide, as an output, the expectation values of the basis product operator components. Like the FID response, the results are stored in vectors or matrices, depending on the simulation mode incorporated. These simulation modes have a single assessment mode, the direct display of the vectors or matrices as described in the previous section, although the responses are for the large of array of basis PO terms, a list that grows by factors of 4 with each increase in the number of spins in the system. Figure AV-11 displays the expectation value of one the 64 aspartate (ABX) basis PO terms, as a function of PRESS timings TE_1 and TE_2, for a range of timings from 0 to 100 ms along each axis.

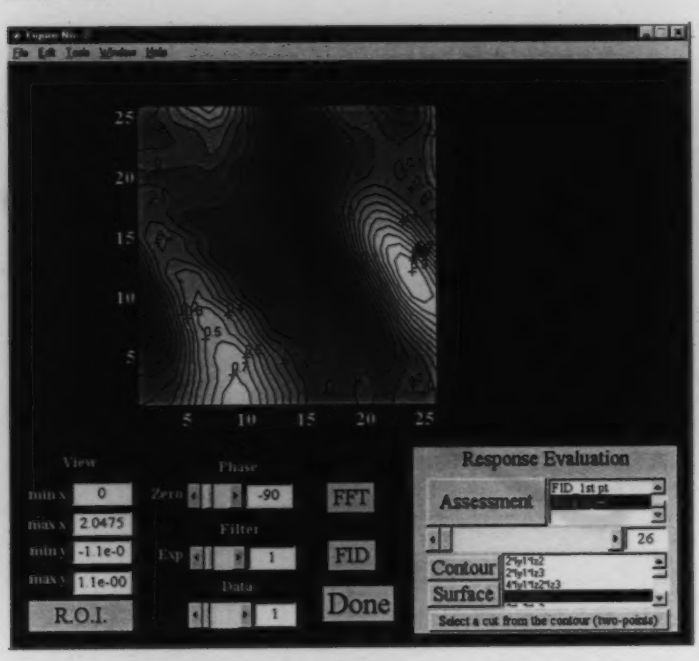

Figure AV-11 The Results window displays a contour plot of expectation values of the ABX spin operator $2I_{1Z}I_{2X}$, as a function of PRESS echo times for TE_1 = 0:4:100 ms, and TE_2 = 0:4:100 ms. The contour plots for the remaining PO terms can be viewed with selection from the PO listbox.

Radio-Frequency Pulses

The list of pulse envelopes that can selected directly in the EDITOR presently includes: 1) sinc-Gaussian, 2) BURP (Band-Selective Uniform Phase) excitation pulse, 3) blank, 4) Optecho refocusing pulse (commonly used on scanner), 5) blank, 6) hyperbolic secant, 7) optimized sinc (90), 8) alternate optimized sinc (90), 9) 2^{nd} alternate optimized (90), 10) Gaussian, 11) sinc-hamming and 12) Dante (including a binomial refocusing pulse). The pulse shape is specified by index entered under *Pulse Shape*. The user should examine the files that define the pulse envelopes to learn how to specify any desired shape.